Kinematics and stellar populations of early-type dwarf galaxies in the Virgo cluster: how relevant is pre-processing in galaxy groups?

Bahar Bidaran

Dissertation

submitted to the

Combined Faculties of the Natural Sciences and Mathematics

of the Ruperto-Carola-University of Heidelberg. Germany

for the degree of

Doctor of Natural Sciences

Put forward by

Bahar Bidaran

born in: Tehran, Iran

Oral examination: November 12, 2021

Kinematics and stellar populations of early-type dwarf galaxies in the Virgo cluster: how relevant is pre-processing in galaxy groups?

Referees: Prof. Dr. Eva K. Grebel

Prof. Dr. Jochen Heidt

Abstract

This thesis is dedicated to answering one particular question: how relevant is pre-processing in shaping present-day properties of early-type dwarf galaxies (dEs) in massive clusters? With the intention of doing so, we present the analysis of the kinematics and stellar population properties of nine early-type dwarf galaxies (dEs) of the Virgo cluster. According to the results of Lisker et al. (2018), these nine dEs were accreted onto Virgo as gravitationally bound members of a massive galaxy group ($M_\star \sim 10^{13}$ M$_\odot$) along the observer's line of sight about 2-3 Gyr ago. We confirm a similar accretion time by investigating their distribution on the projected phase-space diagram. We performed full-spectrum fitting on the spatially binned MUSE/VLT data of these dEs to investigate their kinematics. We quantified their stellar rotation using specific angular momentum (λ_R) and derived diverse kinematic properties in our sample, despite their similar accretion time onto Virgo and stellar mass range. While half of our sample members show higher degrees of rotation, similar to low-mass star-forming field galaxies, the rest show kinematic profiles comparable with Virgo dEs with relatively larger average infall time. Furthermore, we employed Lick absorption features in each dEs' MUSE data and performed a four-step fitting procedure (based on a χ^2 minimization approach) to derive their stellar population properties. We detected relatively younger and metal-poorer stellar populations in these dEs that are noticeably α-enhanced than equally massive dEs in the Virgo and Coma clusters. Similar to other studies on cluster dEs, we detected flat age gradients, negative metallicity gradients, and positive [α/Fe] gradients for our sample dEs. By performing the full-spectrum fitting technique on their averaged MUSE spectra, we detected the presence of a significant peak in the star formation activity of some of our sample members, occurring at an epoch consistent with or even more recent than their accretion time onto Virgo. Through this thesis, we interpret our results by concurrently considering the role of pre-processing and early effects of the Virgo's environment in shaping the observed properties of this unique Virgo dEs sample.

Zusammenfassung

Diese Doktorarbeit ist der Beantwortung der folgenden, spezifischen Frage gewidmet: Wie relevant ist Vorverarbeitung für die Entwicklung der heutigen Eigenschaften von elliptischen Zwerggalaxien in massereichen Galaxienhaufen? Dazu präsentieren wir eine Analyse von neun elliptischen Zwerggalaxien (engl. dwarf ellipticals, dEs) im Virgo-Galaxienhaufen bezüglich ihrer Kinematik und der Eigenschaften ihrer stellaren Populationen. Laut der Ergebnisse von Lisker et al. (2018) sind diese neun dEs vor 2-3 Gyr als gravitativ gebundene, massereiche Galaxiengruppe ($M_* \sim 10^{13}$ M$_\odot$) entlang der Beobachtersichtlinie in den Virgo-Galaxienhaufen eingefallen. Wir bestätigen eine ähnliche Akkretionszeit durch die Untersuchung ihrer Verteilung im projizierten Phasenraumdiagramm. Wir führen einen Fit des gesamten Spektrums aus räumlich eingeteilten MUSE/VLT Daten dieser dEs durch, um ihre Kinematik zu untersuchen. Wir haben ihre stellare Rotation mithilfe ihres spezifischen Drehimpulses (λ_R) quantifiziert und diverse kinematische Eigenschaften unseres Samples hergeleitet. Trotz ihrer ähnlichen Akkretionszeit in den Virgo-Galaxienhaufen und ihrer ähnlichen stellaren Masse weisen die Hälfte unserer Samplemitglieder einen höheren Grad an Rotation auf, ähnlich zu Feldgalaxien mit niedriger Masse und aktiver Sternentstehung, während die restlichen Samplegalaxien kinematische Profile aufweisen, die vergleichbar zu anderen Virgo dEs mit relativ frühen mittleren Einfallzeiten sind. Außerdem haben wir Lick Absorptionsmerkmale in den MUSE Daten aller dEs angewendet und einen vierstufigen Fit-Prozess (basierend auf einem Ansatz für χ^2 Minimierung) durchgeführt, um Eigenschaften ihrer stellaren Populationen herzuleiten. Im Vergle-

ich zu anderen dEs gleicher Masse im Virgo- oder Coma-Galaxienhaufen konnten wir in diesen dEs relativ jüngere und metallärmere stellare Populationen mit einem merklich höheren Aufkommen an α-Elementen nachweisen. Ähnlich zu vorherigen Studien zu dEs in Galaxienhaufen haben wir flache Altersgradienten, negative Metallizitätsgradienten und positive $[\alpha/\text{Fe}]$-Gradienten für die dEs unseres Samples festgestellt. Durch die Anwendung von Methoden zum Fitten des gesamten Spektrums auf die gemittelten MUSE Spektra konnten wir feststellen, dass einige unserer Samplegalaxien besonders ausgeprägte Höchstwerte in ihren Sternentstehungsaktivitäten aufweisen. Der Zeitraum, in dem diese auftreten, stimmt mit ihrer Akkretionszeit in den Virgo-Galaxienhaufen überein und könnte möglicherweise darauf hinweisen, dass sie sogar noch früher in den Galaxienhaufen eingefallen sind. Wir interpretieren unsere Ergebnisse in dieser Doktorarbeit, indem wir zugleich den Einfluss von Vorverarbeitungsprozessen, sowie von frühen Umgebungseffekten des Virgo-Galaxienhaufens auf die Entwicklung von beobachteten Eigenschaften dieses besonderen Samples von Virgo dEs betrachten.

To my parents and brother,

for their unconditional love and constant support

Contents

List of figures

List of tables

"The Milky Way is nothing else but a mass of innumerable stars planted together in clusters".

— Galileo Galilei, "Sidereus Nuncius" in 1610

1

Introduction

On 26 April 1920, a famous discussion known as "the Great Debate" took place between Heber Curtis and Harlow Shapley. The nature of the so-called spiral nebulae was one of the main concerns of their discussion. While Shapley believed that observed nebulae were located in the outskirts of the Milky Way, thus were part of our home galaxy, Curtis suggested that observed spiral structures were large and distant galaxies. Eventually, Edwin Hubble settled the debate in 1924 with his remarkable work that opened the door to hundreds and thousands of beautiful distant worlds in the Universe. This thesis is about a group of nine distant low-mass galaxies, known as dwarf galaxies (or Nebulae if I were sitting among the Great Debate audience). Here you will read their tale, from their previous small host halo to the Virgo cluster. Here I try to address lifetime questions, such as: How do dwarf galaxies form, and how would their journey until their current halo affect their properties?

1.1 Galaxies: Islands of baryons and dark matter

Baryonic and dark matter are the building blocks of a typical galaxy. Galactic baryons consist of dust, gas, and different types of stars that all together sit inside the galaxy's potential well, which is defined by its baryonic mass and dark matter component. The relative fraction of these components changes during a typical galactic lifetime for various reasons. This section is a brief review of galactic structures and properties of their colonies in the Local Universe.

1.1.1 Galaxies from a close perspective

Stars: A typical galaxy contains about 10^6 to 10^{12} stars, while hydrogen and helium predominate the total mass of the interstellar medium (ISM). Once the proto-galaxy grows sufficiently massive, gas cooling becomes more efficient, and the first generation of stars, known as "Population

III", forms. Population III includes hot stars without metals that have relatively short lifetimes and are essential for slightly enriching the galactic ISM. The "Population II" are metal-poor stars that have been formed in the early phases of galactic evolution and cover a wide range of ages and stellar masses. Population II stars consist of hydrogen, helium, and a small fraction of metals (i.e., elements heavier than helium). Massive Population II stars convert their helium to heavier elements such as C, O, Ne, Mg, Si, S, Ar, and Ca through the alpha-process (thus, products are known as alpha-elements). The stellar evolution of massive Population II stars ends as Type II supernovae, which play a vital role in enriching the ISM. On the other hand, iron-peak elements (such as Fe, Cr, Co, Ni, Cu, and Mn) are by-products of Type Ia supernovae in binary systems whose evolution takes place on noticeably different timescales than Type II supernovae (e.g., Tinsley 1979; Greggio and Renzini 1983). From such metal-rich ISM "Population I" stars form. They are young and metal-rich stars, similar to our Sun, and are more likely accompanied by a planetary system. Population I stars can be observed in the spiral arms or thin disks of star-forming galaxies (for a general review: Peletier 2013).

Inside a galaxy, and based on the system's entire history, stars can move on collisionless orbits with different characteristics. Orbits of stars inside a system can have triaxial or spheroidal shapes. These stars are on random motions, which is expected in "pressure-supported" systems. On the other hand, stars in a "rotation-supported" system follow flat and disk-like orbits with axisymmetric shapes (e.g., Cappellari 2016; Li et al. 2018).

Gas: As an indispensable ingredient for star formation in galaxies, gas can be found in three different forms: ionized gas, atomic gas, and molecular gas. Ionized gas can be found in the hot, diffuse, and low-density regions of the ISM, where UV photons of massive stars (such as O and B) can heat up the environment and shape the HII regions. The atomic hydrogen (the most dominant type of neutral gas in the galaxy) can be traced by the HI 21 cm line in both absorption (tracing cold neutral medium; Mebold et al. 1982) and emission (tracing warm neutral medium; Jenkins 2013) states. In most of the galaxies, the neutral gas is extended beyond the optical disk(e.g., about 30 kpc away from Galactic center in Milky Way; Diplas and Savage 1991). Inside giant molecular clouds, with typical sizes of 5 to 200 pc (Murray 2011), resides the cold ($\sim$10-20 K) and molecular H_2 gas, which can be traced by CO, the second most dominant molecule of ISM (Bolatto et al. 2013). The densest molecular clouds are known as the cradle of star formation in galaxies.

Dust: About one percent of ISM's total mass consists of dust grains with the typical size of 0.1 micrometer (Boulanger et al. 2000). Dust is a vital catalyzer for molecule formation in the ISM (particularly H_2) as it balances the ISM's temperature by absorbing up to half of the stellar light and UV radiation. Dust grains are mostly composed of silicon and carbon and are formed in supernovae, envelopes of planetary nebulae, and red giant stars. They re-emit their absorbed energy in the far-infrared and shape the so-called dust continuum emission (Draine 2003).

Dark matter: The possibility of galaxies being embedded in a non-luminous matter first came under the spotlight in the 1880s and later gained attention by observed discrepancies between baryonic gravitational forces and measured velocity dispersions in the Coma cluster (Zwicky 1933). Later on, several studies shed light on the peculiar behavior of the rotation curves at larger radii of spiral galaxies. In a spiral galaxy, the stellar mass density decreases

with the increasing galactocentric distance. Thus, according to Kepler's Second Law and under the assumption of mass to light ratio being unity, the rotational curve of the system (traced by the luminous mass) is expected to decrease at larger galactocentric distances. Despite such expectations then, observations of spiral galaxies showed that the rotation curve of galaxies at high galactocentric distances remains flat, but not decreasing (Babcock 1939; Freeman 1970; Rubin et al. 1978). The presence of a non-luminous, collisionless, and non-baryonic halo that surrounds the main body of the galaxy has been used, ever since, to explain such observed phenomena. A component that is not visible to observers, thus named "dark matter". Dark matter plays a vital role in shaping the galactic potential well and is believed to be perturbed via tidal interactions within dense clusters and galaxy groups (e.g., Pasquali et al. 2019; Niemiec et al. 2019).
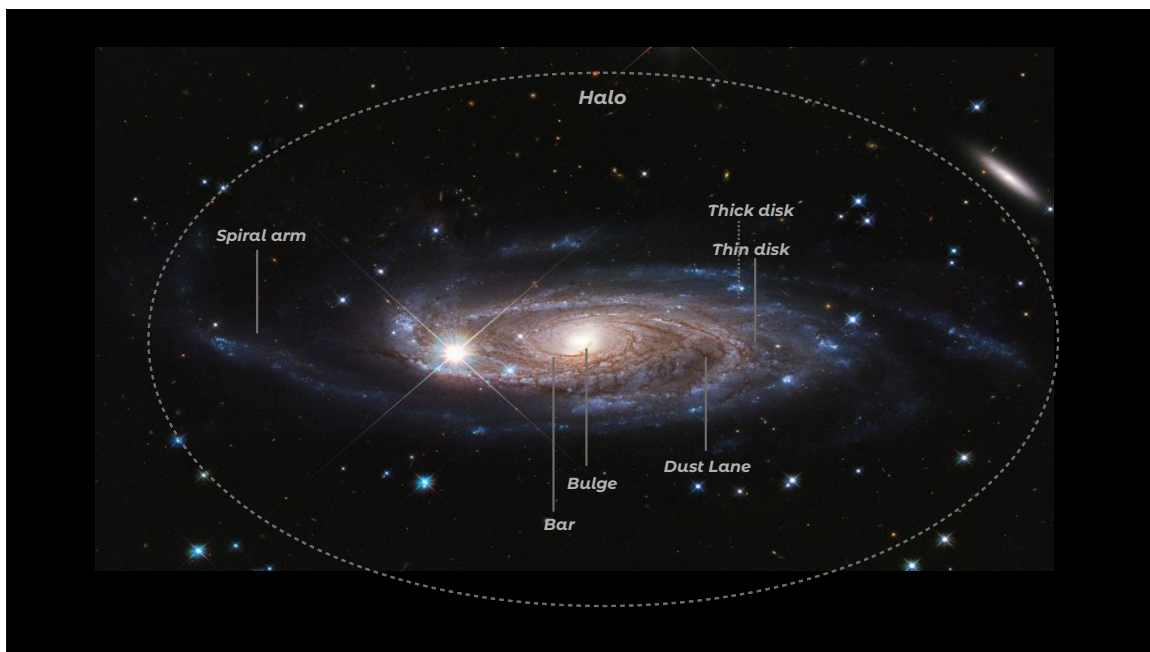
Figure 1.1.1: UGC2885- a barred spiral galaxy in the northern constellation of Perseus. This picture has been released by the Hubble Space telescope to mark its 30th anniversary. Galaxy photo Credit: B. Holwerda/NASA/ESA

As shown in Fig.1.1.1, a given galaxy may feature substructures that are briefly introduced in the following:

Bulge: In the very central part of spiral galaxies sits the bulge, a compact spheroidal component with high stellar density and complex kinematic structure (Gómez et al. 2016). Based on their formation sequence, bulges are divided into two groups: classical bulges and pseudo-bulges. Mergers at high redshifts can destroy the stellar disk and heat the orbital motion of stars in the central part of the merged system. Thus they form classical rotating bulges Naab and Trujillo (2006); Hopkins et al. (2010) with smooth light profiles and characteristic high Sersic index (n>2). Classical bulges are usually old and gas-free. On the other hand,

pseudo-bulges are characterized by their younger stellar population and low Sersic index (n<2) (Fisher and Drory 2008). During the secular evolution of the galaxy, gas and disk materials can lose their angular momentum and be pushed to the central part of the galaxy by bars and spiral arms. The entire mechanism consequently forms pseudo-bulges (Kormendy and Kennicutt 2004).

Disk: The most prominent feature in late-type galaxies is the disk. It hosts a significant fraction of galactic baryonic matter and can be described with exponential surface brightness radial profile (Freeman 1970). So far, the formation of disks has been the subject of several long-standing studies. Some simulations show that consideration of internal galactic feedback, including supernova explosions, can be one possible way of creating disks in galaxies (for other possible formation channels, please check: Fall and Efstathiou 1980; Dalcanton et al. 1997; Mo et al. 1998; van den Bosch 2002). Disks often have high radial-to-vertical axial ratios (ranging from 4 to 6.67) and can be further divided into two sub-parts of thick and thin disks. Gas, dust, young stars, and star clusters are embedded inside the thin disk, building up a young and metal-rich stellar population Marsakov et al. (2011). Spiral arms and ongoing star formation are embedded within the galaxy's thin disk. In contrast to the thin component, the thick disk contains old and metal-poor stars (Majewski 1993) and has bigger scale heights, mainly due to heated stellar orbits Chiba and Beers (2000). Theoretical studies suggest mergers (minor mergers: Quinn et al. 1993; Villalobos and Helmi 2008) and (gas-rich merger: Jones and Wyse 1983; Brook et al. 2004, 2005; Bournaud et al. 2009), accretion of satellites (Statler 1988; Abadi et al. 2003), stellar radial migration (Schönrich and Binney 2009; Binney and Tremaine 2008) and instabilities of bar structure (Minchev and Famaey 2010) as possible channels of thick disk formation. Disks have also been detected in massive early-type galaxies (Krajnović et al. 2011).

Bar: Once stars diverge from their circular orbits, they can get trapped in more elongated ones and form bars in the center of disk galaxies (Sparke and Gallagher 2000). Bars can be detected in around 60 percent of spirals and up to 70 percent of disk-shaped galaxies (Eskridge et al. 2000). They can either be pristine structures (formed due to secular evolution of the galaxy) or tidally induced ones (resulting from mergers) (e.g., Mastropietro et al. 2005; Łokas et al. 2016; Kwak et al. 2019; Cavanagh and Bekki 2020). On average, bars host an older stellar population compared to the galactic disk (Neumann et al. 2020). Recent studies have revealed that while bars play a positive role in fueling star formation of central stellar clusters or the active galactic nuclei (AGN) of their hosts, they are also responsible for quenching star formation in the inner regions of disks (e.g., Neumann et al. 2020).

Stellar halo: A diffuse and extended stellar halo often surrounds the galactic disk in late-type galaxies. A typical stellar halo includes only less than one percent of the total galactic luminous mass. Metal poor and ancient stars and spherical stellar populations, such as globular clusters, populate stellar halos. Stellar remnants of interacting or disrupted satellites can also be found in this diffuse part of a given galaxy. Stellar halos are pressure-supported substructures and are believed to be formed during the early phases of galactic formation (Sommer-Larsen et al. 1997).

1.1.2   An overview on the classification of galaxies

To this date, around two trillion galaxies have been identified in the observable Universe. While some of the observed galaxies resemble our home, the Milky Way, others manifest different shapes and structural properties. Part of this difference is due to the nature of these giant structures, and part is caused by their orientation relative to our observing line of sight. Our primary and extensive knowledge of the formation and evolution of galaxies comes from classifications based on their structural properties, or commonly known as their "morphology".

Morphological classification of galaxies started in the early 20th century by visual inspection of observed images of galaxies in the Local Universe (e.g., pioneering work of Max Wolf in 1909, Heidelberg). In 1926, Edwin Hubble developed a morphological classification system based on four types of galaxies: irregulars, lenticulars, spirals, and ellipticals (Hubble 1926, 1936). To shape the diagram, Hubble separated ellipticals (featureless galaxies with relatively smooth light profiles) from spirals (those with spiral patterns connected to bright centers). He placed elliptical galaxies on the left side of the diagram and divided spiral galaxies into two branches on the right side, featuring barred (lower branch) and normal (upper branch) spiral galaxies. Early on, Hubble's diagram was regarded as a galactic evolutionary sequence. Hence, galaxies on the left and right side of the diagram were denoted as "early-types" and "late-types", respectively. Hubble's primary classification system, "The Hubble sequence of Galaxies" (also known as the "tuning fork"), is the main constituent of classification systems that are used even today. It is essential to mention that Hubble's classification works best for galaxies up to redshift (z) $\sim$ 2. Above this threshold, other classes of galaxies and very faint features are observed. Later on, Hubble's classification system was revised by a number of authors, including de Vaucouleurs (1977); Kormendy (1982); van den Bergh (1976); Kormendy and Bender (2012). In 1974, de Vaucouleurs included galaxies with rings to the classification. In 1996, Kormendy et al. revised the diagram by classifying elliptical galaxies based on their isophote shapes. In Fig.1.1.2, the Hubble classification scheme, revised by Kormendy and Bender (1996), is presented.

Classification of galaxies based on their kinematic structures is another approach that has been recently developed. The latter was possible after developments of new technologies and improvements of spectrographs that allow observers to trace galaxy substructures at higher resolution. In this classification approach, the rotation of a given galaxy can be quantified by its projected specific angular momentum (λ_R):

$$\lambda_R = \frac{\sum_{i=1}^{N} F_i R_i |V_i|}{\sum_{i=1}^{N} F_i R_i \sqrt{V_i^2 + \sigma_i^2}} \tag{1.1}$$

where R_i, F_i, V_i and σ_i are galactocentric distance (to the photometric center), average flux, rotational velocity, and velocity dispersion per each spatial bin i, respectively (Emsellem et al. 2007, 2011). In this regard, galaxies with $\lambda_R > \sqrt{0.31}\epsilon$ (ϵ is the ellipticity) are classified as fast rotators, and those below this threshold are classified as slow rotators (Emsellem et al. 2011). Fig. 1.1.3 shows the distribution of 300 galaxies from the CALIFA survey (Sánchez et al. 2012a) on the V/σ-ϵ and λ_R-ϵ diagrams (taken from Falcón-Barroso et al. 2019). The solid line
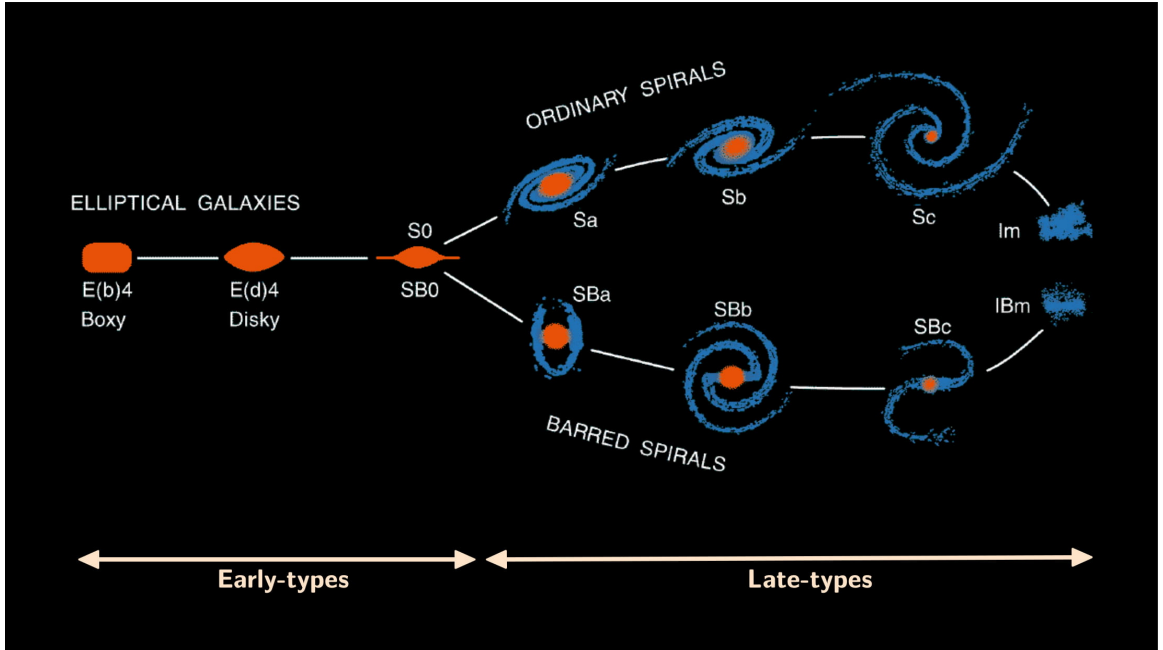
Figure 1.1.2: Revised Hubble sequence diagram by Kormendy and Bender (1996). Elliptical galaxies on the left side are referred to as early-type galaxies. On the right side and based on the presence/absence of barred structures, spiral galaxies are divided into two branches. Spiral galaxies are referred to as late-types. Image is taken from Kormeny's website: https://chandra.as.utexas.edu/tuningfork.html.

corresponds to the separating threshold between slow and fast rotators ($\lambda_R = \sqrt{0.31\epsilon}$), and the dashed line marks the revised version of this separation by Cappellari (2016). In both panels, CALIFA galaxies are color-coded based on their Hubble types and are compared with galaxies in the ATLAS^{3D} survey (gray crosses) (Emsellem et al. 2011). Based on the distribution of galaxies in the two panels of Fig. 1.1.3, late-type galaxies are fast-rotating systems (traced with blue and purple circles). On the other hand, more complex internal kinematics have been detected for early-type galaxies. The dispersed distribution of early-types (denoted by red and orange circles) on both sides of the threshold endorses such complexity.

1.1.3   An overview on the properties of galaxies

Properties of galaxies can be best understood with respect to three parameters: their star formation rate as a function of cosmic time, stellar mass, and the local environment. The first galaxies formed between 500 Myr to 1 Gyr after the Big Bang; an epoch called cosmic dawn (Fan et al. 2006). Based on the standard Λ cold dark matter (ΛCDM) scenario, the first galaxies were formed as low-mass systems, with properties similar to present-day dwarf galaxies. Based on this picture, low-mass galaxies then grew and built more massive systems, either through gas accretion from the cosmic web or mergers. Around z∼6, galaxies started to form high-density regions known as the "proto-clusters". The cosmic star formation density (SFRD) reached its peak at z∼2, which is known as the epoch of cosmic noon. Galaxies observed in this epoch are
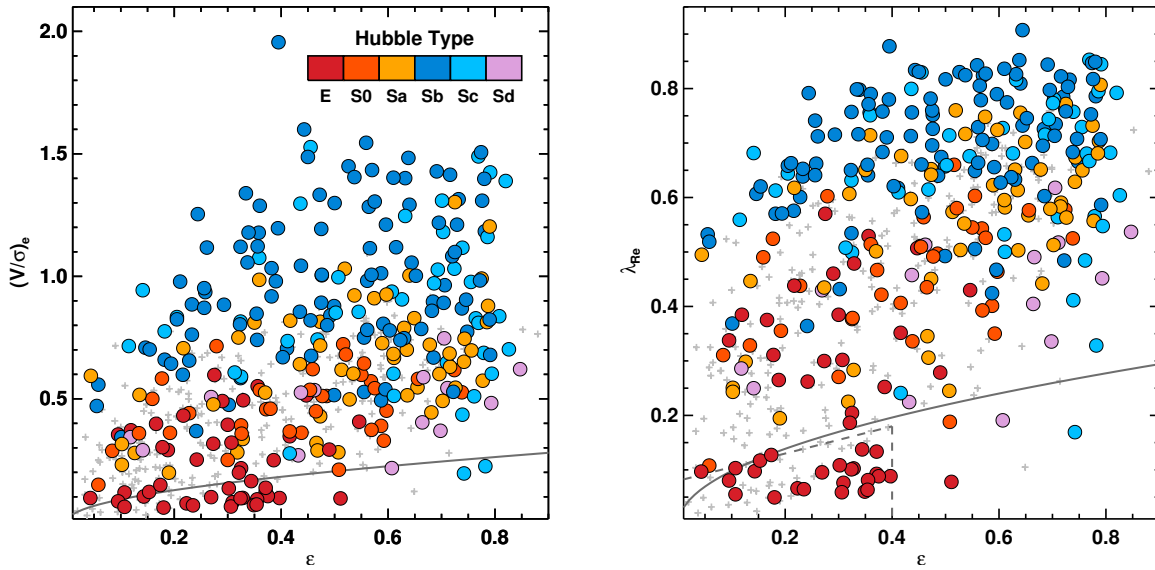
Figure 1.1.3: Distribution of 300 CALIFA galaxies (color-coded circles) and galaxies from the ATLAS^{3D} survey (gray crosses) on the V/σ-ε and λ_R-ε diagrams (Figure taken from: Falcón-Barroso et al. 2019) reproduced with permission © ESO.

in general smaller and disk-dominated (for a thorough review on this topic: Förster Schreiber and Wuyts 2020). Since the cosmic noon, the star formation rate of galaxies started a descending trend, and galaxies' diverse properties became more prominent as a result of their alteration by various internal and external mechanisms.

In the Local Universe, several properties of galaxies correlate with their environment (observed up to redshift 1) and stellar mass (e.g., Gallazzi et al. 2014). Such correlations are best described by scaling relations. Focusing on the effect of stellar mass (left column of Fig.1.1.4), galaxies in the low-mass end of the distribution (with $M_\star < 10^{9.5}$ $M_\odot$) are on average more metal-poor, younger and less α-enhanced. Studies of Gallazzi et al. (2014) indicate that low-mass galaxies up to redshift z = 0.7 have, on average, higher degrees of star formation rate. Low-mass galaxies have lower degrees of rotation (Scott et al. 2020), and their quenched fraction increases with their stellar mass. On the other hand, massive galaxies (with $M_\star > 10^{10.5}$ $M_\odot$) are, on average, older, more metal-rich, and α−enhanced systems. Massive early-type galaxies are often slow-rotating systems with complex internal kinematics, and their internal feedbacks (such as supernova explosions, AGNs, and stellar winds) are assumed as the main driver of their quenching.

By focusing on the effect of galaxies environment, studies in the early 80s and 90s indicate that with decreasing clustercentric distance, the fraction of late-type star-forming galaxies decreases from 60 percent to ∼ zero (e.g., Dressler 1980; Whitmore et al. 1993). As shown in Fig. 1.1.4, massive galaxies with $M_\star > 10^{10.5}$ $M_\odot$ generally host metal-rich and old stellar populations, regardless of their host halo's size. Low-mass galaxies in massive host halos, on the other hand, are on average more metal-rich and older than their counterparts in the less massive host halos (left column of Fig.1.1.4) (Pasquali et al. 2010; Gallazzi et al. 2021). This
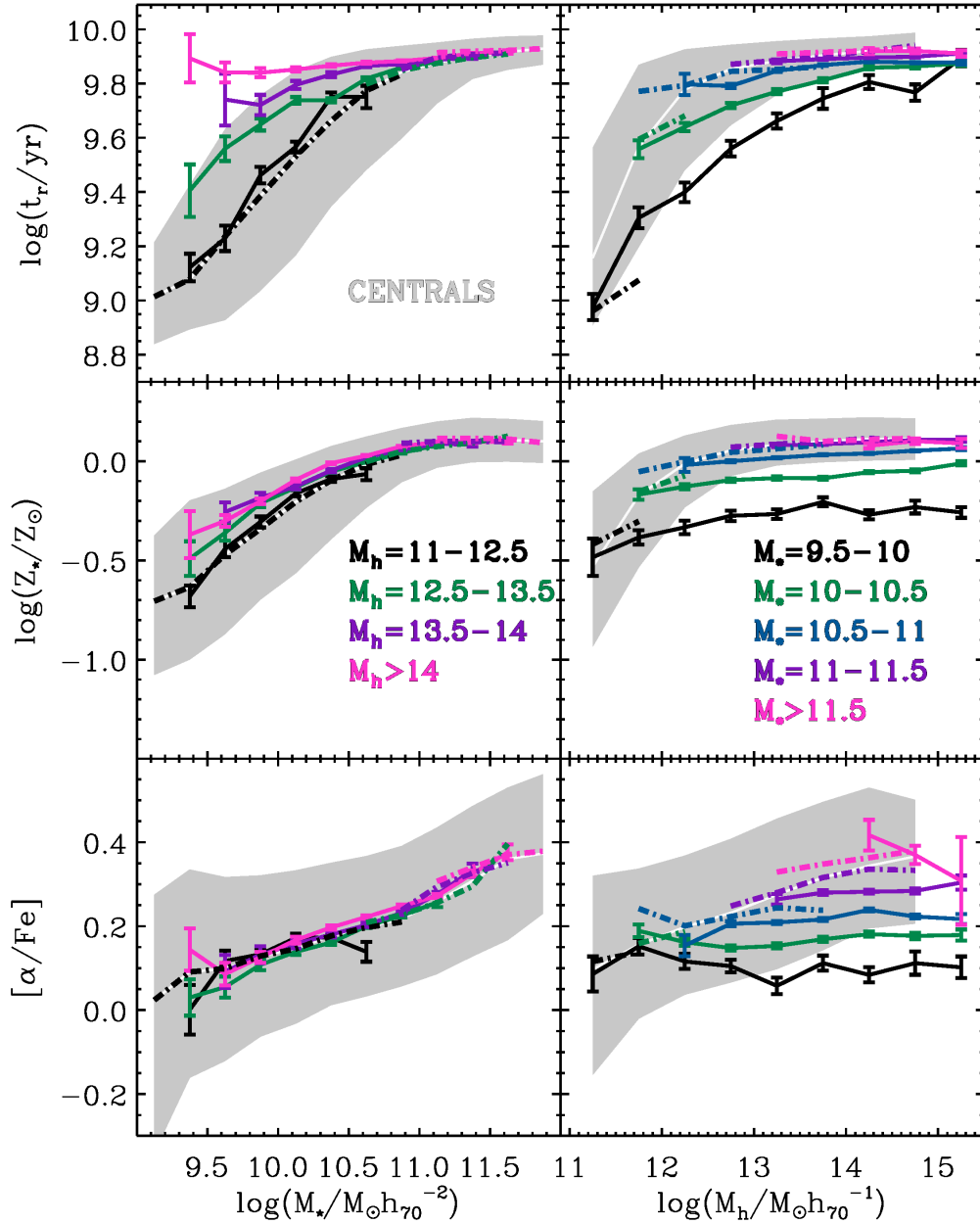
Figure 1.1.4: Stellar population distribution of SDSS galaxies with redshift $z \leq 0.2$, plotted for central galaxies (in gray) and satellite galaxies (color coded based on their host halo mass). Stellar population trends are shown as a function of a galaxy's stellar mass (left column) and halo mass (right column). (Plot taken from: Gallazzi et al. 2021).

is expected due to their low mass budget, thus shallow potential well, that makes them more prone to environmental effects. The effects of the environment on low-mass galaxies is one of

the main topics of this thesis and will be further discussed in Section 1.3.

1.1.4 Groups and Clusters

On the scales of $\sim$ 1-3 h^{-1} Mpc, galaxies are primarily found in gravitationally bound structures known as groups and clusters. These high-density regions of the Universe play vital roles in altering galaxies' properties, particularly low-mass ones. To understand the evolution of galaxies, it is essential to learn about these high-density regions of the Universe first:

- **Groups**: Small galaxy clusters with less than $\sim$ 10 galaxies within $\sim$ 1 Mpc across are known as galaxy groups[1]. Groups are small gravitationally-bound associations of galaxies with a typical mass-to-light ratio (M/L) of 80 $<$ M [M$_{\odot}$]/L [L$_{\odot}$] $<$ 300. They mostly comprise disk galaxies, such as spirals and irregulars. Some of the most known galaxy groups include the Local Group, the Bullet Group (Gastaldello et al. 2014), and Stephan's Quintet (Fig.1.1.5). The typical velocity of galaxies in these small halos falls in the range of 100 - 500 kms^{-1}. X-ray observations can only detect the intergalactic medium (IGM) of very dense galaxy groups ($\sim$50 percent of known groups to date) that contain hot gas with a temperature T $>$ 3$\times$10^6 K (Sparke and Gallagher 2007).

- **Clusters**: Galaxy clusters are structures covering several Mpc across and contain thousands of galaxies. With typical 180 $<$ M [M$_{\odot}$]/L [L$_{\odot}$] $<$ 300, galaxy clusters are dark matter dominated ($\sim$ more than 80 percent of their total mass Allen et al. 2011) and the giant associations of galaxies known in the Universe. Clusters grow over time (in terms of mass, but hardly in size) through the accretion of galaxies, either individually or as gravitationally bound members of smaller groups. Clusters contain mostly early- and late-type galaxies and dwarf galaxies. The intracluster medium (ICM) shines in the X-ray observations, indicating the presence of very hot gas in these structures. The ICM's hot gas contains heavy elements, and toward the cluster's center, it becomes more metal-rich. Star formation in primordial smaller clumps of gas (as merging seeds for forming galaxies), supernova driven pollution from star-forming galaxies within clusters, or expulsion of enriched gas of satellites' ISM via tidal interactions (Byrd and Valtonen 1990) and ram pressure stripping are three credible explanations for the presence of the metal-rich gas in central parts of these structures. Virgo (at the distance of $\sim$ 16.5 Mpc) is the closest rich cluster to us. Virgo is a dynamically young galaxy cluster that features several spiral galaxies and substructures visible in X-ray. This particular cluster is reviewed in more detail in Section 1.1.5. In addition to Virgo, Fornax (at the distance of 20 Mpc), Perseus (at the distance of 80 Mpc), and Coma (at the distance of 100 Mpc) are only some of the other rich galaxy clusters close to us (Sparke and Gallagher 2007). The pioneering work of George O. Abell from 1958 to 1989 indicates the presence of at least 4073 rich galaxy clusters around us (Abell 1958; Abell et al. 1989).

Figure 1.1.5: Stephan's Quintet galaxy group, known as the most photogenic compact galaxy group, is located in the constellation Pegasus and has been discovered first in 1877 by Edouard Stephan. The photo was taken from Wikipedia with credit to Hubble Space Telescope.

1.1.5   Inside the Virgo cluster

At a distance of 16.5 Mpc and within the constellation of Virgo is the Virgo cluster located. Virgo is a rich and dynamically young galaxy cluster with a virial radius of 1.5 Mpc. The

---

[1]However, these numbers are not an absolute division.
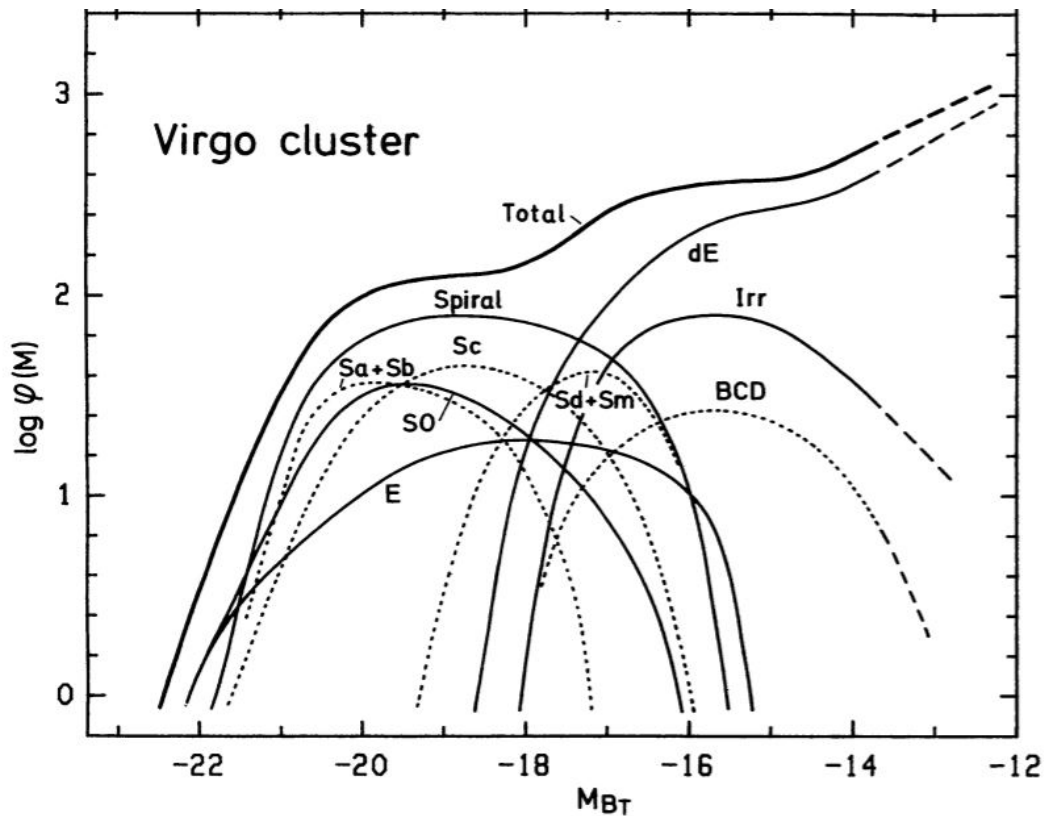
Figure 1.1.6: The luminosity function of different types of galaxies in the Virgo cluster. Plot taken from Binggeli et al. (1988)

latter is estimated based on the velocity of Virgo early-type galaxies and X-ray observations. The total mass of Virgo is estimated to be of the order of 10^{14} $M_\odot$ (Schindler et al. 1999). Virgo has an irregular shape, which is observable in both optical and X-ray wavelength ranges. Inside the cluster, three major substructures are present with centers on three elliptical galaxies, namely M86, M49, and M87. Compared to other ellipticals, M87 is 2.4 times more massive (Schindler et al. 1999), and its location within the cluster coincides with the peak emission of X-ray observations (Böhringer et al. 1994a). Hence, the substructure with a center on M87, also known as Virgo A, is assumed to be the main Virgo subcluster. M49 is the brightest Virgo galaxy that is surrounded by other spiral and irregular galaxies. The substructure surrounding M49 is known as Virgo B. Additionally, less prominent substructures have also been identified in Virgo, known as the N, S, E, B, M, and W clouds (Gavazzi et al. 1999). In 1988, Bingelli et al. calculated the luminosity function of different types of galaxies inside Virgo (presented in Fig. 1.1.6). Based on their studies, the number of early-type dwarf galaxies and giant ellipticals inside Virgo surpasses the number of spiral galaxies (Binggeli et al. 1988). Moreover, the analyses of the color-magnitude diagram of early-type dwarf galaxies in the Virgo cluster show larger scatter than for dEs in more relaxed systems such as Fornax and Coma (Hamraz et al.

2019). In addition to these results, the presence of substructures in this cluster and the velocity distribution of those fast-moving Virgo early-type dwarfs that is more similar to the motion of cluster late-types (Conselice et al. 2001) endorse the unrelaxed and dynamically young nature of the Virgo, which is still under active assembly (e.g., M86 as part of a small merging galaxy group; suggested by Böhringer et al. 1994a).

Between 1984 to 1987, a series of studies on the Virgo cluster were published based on a 150 degree^2 survey (Binggeli et al. 1984; Sandage and Binggeli 1984; Binggeli et al. 1985; Sandage et al. 1985). In these studies and by utilizing photographic plates, the authors focused on identifying the spatial and kinematical structures and substructures of the Virgo cluster. Moreover, they classified more than 1000 galaxy members of the Virgo cluster based on their morphology. They constructed the well-known Virgo Cluster Catalog (VCC) (Binggeli et al. 1985), which played a vital role in building our present-day knowledge of galactic formation and evolution, particularly in unrelaxed environments. Following their pioneering work, other blind and pointed surveys of the Virgo cluster have been carried out in different wavelength ranges, including:

- a Complete X-ray view of the Virgo cluster, mapped by ROSAT ALL-Sky Survey (Böhringer et al. 1994b)
- The Sloan Digital Sky Survey (SDSS) which is a spectroscopic and imaging survey, covering the wavelength range of 3800 to 9200 Å at R $\sim$ 1800 and in the *ugriz* bands (Stoughton et al. 2002)
- The Advanced Camera for Surveys (ACS) Virgo Cluster Survey (ACSVCS), which is high-resolution optical imaging in the F475W and F850LP bands with the Hubble Space Telescope (HST) by Côté et al. (2004)
- The blind extra-galactic Arecibo Legacy Fast ALFA (ALFALFA) survey that mapped HI sources in the Virgo cluster (Giovanelli et al. 2005)
- The Two Micron All Sky Survey (2MASS), which covers the entire Virgo cluster in the near-infrared (i.e., J, H, K$_s$) (Skrutskie et al. 2006)
- The Herschel Virgo Cluster Survey (HeViCS) to detect dust in the IGM (Davies et al. 2010)
- The Virgo far-infrared (VIRGOFIR) survey, which is a $\sim$ 30 degree^2 survey of Virgo at 24 and 70 μm, using Spitzer (Fadda et al. 2010)
- The GALEX Ultraviolet Virgo Cluster Survey (GuViCs), which is a blind Survey covering $\sim$ 40 degree^2 of Virgo in the far ultraviolet (Boselli et al. 2011)
- The Next Generation Virgo Cluster Survey (NGVS) which is an optical imaging survey covering $\sim$ 104 degree^2 in the $u^\star griz$ bandpasses using the MegaCam on the Canada-France-Hawaii Telescope (CFHT) (Ferrarese et al. 2012)

1.2   Galactic evolution in dense environments

As discussed in Section 1.1.3, the environment of galaxies tends to have a critical role in the alteration of their properties. In this section, some of the most famous environmental effects will be reviewed.

1.2.1 Galaxy harassment

Figure 1.2.1: NGC4435 (on the top) and NGC4438 (in the bottom) form an interacting galaxy pair in the Virgo cluster. The image was taken from the Sloan Digital Sky Survey database.

In general, galaxies in clusters and groups are exposed to the combined tidal forces exerted by the halo's potential well and close encounters with other members therein. Moore et al. (1996, 1998) referred to this combined effect as galaxy "harassment". Satellites in the central parts of clusters and those with elongated orbits are expected to experience maximum harassment (Moore et al. 1996). However, substructures inside clusters (such as those in Virgo) and non-virialized infalling groups can significantly increase the rate of galaxy-galaxy encounters within host halos (Moore et al. 1998). Thanks to their shallow potential well, low-mass satellites are

more prone to the effects of harassment within galaxy groups and clusters.

Essentially, the number density of satellites increases toward the center of a given galaxy cluster. Hence, the likelihood of galaxy-galaxy encounters increases (e.g., the tidal interactions between NGC 4435 and NGC 4438 in the Virgo cluster as shown in Fig. 1.2.1). Galaxy-galaxy encounters can affect the distribution of dark matter, gas, dust, and stars in interacting galaxies and, consequently, alter their morphologies, kinematics, and star formation activities (Boselli and Gavazzi 2014; Morales-Vargas et al. 2020). Galaxy-galaxy encounters are more frequent and less efficient in massive clusters due to the satellites' higher relative velocities (Boselli and Gavazzi 2014). In contrast to galaxy-cluster perturbations, galaxy-galaxy encounters often cause asymmetric disturbances in satellites (Byrd and Valtonen 1990).

The deep potential well of massive galaxy clusters can gravitationally perturb satellites by affecting the star formation activity in their disks and nucleus, gas inflow, bar formation, and disk thickness (Merritt 1984; Miller 1986; Byrd and Valtonen 1990). Tidal interactions are strongest in the central parts of clusters. These galaxy-cluster perturbations can decrease the net circular rotation of stars at large galactocentric distances, thus affecting the galaxies' angular momentum (Valluri 1994; Moore et al. 1996). In addition to that, tidal forces exerted by the halo's gravitational potential can push disk gas and molecular clouds in a galaxy toward its center, thus triggering star formation activity in this region (Fujita 1998).

1.2.2 Ram pressure stripping

Ram pressure stripping (RPS), proposed first by Gunn and Gott (1972), is the effect of removing gas and ISM from an infalling satellite galaxy by overcoming its gravitational pressure, hence:

$$\rho_{\mathrm{IGM}} V_{gal}^2 \geq 2\pi G \sum_{star} \sum_{gas} \tag{1.2}$$

where ρ_{IGM} is the IGM's volume density, and V is the velocity of a given galaxy inside the halo while the stellar and gas surface densities are denoted with $\sum_{star}$ and $\sum_{gas}$, respectively. Thus, a satellite galaxy with an infall velocity of ~ 1000 kms^{-1} onto the Virgo cluster (with $\rho_{\mathrm{IGM}} = 2.00 \times 10^{-3}$ atoms/cm^3 Boselli and Gavazzi 2006) and ($T_{\mathrm{cluster}} = 2.3$ KeV Böhringer et al. 1994a) will be exposed to RPS, starting from intermediate clustercentric distances. Consequently, RPS can cause stripped tails, which are observable at HI, Hα and X-ray wavelengths (for massive galaxies see e.g.,Oosterloo and van Gorkom (2005); for low-mass galaxies see e.g., Jáchym et al. (2013); Kenney et al. (2014)). RPS can also cause HI deficiency in late-type spiral galaxies (Giovanelli and Haynes 1985; Morokuma-Matsui et al. 2021), and enhancement or decrease of the galaxy's star formation rate.

Based on their size and orbits, galaxies respond differently to RPS. While RPS is mainly responsible for gas exhaustion, interactions between the cold ISM of infalling satellites and hot IGM of the host halo can induce bow shocks that boost the satellite's central gas density by a factor of $\sim$1.5 (particularly in the case of edge-on stripping, Vollmer et al. 2001). Such thermal instabilities can also increase the frequency of cloud collisions in galaxies, thus enhancing the star formation activity in central regions of infalling satellites (Evrard 1991; Bekki and Couch

2003; Kapferer et al. 2009; Bekki 2014; Vulcani et al. 2018; Roberts and Parker 2020). Studies have revealed that RPS acts more efficiently on satellites with circular orbits (Abadi et al. 1999; Vollmer et al. 2001). Moreover, the efficiency of this particular environmental effect depends on the satellites' stellar mass (Mori and Burkert 2000; Marcolini et al. 2003), their velocity, and their inclination with respect to their orbital plane (Abadi et al. 1999; Vollmer et al. 2001).

1.2.3   Other environmental effects

In addition to galaxy harassment and RPS, satellites may be exposed to some other environmental effects, including:

- **Starvation (also known as strangulation):** To form new stars, galaxies mostly rely on their extended hot gas reservoir. Removal of galaxy's outer halo, within a group or cluster environment, prevents this extended gas reservoir from falling back onto the galaxy's disk and fuel the star formation (Larson et al. 1980; Bekki et al. 2002). Starvation can be efficient in group satellites' quenching (e.g., Kawata and Mulchaey 2008) and transforming late-type spiral galaxies to quiescent S0s (van den Bosch et al. 2008; Rasmussen et al. 2008; Boselli and Gavazzi 2014)

- **Thermal evaporation:** Cowie and Songaila (1977) proposed this environmental effect as one of the possible mechanisms in charge of the removal of the galaxy halo gas, particularly in the interface between the ICM and the galactic ISM, owing to the former's high temperature.

- **Viscous stripping:** Nulsen (1982) first proposed viscous stripping, which is the removal of gas from the interface between a galaxy's ISM and IGM due to viscosity momentum transfer. Viscous stripping depends on the size of the infalling satellite, the temperature of the ISM, and the IGM's density. Hence, viscous stripping is more efficient in rich galaxy clusters, such as the Coma cluster, and in the case of giant galaxies. However, the exact impact of this environmental effect, as well as the thermal evaporation, on properties of satellite galaxies have not yet been quantified in detail (Boselli and Gavazzi 2006).

1.2.4   Pre-processing

In the ΛCDM framework, galaxies are accreted onto the high-density regions of the Universe either individually or as bound members of massive galaxy groups and gradually build up galaxy clusters. Pre-processing describes all environmental induced transformations that a given satellite goes through in its previous environments and up to its infall to the present host halo (Mihos 2004; Fujita 2004). Prior to their infall, galaxies can be members of a galaxy group, experiencing tidal interactions, mergers, RPS, and starvation (e.g., Vijayaraghavan et al. 2015). They can fall into clusters from the filaments of the cosmic web (Adami et al. 2009; Kim et al. 2016; Lee et al. 2021), thus experiencing tidal interactions with other galaxies. They can also come from relatively low-density regions, such as voids or outskirts of filaments, thus preserving most of their primordial properties (Lee et al. 2021). The high bulge-to-disk ratio in lenticular galaxies (Kodama and Smail 2001), the presence of quenched or gas deprived galaxies beyond one virial distance in clusters (Kodama and Smail 2001; Donnari et al. 2021), the reduced star formation

activity of late-type galaxies between one to three virial radii of clusters (e.g., Lewis et al. 2002; Mahajan et al. 2012; Haines et al. 2015), and the observed higher H_2-to-HI ratio for galaxies in the Fornax A group (Kleiner et al. 2021) are only some of the observed phenomena that endorse the vital role of pre-processing in altering present-day characteristics of cluster galaxies.

1.3   Dwarf galaxies: Diverse miniatures of the Universe
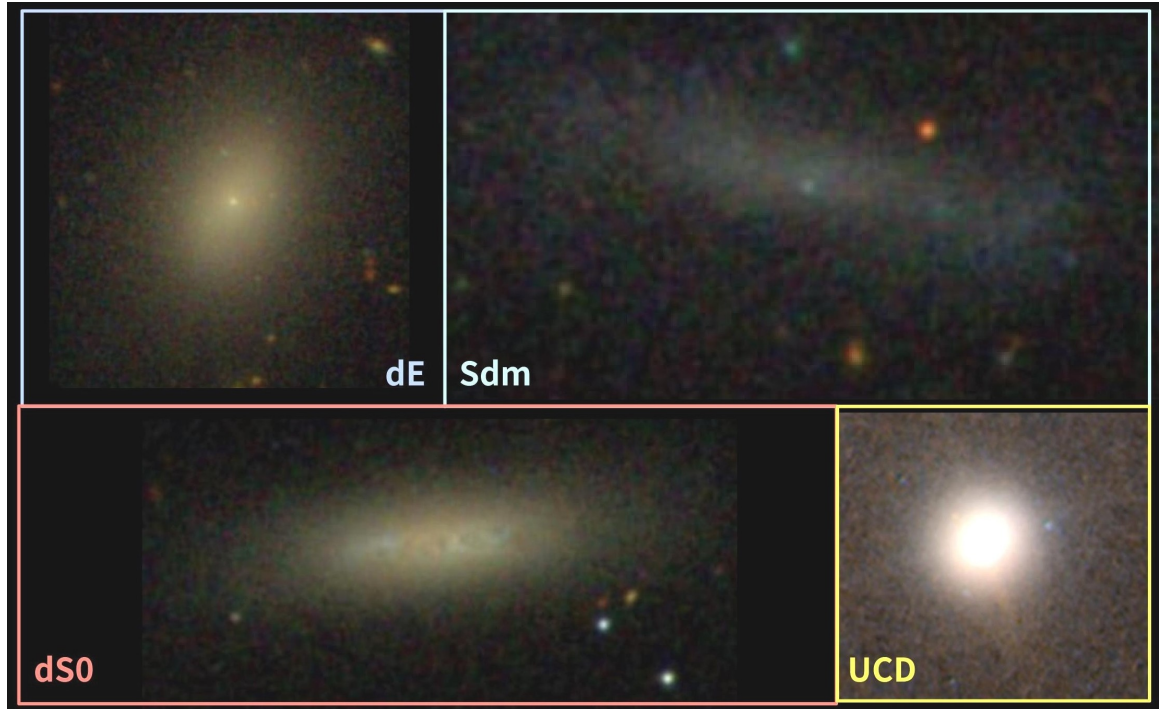
Figure 1.3.1: Different classes of dwarf galaxies. Images of galaxies are taken from the Sloan Digital Sky Survey. The UCD image is taken from: `https://sci.esa.int/web/hubble/-/54659-ultracompact-dwarf-galaxy-m60-ucd1-as-viewed-by-hubble`, with Copyright: NASA, ESA and A. Seth (University of Utah, USA)

Low mass galaxies with the mass range of $M_\star$ [$M_\odot$] $\leq 10^{10}$ (Grebel 2001), known as dwarf galaxies, shape a large population of clusters and groups. Dwarf galaxies first came under the spotlight during the 1930s and by the discovery of two Local Group dwarfs, Fornax and Sculptor (Shapley 1938). One decade after Shapley's discovery, the Palomar Sky Survey (Harrington and Wilson 1950; Wilson 1955) identified a more significant number of Local Group dwarf galaxies. Simultaneously, searches for dwarf counterparts out of the Local Group were initiated, and several satellite systems around giant galaxies were identified (e.g., Holmberg 1950, 1969). Meanwhile, many dwarf systems in nearby galaxy clusters were discovered (e.g., Reaves 1983; Hodge 1959, 1960; Hodge et al. 1965). About two decades later, and thanks to advancements in detector technologies, surveys could map the spatial distribution of dwarf galaxies in other clusters more extensively. Consequently, studies could shed light on the nature of dwarf galaxies

through investigating their scaling relations and luminosity functions (e.g., Binggeli et al. 1985; Binggeli and Cameron 1991; Caldwell and Bothun 1987; Sandage et al. 1985). Further insights into the stellar population of dwarf galaxies became possible by using early spectroscopic and multi-band observations (e.g., Bothun and Caldwell 1984; Bothun et al. 1985). Observations of dwarf galaxies at distances beyond our Local Group were not straightforward then. For the sensitivity of photographic plates of that time, dwarf galaxies were too faint (Davies and Morgan 1994), and this low surface brightness could cause systematic errors in measurements (Impey et al. 1988), especially at typical distances of the Virgo cluster and beyond.

Advancements in observing facilities have significantly increased our knowledge in the realm of dwarf systems. Based on their morphologies and colors, dwarf galaxies are divided into multiple classes (Grebel 2001), including:

- **Dwarf spiral galaxies (dSa, dSb, dSc, dSd, and dS0):** As the most massive types of dwarf galaxies, dSs are mostly found in the field and galaxy clusters. DSs have continuous, yet low, star formation rates, and their internal kinematics are diverse (Grebel 2001).

- **Dwarf irregular galaxies (dIrrs):** As their name suggests, dIrrs are characterized by an irregular appearance traced both in optical and radio observations, which goes hand in hand with their complex stellar and gas kinematics. Scattered clumps of HII regions, traced in optical bands indicate localized star formation activities in these systems. DIrrs are observed in different types of environments (Grebel 2001).

- **Blue compact dwarf galaxies (BCDs):** This sub-class of low-mass galaxies is mainly known for their compact shapes, high surface brightness in their inner parts, active star formation, and starbursts in their centers (Grebel 2001).

- **Dwarf elliptical galaxies (dEs):** DEs are primarily observed in the vicinity of massive galaxies and the high-density regions of the Universe, such as galaxy groups and clusters. They are mostly gas deficient systems with diverse kinematic structures and complicated star formation histories. This thesis focuses on the properties of early-type dwarf galaxies (elliptical dwarfs). Thus, in the following subsections, they will be introduced in more detail.

- **Dwarf spheroidal galaxies (dSphs):** dSphs are dark matter dominated, gas deficient, old, low-mass dwarf galaxies. They are pressure supported systems that are often observed in groups, clusters, and in the vicinity of massive galaxies. DSphs are the least massive galaxies (known to date) and the most numerous type of dwarf galaxies in the Universe (Grebel 2001).

- **Ultra compact dwarf galaxies (UCDs):** These subclass of low-mass systems are bigger than the most giant globular clusters observed in the Milky Way yet are more compact than dwarfs of a similar size. UCDs are mostly dominated by old stellar populations and are believed to be the results of either tidally stripped dwarfs or simply old objects that formed from the primordial dark matter fluctuations in the early phases of the Universe. UCDs are often observed in central parts of clusters.

- **Tidal dwarf galaxies:** These types of dwarf galaxies are believed to be formed from the merger debris of giant galaxies. This subclass of dwarfs is dark matter deficient and more metal-rich, given their stellar mass and luminosity range. The main characteristics of tidal

dwarf galaxies are believed to be set mainly by the evolutionary stage of progenitors that were involved in the merger event (e.g., Hunter et al. 2000; Duc and Brinks 2001).

1.3.1 Early-type dwarf galaxies (dEs)

Early-type dwarf galaxies (dEs) are low-mass, often quenched, and relatively faint ($M_B \geq$ -16 mag) galaxies with smooth light profiles and featureless appearance (Ferguson and Binggeli 1994). In recent decades, our understanding of dEs and their characterization has been improved significantly. Presence of substructures (e.g., Lisker et al. 2009; Michea et al. 2021), extended star formation histories, observation of HI gas (Buyle et al. 2005) and diverse kinematics are only part of the information that we have acquired from these seemingly simple galaxies.

The first observational evidence on the presence of disk and two-component substructures in dS0 and dEs was found by Sandage and Binggeli (1984) and Binggeli and Cameron (1991). In about two decades, disk substructures (such as bars and spiral arms) were further detected in some observed dEs (Jerjen et al. 2000; Barazza et al. 2002; Geha et al. 2003; Graham and Guzmán 2003; De Rijcke et al. 2003). In particular, Lisker et al. (2006b,a) reported on the presence of disk features in a large number of Virgo dEs. These results were based on a systematic search on SDSS images of 476 Virgo dEs and performing the unsharp masking technique. Through this study, disk features were identified in more than half of the investigated sample. Furthermore, Lisker et al. (2006b,a) reported a positive correlation between the presence of disk features and the surface brightness of dEs, in a sense that dEs with disk features dominated the bright end of their investigated distribution. In their study, Lisker et al. (2007) have shown that, except for the nucleated subclass, dEs exhibit oblate shapes, similar to the thick disk of galaxies.

Despite their monotonous overall light distribution and shape, dEs have a rather complex and diverse kinematic structure. In general, the stellar rotational velocity of dEs falls within the range of 0 to 50 kms^{-1}, while their velocity dispersion ranges from 30 to 50 kms^{-1} (e.g., Toloba et al. 2011). In this regard, some dEs are pressure-supported systems with stars on random orbits, while others show well-defined rotating stellar structures (Simien and Prugniel 2002; Pedraz et al. 2002; Geha et al. 2003; van Zee et al. 2004; Chilingarian et al. 2008; Toloba et al. 2009; Janz et al. 2017). What is more, several studies of dEs in different environments report the existence of so-called kinematically decoupled cores (KDC) in these galaxies (e.g., see Geha et al. 2003; Koleva et al. 2011; Ryś et al. 2013; Toloba et al. 2014; Guérou et al. 2015). In this regard, Toloba et al. (2014) have shown that about six percent of dEs in the Virgo cluster host a KDC. Somewhat more recently, active galactic nuclei (AGN) have been detected in hundreds of early- and late-type dwarf galaxies, which are believed to be powered by central low- or intermediate-mass black holes ($10^2 < M_{BH} \leq 10^6$) in these systems. While AGNs leave their mark on the gas kinematics of dwarf galaxies, the presence of a black hole can shape the gravitational potential, thus modify kinematics of stars in these low-mass systems (for recent reviews on this topic: Mezcua 2017; Greene et al. 2018).

Further investigations of dEs revealed rather complicated star formation histories. While some observations of these systems traced old stellar populations with ages $\sim$ 14 Gyr, others shed light on the presence of young stellar populations ($\sim$ 2 Gyr) that indicate recent episodes

of star formation in dEs (e.g., Poggianti et al. 2001; Caldwell et al. 2003; Geha et al. 2003; Lisker et al. 2006b; Michielsen et al. 2008; Chilingarian et al. 2008; Koleva et al. 2009; Sybilska et al. 2017). Such diversity is also present in the distribution of dEs metallicities, as it ranges from solar ([M/H] $\sim$ 0.00 dex) values to metal-poor regimes ([M/H] $\sim$ -1.30 dex). Studies have revealed that dEs with disk features tend to have younger and more metal-rich stellar populations compared to those lacking such sub-structures (e.g. Paudel et al. 2010). In this regard and from a sample of 39 Virgo dEs, Toloba et al. (2014) reported the average light-weighted age of 5.46 $\pm$ 0.81 Gyr and the average light-weighted metallicity of -0.64 $\pm$ 0.09 dex for disk dEs. They also found that dEs without any detected disk features tend to show a similar range of metallicities ($\sim$ -0.59 $\pm$ 0.07 dex), but with an average age of $\sim$ 6.85 $\pm$ 0.76 Gyr. Koleva et al. (2011) reported on a strong negative correlation between the luminosity and age gradient in faint dEs (with M_B > -17 mag) of Virgo and Fornax clusters. Their results indicated that prolonged star formation activity of dEs is mostly embedded in their centers.

1.3.2   Dwarf galaxies in the Local Group

DSphs are the numerically dominant type of dwarf galaxies in the Local Group (LG). Together with the LG dEs (i.e., NGC205, NGC185, and NGC147), they are mostly found as orbiting satellites of either M31 or the Milky Way. In addition to these two types of dwarf galaxies, the LG is the host to $\sim$ nine dIrrs which are not bound to any of its members (Sparke and Gallagher 2007). Thanks to the vicinity of LG dwarfs, extensive investigation of the resolved stellar systems in these galaxies is possible. Such investigations have provided us with detailed information about dwarf structures, kinematics, and stellar populations through the last decades.

In terms of kinematics, most of the LG dwarfs are believed to be triaxial systems. Depending on their stellar mass, diverse kinematics have been observed for LG dIrrs. Solid-body rotations have been detected in massive dIrrs, while their low-mass counterparts do not show an evident net stellar rotation (Grebel 2001). DEs and dSphs in the LG have oval shapes embedding low degrees of stellar rotation, if any (Sparke and Gallagher 2007). Among three dEs of the Local Group, NGC205 shows tidally interrupted stellar orbits at its larger radii. On account of its vicinity to M31, the perturbed stellar kinematics of NGC205 is interpreted as a result of tidal interactions with its giant companion (Geha et al. 2006).

Most of the dSphs and dEs of the Local Group have extended star formation histories. Their ages range from $\sim$14 Gyr, traced in their old stellar populations, to younger stars formed about a few Gyr ago (e.g., Mateo 1998; Grebel 1999). Studies have revealed that with decreasing distance to the MW center, the fraction of the old stellar population increases within MW satellites. Studies detected metallicity gradients with negative slopes in the Local Group's dSphs, including Sextans, Tucana, Sculptor, and Andromeda VI (Harbeck et al. 2001). Moreover, studies revealed age gradients with positives slopes in Fornax (Stetson et al. 1998), Sextan (Okamoto et al. 2008; Battaglia et al. 2011), and possibly in Carina (Norris et al. 2017). However, no clear correlation between environment (i.e., distance to the massive host galaxy) and gradients of stellar populations in LG dwarfs has been detected (Harbeck et al. 2001).

1.3.3   Early-type dwarf galaxies in the Local Universe

Thanks to their shallow potential well and large numbers, dwarf galaxies are regarded as essential and sensitive probes of the environment. The quantification of environmental effects on dEs commonly considers their clustercentric distances or local densities. Such approaches are necessary for understanding the evolution of low-mass galaxies within dense structures of the Universe, albeit with their flaws, which are reviewed in the next Chapter.

In the Virgo cluster, Lisker et al. (2007) showed that dEs with different types of morphological properties tend to occupy different cluster regions. They have shown that while dEs with disk features and blue cores tend to be spread throughout the cluster, nucleated dEs (even with a weak nucleus) are more centrally concentrated (also in Ferguson and Sandage 1989). By investigating 31 Virgo dEs, Toloba et al. (2011) showed that the kinematics of these low-mass systems is also dependent on their clustercentric distances: while dEs in the central parts of Virgo are pressure-supported, toward more extended clustercentric distances, the number of rotation-supported dEs increases. A similar (kinematic) morphology-density relation has been reported for more massive elliptical galaxies by Cappellari et al. (2011). Ryś et al. (2013) investigated the dynamical to stellar mass ratios of 9 Virgo dEs as a function of their 3D clustercentric distances and showed a possible positive correlation between these two parameters. Based on their results, the dark matter fraction in dEs decreases toward lower clustercentric distances. Lisker et al. (2013) have shown that with decreasing clustercentric distances, the number of red and quenched dEs in Virgo (as well as Coma cluster) increases.

Moving toward a less massive yet more distant cluster, dwarf members of Fornax tend to show similarities with the Virgo dEs. By investigating 564 Fornax dwarf galaxies, Venhola et al. (2019) showed that the population of red dwarf galaxies increases toward the cluster center. This is consistent with results of Eigenthaler et al. (2018) who showed that faint dwarfs that are embedded within the Fornax core ($r < R_{vir}/4$) are, on average, older than ~ 5 Gyr. The study of Venhola et al. (2019) indicates that in the core of the Fornax cluster, the number density of nucleated dEs is higher, and these regions are almost devoid of non-nucleated dEs or late-type dwarf galaxies. By focusing on 31 Fornax dEs, results of Scott et al. (2020) have shown that the number of slowly rotating dEs decreases toward the Fornax cluster outskirts.

In the Coma cluster, a strong correlation between clustercentric distance and the stellar populations of dEs with $M_r = $ -17.5 mag was reported by Smith et al. (2009). DEs with α-enhanced and old (~ 10 Gyr) stellar populations predominate the core of the Coma cluster, whereas, toward the cluster's outskirts, dEs are found to be younger (~ 3 Gyr) with solar-scaled α-enhanced stellar populations. DEs residing in Coma's outskirts show clear signs of recent or ongoing star formation.

DEs can be found in low density environments (known as the field) (e.g., Gu et al. 2006; Janz et al. 2017), albeit with a lower probability than in the galaxy clusters and groups. Geha et al. (2012) have shown that field dEs are mostly star forming systems, and quenched field dEs are extremely rare cases (< 0.06 percent). This probability decreases to null for dEs with $M_\star < 10^9$ $M_\odot$. Results of Janz et al. (2017) show that field dEs can have a diverse range of stellar rotation, ranging from values typical for pressure supported systems to rotation supported ones.

1.3.4   Possible formation channels of dEs

Even though dEs are one of the most frequent types of galaxies in the Universe, their formation is a long-established question in the field. Several studies attempted to answer this question, yet their suggested scenarios lack the explanation for some of the observed properties. The hierarchical merging scenario and the transformation of low-mass star-forming galaxies under environmental effects have recently gained a reputation among several proposed explanations.

The hierarchical ΛCDM scenario (Somerville and Primack 1999; Steinmetz and Navarro 2002) introduces dwarf galaxies as the building blocks of our present-day Universe. Based on this scenario, the first galaxies were formed due to gravitational instabilities that planted the primary seeds to form rotating dark matter halos. After gas cooling within these halos, low-mass systems with their first population of stars formed. The initial thick disk within these primordial galaxies was a pressure-supported structure, with random stellar motions surpassing their net rotation. Results of Moster et al. (2010) showed that stellar-to-halo mass of such low-mass galaxies at high redshift is low, indicating the dominance of dark matter component in these primordial structures. In these low-mass systems, the star formation rate was not significant and the circular velocity curves raised, only slowly, in the outer regions of the galaxy. Given the similarities between such primordial systems and present-day properties of dEs in clusters and groups, it stands to reason that at least part of today's dEs population consists of ancient objects that formed in the early Universe but did not follow the same path (e.g., merging) as their counterparts (de Rijcke et al. 2005). Observation of some quenched dEs with lower degrees of rotation in the field (Janz et al. 2017) and spheroidal nucleated dEs with circular orbits in the central parts of Virgo (Lisker et al. 2009) endorse the formation channel that hierarchical ΛCDM scenario pictures for us (more on this topic in Wheeler et al. 2017).

Meanwhile, the (kinematic) morphology-density relation of dEs (Binggeli et al. 1987; Toloba et al. 2014; Scott et al. 2020), the detection of stripped gas tails, and prolonged star formation activities with signs of ongoing or recent star formation in some dEs (primarily in the cluster's outskirts) motivate other formation scenarios. In 1985, Kormendy suggested that part of today's dE population in rich galaxy clusters may be the remnants of star-forming late-type infalling galaxies that were transformed by a combination of environmental effects inside the cluster (Kormendy 1985). An infalling star-forming dE -or its progenitor- can lose its gas either due to ram pressure stripping or starvation. In the meantime, it can undergo tidal interactions with the gravitational potential of the host halo and its other members, thus experiencing morphological and dynamical transformations. Based on this scenario, the end product of several Gyrs inhabiting the cluster or group would then be quenched, red, and dynamically hot (spheroidal) dEs which eventually sunk to the central parts of their host halo (see, e.g., Kormendy 1985; Binggeli et al. 1988; Bender et al. 1992; Moore et al. 1996; Geha et al. 2010; Toloba et al. 2011; Janz et al. 2012; Kormendy and Bender 2012; Ryś et al. 2013; Lisker et al. 2013; Boselli and Gavazzi 2014; Penny et al. 2014; Bialas et al. 2015; Aguerri 2016; Hwang et al. 2018).

1.4   Thesis scientific motivation

Even though dwarf galaxies share several similar properties (e.g., color and Sersic index), they are not entirely identical. The comparison of any two dwarf galaxies sheds light on the underlying diversities that are rather hard to explain, given accepted formation scenarios. What is the leading cause of such diversity? Different formation channels suggest different progenitors as possible sources of the observed diversities. As explained in Section 1.3.4, dEs might have been formed as primordial objects or after the environmental transformation of late-type galaxies. However, distinguishing between these two sub-populations in clusters is not straightforward, mainly due to destructive effects of the environment after several Gyr that removes footprints of the dE's progenitors. Nonetheless, by shifting our focus to dynamically young galaxy clusters (such as Virgo), we might be able to capture recently accreted satellites. Despite being disturbed due to the cluster's environment, they have partially managed to keep the record of their progenitors. By comparing the newly accreted satellites with their counterparts in the field and more ancient infallers of the cluster, we can better understand the role of the environment in the diversity mentioned above. Likewise, such comparison would reflect the relevance of pre-processing in present-day properties of dEs and the formation of their diverse populations in clusters.

The work undertaken in this thesis focuses on studying members of a newly accreted group of galaxies onto the Virgo cluster to i) better understand the evolutionary track of low-mass galaxies within clusters, particularly in their early stages of infall; and ii) to investigate the role of pre-processing in shaping present-day properties of cluster dwarf galaxies. The main scientific questions of this thesis can be summarized as follow:

- How would the environment affect infalling satellites during their early stages of accretion?
- How relevant is pre-processing in the present-day properties of cluster early-type galaxies?
- For a typical dwarf galaxy observed today, which one matters the most: their birth site (nature) or their environment in later stages (nurture)?

1.5   Thesis Outline

In this chapter, we gave a brief introduction to the general properties of galaxies, their habitats, and properties with respect to their stellar mass, redshift, and environment. Furthermore, we introduced dwarf galaxies and their different sub-classes. By focusing on early-type dwarf galaxies (dEs), we briefly reviewed their properties in the Local Group and the Local Universe, as well as their possible formation scenarios.

The rest of this thesis is structured as follow:

- **Chapter 2:** In this chapter, we introduce nine Virgo dEs that were discovered by Lisker et al. (2018) as possible members of an accreted massive galaxy group onto Virgo. These nine dEs shape the main sample of this thesis. We investigate their accretion time using a projected phase-space diagram. Moreover, we review the reduction procedure of their MUSE data sets. Furthermore, we introduce two comparison samples, consisting of low-mass galaxies in the field (field control sample) and the Virgo cluster (Virgo control sample).

- **Chapter 3:** In this chapter, we investigate the kinematics of dEs in the accreted group and quantify their stellar rotation using their projected specific angular momentum. Through comparison of our results with two other control samples, we investigate the role of the Virgo's environment and pre-processing in the kinematic alteration of satellite galaxies.

- **Chapter 4:** In this chapter, we investigate the stellar populations of dEs in the accreted group, using spectral line indices. Furthermore, we compare the age, metallicity, and α-enhancement of the accreted dEs with those in the comparison samples. Through this comparison, we further investigate the role of pre-processing in shaping present-day properties of satellite galaxies as well as shedding light on the possible progenitors of dEs.

- **Chapter 5:** In this chapter, we investigate star formation histories of dEs in the accreted group, using the full-spectrum fitting technique. Through this investigation, we take a closer look at the effect of group accretion event on the star formation activity and mass assembly of its dE members.

- **Chapter 6:** In this chapter, we introduce two new galaxies that have been discovered through investigations of our MUSE data.

- **Chapter 7:** In this chapter, we summarize the main results of this thesis and show the importance of both pre-processing and current halo environment in shaping present-day properties of cluster dEs. The main scientific questions of this thesis are addressed in this chapter.

"If you are irritated by every rub, how will your mirror be polished?"

— Rumi

2

Data

This chapter is a partially revised version of Bidaran et al. (2020). "On the accretion of a new group of galaxies onto Virgo: I. Internal kinematics of nine in-falling dEs", published in MNRAS 497, Issue 2, pp.1904-1924

2.1 Main sample: A newly accreted group of Virgo dEs

The primary sample of this thesis is built upon results of Lisker et al. (2018) who, during investigations of dwarf galaxies in the Virgo cluster, detected a recently accreted group of nine Virgo dEs. This detection has been mainly rooted in the observer's phase-space distribution of Virgo satellites. Thus, to understand this sample's selection procedure and unique condition, it is better first to describe how they were detected. Following that, the sample members, as well as observation and reduction procedures, are reviewed. Additionally, in Section 2.3, two other comparison samples that are going to be utilized through the rest of this thesis are briefly presented.

2.1.1 Phase-Space diagram: A diagnostic tool

As discussed in Section 1.3.3, projected clustercentric distance is a common, yet not totally accurate, approach to quantify the dependence of satellites' properties on their environment. In contrast to satellites in the cluster's core, those that reside in the cluster's outskirts are believed to be less affected by their host halo's environment. Even so, the projected clustercentric distance is impotent to accurately distinguish between these two cases along the observer's line of sight and particularly in central regions of massive clusters. The latter is particularly relevant for new infalling satellites that often follow eccentric orbits in their new host halo (Wetzel 2011; Smith

et al. 2015). Quantifying satellites' properties based on their projected clustercentric distance is even less accurate in non-relaxed clusters such as Virgo. As discussed in Section 1.3.3, Virgo features some irregular high-density regions that are not co-spatial with the central M87 galaxy. Thus, the Virgo satellites' local density does not necessarily scale with their distance to the cluster's center and, inevitably, is less sensitive to the projected clustercentric distance (Sybilska et al. 2017). It is worth mentioning that by utilizing the projected clustercentric distance or the local density of satellites in distant halos (Sybilska et al. 2017), results are mainly interpreted based on the present-day environment of galaxies, but not based on the evolutionary path they have gone through during their lifetime. Among other things, such approaches provide limited insight on the pre-processing of galaxies and the environmental conditions at their birth site (i.e., where their bulk of stars formed).

Many studies have focused on both the clustercentric distance and velocity of satellites by constructing the so-called "phase-space" diagram to partly remedy the projection effect. Oman et al. (2013) showed that in different stages of their accretion onto a halo, satellites occupy different regions of the phase-space diagram (also in Rhee et al. 2017). Based on the 2D phase-space distribution of SDSS galaxies, Mahajan et al. (2012) investigated the relation between star formation and stellar mass of satellite galaxies. Furthermore, Haines et al. (2015) and Oman and Hudson (2016) investigated the quenching timescale of satellite galaxies using this diagnostic diagram. By utilizing the 3D phase-space in cosmological simulations, Jaffé et al. (2015) explained the detected neutral gas distribution in Abell 963 as a consequence of ram pressure stripping of its satellites. Smith et al. (2015) quantified the tidal mass loss of cluster satellites based on their distribution in the phase-space diagram (see also Serna and Gerbal 1996; Adami et al. 2005).

While the 3D phase-space diagram turned out to be a conducive diagnostic tool, it cannot be directly employed for observed data. The determination of orbital parameters (such as 3D velocity and 3D radius) for satellites in distant halos is not straightforward, and observers only have access to their projected parameters, such as line-of-sight velocity and projected distance. Therefore, Rhee et al. (2017) constructed the "projected phase-space" diagram using the Yonsei Zoom-in Cluster simulation (Teyssier 2002; Choi and Yi 2017). They concluded that, while projection effects smear the distributions of satellites with different infall times, the distribution peak of each population (defined so by its own infall time) tends to occupy, nonetheless, distinct parts of the projected 2D phase-space diagram. In this context, the infall time of a given satellite is the first time when it passes through the virial radius of the progenitor of its present-day host halo.

By using simulated 2D phase-space diagram of Rhee et al. (2017) and drawing zones of different constant infall times, Pasquali et al. (2019) applied these time zones to the observed 2D phase-space diagram of SDSS satellites in host halos of different masses, distinguishing galaxies on the basis of their stellar masses. In this study, and for the first time, Pasquali et al. (2019) computed the average star formation rate (SFR) and stellar population properties (such as age, metallicity, and $[\alpha/\text{Fe}]$) of satellites of different stellar masses and in differently massive halos, as a function of their infall time. Their results indicate that with increase of the average infall time, satellites at fixed stellar masses and halo masses, experience decreases in their SFR

while becoming older and metal-richer. Using the projected phase-space diagram, Rhee et al. (2020) investigated possible correlations between star formation rate and infall time of satellite galaxies at different stellar masses and confirmed the "delayed-then-rapid" quenching trend for satellites with $M_\star > 10^{9.5}$ $M_\odot$ (see also Oman et al. 2021). The latter is consistent with results of Pasquali et al. (2019) where age, metallicity, and $[\alpha/\text{Fe}]$ abundance ratio of satellite galaxies were studied with respect to their average infall time. Based on this study, correlations between satellites properties and the average infall time is more substantial for satellites with $M_\star < 10^{10.5}$ $M_\odot$ in halos with $M_\star > 10^{13.5}$ $M_\odot$ (also in Gallazzi et al. 2021). Focusing on a specific galaxy type, Pak et al. (2021) reported a positive correlation between age and $[\alpha/\text{Fe}]$ abundance ratio of SAMI passive spiral galaxies and their average infall time. The authors of this study show that both the age and $[\alpha/\text{Fe}]$ abundance ratio of passive spiral galaxies, in groups and clusters, increase with their average infall time, in agreement with the general trends found by (Pasquali et al. 2019).

.

2.1.2   Selection of the main sample

Lisker et al. (2018) investigated the observer's phase-space distribution of 625 Virgo galaxies in six different intervals of absolute r-band magnitudes (M_r), as presented in Fig. 2.1.1. In this plot, different colors indicate different morphological classes, and dwarf galaxies (dEs, dS0 and Ims) are denoted with filled circles. As an evident trend, the number density of dEs grows toward fainter intervals. Among different panels, the $-17 \geq M_r > -18$ mag interval captures further attention. Despite fainter bins, dEs within this magnitude range show a non-symmetric phase-space distribution. Furthermore, the concentration of nine Virgo dEs (eight with disk features) in a particular region of the diagram in this panel is a special feature that cannot easily be detected in the other magnitude bins. These nine Virgo dEs (marked with black rectangular in Fig. 2.1.1) are located at the distance of d = 1.5 Mpc to M87 and have $V_{rel} = 700$ kms^{-1}. Despite their similar location on the phase-space diagram, these nine dEs are azimuthally spread around the Virgo's core (i.e., M87).

N-body simulations of cluster mergers have shown that in the event of a merger of a massive group with a cluster, the core and outer parts of the group get separated into two components (Vijayaraghavan et al. 2015). The core of the group accretes onto the cluster center and starts to oscillate there. Meanwhile, the groups' outskirts form shell-like over-densities at larger distances and close to the orbital apocenter. In Fig 2.1.2, the observer's phase-space distribution of a massive merger event (a group with $M_{\text{group}} = 5 \times 10^{13}$ $M_\odot$ falling onto a cluster with $M_{\text{cluster}} = 5 \times 10^{14}$ $M_\odot$) along the observer's line of sight is presented. In the upper right panel and 2.4 Gyr after the event, two distinct components of the accreted group are shown, mimicking an over-density similar to that observed for the Virgo dEs within the $-17 \geq M_r > -18$ mag interval. Results of Vijayaraghavan et al. (2015) show that the over-densities on particular parts of the observer's phase-space diagram, which are not accompanied by any spatial segregation in the cluster, can be likely the signature of a recent ($\sim$ 2-3 Gyr ago) massive merger event along the observer's line of sight. Based on these results and as detailed by Lisker et al. (2018), it stands to reason that the nine notably aggregated dEs in the particular region of the observer's
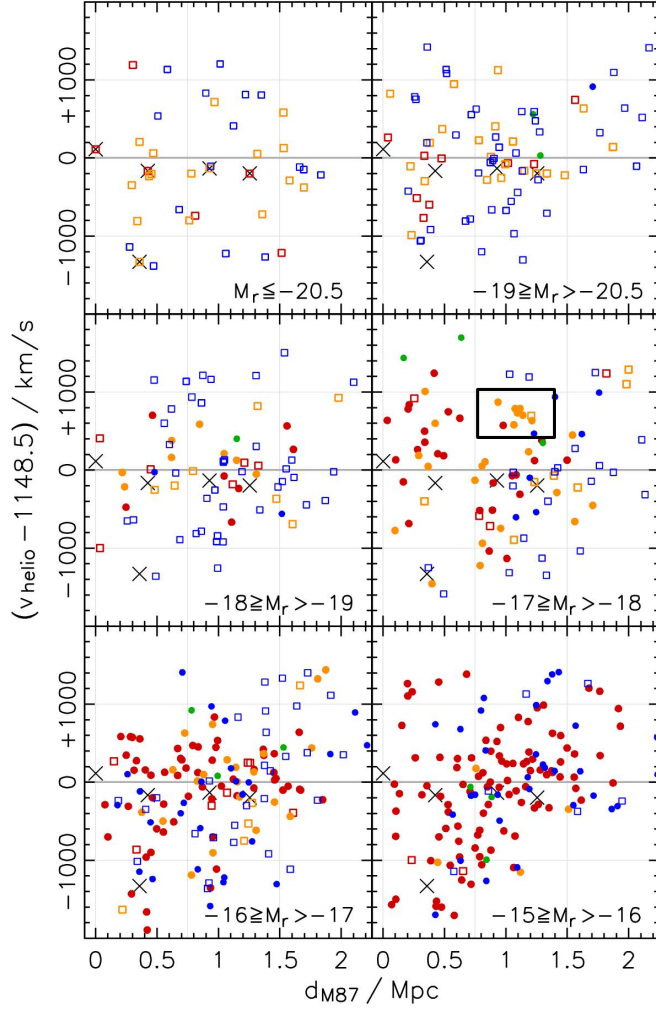
Figure 2.1.1: The observer's phase-space distribution of 625 Virgo dEs. Colors denote different morphological classes (green = "Im/dEs", Red ="E/dE", orange "dEs(dis)/dS0/S0", and blue= "spirals and irregulars"). Dwarf and irregular galaxies are marked with filled circles, while non-dwarf galaxies are denoted with squares. The main sample of this thesis is marked with black rectangular. Giant early-type galaxies of Virgo (i.e., M87, M86, M49, M84, and M60) are denoted with black crosses. The plot took from Lisker et al. (2018) and reproduced with permission ©AAS.

phase-space diagram are the remnants of an accreted massive galaxy group onto the Virgo cluster, along the line of sight and about 2-3 Gyr ago. This scenario is also endorsed by the separate study of Sorce et al. (2021).

Further support of a similar and relatively recent accretion time of these nine dEs comes from studies of Pasquali et al. (2019), and Smith et al. (2019), who showed that cluster galaxies with different infall times to their current halo occupy different zones of the projected phase-space diagram. In the left panel of Fig. 2.1.3, the projected phase-space distribution of Virgo
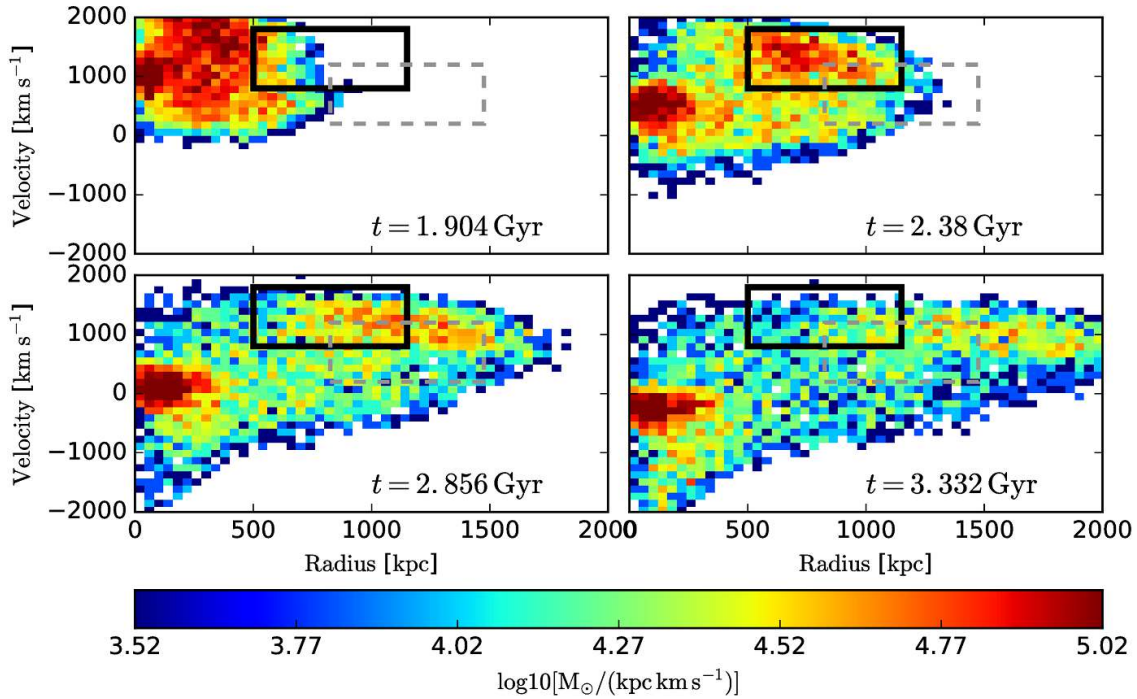
Figure 2.1.2: The observer's phase-space distribution of an accreted 5×10^{13} $M_\odot$ galaxy group onto a cluster with 5×10^{14} $M_\odot$, along the observer's line of sight. Each panel shows how the distribution of infalling satellites varies with respect to the time since infall. One can note the configuration within the black box in the top right panel, which is comparable with the observer's phase-space configuration of Virgo dEs in the the $-17 \geq M_r[mag] > -18$ interval of Fig. 2.1.1. Plot taken from Lisker et al. (2018) and reproduced with permission ©AAS.

dEs with $-17 \geq M_r > -18$ mag is presented. Our nine dEs are presented with squares. The labeled zones of the diagram mark different average infall times to the Virgo cluster and are taken from Pasquali et al. (2019), and Smith et al. (2019). Based on the projected phase-space locus of these nine dEs, it is evident that they all share a similar accretion time to the Virgo cluster, consistent with results of Lisker et al. (2018). The right panel of Fig. 2.1.3 shows the spatial distribution of our dEs (colored squares) and other Virgo dEs with a similar range of M_r. Evidently, these nine dEs are azimuthally spread around M87.

In Table 2.1.1, the name of each target, its type, coordinates, recession velocity, effective radii from r-band photometry images, r-band absolute magnitude (M_r), color, ellipticity, and total exposure time (TET) of observations, are summarized. All the values were taken from Lisker et al. (2006b), except for the recession velocities, which were taken from SDSS DR15 (Aguado et al. 2019). The reported values of M_r and color were corrected for Galactic extinction by Lisker et al. (2006b) and Janz and Lisker (2008, 2009). (g-r) colors were computed by Lisker et al. (2006b) and Janz and Lisker (2008, 2009) using a distance modulus of m-M = 31.09 mag, where m and M denote the apparent and the absolute magnitudes, respectively.

Table 2.1.1: The main sample

Object	type	α (J2000)	δ (J2000)	$V_{\mathrm{recession}}^{a}$ [km s^{-1}]	R_{e}^{b} [arcsec]	M_{r}^{b} [mag]	$g\text{-}r^{a}$ [mag]	ϵ^{b}	TET [hour]
VCC 0170	dE(bc)	12 15 56.30	+14 25 59.2	1415.0	31.57	-17.62	0.59	0.34	4
VCC 0407	dE(di)	12 20 18.80	+09 32 43.1	1876.7	18.38	-17.37	0.61	0.43	2
VCC 0608	dE(di)	12 23 01.70	+15 54 20.2	1819.7	25.77	-17.58	0.60	0.35	5
VCC 0794	dE(nN)	12 25 21.61	+16 25 46.9	1672.8	37.33	-17.29	0.61	0.65	3
VCC 0990	dE(di)	12 27 16.93	+16 01 28.1	1717.8	10.31	-17.43	0.62	0.30	3
VCC 1833	—	12 40 19.70	+15 56 07.1	1705.8	8.52	-17.44	0.61	0.19	1.5
VCC 1836	dE(di)	12 40 19.50	+14 42 54.0	2002.6	42.27	-17.45	0.58	0.66	4
VCC 1896	dE(di)	12 41 54.60	+09 35 04.9	1885.7	14.98	-17.04	0.62	0.05	3
VCC 2019	dE(di)	12 45 20.40	+13 41 34.1	1819.7	18.60	-17.65	0.63	0.22	2

Columns are: Name of target, morphological type, RA and DEC, recession velocity ($V_{\mathrm{recession}}$), effective radius (R_e) (half-light major axis), r-band absolute magnitude, g-r color measured at $1R_{\mathrm{e}}$, ellipticity at $1R_{\mathrm{e}}$, and total exposure time (TET). a: SDSS DR15 (Aguado et al. 2019), b: Lisker et al. (2006b, 2007)
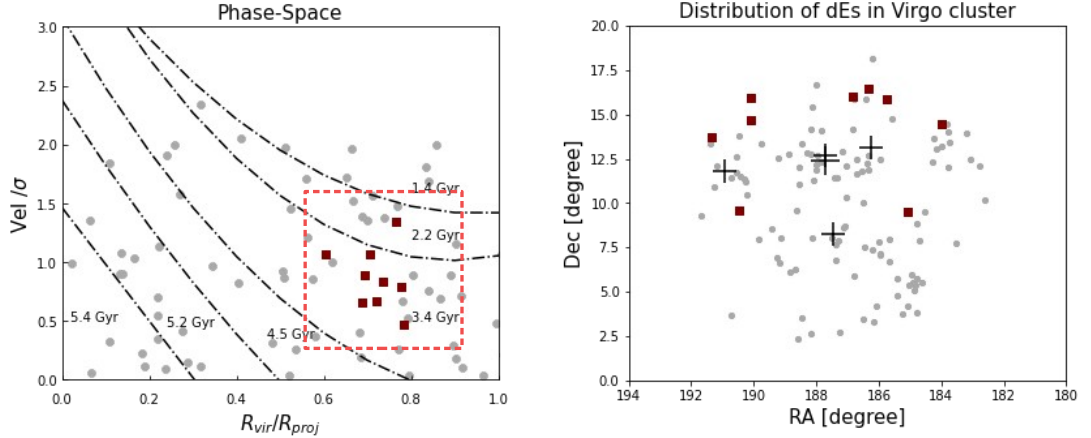
Figure 2.1.3: *Left panel*: the projected phase-space distribution of Virgo dEs with $-17 \geq M_r[mag] > -18$ is presented. DEs within this magnitude interval are shown with gray circles. Nine dEs of our interest are shown with dark red squares and are further marked with a red box. Different zones of this projected phase-space diagram correspond to different infall times onto the Virgo cluster. Zones are taken from Pasquali et al. (2019) and Smith et al. (2019). *Right panel*: the spatial distribution of Virgo dEs are shown. Positions of Virgo giant early-type galaxies (from left to right: M60, M87, M49, M86) are marked with black crosses.

2.2　Multi-Unit Spectroscopic Explorer (MUSE)

These nine Virgo dEs (as introduced in Table 2.1.1) shape the primary sample of this work. Their SDSS images are shown in Fig. 2.2.1. The entire sample was observed with the Multi-
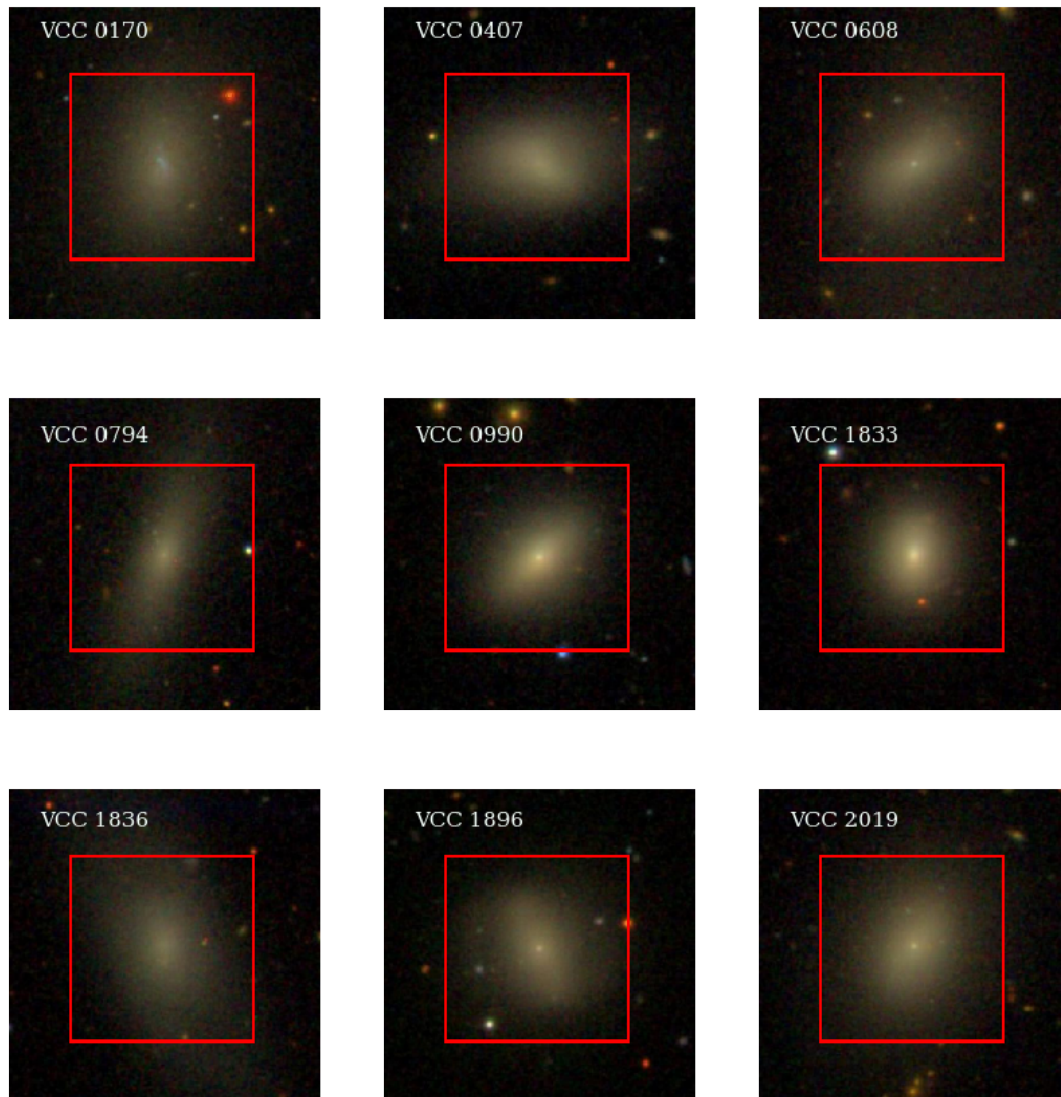
Figure 2.2.1: SDSS images of the main sample. Red squares mark the MUSE's field of view (1×1 arcmin^2).

Unit Spectroscopic Explorer (MUSE) instrument following a science verification proposal in the period of December 2016 to February 2017 and February 2018 to July 2018 (P98, ESO programs 098.B-0619 and 0100.B-0573; PI: Thorsten Lisker).

The MUSE instrument is mounted on the Very Large Telescope (VLT) of the European Southern Observatory (ESO) (Fig. 2.2.2). The telescope is located in Paranal, Chile. MUSE is an optical integral-field spectrograph (IFU) that provides spatially resolved spectra by utilizing a combination of imaging and spectroscopy techniques (Bacon et al. 2010, 2014). Among the current available IFUs, MUSE is the most powerful instrument with a resolving power of $\sim$

Figure 2.2.2: Installation of MUSE instrument on VLT. Image credit: G. Hüdepohl/ESO- https://www.eso.org/public/images/muse-d8b3029/

3000. Through combining data from its 24 identical sub-IFUs, MUSE covers a field of view of 1×1 arcmin^2 with a pixel scale of 0.2 arcsec/pixel. The instrument's field of view is marked in the SDSS images of our sample in Fig 2.2.1. MUSE covers a comprehensive optical wavelength range of 4750 to 9350 Å with a sampling of 1.25 Å per pixel and average instrument resolution of (FWHM) 2.51 Å

For thorough investigations, it should be noted that the MUSE instrument resolution is wavelength-dependent. In Fig. 2.2.3, three different estimates of this dependence are presented. The dark-red line represents MUSE's average instrument resolution (provided by Dr. Lodovico Coccato - private communication). The dark-blue line shows the MUSE instrumental resolution estimated by Mentz et al. (2016), using features of sky flat field exposure. Based on their measurements, MUSE's resolution increases from 65 kms^{-1} at 4650 Å to 35 kms^{-1} at 9300 Å . The light blue line shows the polynomial function that, according to equation 8 of Bacon et al. (2017), best represents the FWHM variation of MUSE instrumental resolution as a function of wavelength.
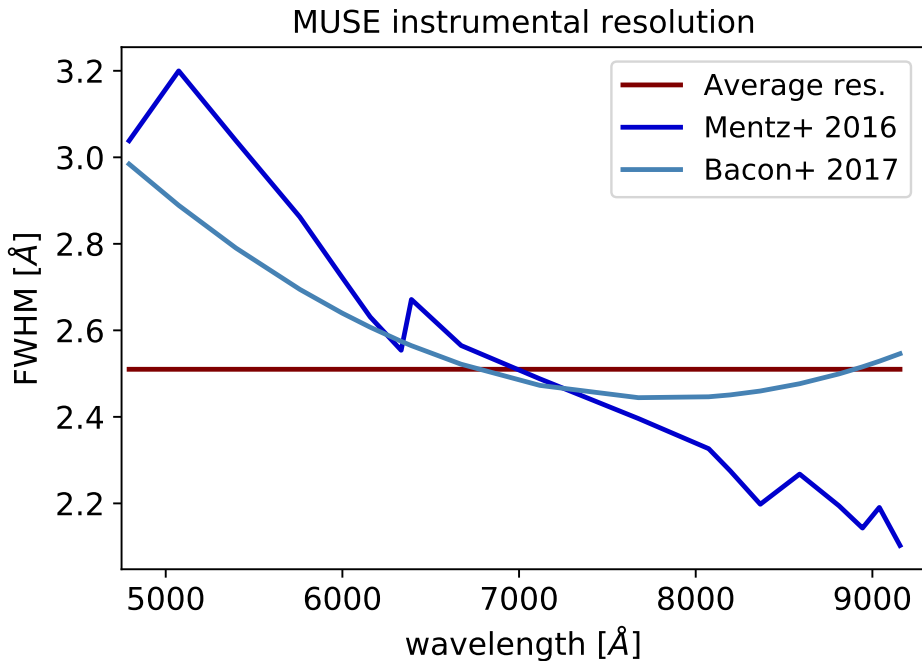
Figure 2.2.3: MUSE instrumental resolution as a function of wavelength.

2.2.1   Data reduction

The reduction of MUSE raw data was carried out in two steps and within an ESO Reflex workflow. The latter is a dedicated environment designed for ESO pipelines that enable users to reduce VLT raw data in a user-friendly environment. Within this environment, we have first used the standard MUSE Data Reduction pipeline (version 2.4.2) (Weilbacher et al. 2012, 2016) to reduce the data and produce MUSE science data cubes. As the second step, we applied the ZAP (Zurich Atmosphere Purge) algorithm to these cubes to further remove sky residuals. A thorough explanation of each step of MUSE data reduction is presented by Weilbacher et al. (2020). Here, we review these steps briefly.

The standard MUSE Data reduction pipeline is divided into two main parts: basic processing and post-processing. Basic processing is the first step, which is activated through a module called "*MUSE-Scibasic*". In this step, basic calibrations and science reductions are performed on individual CCDs; thus, they are repeated 24 times for all sub-IFUs of the instrument. Bad and saturated pixels are marked in this step, and artifacts from individual IFUs instruments are removed from the data. Furthermore, bias and lamp flat-field corrections, wavelength, and geometry calibrations, and twilight sky corrections are performed in this step on the raw data. All the steps mentioned above are performed automatically and in the correct order by the pipeline. The final result of this first step is a pixel table which will be fed to the post-processing part.

The post-processing step is activated through the "*MUSE-Scipost*" module. During this step, the atmospheric refraction is corrected. Furthermore, flux calibration of the data takes

place by converting the pixel table of the last step into flux units. During the observation, the flux of the night sky varies on a relatively short timescale. Thus, after subtraction of the sky continuum (which changes relatively slower), the sky lines are subtracted by re-constructing the sky spectrum using user-selected sky pointings. During this step, the user selects a spatial section of the science cube, which is devoid of the main object and other luminous sources (e.g., stars), based on which the software models the sky spectrum that will be used for performing sky subtraction. Furthermore, corrections of telescope motion and spatial coordinates will be performed by the pipeline. Then, through a module called "*MUSE-exp-combin*", multiple corrected exposures of a particular object will be combined to generate the final MUSE science data cube. Usually, in the generated MUSE cubes, north and east are toward up and left, respectively.

In addition to the standard MUSE reduction procedure, we applied the MUSE-ZAP routine (v.2.2, Soto et al. 2016) on the final MUSE cubes to further correct the sky residuals. The ZAP algorithm uses principal components to minimize sky lines in the cube.

2.3 Control samples

In this work, the properties of the main sample are compared with two control samples, namely the "Virgo control sample" and the "field control sample". We have constructed these samples from available information in the literature. To prevent systematic biases, the Virgo control sample contains galaxies with a similar absolute r-band magnitude (M_r) range to our main sample. Here we have used dEs' M_r as a proxy of their stellar masses (for stellar mass range of the main sample check Section 8.3 of Chapter 8). We could not construct our Virgo control sample solely based on dEs' stellar mass, as we did not have that information for all the dEs available in the literature and the fact that different analyses have employed different assumptions and methods for deriving this parameter.

2.3.1 Virgo control sample

The Virgo control sample consists of dEs, and it is constructed from three main studies:

- Sybilska et al. (2017) (hereafter S17): A sample of 20 Virgo dEs with a magnitude range of $14 < m_r$ [mag] < 12 observed with the SAURON spectrograph at the William Herschel Telescope. Based on M_r, we selected nine Virgo dEs from this study. Please note that Ryś et al. (2014) (hereafter R14) investigated the kinematics of this sample.

- Toloba et al. (2015) (hereafter T15): A sample of 39 Virgo dEs with a magnitude range of -19<M_r [mag]<-16 that were observed using three different telescopes (William Herschel Telescope, Isaac Newton Telescope, and VLT using FORS2 spectrograph). Based on M_r, 14 dEs were selected from the main T15 sample.

- Paudel et al. (2011) (hereafter P11): A sample of 26 nucleated Virgo dEs with a magnitude range of -18.59<M_r [mag]<-15.39 observed using the FORS2 spectrograph on the VLT. Based on M_r, four dEs from the P11 sample were selected. Note that the original study of P11 involved only the stellar population analysis of their sample. Thus, the four selected dEs from P11 are not included in the kinematic investigations of Chapter 3.

Table 2.3.1: The Virgo control sample

Object	type	α (J2000)	δ (J2000)	R_{e} [arcsec]	M_{r} [mag]	ϵ	σ	Ref.
VCC0308	dE(bc)	12 18 50.90	+07 51 43.40	18.70	-17.96	0.07	35.6	1
VCC0543	dE(nN)	12 22 19.53	+14 45 38.81	19.00	-17.69	0.46	39.6	1
VCC0856	dE(do)	12 25 57.93	+10 03 13.56	17.00	-17.80	0.13	32.8	1
VCC1183	dE(di)	12 29 22.51	+11 26 01.99	18.60	-17.86	0.40	42.3	1
VCC1407	dE(N)	12 32 02.74	+11 53 24.26	11.70	-17.03	0.17	42.3	1
VCC1431	dE(N)	12 32 23.41	+11 15 46.90	09.60	-17.67	0.03	60.5	1
VCC1528	dE(nN)	12 33 51.62	+13 19 20.79	11.20	-17.44	0.09	48.0	1
VCC1545	M32-type	12 34 11.53	+12 02 56.27	11.90	-17.23	0.13	50.9	1
VCC1861	dE(N)	12 40 58.60	+11 11 04.10	20.10	-17.85	0.01	30.0	1
VCC0021	dE(bc;N)	12 10 32.15	+10 11 19.04	15.28	-17.10	—	28.9	2
VCC0750	dE(N)	12 24 49.58	+06 45 34.49	19.63	-17.00	—	43.5	2
VCC0751	dE(di;N)	12 24 48.30	+18 11 47.00	12.43	-17.50	—	32.1	2
VCC0781	dE(bc;N)	12 25 15.17	+12 42 52.59	13.51	-17.20	—	38.0	2
VCC0940	dE(di;N)	12 26 47.07	+12 27 14.17	19.92	-17.40	—	40.4	2
VCC1122	dE(N)	12 28 41.71	+12 54 57.08	17.49	-17.20	—	32.1	2
VCC1355	dE(N)	12 31 20.21	+14 06 54.93	30.59	-17.60	—	20.3	2
VCC1453	dE(N)	12 32 44.22	+14 11 46.17	19.05	-17.90	—	35.6	2
VCC1549	dE(N)	12 34 14.83	+11 04 17.51	12.24	-17.30	—	36.7	2
VCC1695	dE(di;nN)	12 36 54.85	+12 31 11.93	24.17	-17.70	—	24.4	2
VCC1895	dE(nN)	12 41 51.97	+09 24 10.28	16.48	-17.00	—	23.8	2
VCC1910	dE(di;N)	12 42 08.67	+11 45 15.19	13.53	-17.90	—	37.0	2
VCC1912	dE(di,bc)	12 42 09.07	+12 35 47.93	22.71	-17.90	—	36.0	2
VCC1947	dE(di;N)	12 42 56.34	+03 40 35.78	9.42	-17.60	—	48.3	2
VCC1167	dE(N)	12 29 14.69	+07 52 39.22	27.30	-17.04	—	—	3
VCC1254	dE(N)	12 30 05.01	+08 04 24.18	14.90	-17.19	—	—	3
VCC1355	dE(N)	12 31 20.21	+14 06 54.93	29.60	-17.67	—	—	3
VCC1945	dE(N)	12 42 54.09	+11 26 18.09	21.50	-17.14	—	—	3

Columns are: Name of target, morphological type, RA and DEC, effective radius, r-band absolute magnitude, ellipticity at $1R_{\mathrm{e}}$, velocity dispersion at $1R_{\mathrm{e}}$ and the reference from which information on kinematics and stellar populations are obtained. Except for the velocity dispersion, the information presented in this table was taken from Lisker et al. (2006a,b).
1: Sybilska et al. (2017), 2: Toloba et al. (2015), 3: Paudel et al. (2011)

In Table 2.3.1, details of the Virgo control sample are presented. For each dE in this control sample, the table contains information on the type, coordinates, effective radius, absolute r-band magnitude, ellipticity, stellar velocity dispersion, and reference to the original study.

In the left panel of Fig. 2.3.1, the projected phase-space distribution of the Virgo control sample is presented. Different studies are marked with different symbols and colors. Our main sample of Virgo dEs is marked with brown squares. In the right panel, the spatial distribution of the Virgo control sample is presented. In this panel, positions of Virgo giant early-type galaxies are marked with black crosses.
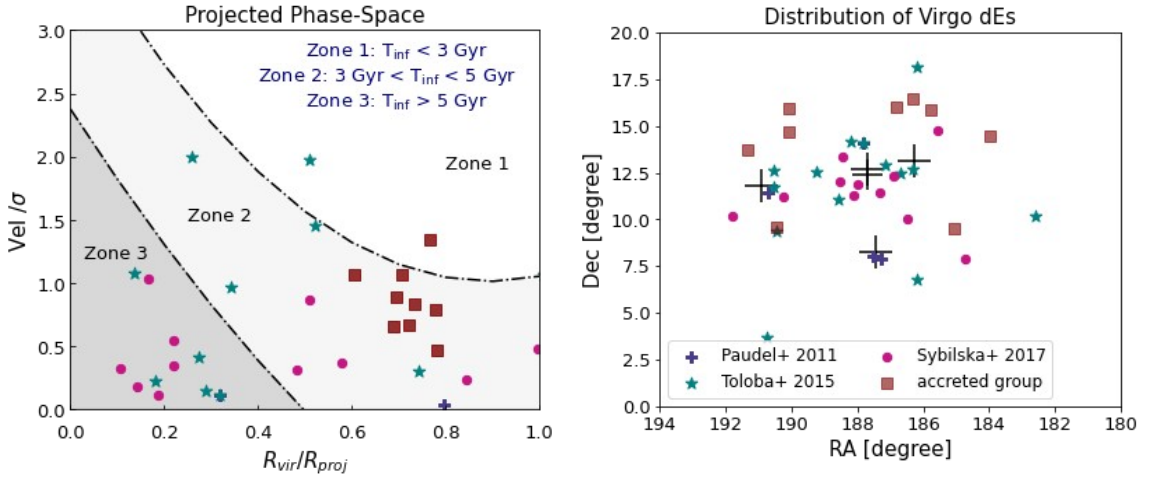
Figure 2.3.1: *Left panel*: the projected phase-space distribution of the Virgo control sample is presented. Different zones, as explained in this panel, denote different average infall times (T_{inf}) based on Pasquali et al. (2019); Smith et al. (2019). *Right panel*: the spatial distribution of the Virgo control sample is presented. dEs are color-coded based on the study from which information is obtained. Positions of Virgo giant early-type galaxies (from left to right: M60, M87, M49, M86) are marked with black crosses.

2.3.2 Field control sample: CALIFA survey

The Calar Alto Legacy Integral Field Area (CALIFA) survey was designed to investigate the evolution of galaxies through cosmic time by a detailed spectroscopic study of ~ 600 galaxies in the Local Universe (Sánchez et al. 2012b; Walcher et al. 2014; Falcón-Barroso et al. 2017). We constructed our field control sample by selecting 10 star-forming field galaxies with $M_\star < 5 \times 10^9$ $M_\odot$ from the CALIFA survey. The selected galaxies fall within a similar stellar mass range as dEs in our main and control samples. The stellar mass range of our sample, derived from the color-to-(M/L) conversion introduced by Bell et al. (2003) is $8.9 \leq \log(M_\star\,[M_\odot]) \leq 9.2$. More information on the stellar masses of our sample dEs is provided in Section 8.3 of Chapter 8. We

Table 2.3.2: The Field control sample

Object	type	α (J2000)	δ (J2000)	R_{e}^a [arcsec]	M_{r} [mag]	ϵ	$M_{\star}$ ($\times 10^{10}$) [M$_\odot$]	λ_{Re}
NGC0216	Sd	00 41 27.16	-21 02 40.82	20	-18.99	0.711	0.19	0.52
NGC3057	Sdm	10 05 39	+80 17 12	32	-19.17	0.269	0.12	0.43
NGC5682	Scd	14 34 44.97	+48 40 12.83	26	-19.39	0.764	0.25	0.68
NGC7800	Ir	23 59 36.75	+14 48 25.04	32	-19.56	0.607	0.19	0.19
UGC05990	Sc	10 52 37	+34 28 58	12	-18.32	0.742	0.16	0.17
UGC08231	Sd	13 08 37.55	+54 04 27.73	19	-19.28	0.664	0.14	0.40
UGC08733	Sdm	13 48 38.99	+43 24 44.82	30	-19.75	0.437	0.26	0.46
UGC10650	Scd	17 00 14.58	+23 06 22.83	23	-19.32	0.782	0.20	0.33
UGC10796	Scd	17 16 47.72	+61 55 12.42	20	-19.56	0.416	0.28	0.24
UGC12054	Sc	22 29 32.44	+07 43 33.68	15	-18.41	0.739	0.10	0.41

Columns are: Name of target, morphological type, RA and DEC, effective radius, r-band absolute magnitude, ellipticity at $1R_{\mathrm{e}}$, stellar mass, and specific angular momentum at $1R_{\mathrm{e}}$. All the values were obtained from Falcón-Barroso et al. (2019).

selected members of our field control sample based on their stellar masses (but not their M_r) since we could not find any galaxy in this survey within the required M_r range that fulfills the criteria of field galaxies. The constructed field control sample consists of late-type spiral and irregular galaxies, and we summarize their properties in Table 2.3.2.

"I am deathless, I am the eternal Lord; For having spread the seed of the Word."

—Ferdowsi, "Shahnameh: The Persian Book of Kings"

3

Internal kinematics of in-falling dEs

This chapter is a partially revised version of Bidaran et al. (2020). "On the accretion of a new group of galaxies onto Virgo: I. Internal kinematics of nine in-falling dEs", published in MNRAS 497, Issue 2, pp.1904-1924

How would pre-processing of our sample dEs affect their stellar kinematics (such as the rotation velocity and velocity dispersion)? This chapter aims to address this question by analyzing the stellar kinematics of our sample dEs and quantifying them by using the stellar specific angular momentum. To do so, we perform the full spectrum fitting technique (using the public pPXF code) over our sample's MUSE data.

3.1 Introduction

Galaxy rotation can be quantified in terms of specific angular momentum (λ_R). The λ_R is a proxy for the projected angular momentum of a galaxy, which is often described as an indispensable metric in studies of galaxy evolution (Emsellem et al. 2007; Jesseit et al. 2009; Emsellem et al. 2011). Through the evolution of a given galaxy, this parameter is affected by gas accretion and star formation activity as well as by the galaxy's interactions with its surrounding environment (see Jesseit et al. 2009; Naab et al. 2014; Yozin and Bekki 2016; Penoyre et al. 2017; Walo-Martín et al. 2020). This makes λ_R a valuable but degenerate metric for a better understanding of galaxy formation and evolution. Investigations of Ryś et al. (2014, hereafter R14) show that dEs in Virgo (as well as two dEs in the field) tend to show flat λ_R profiles up to one effective radius. A similar relatively flat profile is also observed for dwarf galaxies in Fornax (Scott et al. 2020). As suggested by R14, if host halos, such as clusters, are in charge of any transformation in the kinematics of dE progenitors, then at a fixed stellar mass, cluster dEs with different infall times are expected to exhibit different internal kinematics. In this picture, dEs with a more

recent infall time are expected to show internal kinematics intermediate between low-mass field galaxies and cluster dEs accreted at earlier times. Studies of Toloba et al. (2011) show that in the outer parts of the Virgo cluster and at a fixed range of luminosity, dEs tend to show similar rotation curves to late-type galaxies. This is particularly expected in a dynamically young galaxy cluster with ongoing processes of assembly and a diverse yet complete population of galaxies, such as Virgo (Boselli and Gavazzi 2006; Boselli et al. 2018). In contrast, if dEs are already systems that formed with low and flat λ_R profiles (Wheeler et al. 2017), their environment or infall time will not significantly modify their specific angular momentum. Observations of dEs with low degrees of rotation in the field by Janz et al. (2017) also challenge the idea that only tidal interactions in clusters can decrease their λ_R.

Since members of our primary sample are in their initial phase of accretion onto Virgo, the assembly history and dynamical characteristics of their previous environment (i.e., the parent group) should still be preserved in their kinematics and stellar populations. This accreted group of Virgo dEs provides a unique opportunity for investigating the role of a massive galaxy cluster environment in the evolution of dEs' internal dynamics, particularly during their early stages of accretion. In addition to Virgo, environmental mechanisms in their previous host halo (such as ram pressure stripping, tidal interactions, and starvation) have possibly affected the evolution of these nine dEs before their accretion onto the cluster. Thus, studying this group of dEs can also address the role of pre-processing in shaping present-day properties of the "typical" dE population in clusters, as suggested by Toloba et al. (2014) and Sybilska et al. (2017).

This chapter is organized as follows: In Section 3.2 the methods and approaches that are used in this kinematic investigation are discussed in detail. Section 3.3 shows the kinematic maps and the specific angular momentum (λ_R) profiles of dEs in the main sample. Here, these properties are further compared with those of the field and Virgo control samples. Results are discussed in Section 3.4, followed by conclusions in Section 3.5.

3.2   Methods

Our sample consists of low-surface-brightness objects. To accurately measure their kinematic properties, the signal-to-noise ratio (SNR) in each data cube needed to be increased to a minimum threshold. While considering only spaxels with $SNR > 3$, we increased the final SNR for each galaxy by binning spaxels through the Voronoi binning method developed by Cappellari and Copin (2003). This routine is an optimized fitting algorithm that spatially bins data so that each final bin achieves a targeted SNR. While setting low values for the target SNR can affect the quality of the fits, increasing it to higher values results in larger bins and, consequently, in a loss of spatial information, especially in the outskirts of a galaxy. After fine-tuning based on the characteristics of our data set (surface brightness and size of the dEs investigated in this study), we found a minimum SNR of 40 to provide a better compromise between the spatial sampling of the galaxy's outskirts and the accuracy of the measured kinematics. The spectrum assigned to each bin is the averaged spectrum of all spaxels within the defined bin. For better accuracy of the fits, sky residuals, particularly in the red part of the spectrum, are masked. Later on, the stellar kinematics (i.e., rotational velocity and the velocity dispersion of the stellar component)

of each galaxy were computed by fitting its binned spectra between 475 and 960 nm.
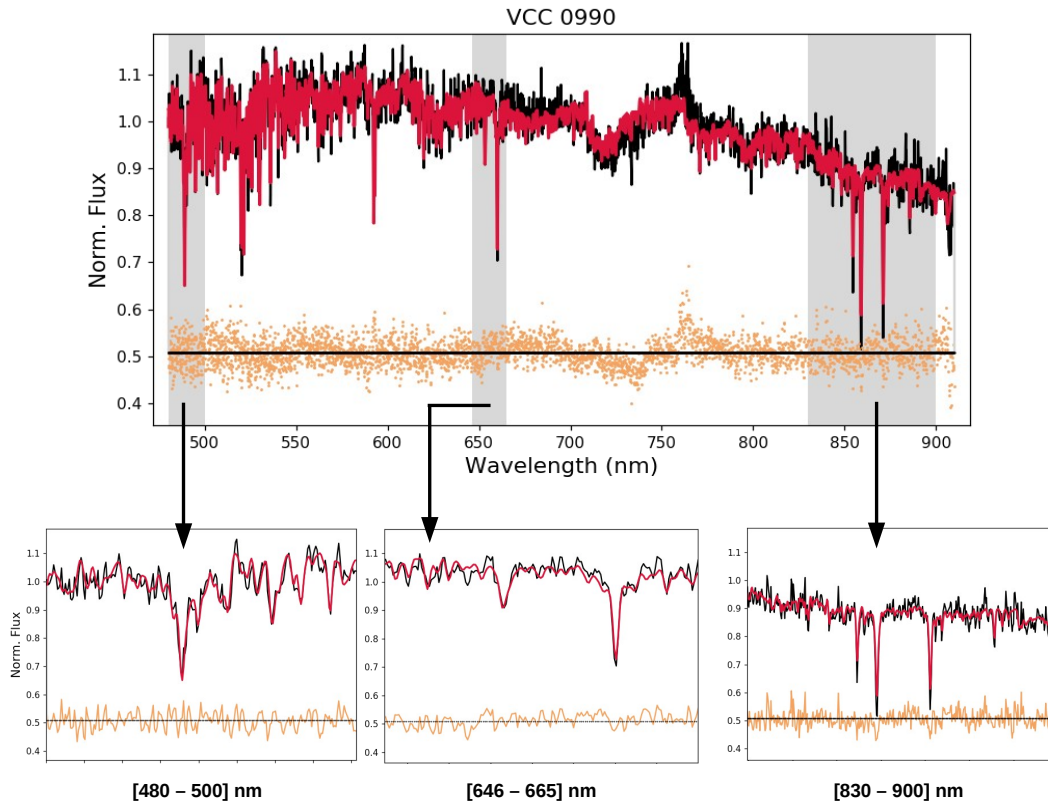
Figure 3.2.1: Example of a pPXF fit of a central bin of VCC0990. The top panel presents the full range of the observed spectrum, while in the lower panels, a zoomed-in view is provided for a better illustration of the fitting accuracy and high quality of the data. In all the panels, the observed spectrum is shown in black, while the best pPXF fit is plotted in red. The residuals between the observed spectrum and its best fit are plotted in orange shifted up by 0.5 for legibility.

For the fitting, we utilized the Extended MILES library (E-MILES) based on BaSTI isochrones (Pietrinferni et al. 2004a). The E-MILES stellar library has moderately high resolution in the range of 1680-50000 Å covering a relatively large range of ages (53 values, from 30 Myr to 14 Gyr) and metallicities (12 [M/H] values from -2.27 to +0.4 dex). The spectral resolution of E-MILES is constant with an FWHM $\sim$ 2.51 Å (Vazdekis et al. 2010, 2016). In the subsection 3.2.1, we discuss the effect of employing different stellar libraries with different spectral resolutions on our kinematic measurements.

The E-MILES library was fitted to each bin's averaged spectrum through the penalized pixel-fitting algorithm (pPXF) introduced by Cappellari and Emsellem (2004) and Cappellari (2017). From an observed spectrum, pPXF derives the line-of-sight velocity and velocity dispersion, parameterized via Gauss-Hermite moments and using an approach of maximum penalized like-

lihood. In this study, the continuum slope was determined using additive Legendre polynomials available in pPXF with a degree of 6. As an example, in Fig. 3.2.1 we show the spectrum of a central bin in VCC0990. The plotted spectrum was chosen to show the quality of the data reduction, performed fits and the degree of telluric lines contamination in the central regions of each dE in our data set.

We obtained error estimates on the kinematics (i.e., stellar rotation velocity and velocity dispersion) derived from each bin's averaged spectrum by using Monte-Carlo simulations. We ran a loop of 50 realizations for each spectrum. We created a simulated spectrum from the original one in each loop by adding the fit residuals, randomly reshuffled among different wavelengths, to the original flux. The final reported error of each bin is the standard deviation of the velocities obtained from the 50 realization loops.

3.2.1 The effect of instrumental resolution

In order to measure the kinematics of a galaxy (particularly the velocity dispersion) by fitting a stellar library, the data and the template library should have the same velocity scale. The latter is possible through the convolution of the library to the instrument's spectral resolution. To do so, the chosen library needs to have a higher resolution than the observed data. However, the MUSE spectral resolution is not constant with wavelength (Fig. 2.2.3), being lower in the blue part of the spectrum (4750 to 5500 Å) and higher in the red part (8400 to 9600 Å) (Krajnović et al. 2015; Guérou et al. 2015; Mentz et al. 2016; Vaughan et al. 2018; Emsellem et al. 2019). The instrument resolution in the red part of the spectra is even higher than the spectral resolution of the E-MILES library. This makes the measurement of the velocity dispersion in low-surface-brightness galaxies, such as dEs, challenging as the velocity dispersion of the targeted dEs can be lower than the instrument resolution. This issue has already been mentioned in different studies of low-mass systems (e.g., see Emsellem et al. 2004; Ganda et al. 2006; Johnston et al. 2019; Emsellem et al. 2019).

Following Emsellem et al. (2019), in order to test the robustness of our velocity dispersion measurements and their dependence on the library resolution, we repeated the fitting procedure by using the calcium II triplet (CaT) library (Cenarro et al. 2001), which covers the wavelength range of the Ca triplet lines (8350-9020 Å) at higher spectral resolution than the E-MILES library (FWHM $\sim$ 1.5 Å). The CaT library contains 706 stellar spectra covering the [Fe/H] range from -3.45 to 0.6 dex. Due to the small spectral coverage of this new library, we performed the pPXF fitting between 8400 and 9000 Å. Adopting an instrument FWHM of 2.51 Å, we present the results of this test in Fig. 3.2.2 for three dEs. In all panels, the distribution of the velocity dispersion measured using the E-MILES library is traced in blue, while the distribution of velocity dispersion derived with the CaT library is plotted in orange. Derived values are from binned spectra of each galaxy. The mean value of each distribution is shown with a thick dashed line while the dotted lines of the same color trace the $\pm$ 1 standard deviation of the distribution.

As shown in Fig. 3.2.2, and consistent with the results of Emsellem et al. (2019) (albeit for different sets of stellar libraries), fitting using both the E-MILES and CaT libraries retrieves a similar range of values for the velocity dispersion in three dEs of our sample. This means that the velocity dispersion of the stellar component obtained in this study from the full spectrum
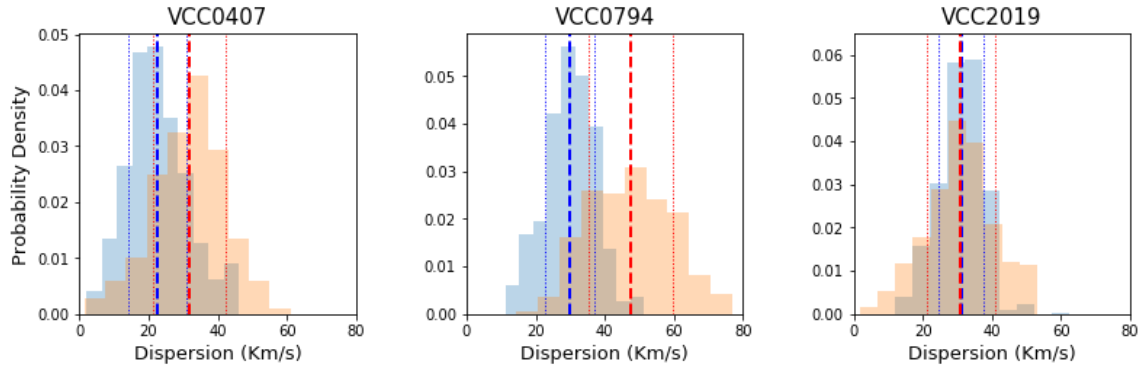
Figure 3.2.2: The distribution of velocity dispersion measured through 1) the full spectrum fitting using the E-MILES library (in blue) and 2) the Ca triplet lines using the CaT library (in orange) for three dEs in our sample. The mean value of each distribution is shown with a thick dashed line, while the thin dotted lines represent the standard deviation of the mean of the distribution.

fitting is reliable and is not particularly affected by the instrument or library resolution. This is true for six dEs in our sample. The remaining three dEs have lower SNR due to shorter exposure time (VCC1833) or extended size (VCC 1836 and 0794) that cannot be fully mapped using MUSE. For these reasons, the sky background was not properly modeled and subtracted, thus hampering the quality of the fits in the CaT region (for the effect of sky residuals also check Johnston et al. 2019). We believe this inadequate background subtraction can cause an offset between two sets of measurements (i.e., blue and orange distributions), whose mean values are nevertheless within 1σ. As an additional test, we used the varying resolution that mimics the MUSE instrument resolution, introduced by Guérou et al. (2015) and Bacon et al. (2017). Results of this test showed no particular difference in comparison to those obtained by using a fixed resolution of FWHM = 2.51 Å (Bacon et al. 2010).

3.3 Results

For each dE, the maximum rotation velocity and velocity dispersion at 0.5 R_e are reported in Table 3.3.1. Except for VCC0170, maps of stellar velocity and the velocity dispersion of our sampled dEs, along the line of sight, are shown in Fig. 3.3.1 and 3.3.2. The error maps of the stellar velocity and velocity dispersion are presented in Section 8.1 of Chapter 8. The left panels show the stacked MUSE data cubes obtained by averaging the flux across the full delivered spectral range. From each dE's MUSE stacked image, isophotes (over-plotted in solid black
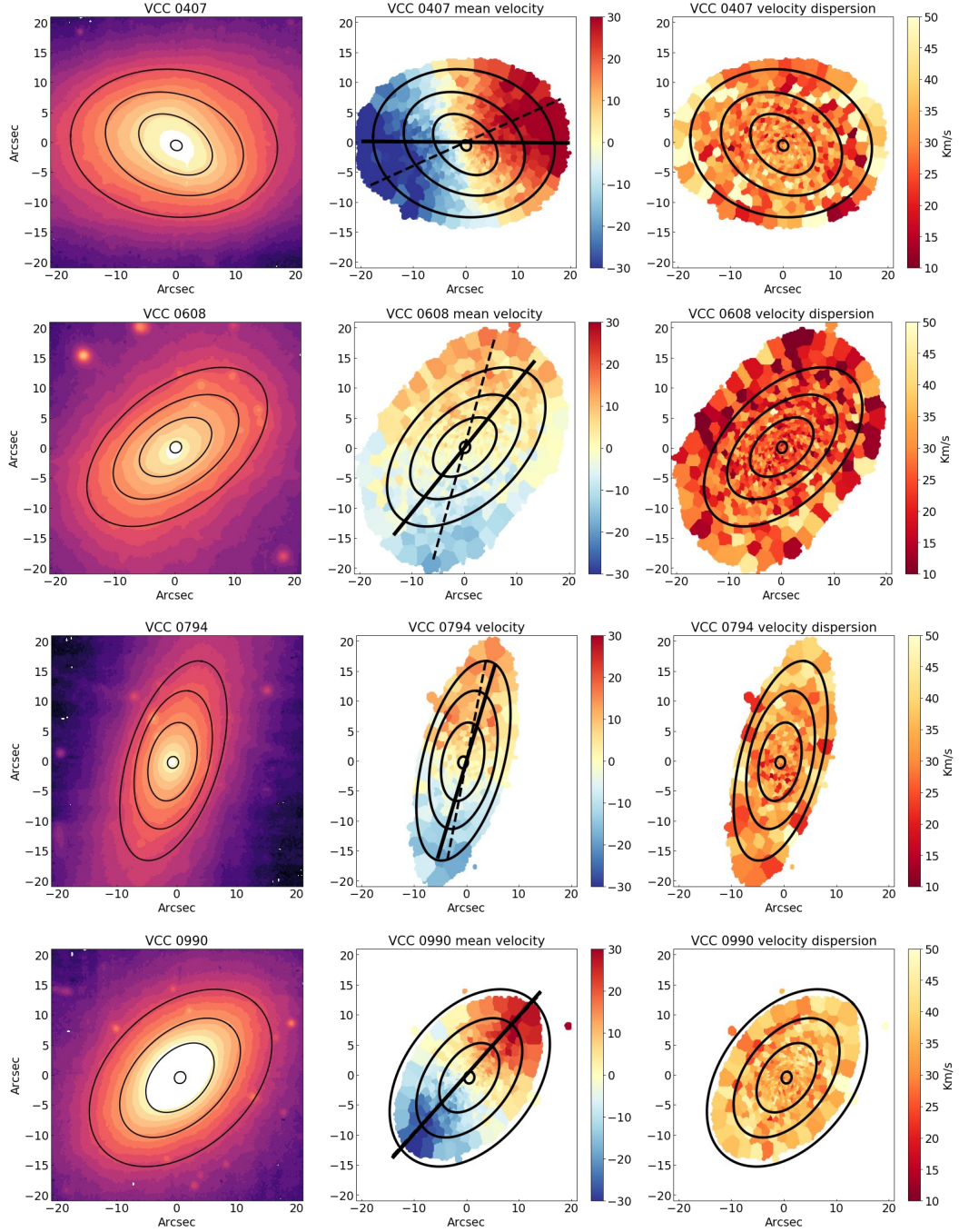
Figure 3.3.1: Stacked MUSE images and stellar kinematic maps of our sample of dEs. In the left-hand panels, the stacked MUSE image of each galaxy is shown with black isophotes over-plotted. From the inside out, the isophotes indicate regions with a surface brightness of 20.59, 21.00, 21.85, and 22.52 mag/arcsec^2 (ABmag). In the middle panels, the line-of-sight velocity map of the stellar component of each dE is plotted. The kinematic position angle (PA$_{\mathrm{kin}}$) and photometric position angle of the major axis (PA$_{\mathrm{phot}}$) are traced with dashed and solid lines, respectively. In the right panels, the associated velocity dispersion map is shown. For a better comparison, the isophotes are drawn in all the panels.
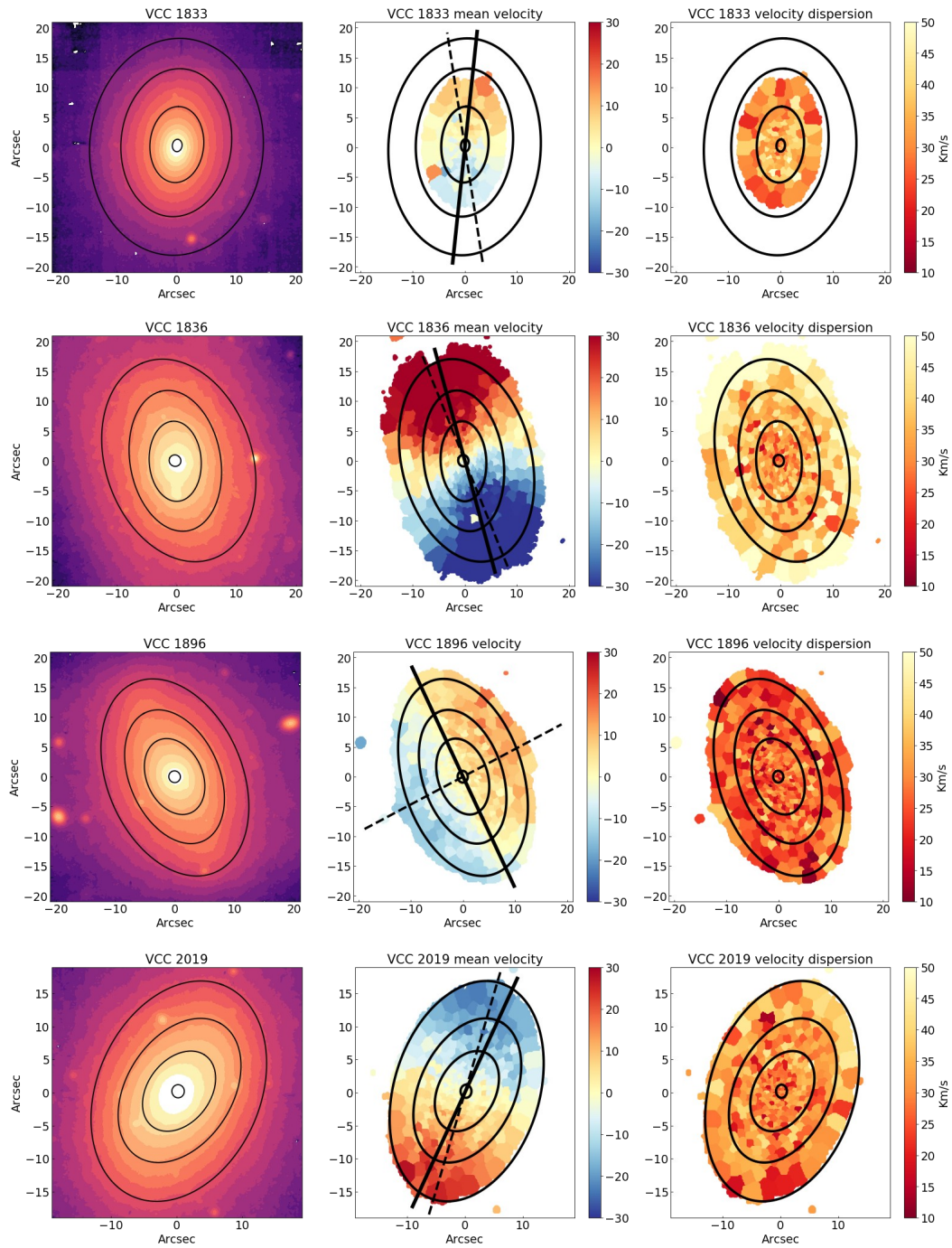
Figure 3.3.2: Continued.

Table 3.3.1: Kinematic parameters of the main sample

Object	$V_{\rm rad}$ [km s^{-1}]	$V_{\rm max}$ [km s^{-1}]	$\sigma_{0.5\rm R_e}$ [km s^{-1}]	$PA_{\rm ph}$ [deg]	$PA_{\rm kin}$ [deg]	Ψ [deg]	$\lambda_{0.5Re}$	λ_{Re}
VCC 0170	1403.4	11.0 ± 15.0	24.5 ± 20	175.41 ± 0.51	155.2 ± 15.5	20.2 ± 15.5	0.39	0.45*
VCC 0407	1881.5	30.6 ± 9.0	30.9 ± 18.0	89.56 ± 1.94	111.1 ± 3.1	20.4 ± 3.6	0.40	0.67
VCC 0608	1807.7	7.8 ± 14.0	21.6 ± 19.0	137.1 ± 1.77	180.0 ± 12.4	42.9 ± 12.5	0.21	0.38
VCC 0794	1669.0	10.2 ± 6.0	30.3 ± 20.0	161.7 ± 0.42	167.6 ± 3.1	5.9 ± 3.1	0.27	0.48*
VCC 0990	1715.1	10.5 ± 4.0	31.5 ± 6.0	134.5 ± 0.24	133.8 ± 4.6	0.5 ±4.6	0.24	0.27
VCC 1833	1711.4	4.9 ± 2.0	32.6 ± 4.0	172.8 ± 0.38	189.6 ± 5.0	16.7 ± 5.0	0.11	0.15
VCC 1836	1985.2	36.9 ± 7.0	34.6 ± 17.0	16.97 ± 0.18	24.8 ± 3.1	7.8 ± 3.1	0.53	0.55*
VCC 1896	1872.5	9.3 ± 7.0	23.0 ± 17.0	27.5 ± 0.58	110.2 ± 3.1	82.7 ± 3.1	0.23	0.22
VCC 2019	1822.1	17.3 ± 6.0	30.9 ± 15.0	153.2 ± 0.96	160.6 ± 9.3	7.2 ±0.3	0.30	0.73

The columns contain the name of the targets, the mean systemic line-of-sight velocity within 0.1 $R_{\rm e}$, maximum velocity ($V_{\rm max}$), and velocity dispersion (σ) at 0.5 $R_{\rm e}$, the position angle of the photometric major axis ($PA_{\rm ph}$) from Alam et al. (2015), the kinematic position angle ($PA_{\rm kin}$), the kinematic misalignment angle (Ψ), the specific angular momentum at 0.5 $R_{\rm e}$ ($\lambda_{0.5Re}$) and at 1 $R_{\rm e}$ (λ_{1Re}). Please note that values marked with a star are measured through extrapolation of the λ_R profile.

lines on the image and maps) were measured by using the Ellipse method (Jedrzejewski 1987). The middle panels present the stellar velocity map of each dE, corrected for the galaxy's systemic radial velocity. The latter was measured by averaging the line-of-sight velocity of binned data within 0.1 $R_{\rm e}$ of a galaxy (to avoid offsets due to rotation of the galaxy in the outer regions). This radial velocity is reported in Table 3.3.1 and is in agreement with what was measured in SDSS DR15 (Aguado et al. 2019). We find that the stellar component in our sample of dEs rotates with $V_{\rm max}$ ranging from ≈ 5 km s^{-1} in VCC 1833 to ≈ 37 km s^{-1} in VCC1836. Lisker et al. (2006b) reported the likely presence of an inclined disk within VCC 0990 and VCC 0407. These objects show a relatively higher rotation with $V \geq 30$ km s^{-1}, consistent with the value obtained with long-slit spectroscopy by Toloba et al. (2015).

The velocity dispersion map of each dE is shown in the right column of Fig. 3.3.1 and 3.3.2. As shown in the maps, the velocity dispersion profile of our sample of dEs has a shallow gradient with $20 \leq \sigma \leq 35$ km s^{-1} within the field of view. A velocity dispersion gradient, although not statistically significant, is observed in VCC 1836, rising from 27.5 ± 3 km s^{-1} in the central regions to more than 40.0 ± 18.0 km s^{-1} in the outskirts of the galaxy.

The stellar kinematics of VCC0170 was measured following the same steps as for the other dEs in our sample after masking the gas emission lines in its central region (Section 3.3.1). The velocity map of VCC 0170 indicates rotation at $V_{\rm max} \approx 18$ km s^{-1} in the outskirts of the galaxy. Like other members of our sample, VCC0170 has a flat velocity dispersion as a function of radius. The stacked image from the MUSE cube, the velocity map, and the velocity dispersion map of VCC0170 are presented in the lower panels of Fig. 3.3.3.

To better visualize possible kinematic misalignment, the position angle of the major photometric axis ($PA_{\rm phot}$) is overplotted with a solid black line on the velocity map of each galaxy. For each dE, this parameter was retrieved from reported values in the g, r, and i bands from
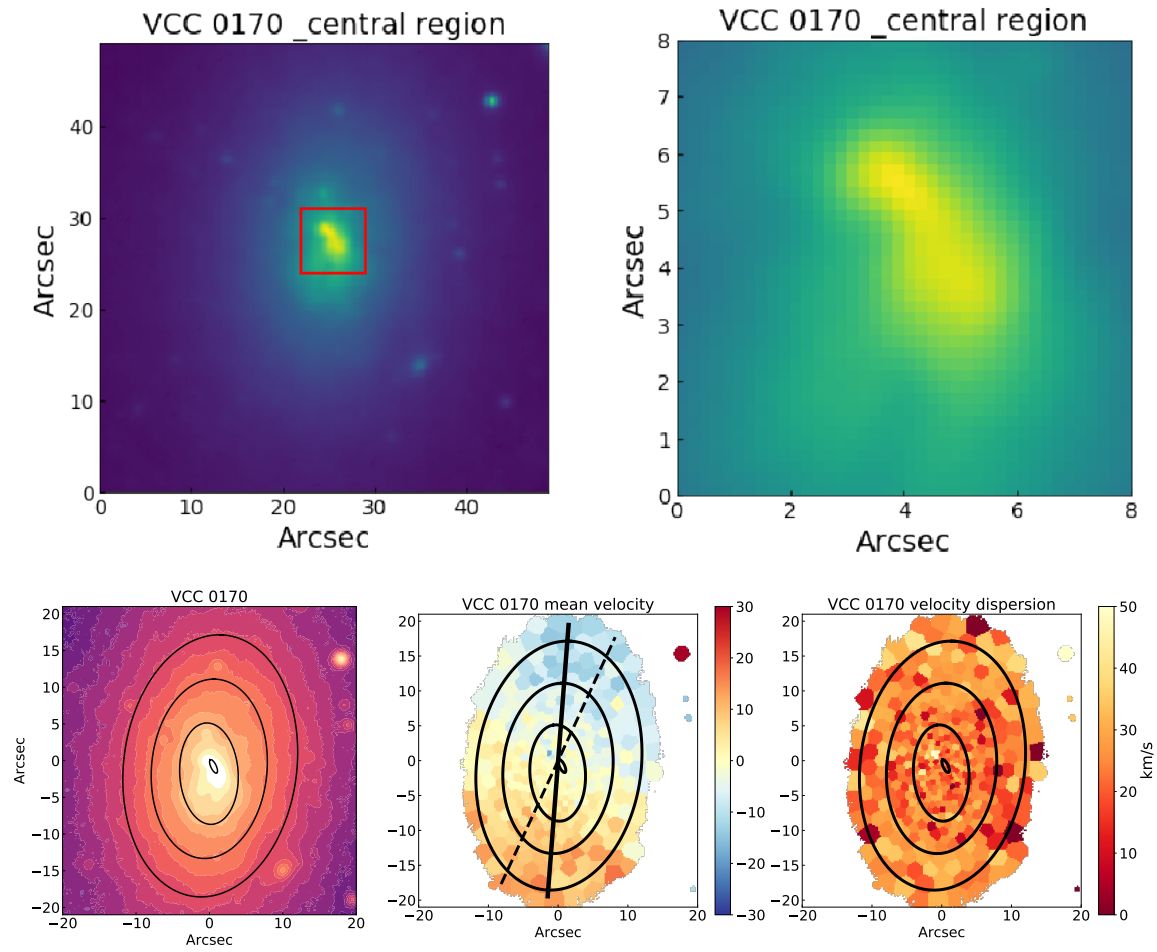
Figure 3.3.3: VCC0170 and its central gas component. *Top panels*: On the left side, the MUSE stacked image is presented where the central region is marked with a red box, 8×8 arcsec^2 in size. In the right panel, a zoomed-in image of this particular region is provided, where the irregular shape of the core can easily be recognized. *Bottom panels*: The kinematic maps of the stellar component in VCC0170. The left panel shows the MUSE stacked image while the rotation velocity and the velocity dispersion of the stellar component are plotted in the middle and right panels, respectively. Isophotes, kinematic and photometric position angles are also over-plotted as in Fig. 3.3.1

SDSS DR15 (Alam et al. 2015). In this study, the (PA_{phot})s were obtained by using the Ellipse method. For each galaxy, we averaged the available PA values and computed the corresponding standard deviation. They are listed in Table 3.3.1. On the same maps, the kinematic position angle (PA_{kin}) of each galaxy is shown with a black dashed line. We measured the PA_{kin} following the method of Krajnović et al. (2006) and using the kinematic maps of each dE (also reported in Table 3.3.1). To better quantify possible offsets, we computed the kinematic misalignment
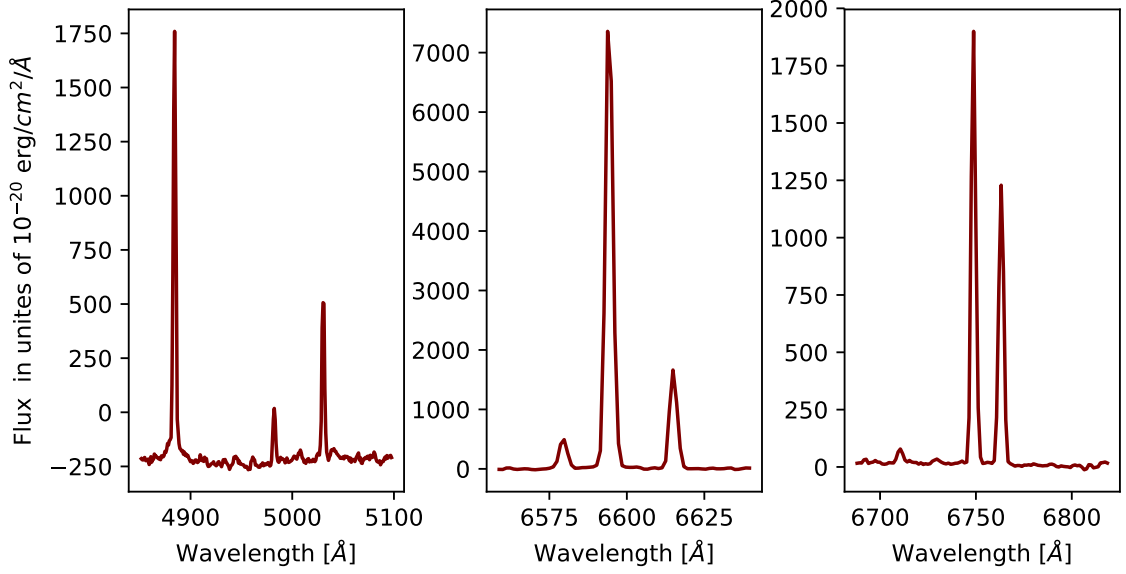
Figure 3.3.4: The observed nebular spectrum of the central region in VCC0170, corrected for the underlying galaxy emission. From left to right, the first panel shows: Hβ, [OIII]λ 4958, and [OIII]λ 5007; the second panel: [NII]λ 6548, Hα, [NII]λ 6583, and the third shows: [SII]λ 6717 and [SII]λ 6731.

angle Ψ as defined by Franx et al. (1991):

$$sin\Psi =| \; sin(PA_{\mathrm{phot}} - PA_{\mathrm{kin}}) \; | \tag{3.1}$$

The resulting values are listed in Table 3.3.1.

VCC1896 has the highest misalignment between its photometric and kinematic position angles ($\Psi = 82.7 \pm 3.1$) and shows prolate-like rotation, with $V_{\mathrm{max}} \approx 9.3$ kms^{-1} and $\sigma \approx$ 23.0 kms^{-1}. This is consistent with measurements of Penny et al. (2015). VCC0608 is another member of our sample that shows high kinematic misalignment ($\Psi = 42.8 \pm 12.5$). Lisker et al. (2006b) reported a possible disk substructure within this galaxy. VCC0608 also exhibits an overall boxy shape in its MUSE constructed image. We will discuss these two cases in more detail in Section 3.4.2.

Several studies of the Virgo cluster report the existence of so-called kinematically decoupled cores (KDC) in early-type dwarf galaxies (e.g., see Geha et al. 2003; Koleva et al. 2011; Ryś et al. 2013; Toloba et al. 2014; Guérou et al. 2015). Observations of Toloba et al. (2014) show that about six percent of dEs in the Virgo cluster host a KDC. However, we do not detect any of these features in our sample of nine Virgo dEs. Although our sample is not statistically significant, thus not representative, the zero detection in this study is consistent with the results of Toloba et al. (2014).

Table 3.3.2: List of optical emission lines and their observed fluxes in VCC0170

Emission Line	Observed Flux $\times 10^{-15} (\text{ergs}^{-1}\text{cm}^{-2})$
H_α	4.76
H_β	1.64
[OIII] λ 4959	0.20
[OIII] λ 5007	0.66
[NII] λ 6548	0.35
[NII] λ 6583	1.04
[SII] λ 6717	1.12
[SII] λ 6731	0.80

Columns are: Name of nebular emission line, observed flux.
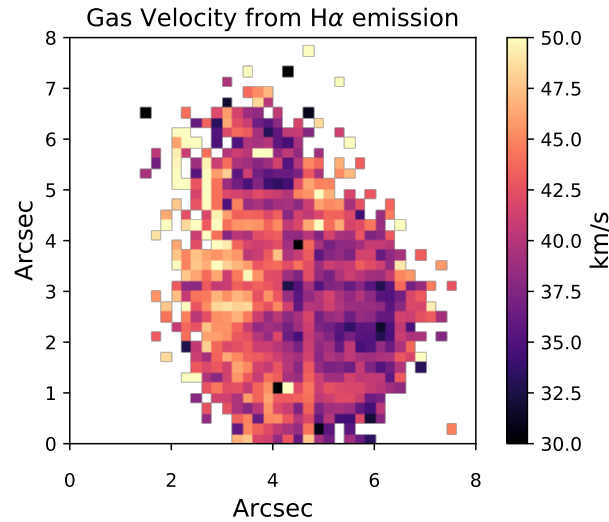
Figure 3.3.5: The gas velocity map from the Hα emission line observed in the central part of VCC0170. This region is marked in the top right panel of Fig. 3.3.3. The gas velocity here is relative to the stellar velocity.

3.3.1 Gas emission lines in VCC 0170

Except for VCC0170 and VCC1836, our sample of dEs lacks nebular emission lines. In the case of VCC1836, the observed emission lines are produced by a background galaxy at redshift $z = 0.552$ (see Chapter 6 for a complete analysis).

The detection of nebular emission lines in the central part of VCC0170 is consistent with its blue color, which is likely due to young massive stars. While this galaxy was initially classified as a late-type galaxy by Gavazzi et al. (2005), it was recognized as a dE member of Virgo by Lisker et al. (2006b), who also pointed out an irregularly-shaped distribution of the blue color in the central part of VCC0170. HI emission also is observed within the central part of this galaxy,

indicating a $\frac{M_{HI}}{M_{bar}}$ ratio of less than one percent (Gavazzi et al. 2005; Lisker et al. 2006b,a). Here M_{bar} denotes the baryonic mass.

As shown in the top right panel of Fig. 3.3.3, the irregular shape of VCC0170's core is also visible in the MUSE stacked image. This is the region marked with a red box in the top left panel of Fig. 3.3.3, which covers an area of 8×8 arcsec^2 (0.40 kpc^2 at an assumed distance of 16.5 Mpc). We summed all the MUSE spaxels within this marked region, modeled the spectrum of the underlying stellar population with pPXF, and finally subtracted this model to obtain nebular optical emission lines of Hβ, [OIII] λ 4959, [OIII] λ 5007, [NII]λ 6548, Hα, [NII]λ 6583, [SII] λ 6717, and [SII] λ 6731. These emission lines are shown in Fig. 3.3.4. We corrected the Hβ and Hα fluxes for Galactic foreground extinction using $A_v = 0.089$ mag from Schlafly and Finkbeiner (2011). We also used the following Balmer decrement to correct the nebular emission lines for intrinsic reddening:

$$E(B - V) = log(f(H_{\alpha})/\mathrm{f}(\mathrm{H}_{\beta}) \times 2.85)) \times (0.4(\kappa_{\mathrm{a}} - \kappa_{\mathrm{b}}))^{-1} \qquad (3.2)$$

where f(H$_\alpha$) and f(H$_\beta$) are the observed H$_\alpha$ and H$_\beta$ fluxes while κ_a and κ_{b} are defined based on equations (3a) and (3b) of Cardelli et al. (1989). We derived E(B-V) = 0.018 mag. In both cases, corrections were carried out using the extinction law of Cardelli et al. (1989). We obtained an Hα luminosity of 1.75×10^{38} W. The observed fluxes of the identified emission lines are listed in Table 3.3.2.

To understand the nature of these detected emission lines, we took advantage of the "Baldwin, Phillips, and Terlevich" (BPT) diagram (Baldwin et al. 1981). The BPT diagram is a diagnostic tool that, based on the ratio of optical emission lines, can distinguish different possible sources of ionization in a given galaxy (i.e., star formation, AGN, or LINERs). Based on the location of VCC0170's central region on the BPT diagram (Fig. 3.3.6), we confirm that the presence of nebular emission lines from this irregularly shaped region is due to star formation. Furthermore, we have measured the kinematics of detected gas inside the marked region in Fig. 3.3.3 by fitting a Gaussian function to the Hα line for each spaxel with SNR $\geqslant$ 3. We chose this particular emission line since it has a higher SNR in comparison to other available lines (see Fig. 3.3.4). The resulting gas velocity map is shown in Fig. 3.3.5. We see that the gas component has a systematic offset in velocity ($\approx 40 \pm 8.0$ km s^{-1}) with respect to the underlying stellar component.

3.3.2 Specific Angular Momentum

To parameterize the rotation in our sample of dEs and in order to compare it with other dEs in the Virgo cluster and the CALIFA field galaxies, we derived the specific angular momentum (λ_R) profile of each dE, following Emsellem et al. (2007) and as described in Equation 1.1 of Chapter 1. The photometric center is measured from each dE's MUSE stacked image using the Multi-Gaussian Expansion (MGE) fitting algorithm introduced by Emsellem et al. (1994) and adapted by Cappellari (2002).

The resulting λ_R profiles are shown in the left panel of Fig. 3.3.7 with different shades of blue and red. For a better comparison, the range of λ_R profiles of Virgo dEs in the R14 sample
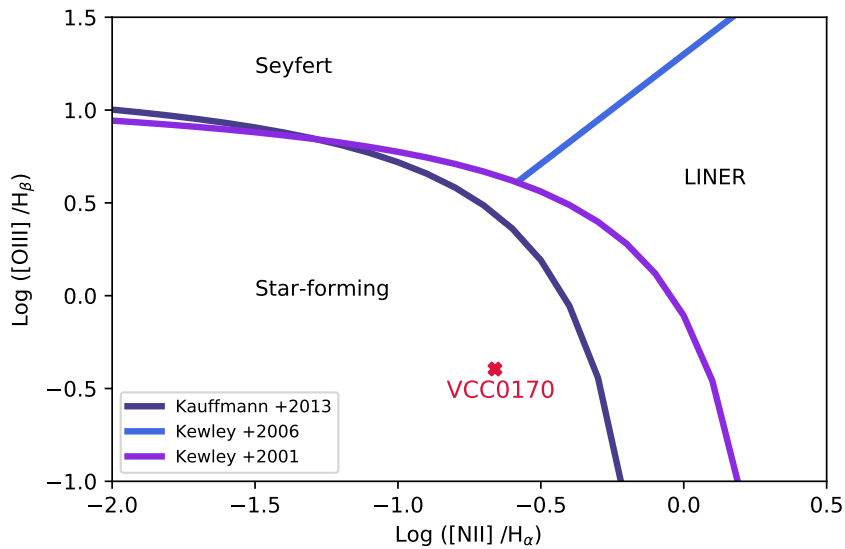
Figure 3.3.6: The BPT diagnostic diagram for VCC0170. The empirical division of Kauffmann et al. (2003) and the theoretical division of Kewley et al. (2001) between AGN (right side of the diagram) and star-forming (left side of diagram) galaxies are plotted with solid dark blue and purple lines, respectively. The Seyfert-LINER division of Kewley et al. (2006) is also marked with a light blue line.

is also shown by a red-shaded region on the same panel. Similarly, the range of λ_R profiles of the CALIFA field galaxies is shown by a blue-shaded region. Their λ_R profiles were measured by Falcón-Barroso et al. (2019).

In the left panel of Fig. 3.3.7, five dEs in our sample, namely VCC0170, VCC0407, VCC0794, VCC1836, and VCC2019, show λ_R profiles similar to those of the CALIFA field galaxies. We trace their λ_R profiles with different shades of blue. The remaining four dEs in our sample, namely VCC0608, VCC0990, VCC1833, and VCC1896, exhibit λ_R profiles comparable with the R14 sample (the red region); hence they are traced with different shades of red.

Although the dEs investigated in this study have quite similar stellar masses, the large spread in the values and slopes of their λ_R profiles are noticeable. VCC0170, VCC0407, and VCC2019 are characterized by steeper profiles that rise from $\lambda_R = 0.06$ at the center to $\lambda_R = 0.6$ at about 1 R_e. The λ_R profile of VCC1836 shows a truncation at about 0.40 R_e. This galaxy is the most extended member of our sample, and the MUSE field of view is too small for sampling up to 1 R_e. The same explanation applies to the λ_R profiles of VCC0170 and VCC0794, which only reach 0.60 R_e and 0.50 R_e, respectively.

In the right panel of Fig. 3.3.7, we plot the λ_{Re}-ϵ diagram (λ_{Re} vs. ellipticity) for the same set of galaxies as shown in the left panel. Here λ_{Re} is the value of the specific angular momentum at one effective radius. The ellipticity of our sampled dEs is taken from Table 2.1.1. Ellipticity of Virgo dEs and the CALIFA field galaxies are taken from Ryś et al. (2014) and Falcón-Barroso et al. (2019), respectively. In this diagram, our dEs are denoted with squares and color-coded as in the same figure's left panel. dEs in the R14 sample and the CALIFA field
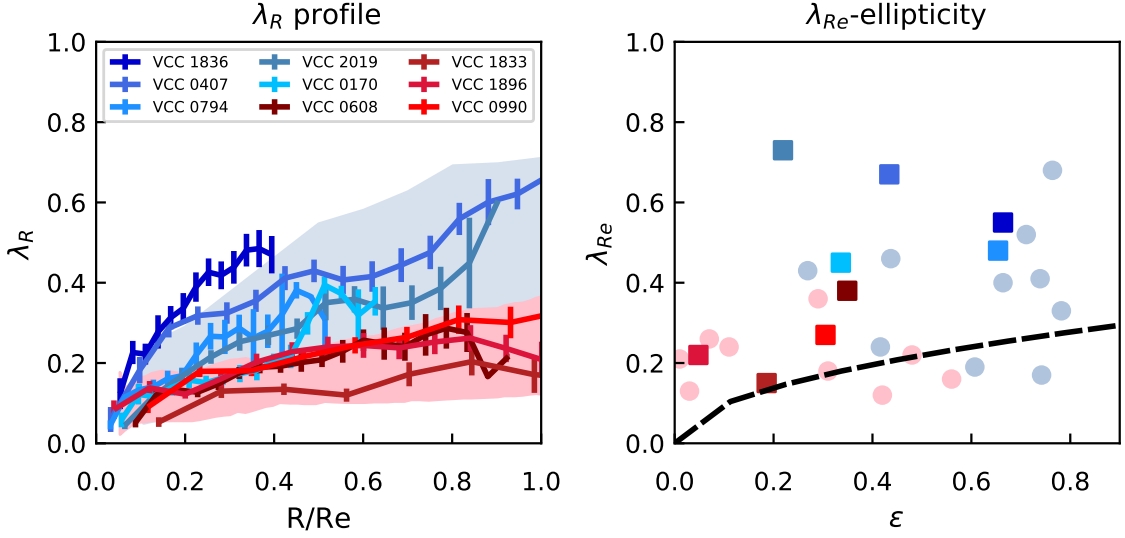
Figure 3.3.7: *Left panel:* The specific angular momentum profiles. The red-shaded area shows the minimum-to-maximum range of the λ_R profiles of Virgo dEs in the R14 sample. The blue-shaded region represents the minimum-to-maximum range of the λ_R profiles of the CALIFA field galaxies. dEs in our sample with low λ_R profiles similar to the R14 sample are traced with lines of different shades of red. Profiles of those dEs overlapping with the CALIFA galaxies are traced with lines of different shades of blue. *Right panel:* λ_{Re} -ϵ diagram distribution for our sample of dEs (color-coded squares), dEs in the R14 sample (red circles) and ten CALIFA field galaxies from Falcón-Barroso et al. (2019) (blue circles). The dashed black line corresponds to the separating threshold between slow- and fast-rotators $(0.31 \times \sqrt{\epsilon})$ introduced by Emsellem et al. (2011).

galaxies are denoted with pink and blue circles, respectively. As mentioned earlier, three dEs in our sample are too extended for the MUSE field of view to be mapped up to $1\ R_{\mathrm{e}}$. For these three galaxies, the λ_{Re} value at $1\ R_{\mathrm{e}}$ is measured through extrapolation of their λ_R profiles. The obtained values of λ_R at $1\ R_{\mathrm{e}}$ and $0.5\ R_{\mathrm{e}}$ are reported in Table 3.3.1. The black dashed line in Fig. 3.3.7 corresponds to $(0.31 \times \sqrt{\epsilon})$, which is the threshold separating slow from fast-rotating galaxies, according to Emsellem et al. (2011). The λ_{Re}-ϵ diagram indicates that, at a fixed stellar mass, on average, the CALIFA field galaxies show higher values of λ_R and ellipticity in comparison to dEs in Virgo. The low λ_R dEs in our sample are mostly distributed close to the boundary separating the fast- from the slow-rotating galaxies. As mentioned in Section 2.1.2, our sample of dEs is located in the outskirts of the Virgo cluster, and according to the right panel of Fig. 3.3.7, they are fast-rotating systems. This is consistent with the results of Boselli et al. (2014) who showed that fast-rotating galaxies are mostly observed in the outskirts of Virgo.
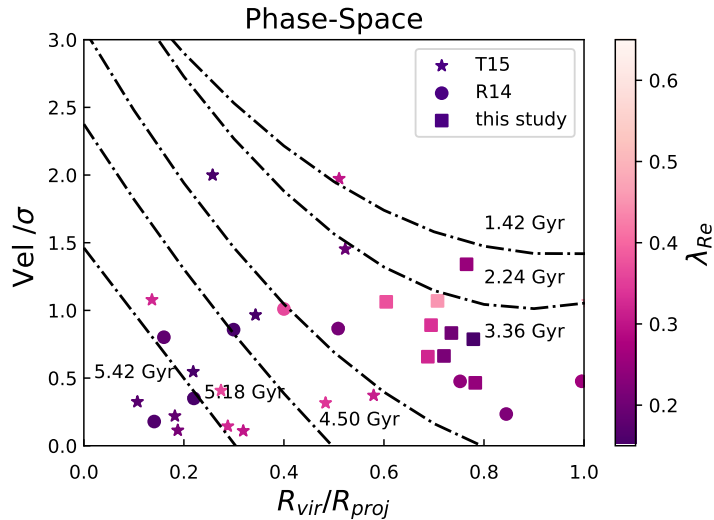
Figure 3.4.1: Projected phase-space distribution of our sample of dEs and those of R14 and T15. The different labelled zones of the diagram, taken from Pasquali et al. (2019) and Smith et al. (2019), represent different average infall times onto the host halo (shown here for the Virgo cluster).

3.4   Discussion

3.4.1   Rotation in dEs

The resulting kinematic maps of our sample show different degrees of rotation (Fig. 3.3.1 and 3.3.2). This result is consistent with other investigations of Virgo dEs available in the literature. Toloba et al. (2011, hereafter T11) investigated a sample of 21 dEs in Virgo with $-15 \geq M_r > -18$ mag and reported a similar range of rotational velocities, from 0 to 50 km s^{-1}. The velocity dispersion of the T11 sample also varies between 30 to 50 km s^{-1}. Meanwhile, by focusing on a smaller sample of Virgo dEs with a similar range of M_r, R14 investigated 12 dEs and showed that their rotational velocity varies from 0 to 40 km s^{-1}. The velocity dispersion maps of dEs in that study also show a flat radial gradient, with values ranging from 40 to 60 km s^{-1}. DEs investigated in this study show similar degrees of rotation as in the results of T11 and R14 but are skewed toward higher values, especially at higher galactocentric distances.

To better estimate the environment's role in the transformation of the dEs' kinematics, one needs to consider their infall time (i.e., how long ago a dE crossed the virial radius of its present-day host halo). That is mainly because environmentally induced mechanisms such as tidal interactions and ram pressure stripping occur over different but not short time scales (Boselli and Gavazzi 2006; Tinker and Wetzel 2010; Bialas et al. 2015). According to Boselli and Gavazzi (2006), ram pressure stripping occurs with a typical timescale of less than 1 Gyr, and tidal interactions happen on a timescale of ~ 2 Gyr, which corresponds to the crossing time of the Virgo cluster. Average values of infall time can be derived using a galaxy's position in the projected phase-space diagram of their host halo (Rhee et al. 2017; Pasquali et al. 2019; Smith et al. 2019). Based on their position in the observer's phase-space (Fig. 3.4.1), we know

that our dEs are in their initial phase of accretion to the Virgo cluster, i.e., they were accreted onto Virgo around 2-3 Gyr ago (Vijayaraghavan et al. 2015; Lisker et al. 2018). On the other hand, the position of the R14 and T15 samples in the observer's phase-space diagram reveals that around 60 percent of them had an earlier average infall time compared to our sample of dEs. This difference in the accretion time may explain our dEs' overall higher rotational velocity compared to the population investigated by R14 and T15. We notice here that, when inferring the average infall times from the projected phase-space diagram of galaxy clusters, Pasquali et al. (2019) consider accretion to the whole cluster and not infall onto its dominant structures or substructures. The latter case would possibly deliver more accurate infall times in the Virgo cluster, which is noticeably structured. Thus, the comparison of infall time of the different Virgo dE samples considered here should be taken with some caution.

Furthermore, results of Falcón-Barroso et al. (2017) for the CALIFA field galaxies show higher values of rotational velocity (from 20 to 100 $\mathrm{km\,s^{-1}}$) and velocity dispersion (from 20 to 90 $\mathrm{km\,s^{-1}}$). Our sample of dEs shows lower degrees of rotation in comparison to the CALIFA field galaxies. As already discussed in Chapter 1, such differences between the kinematics of low-mass field galaxies and Virgo dEs can be expected due to the cluster's role in transforming its accreted members. Besides, before their infall to Virgo, our sample of dEs belonged to a rather massive galaxy group, which models predict to have been as massive as 10^{13} $\mathrm{M}_\odot$ (Lisker et al. 2018). Therefore, the relatively lower degrees of rotation observed in our sample dEs, compared to the CALIFA field galaxies, may be understood in light of pre-processing in their parent group. This will be discussed in more detail in Section 3.4.3.

3.4.2 Stellar rotation in VCC0608 and VCC1896

Among the dEs investigated in this study, VCC0608 and VCC1896 present a relatively high offset between their photometric and kinematic position angles. These two dEs can not be classified as regular rotators. In this subsection, we will discuss different possible explanations for the presence of such an irregular kinematic structure.

VCC1896 with $\Psi = 82.7° \pm 3.1°$ has the highest offset between its photometric and kinematic axis. Taken at face value, VCC1896 would look like a dE with minor axis rotation. Lisker et al. (2006b, 2009) reported the existence of two rather faint spiral arms for VCC1896 and a bar aligned with the outer photometric minor axis of this galaxy (see also Michea et al. 2021). Mastropietro et al. (2005) showed that, due to tidal interactions, asymmetric features and open spiral arms could be formed in those dEs that are located in the outskirts of the cluster. In addition to that, and as shown by Kwak et al. (2019), the cluster tidal field can trigger the formation of weak spiral arms in disk dEs. N-body simulations of Smith et al. (2021) showed that pericenter passages very close to the core of the cluster could induce similar substructures in cluster dEs. These results might explain the existence of the faint spiral arms in VCC1896. Due to their low surface brightness, the faint spiral arms of VCC1896 are not detected in our MUSE data cube; therefore, they are not present in the kinematic maps of this dE. We only detected the bright bar of this dE in its MUSE cube. While the presence of the bar explains the high offset between kinematic and photometric PA, it may also be a morphological feature relevant to the evolution of VCC1896.

The bar in the central region of VCC1896 can either be a pristine structure that formed and developed through standard processes or a tidal feature that formed as a result of interactions with the environment (e.g., see Mastropietro et al. 2005). Tidal interactions are known as one of the most dominant mechanisms that can induce instabilities in the stellar disk of galaxies and form bars, particularly in central regions of galaxy clusters and groups (Łokas et al. 2016). Moreover, Kwak et al. (2019) showed that tidal effects due to galaxy-galaxy interactions, which are more dominant in the central parts of a cluster, can be efficient in causing instabilities to bar formation in dwarf galaxies in a Virgo-like halo. As for Virgo, observations of Janz et al. (2012) also confirm that dEs with bars are mostly observed in the central parts of the cluster. Also, simulations have shown that bar instabilities can be triggered in Local Group dwarf galaxies after their first pericenter passage (Gajda et al. 2016). However, based on Pasquali et al. (2019), the probability of having already experienced a first pericenter passage for galaxies with a similar average infall time as VCC1896 is not exceptionally high. Thus, the presence of a bar structure in VCC1896 may be interpreted in the light of pre-processing in its parent group and less likely in Virgo.
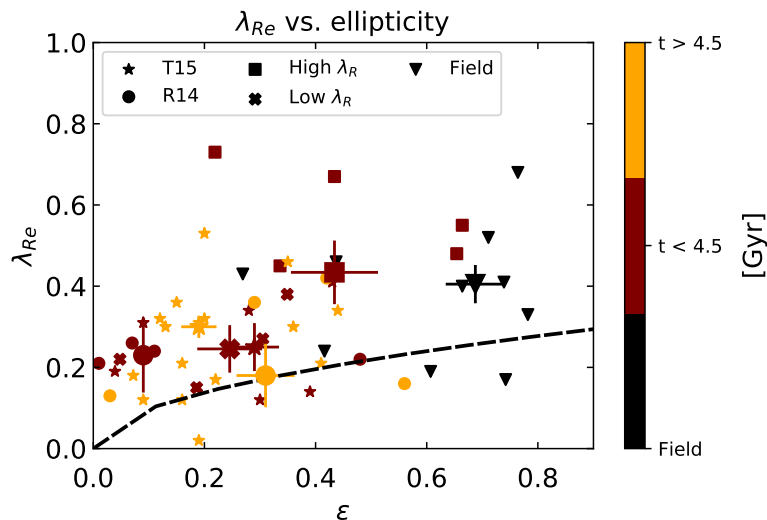
Figure 3.4.2: The λ_{Re}-ϵ diagram color coded based on the average infall time of each galaxy. The CALIFA field galaxies are denoted with black triangles. Our sample of dEs with high and low values of λ_{Re} are traced with squares and crosses, respectively. The R14 sample dEs are marked with circles. The T15 sample dEs are marked with stars. The median ellipticity and λ_{Re} of each group of galaxies are also denoted with their corresponding symbol, but bigger, and error bars. The dashed black line corresponds to the separating threshold between slow- and fast-rotators ($0.31 \times \sqrt{\epsilon}$) introduced by Emsellem et al. (2011).

VCC0608 with $\Psi = 42.9° \pm 12.5°$ is the second dE in our sample, showing significant misalignment between its kinematic and photometric minor axis. The observed kinematic misalignment can trace past or ongoing tidal interactions with the massive halo of Messier 100 (sitting at the projected distance of ~ 28.7 kpc to VCC0608 and an assumed Virgo distance of 16.5 Mpc). VCC0608 is a boxy-shaped galaxy as its isophotes on the MUSE stacked image show $A_4/a \approx -0.02 \pm 0.003$ at $1~R_e$. In this regard, VCC0608 shares similarities with LEDA

074886 (Graham et al. 2012), which is also a boxy-shaped dwarf galaxy with M $\approx 10^9$ M$_\odot$ in the halo of NGC 1407. Following the same argument as in Graham et al. (2012), the boxy shape of VCC0608 and its high kinematic misalignment angle may indicate that this galaxy is the remnant of a past nearly edge-on merger of two disk dwarf galaxies (see, e.g., Naab and Trujillo 2006). In this case, the inner disk of the galaxy is believed to have formed from gas-driven inward during the merger event (Graham et al. 2012). In that case, a younger stellar population is expected to be observed in the central region of VCC0608. We will comment on this in Chapter 4.

3.4.3   Group vs. cluster environment

Based on the kinematic analysis performed in this study, we found that the specific angular momentum (λ_R) profile of our sample of dEs is intermediate between that of dEs in Virgo and CALIFA low-mass galaxies in the field.

The angular momentum is often described as an essential metric for understanding the evolution of low-mass galaxies. This parameter may reflect conditions of low-mass galaxies' early environments, where these objects formed or spent most of their lives (see, e.g., Shi et al. 2015). The angular momentum is typically parametrized in terms of the projected stellar specific angular momentum along the line of sight (λ_R). This parameter is weighted according to the luminosity; thus, it is considered to be a relevant proxy for real stellar specific angular momentum of a galaxy (Emsellem et al. 2007; Jesseit et al. 2009; Emsellem et al. 2011). Studies have revealed that, through the lifetime of a galaxy, mechanisms such as gas accretion and star formation can effectively increase the angular momentum of the entire structure. For instance, Zoldan et al. (2019) showed that at a fixed stellar mass, gas-rich systems tend to have higher degrees of rotation. Meanwhile, other studies show that mergers and tidal heating of the disk can decrease the net rotation of a galaxy, thus, its angular momentum (for example, see van den Bosch et al. 2001; Brook et al. 2011; Naab et al. 2014; Penoyre et al. 2017; Greene et al. 2018). Tidal interactions frequently occur in galaxy groups or central parts of a galaxy cluster, mostly due to interactions with the halo's tidal field and encounter with other cluster members. Tidal interactions are known to be one of the effects responsible for the evolution of λ_R as well as for the morphological transformation of galaxies in clusters and groups (e.g., Lisker et al. 2006b; Boselli and Gavazzi 2006; Lisker et al. 2007; Michielsen et al. 2008; Toloba et al. 2009; Lisker et al. 2009; Kormendy et al. 2009; Geha et al. 2010; Toloba et al. 2011; Janz et al. 2012; Toloba et al. 2012; Ryś et al. 2014). On the other hand, ram pressure stripping is expected to have a marginal effect on altering the λ_R profile of a galaxy (Yozin and Bekki 2016). Following the scenario suggested by R14, cluster low-mass galaxies with earlier infall times (i.e., with more pericenter passages) are expected to experience a more significant tidally-driven change of λ_R. Accordingly, newly accreted low-mass galaxies are expected to exhibit internal kinematics intermediate between low-mass field galaxies and "more ancient infallers" in the cluster. Such expected intermediate kinematics is shown in the left panel of Fig. 3.3.7. In this plot, our sampled dEs, with an average infall time of 2-3 Gyr to Virgo, distribute between the CALIFA low-mass galaxies in the field and the Virgo dEs in the R14 sample. The latter sample has been exposed to environmental effects for a longer time ($\sim$ 1-2 Gyr more), according to the lower

panel of Fig. 3.4.1.

Along with λ_R, the ellipticity of a satellite galaxy is also expected to decrease with infall time on the ground of tidally-driven effects that can thicken the stellar disk of a system. For instance, D'Eugenio et al. (2015) show that in a rich cluster, the fraction of spheroidal early-type galaxies increases toward lower clustercentric distances (but see: Weijmans et al. (2014)). In Fig. 3.4.2 we represented the same λ_{Re}-ϵ diagram of Fig. 3.3.7 where different groups of galaxies are now color-coded according to their average infall time, as read from the bottom panel of Fig. 3.4.1. DEs with high and low values of λ_{Re} in our sample are marked with squares and crosses, respectively. Circles denote the R14 dE sample, and, additionally, the T15 sample is indicated with stars. In Fig. 3.4.2, the CALIFA field galaxies (denoted with triangles) with an assigned average infall time of zero Gyr exhibit, on average, higher ellipticity than Virgo dEs. The average ellipticity and λ_{Re} of each group are indicated by their corresponding symbols, but more oversized, and error bars. A spread, similar to that of the λ_R profiles, is also visible in the ellipticity of the nine dEs investigated in this study. The ellipticity of the low-λ_R dEs in our sample is comparable to those dEs in the T15 sample of similar infall times. The ellipticity of low-λ_R dEs in our sample is also comparable to those dEs in the R14 sample that have, on average, earlier infall times.
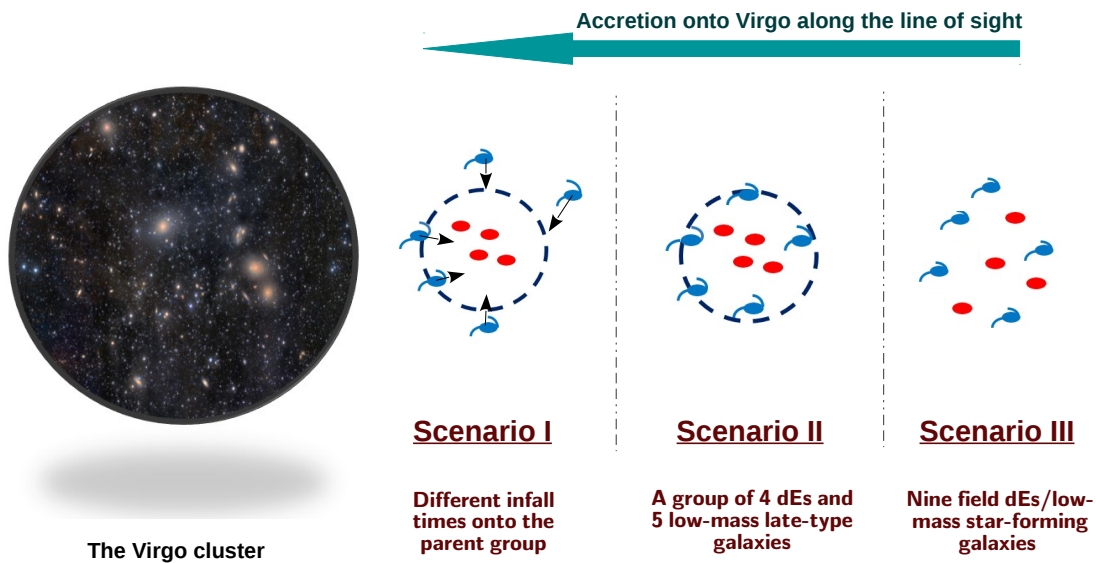
Figure 3.4.3: A schematic presentation of three proposed accretion scenarios. The red and blue symbols represent dEs with low and high λ_R profiles, respectively. The dashed line represents the virial radius of dE's parent galaxy group. The length of arrows in the scenario I indicate the possibility of dEs' different accretion times onto their parent galaxy group. A brief explanation of each scenario is provided in the plot.

Given their similar stellar masses and comparatively short infall time to Virgo, the spread in the λ_R profile of our sample of dEs is rather large (Fig. 3.3.7). One possible explanation is that the Virgo environment has had an only marginal impact on the evolution of the λ_R

profiles of our sample of dEs (if any) on the ground that their recent infall time decreases their probability of having already experienced a pericenter passage. In this regard, Pasquali et al. (2019) showed that near 40 percent of satellite galaxies with an average infall time of 3.6 Gyr have not experienced their first pericenter passage yet. Environmental processes during pericenter passages are more efficient in altering λ_R rather than at higher clustercentric distances (Villalobos et al. 2012).

According to the scenario proposed by Lisker et al. (2018), prior to their infall to Virgo, our sample of dEs were probably members of a rather massive galaxy group (10^{13} M$_\odot$) where the probability of tidal interactions is high (Tal et al. 2009) due to lower velocity dispersion of the halo (Boselli and Gavazzi 2006). Villalobos et al. (2012) have shown that in an equally massive halo, the λ_R profile of a galaxy progressively flattens and decreases in value as the galaxy undergoes more and more pericenter passages. The latter is mainly by virtue of substantial dynamical disturbances that often arise after several orbital periods (i.e., > 4 Gyr). In this regard, the diversity in ellipticity and λ_R profiles of our sample of dEs may be a reflection of their different infall times onto the previous host halo. Hence, the four dEs with λ_R profiles as low as those of the Virgo dEs in the R14 sample (in red in Fig. 3.3.7) may have been accreted earlier onto their previous host halo, and therefore evolved more strongly under their group's environmental mechanisms. They include two galaxies with footprints of tidal interactions in their kinematics (i.e., VCC1896 and VCC0608 in Section 3.4.2). Contrarily, the remaining five dEs with λ_R profiles similar to those of the CALIFA field galaxies (blue profiles in Fig. 3.3.7) may have experienced partial transformation mainly due to their comparatively lower number of pericenter passages in this previous host halo, if any. In this picture, what we have measured for our sample of dEs may be considered as the result of pre-processing in a different environment than Virgo. A schematic presentation of this scenario is illustrated in Fig. 3.4.3 as Scenario I.

Stripping the gas content of galaxies is a known effect of high-density environments (i.e., massive galaxy groups and clusters) mainly due to ram pressure stripping (Boselli and Gavazzi 2006; Boselli et al. 2008). The efficiency of such mechanism depends directly on the density of the inter-cluster medium, as well as on the speed and orbit of the accreted galaxy (e.g., Gunn and Gott 1972; Vollmer et al. 2001; Steyrleithner et al. 2020). Ram pressure stripping can be noticeably efficient for low-mass galaxies, mainly due to their shallow potential well. According to Boselli et al. (2008), and Boselli et al. (2014), low-mass systems, if gas-rich, can become quiescent systems on rather short timescales in the Virgo cluster. Thus, both the previous parent group and the Virgo cluster could have been responsible for gas stripping in our sample of dEs (for gas stripping in groups see Brown et al. 2017). Moreover, McPartland et al. (2016) and Ebeling and Kalita (2019) show that the efficiency of ram pressure stripping is highest when the velocity vectors of galaxies in a group being accreted onto a cluster are aligned with, thus add up to the velocity vector of the infalling group itself.

Ram pressure can perturb and make the gas content of galaxies unstable (Kronberger et al. 2008; Steyrleithner et al. 2020). We observe these effects in VCC0170, whose gas component exhibits a velocity offset from the galaxy's stellar body and nebular emission lines consistent with recent/ongoing star formation (Roediger et al. 2014). This finding allows us to envisage an alternative scenario (illustrated as Scenario II in Fig. 3.4.3). In our sample, those dEs with

higher values of λ_R could have been low-mass, late-type, star-forming galaxies in the previous host halo, which lost most of their gas reservoir after infall to Virgo, mostly via ram pressure stripping (Toloba et al. 2009; Boselli et al. 2014). As already explained in the first scenario, tidal interactions only develop during several orbital periods, comparable to the cluster dynamical time-scale. Therefore, our dEs with high but comparable values of λ_R and ellipticity to field galaxies have experienced little dynamical transformation thus far in Virgo. In this picture, the low-λ_R dEs in our sample could have been accreted to Virgo as early-type galaxies that likely lost their gas content and were transformed dynamically in their previous environment. Moreover, tidal disturbances (such as in VCC0608 and VCC1896) indicate tidal encounters that occurred in the past, but possibly not in Virgo, due to their rather recent infall time. We then suggest that the low-λ_R dEs in our sample have likely been processed by their previous group in both the first and second scenarios. This second scenario is more in line with what was suggested by Toloba et al. (2009, 2011, 2015). Further analysis on age, metallicity, and star formation history of this sample can provide us with a better understanding of their evolution before and after accretion onto the Virgo cluster and thus evaluate this scenario.

Alternatively, the observed spread in the λ_R profiles and ellipticity of our sample could be consistent with a recently accreted population of field dEs, with intrinsically different degrees of rotation and ellipticity (illustrated as Scenario III in Fig. 3.4.3). Janz et al. (2017) studied a sample of nine isolated quenched dEs in the Local Volume and reported diverse kinematics for this sample. In this regard, the four low-λ_R dEs in our sample could originally have been primordial slow-rotating objects with rather flat λ_R profiles even before entering a high-density environment. The latter is consistent with the results of Wheeler et al. (2017), who show that in the absence of external tidal fields, isolated dwarf galaxies can be formed as dispersion-dominated systems. In this alternative interpretation, the dEs with higher values of λ_R can intrinsically be different from their low-λ_R counterparts in our sample, exhibiting kinematics due to relatively minor or moderate processing thus far in the cluster. Geha et al. (2012) showed that the fraction of field dEs in the same stellar mass range of our sample and with no active star formation is less than 0.2 percent (corresponding to a total number of 4 galaxies). According to this study, we cannot firmly rule out the possibility that the low-λ_R dEs in our sample were also field members accreted to Virgo. However, it would be a rare coincidence that these four field galaxies were accreted on to Virgo with a similar velocity as the accreted group and at the same time. We believe that constructing a more statistically rich sample of dEs in different environments (such as field, groups, and galaxy clusters) and particularly outskirts of Virgo can provide us with a complete picture of the role of the environment in altering kinematics and other properties of low-mass galaxies.

3.4.4   Kinematic comparison with the Local Group dEs

Our dEs share a similar morphological type (but not the same stellar mass range) with three Local Group satellites: NCG205, NGC147, and NGC185. These three systems are within close distance to us; thus, their kinematics are derived using their resolved stars and not their integrated light as for more distant objects.

Geha et al. (2010), investigated NGC 147 and NGC185 up to $\sim$8 Re and reported on well-defined rotating stellar bodies in these two satellites. Based on their results, NGC 147 and NGC185 are rotating systems along their major-axis with rotational velocities of 17 km s^{-1} and 15 km s^{-1}, respectively. Moreover, their studies indicate a descending velocity dispersion profile with an average $\sigma = 16$ and 24 km s^{-1}, respectively. Their measurements introduced NGC185 and NGC 147 as two rotationally supported dEs. NGC205, on the other hand, shows a perturbed stellar system beyond its 4.5 arcmin radius with a maximum rotational velocity of 11 km s^{-1} and velocity dispersion of 35 km s^{-1} (Geha et al. 2006). Given its small line-of-sight distance to M31 ($\sim$39 kpc McConnachie et al. 2005), NGC205 is believed to be tidally interrupted by this giant galaxy (e.g., Geha et al. 2006). Photometric and kinematic results of this particular dE are in line with the proposed hypothesis.

Focusing on the behavior of Local Group dEs within 1 Re (the spatial coverage provided by our MUSE data), the rotational velocity of NGC147 and NGC185 drops to < 10 km s^{-1}. The velocity dispersion, on the other hand, rises to ~ 20 km s^{-1} for both galaxies. Within the same galactocentric distance, our sample dEs and the Virgo comparison sample show higher degrees of rotational velocity and velocity dispersion than dEs in the Local Group. One possible explanation behind this discrepancy may be the different stellar masses of the two compared populations [1]. Local Group dEs are less massive than those investigated in this study. Low-mass systems as massive as Local Group dEs are expected to have intrinsically lower rotational velocities (Falcón-Barroso et al. 2019; Scott et al. 2020). In addition, these low-mass systems are more susceptible to tidal interactions within groups and clusters, as already noted for NGC205, which can slow them down more efficiently than in the case of more massive galaxies.

3.5 Conclusions

In this chapter, we presented the kinematics of dEs in our main sample. We measured the line-of-sight velocity and velocity dispersion across the stellar body of each dE, using pPXF on the full spectral range delivered by MUSE. Later on, we used these values to compute the λ_R profiles of our sampled dEs to compare them with other similar measurements for different environments available in the literature. The main results of our analysis can be summarized as follows:

- The stellar component of our sample of dEs shows a rather similar range of rotational velocities in comparison to other dEs in Virgo (from 5 to 40 km s^{-1}). The velocity dispersion of their stellar component varies between 20 to 35 km s^{-1}.

- We investigated the kinematic misalignment angle of the dEs in our sample, and we report two cases of misaligned kinematics, namely VCC1896 and VCC0608. In the case of VCC1896, we show that the observed offset between the kinematic and photometric position angle is basically due to the presence of a bright bar that dominates the photometric measurements. We also find a high kinematics misalignment for the boxy-shaped VCC0608. Past or ongoing tidal interactions with the massive halo of M100 or a past major

---

[1] Local Group dEs have the stellar mass range of $7.78 \leq \log(M_\star \, [\text{M}_\odot]) \leq 8.48$ (McConnachie 2012) whereas our sample dEs have the stellar mass range of $8.9 \leq \log(M_\star \, [\text{M}_\odot]) \leq 9.2$ (see Chapter 8).

merger, considering similarities between this particular dE and the galaxy LEDA 074886, may be possible causes of the observed high kinematic misalignment in this galaxy.

- VCC0170 is the only dE in our sample that shows strong nebular emission lines in its very central region due to star formation, presumably triggered by recent/ongoing gas stripping in Virgo. Further analysis of this particular dE's star formation history and metallicity (to be discussed in the next chapter) may shed light on the origin of the asymmetrical structure in the center of VCC 0170.

- The λ_R profile and ellipticity of the dEs investigated in this work show, on average, intermediate values between the dEs studied by Ryś et al. (2014), which were on average accreted earlier onto Virgo, and CALIFA field galaxies of the same stellar mass (from Falcón-Barroso et al. 2019).

- Given their infall time to Virgo and similar stellar masses, the spread in the λ_R profile of our nine dEs can be interpreted as follows: the low-λ_R dEs were likely transformed in and by their previous host group, before their infall onto Virgo, while the high-λ_R dEs were only partially transformed in their parent host. The latter sub-group of dEs may be experiencing ram pressure stripping in Virgo.

"The moving finger writes, and having written moves on. Nor all thy piety nor all thy wit, can cancel half a line of it. "

—Omar Khayyam, Persian polymath, mathematician, astronomer, philosopher, and poet.

4

Stellar populations of in-falling dEs

This chapter will be submitted for publication in MNRAS as Bidaran et al., "On the accretion of a new group of galaxies onto Virgo: II. Stellar populations unveiling the pre-processed nature".

How would pre-processing of our sampled dEs affect properties of their stellar populations (such as age, metallicity, and the level of the α-enhancement)? This chapter tries to address this question by measuring their stellar population properties. To do so, we measured a set of Lick spectral indices in the observed spectra and fitted them with those of synthetic stellar populations through a four-step routine.

4.1 Introduction

DEs are generally dominated by metal-poor stellar populations (-1.30< [M/H] [dex] <0.00) and cover a rather wide range of ages (3< Age [Gyr] <14). In rich galaxy clusters and at a larger clustercentric distance, the number of red and quenched dEs decreases (Chilingarian et al. 2008; Smith et al. 2009; Lisker et al. 2013). In the Coma cluster, Smith et al. (2009) have shown that the population of young ($\sim$ 3 Gyr) dwarfs with solar-scaled abundance ratios increases toward the cluster's outskirts. They also found that in the Coma's center, dwarf galaxies are mostly old ($\sim$ 10 Gyr) and Mg-enhanced. Similar behavior is also observed in Abell 496 by Chilingarian et al. (2008). In the Virgo cluster, studies have traced solar [α/Fe]-abundance ratios in most of the observed dEs to date (Geha et al. 2003; van Zee et al. 2004), showcasing similar characteristics as metal-rich stars of Milky Way (MW) and Large Magellanic Cloud (LMC) (Sybilska et al. 2017). On spatially resolved scales, studies have revealed that dEs with disk substructures are mostly dominated by younger and more metal-rich stellar populations (Paudel et al. 2010; Toloba et al. 2014). A limited number of studies also shed light on the presence of positive age gradients and negative metallicity gradients in dEs (Chilingarian et al. 2008; Koleva et al. 2009, 2011;

Sybilska et al. 2017). Gradients of stellar population properties of cluster dEs, and similarly some of Local Group dEs (e.g., Ho et al. 2015), endorse centrally concentrated and prolonged star formation in these systems (also check Paudel et al. 2010). While the spatial variation of stellar population properties in massive galaxies have been investigated systematically by many studies, few works have pushed their analysis beyond the Local Group dEs (except for Chilingarian et al. 2008; Koleva et al. 2009, 2011; Goddard et al. 2017; Sybilska et al. 2017).

Star formation activity and spatial distribution of stellar population parameters (such as age and metallicity) in a given galaxy are mainly governed by its internal and external conditions at both of the formation and evolution phases. Primordial galaxies are believed to be formed through monolithic (dissipative) collapse (Larson 1974; Arimoto and Yoshii 1987) during which the central stellar population grows more metal enhanced by retaining the gas that is enriched by stellar evolution. In this classical picture, stellar orbits remain untouched, hence, positive age and rather steep negative metallicity gradients are expected. This picture has been tested by several authors, particularly with the focus on the central regions of massive early-/late-type galaxies (e.g., La Barbera et al. 2011; Goddard et al. 2017; Martín-Navarro et al. 2018; Ferreras et al. 2019; Zibetti et al. 2020). For instance, observations of Kobayashi and Arimoto (1999) and result from Pipino et al. (2008)'s hydrodynamical simulations predict a metallicity gradient range of -0.5 to -0.2 dex, per decade of radius, for ETGs, at any stellar mass. However, the observed scatter in the slope of stellar population gradients, particularly toward more massive galaxies, is noticeable (e.g., Pipino et al. 2008). Within the context of hierarchical formation scenarios (e.g., Cole et al. 2000), galaxies can grow in size and mass through mergers. Such events are extreme and can alter dynamics and star formation activity of merging pairs, depending on the event's conditions (i.e., dry/wet or major/minor mergers). Thus, mergers can flatten/steepen pre-existing age and metallicity gradients of galaxies (e.g., Bekki and Shioya 1999; Pipino et al. 2008). These two complementary scenarios act simultaneously and create noticeable scatter in observed trends, hence, introduce challenges in interpreting the physics behind.

It is still a matter of debate whether stellar population gradients of dEs (and even more massive galaxies), are set mainly by their stellar mass ("nature") or environmental effects ("nurture). Using long-slit spectroscopy, Koleva et al. (2011) (hereafter K11) investigated 40 galaxies within the mass range of 10^7 to 10^{12} M$_\odot$, consisting of 14 dEs/dS0s plus lenticulars and elliptical galaxies in the Fornax and Virgo clusters. They have detected negative metallicity gradients and moderately positive age gradients for Fornax dEs. Except for faint dEs, they could not detect any meaningful correlation between age or metallicity gradients of galaxies and their velocity dispersion, stellar mass, or luminosity. Based on these results, K11 concluded that stellar population gradients of dwarf galaxies reflect those of their progenitors, and the environment has minimum effect on altering these properties. The latter is consistent with results of Sybilska et al. (2017) (hereafter S17), who investigated a sample of 20 Virgo dEs, using SAURON IFU data together with 258 massive early-type galaxies from the ATLAS3D survey (Cappellari et al. 2011). They also could not detect any meaningful correlation between stellar population gradients and the velocity dispersion of early-types. By focusing on more massive and passive galaxies (in the range of $10^{9.5}$ to 10^{12} M$_\odot$), Santucci et al. (2020) show that satellite and central galaxies, at any given stellar mass and despite their different host halo sizes, exhibit similar stellar population gradients. They concluded that central and satellite galaxies form their inner

stellar populations (<1Re) in a similar fashion. Also, for galaxies with comparable stellar masses, Ferreras et al. (2019) found marginal differences between metallicity [M/H] gradients of field and cluster galaxies.

Nonetheless, observed trends for low-mass galaxies ($M_\star < 10^{10}\,M_\odot$), thus far, may noticeably be affected by the limited size of investigated samples as well as different, and not consistent, measurement methods or data sets used for retrieving the stellar populations. DEs have shallow potential wells, hence, they can be good tracers of environmental effects. On that account, our knowledge of the role of the environment in shaping stellar population gradients of galaxies (if any) can still be benefited from increasing the size of observed dEs and conducting investigations with respect to dEs' external (i.e., infall time, local environment) and internal (stellar mass, velocity dispersion) conditions.

In this chapter, we will push our analysis further and investigate the spatial distribution of stellar populations in our sampled dEs. Thanks to their recent accretion, our sampled dEs may still have preserved the "memory" of their previous host halo which can be traced and investigated through stellar population gradients. Through comparison with other cluster dEs, we try to understand the possible role of pre-processing in shaping present-day stellar populations of cluster dEs. By adding more massive early-types to this comparison, we also try to understand how similarly/differently, compared to more massive galaxies, the stellar properties of dEs depend on their global properties (i.e., stellar mass or velocity dispersion). Results of this investigation can also be beneficial in understanding how dense environments, such as the Virgo cluster, alter stellar population properties of their satellites during their early stages of infall.

This chapter is organized as follows: In Section 4.2 we introduce two additional dE samples in the Fornax and Coma clusters that are used as comparison samples. In Section 4.3 we describe our approach for retrieving stellar population parameters of our sampled dEs from their MUSE cubes. In Section 4.4 we present the stellar population maps of our sampled dEs and quantify variations by constructing stellar population gradients. We compare our results with other cluster dEs and more massive ETGs in this section. We discuss our results in Section 4.5 and the conclusions of this study follow in Section 4.6.

4.2   Including dEs of Fornax and Coma clusters

In addition to the Virgo comparison sample introduced in Chapter 2, here we take advantage of available results for other dE samples in Fornax and Coma clusters:

- Fornax dEs: 13 dEs in the Fornax cluster with a magnitude range of -17.9 $< M_B$ [mag] <-15.7 observed with FORS2 spectrograph on the VLT and Gemini Multi Object Spectrographs (GMOS). We included this sample in our analysis in Sections 4.4.5 and 4.4.6 (Koleva et al. 2011).

- Coma dEs: 89 dEs in the Coma cluster with a wide magnitude range of 20$< m_r$ [mag]<11 observed at MMT with Hectospec fiber-fed spectrograph (Smith et al. 2009). From this study we selected 47 Coma dEs whose stellar mass is within the same range as our sampled dEs in Virgo. We include this sample in our analysis in Section 4.4.

Table 4.3.1: Our sampled dEs in Virgo

Object	type	z^a	$g\text{-}r^a$ [mag]	A_V^b [mag]	σ_{Re} ^{c} [kms^{-1}]
VCC 0170	dE(bc)	0.00472	0.59	0.089	27.1 ± 10.6
VCC 0407	dE(di)	0.00626	0.61	0.057	32.3 ± 8.8
VCC 0608	dE(di)	0.00607	0.60	0.072	25.1 ± 9.2
VCC 0794	dE(nN)	0.00558	0.61	0.065	33.0 ± 7.5
VCC 0990	dE(di)	0.00573	0.62	0.080	36.0 ± 5.6
VCC 1833	—	0.00569	0.61	0.099	34.4 ± 6.0
VCC 1836	dE(di)	0.00668	0.58	0.079	38.5 ± 8.2
VCC 1896	dE(di)	0.00629	0.62	0.047	27.0 ± 7.2
VCC 2019	dE(di)	0.00607	0.63	0.060	31.2 ± 6.5

Columns are: Name of target, morphological type, redshift (z), $g\text{-}r$ color measured at $1R_{\mathrm{e}}$, foreground Galactic extinction in V-band (A_V), velocity dispersion at 1 R$_e$ (σ_{Re}).
a: Lisker et al. (2006b), b: Schlafly and Finkbeiner (2011), c: Chapter 3

4.3 Analysis

4.3.1 Setup and pre-processing of data

To improve our results' accuracy, it is required to first increase our data's signal-to-noise ratio (SNR) to a constant minimum threshold. Such an SNR threshold should provide an optimal compromise between the accuracy of measured properties and the spatial sampling of dEs' outskirts. Given the size of each dE in our sample and their surface brightness range, we found a minimum SNR of 100, per bin to be an appropriate choice for retrieving stellar population properties. After correcting our data set for undesired light sources (such as background galaxies and foreground stars) and discarding spaxels with SNR<3, we spatially binned each dE's MUSE data cube using the adaptive spatial Voronoi binning method, developed by Cappellari and Copin (2003). As explained in Chapter 3, this optimized binning algorithm assigns spaxels to different bins so that the ultimate SNR of each bin meets the defined minimum threshold. Here each binned spectrum is the average over all spaxels' spectra within the related bin.

In the next step, we used the Cardelli Galactic extinction law (Cardelli et al. 1989) to correct all the binned spectra for Galactic foreground extinction. Here we adapted R$_v$ = 3.10 and A$_V$ values as reported in Table 4.3.1. Additionally, we corrected dEs' binned spectra for possible traces of nebular emission lines. As discussed earlier in Chapter 3, we have detected relatively strong nebular emission lines (i.e., Hβ, Hα, [OIII], [NII] and [SII]) in the central regions of VCC0170. Except for this dE, we did not detect any nebular emission lines in other dEs of our sample. Nevertheless, we performed this correction on all the sample members, using the GANDALF (Gas AND Absorption Line Fitting; Sarzi et al. 2006; Falcón-Barroso et al. 2006) package. This software treats each emission line as a Gaussian function and interactively fits the stellar continuum and emission lines simultaneously. The residual emission line spectrum obtained for the best fit is subtracted from the observed spectrum. We used these corrected binned spectra to measure line indices and later to determine our sampled dEs' stellar
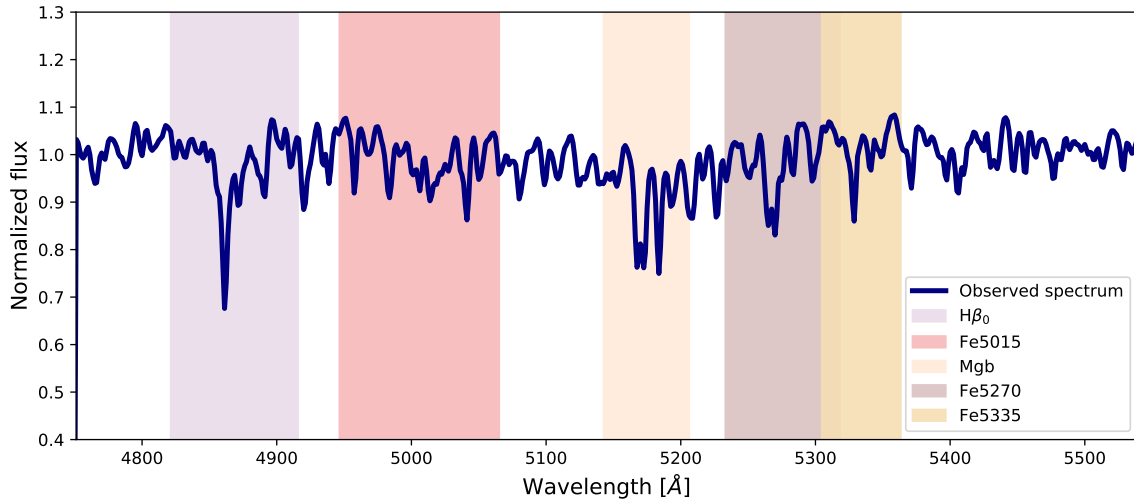
Figure 4.3.1: A schematic of indices' positions on the observed and normalized spectrum. From left to right, the following banpasses are marked: Hβ_0, Fe5015, Mgb, Fe5270, and Fe5335. Please note that each colored bandpass includes the corresponding lines and the blue and red continuum regions used to compute the line index. The normalized spectrum belongs to VCC2019. It also should be noted that the flux normalization is only done in this plot for legibility, and measurements were performed using the original flux.

populations.

4.3.2 Line-strength measurements

To measure SSP-equivalent stellar population properties of each dE (i.e., age, metallicity, and [α/Fe]), we need to focus on absorption features that are sensitive to such properties. Based on the index bands defined in Table 4.3.2, we measured age-sensitive (Hβ and Hβ_0) and metallicity-sensitive (Fe5015, Mgb5177, Fe5270, and Fe5335) indices (position of these indices are marked in Fig. 4.3.1). Prior to the measurement, we convolved the corrected binned spectra in order to achieve the 5 Å resolution of LIS-5Å system in which the line indices of Table 4.3.2 are defined (Vazdekis et al. 2010). The convolution is based on a Gaussian kernel for which the FWHM$_{final}$

Table 4.3.2: List of indices used in this study

Index	Blue bandpass [Å]	Central bandpass [Å]	Red bandpass [Å]	Reference
Hβ	4827.875-4847.875	4847.875-4876.625	4876.625- 4891.625	(Trager et al. 1998)
Hβ_o	4821.175-4838.404	4839.275-4877.097	4897.445- 4915.845	(Cervantes and Vazdekis 2009)
Fe5015	4946.500-4977.750	4977.750-5054.000	5054.000- 5065.2500	(Trager et al. 1998)
Mgb5177	5142.625 - 5161.375	5160.125-5192.625	5191.375- 5206.375	(Trager et al. 1998)
Fe5270	5233.150-5248.150	5245.650-5285.650	5285.650- 5318.150	(Trager et al. 1998)
Fe5335	5304.625- 5315.875	5312.125-5352.125	5353.375- 5363.375	(Trager et al. 1998)

Columns are: index's name, its corresponding blue pseudo-continuum, main absorption feature, red pseudo-continuum, and the reference where the index has been defined.

Table 4.3.3:   Measured indices and SSP-equivalent properties of the main sample

Object	Hβ (Å)	Hβ$_0$ (Å)	Mgb (Å)	Fe5015 (Å)	Fe5270 (Å)	Fe5335 (Å)	[MgFe] (Å)	<Fe> (Å)	Age (Gyr)	[M/H] (dex)	[α/Fe] (dex)
VCC 0170	3.39 ± 0.08	4.50 ± 0.17	1.60 ± 0.11	2.75 ± 0.25	1.71 ± 0.09	1.49 ± 0.21	1.62 ± 0.07	1.60 ± 0.11	$2.10^{+0.16}_{-0.38}$	$-0.61^{+0.04}_{-0.04}$	$0.26^{+0.09}_{-0.08}$
VCC 0407	2.70 ± 0.07	3.63 ± 0.12	1.89 ± 0.11	3.59 ± 0.22	2.01 ± 0.11	1.83 ± 0.18	1.92 ± 0.07	1.92 ± 0.10	$5.78^{+7.34}_{-1.02}$	$-0.59^{+0.06}_{-0.06}$	$0.20^{+0.08}_{-0.06}$
VCC 0608	2.79 ± 0.14	3.79 ± 0.09	1.89 ± 0.17	3.58 ± 0.23	1.95 ± 0.13	1.77 ± 0.09	1.89 ± 0.10	1.86 ± 0.08	$4.55^{+1.06}_{-0.53}$	$-0.57^{+0.06}_{-0.08}$	$0.22^{+0.08}_{-0.08}$
VCC 0794	2.12 ± 0.09	2.89 ± 0.07	1.86 ± 0.08	2.81 ± 0.18	1.75 ± 0.15	1.50 ± 0.20	1.77 ± 0.07	1.62 ± 0.12	$9.98^{+0.31}_{-0.40}$	$-0.73^{+0.02}_{-0.02}$	$0.43^{+0.06}_{-0.08}$
VCC 0990	2.37 ± 0.12	3.40 ± 0.17	2.28 ± 0.20	4.17 ± 0.20	2.29 ± 0.12	2.00 ± 0.09	2.14 ± 0.09	2.18 ± 0.11	$7.77^{+3.59}_{-1.59}$	$-0.53^{+0.06}_{-0.06}$	$0.14^{+0.08}_{-0.08}$
VCC 1833	3.08 ± 0.08	4.28 ± 0.20	2.36 ± 0.16	4.10 ± 0.33	2.20 ± 0.10	1.95 ± 0.18	2.24 ± 0.09	2.08 ± 0.10	$1.85^{+0.51}_{-0.32}$	$-0.18^{+0.14}_{-0.10}$	$0.28^{+0.06}_{-0.08}$
VCC 1836	2.81 ± 0.14	3.71 ± 0.11	1.57 ± 0.09	3.14 ± 0.14	1.77 ± 0.09	1.56 ± 0.13	1.64 ± 0.06	1.66 ± 0.08	$6.84^{+5.96}_{-2.25}$	$-0.77^{+0.08}_{-0.06}$	$0.28^{+0.04}_{-0.04}$
VCC 1896	2.16 ± 0.09	3.04 ± 0.12	2.19 ± 0.07	3.55 ± 0.16	2.04 ± 0.10	1.95 ± 0.09	2.10 ± 0.05	1.99 ± 0.07	$10.50^{+0.48}_{-0.53}$	$-0.59^{+0.02}_{-0.02}$	$0.26^{+0.04}_{-0.06}$
VCC 2019	2.34 ± 0.09	3.07 ± 0.15	2.17 ± 0.07	3.71 ± 0.14	2.09 ± 0.10	1.87 ± 0.07	2.10 ± 0.05	1.98 ± 0.06	$10.46^{+0.48}_{-1.02}$	$-0.59^{+0.04}_{-0.02}$	$0.26^{+0.04}_{-0.04}$

Columns are: (1) Name of targets, (2 -9) measured indices and their corresponding errors, (10-12) light-weighted age, metallicity and [α/Fe]. All the values are measured from dEs' integrated spectra.

is defined as:

$$FWHM_{final} = \sqrt{FWHM^2_{LIS5.00} - (FWHM^2_{gal} + FWHM^2_\sigma)} \qquad (4.1)$$

where FWHM$_{gal}$ is the wavelength-dependent MUSE resolution (Bacon et al. 2017) and FWHM$_\sigma$ corresponds to the velocity dispersion of each bin measured in a similar way as in Chapter 3.

To estimate the random error on each measured index, we considered three possible uncertainty sources: the error on velocity dispersion (affecting broadening of the absorption line), the error on redshift estimate (affecting the accurate placement of band-passes), and the error on the flux (affecting depth of the absorption line) (Kuntschner et al. 2006). Thus, we perturbed each binned spectrum using a Gaussian distribution whose width was set as the difference between binned flux and its corresponding noise. Furthermore, we randomly shifted perturbed spectra based on a normal Gaussian distribution of redshift errors. Additionally, in each perturbation, we changed the convolution kernel's size by randomly shifting the velocity dispersion within a normal distribution constructed based on the corresponding σ errors. Based on this error treatment, we ran 125 Monte Carlo (MC) iterations for each bin in a given dE, and assumed the standard deviation of the multiple index measurements to be the error on that index. Based on our data set's characteristics, we considered an additional minimum error of 0.05 Å on the relevant indices. The latter is to avoid meaningless and small uncertainties on the final estimation of parameters. We present the Hβ$_0$, Mgb5177, and Fe5335 maps for each dE in Fig.4.3.2 and 4.3.3 and their corresponding error maps are presented in Section 8.2 of Chapter 8.

To compare our results with the literature on similar bases, we also repeated our measurements on each dE's integrated spectrum. The latter is an averaged spectrum that represents the entire galactic body up to 1Re. We constructed this integrated spectrum by averaging over each dE's MUSE cube after discarding spaxels with SNR < 3. We applied the corrections mentioned in Section 4.3.1 and measured indices and their corresponding errors, as explained earlier in this section. Results on integrated spectra are reported in Table 4.3.3.
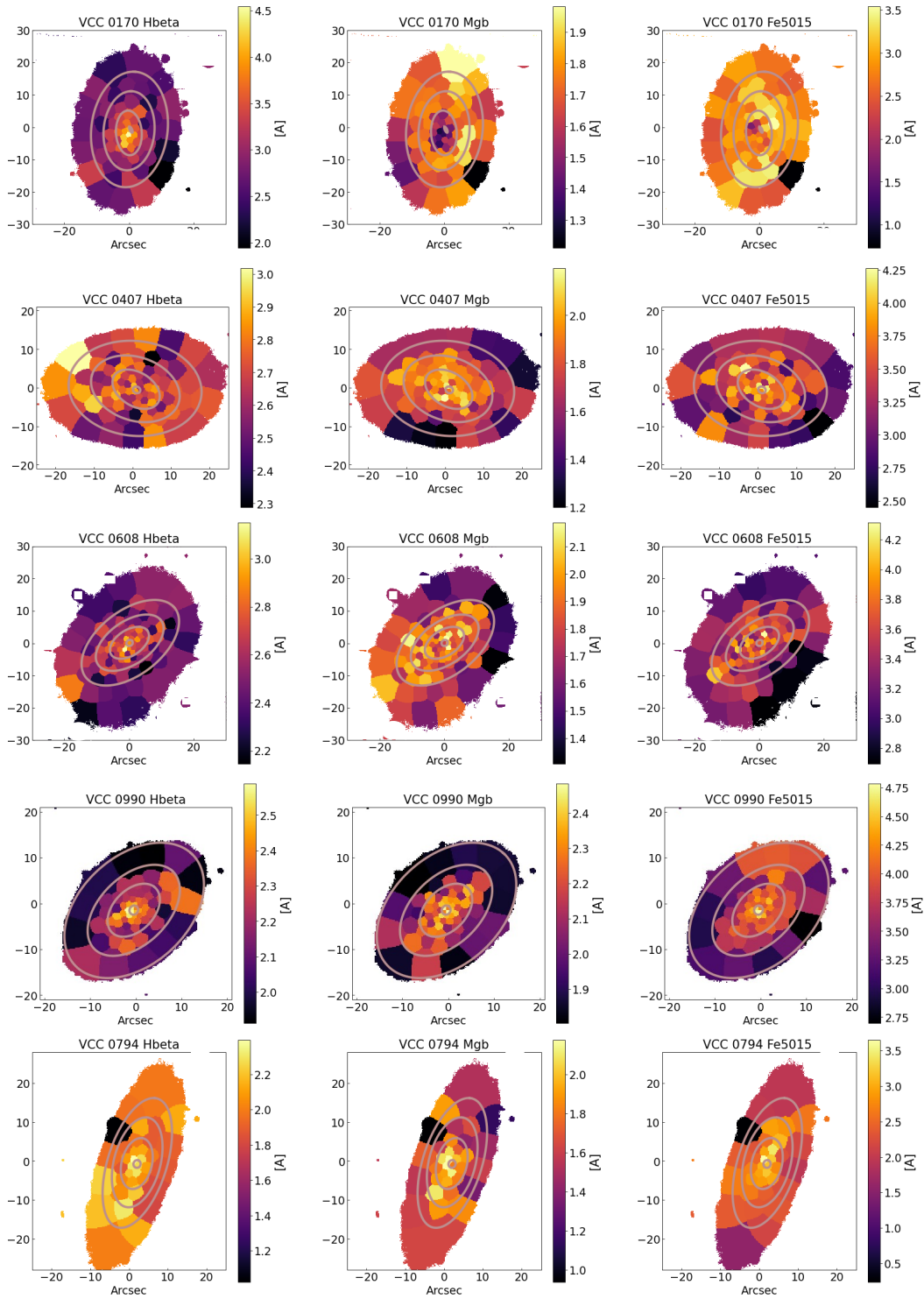
Figure 4.3.2: Indices maps of our sample of dEs. For each dE and from left to right, Hβ, Mgb5177 and Fe5015 maps are presented. On all three maps, isophotes (measured from MUSE stack images in Section 3.3.1) are over plotted. From the inside out, the isophotes indicate regions with a surface brightness of 20.59, 21.00, 21.85, and 22.52 mag/arcsec^2 (ABmag).
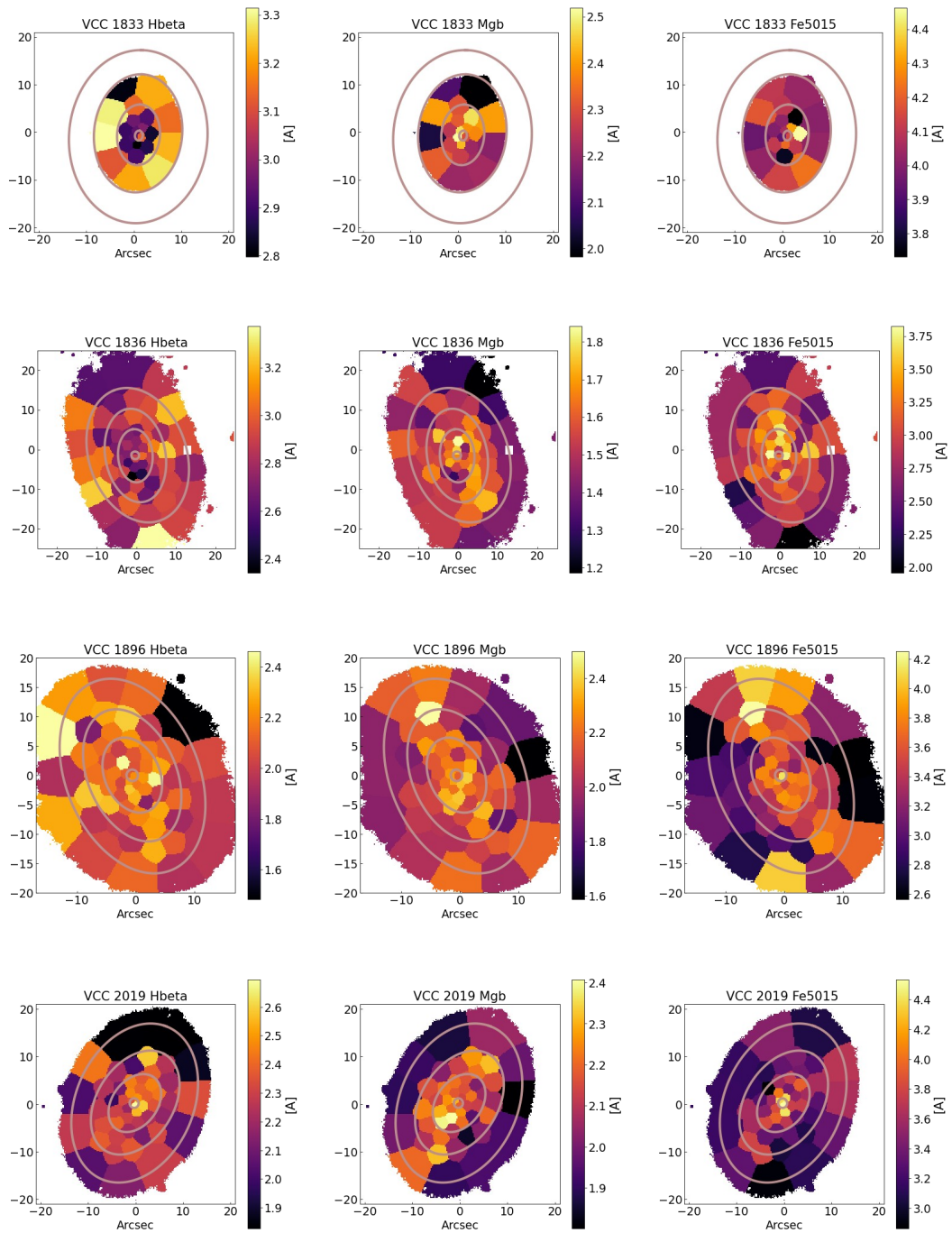
Figure 4.3.3: Continued.

4.3.3   Stellar library: Single stellar population models

In this study, we utilized 456 single stellar population (SSP) models of Vazdekis et al. (2010) based on the MILES stellar library (Sánchez-Blázquez et al. 2006; Cenarro et al. 2007; Falcón-Barroso et al. 2011). We have constructed our SSP models with the age range of 0.5 to 14.00 Gyr; metallicity range of -1.26 to 0.06 dex, and $[\alpha/Fe]$ values of 0.00 (dex; solar-scaled models) and 0.40 (dex; α-enhanced models). We employed SSPs with constant spectral resolution (FWHM of 2.51 Å), BASTI isochrones (Pietrinferni et al. 2004b) and a bi-modal initial mass function (IMF) with the slope of 1.3 (Vazdekis et al. 1996). In this study, SSP models are broadened to the LIS-5 Å system.
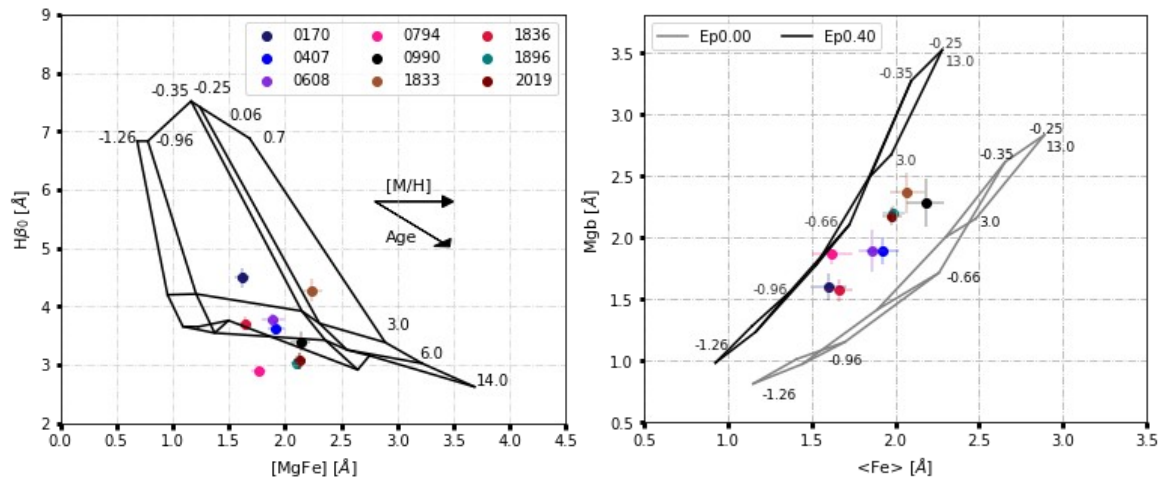
Figure 4.3.4: *Left panel:* The Hβ_0 vs. [MgFe] grid. SSP model predictions with $[\alpha/Fe] = 0.4$ are plotted with black solid lines. Following the horizontal arrow from left to right, metallicities increase from -1.26 to +0.06 dex. Similarly, along the diagonal arrow and from top to bottom, ages increase from 0.7 to 14 [Gyr]. *Right panel:* The Mgb vs. < Fe > grid. Model predictions with $[\alpha/Fe]$=0.00 and 0.4 dex for two ages (3.0 and 13 Gyr) and the metallicity range of [-1.26, -0.96, -0.66, -0.35, -0.25] dex are shown with gray and black solid lines, respectively. In both panels, our sampled dEs are denoted with color coded circles.

In Fig.4.3.4, we compare measured indices from dEs' integrated spectra with the SSP models' predictions. To estimate age and metallicity, we constructed the Hβ_0 vs. [MgFe] grid (shown for SSPs with $[\alpha/Fe] = 0.40$ dex in the left panel). The metallicity sensitive and composite [MgFe] index is derived as in Thomas et al. (2003):

$$[MgFe] = \sqrt{Mgb \times (0.72 \times Fe5270 + 0.28 \times Fe5335)} \qquad (4.2)$$

In this grid, diagonal lines have constant and similar metallicities (from left to right: -1.26, -0.96, -0.35, -0.25, and 0.06 dex), while horizontal lines have constant and similar ages (from

top to bottom: 0.7, 3.0, 6.0, and 14 Gyr).

The Mgb-<Fe> grid (with <Fe> being the average of Fe5270 and Fe5335) is presented in the right panel of Fig.4.3.4. This grid is a good indicator for $[\alpha/Fe]$ ratios in galaxies. Gray solid lines trace solar-scaled models (with $[\alpha/Fe] = 0.00$ dex) and black solid lines represent α-enhanced models ($[\alpha/Fe] = 0.40$ dex). In this grid, we have plotted SSP predictions for two ages of 3.0 and 13.0 Gyr. Models trace a similar metallicity range as in the left panel of Fig.4.3.4. Note that in this work, we use Mgb5177 as a proxy for α abundance. In both panels of Fig. 4.3.4, colored circles show the indices measured from the integrated spectra of our sampled dEs.
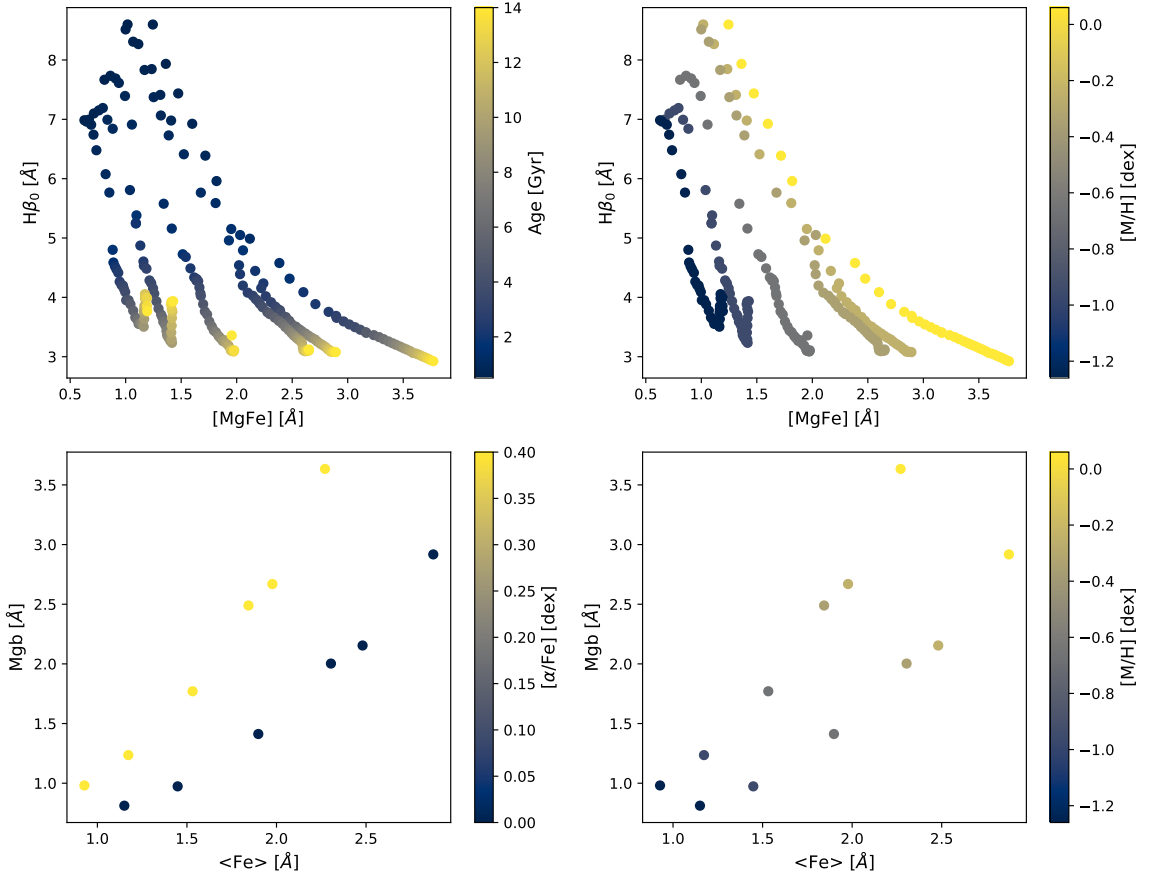
Figure 4.3.5: *Top row:* $H\beta_0$ -[MgFe] grids plotted for original SSP models. Each point represents one SSP and it is color coded based on its age (left panel) and [M/H] (right panel) values. *Bottom row:* Mgb-<Fe> grids plotted for original SSP models. Similar to the top row, each point represents one SSP and it is color coded based on its $[\alpha/Fe]$ (left panel) and [M/H] (right panel) values. Please note the uneven spacing of models and limited coverage of $[\alpha/Fe]$ values.

For ages > 6 Gyr, SSP models are degenerate, shaping a fold on the surface of the grid. This effect is better visualized in the top row panels of Fig. 4.3.5. As illustrated in this figure, the $H\beta_0$ value of SSP models decreases by moving from younger (~ 0.7 Gyr) to older ages (~ 11 Gyr). However, by shifting to older SSPs (~ 14 Gyr) the $H\beta_0$ values start to increase again.

This effect is more prominent for metal-poor SSPs (with [M/H] < -0.35 dex). This trend can affect the χ^2 minimization approach that we have utilized for measuring SSP- equivalent properties. Thus, to take full advantage of data and the library's resolution, we constructed a finer grid by oversampling the SSP models.

To do so, we linearly interpolated in age-[M/H]-[α/Fe]-[index] space and reduced the stepping of models. We reduced the metallicity and [α/Fe] steps to 0.02 dex and 0.015 dex, respectively. The uneven spacing of young and old SSPs in the original library forced us to divide SSPs into two groups of young (0.5 < age [Gyr]< 3) and old (3 < age [Gyr] < 14) models. To keep the number density of models constant over the entire new grid, we reduced the age steps to 0.01 Gyr for young SSPs and to 0.04 Gyr for old SSPs. Furthermore, to reduce systematic errors for those bins with conditions close to the library's limits on [α/Fe] values, we extrapolated this axis with similar steps of 0.015 dex, to higher and lower limits. Thus, the final range of [α/Fe] employed in our study is -0.3 to 0.8 dex. The new interpolated library is shown in Fig. 4.3.6.

4.3.4 Our fitting approach to measure SSP-equivalent properties

To convert measured indices to model-predicted stellar population properties, we employed a minimum χ^2 estimation approach in four steps, each time over a certain pair of indices. In each step, we tried to maximise the likelihood function below, while considering the errors on the measured indices:

$$\chi^2 = \sum_{n=1}^{N} \left(\frac{y_n - M(age, [M/H], \alpha)}{\sigma_n} \right)^2 \tag{4.3}$$

where y_n denotes data values with error σ_n and M(age,[M/H],α) denotes model parameters. A schematic of these four steps is presented in Fig.4.3.7. Description of this fitting approach is as follows:

- **Step 1:** In this step (top left panel of Fig.4.3.7), we construct the Hβ_0-[MgFe] grid for solar-scaled SSP models. Based on the position of the galaxy or bin on this grid, we fit the SSP-equivalent age and [M/H] through running the χ^2 minimization. We construct the probability distribution function (PDF) of age in this step by repeating the fitting procedure for 25 times in an MC framework. In each MC run, we shift measured indices accounting for their corresponding errors. The resulting age PDF from this step is passed to Step two.

- **Step 2:** In this step (top right panel of Fig.4.3.7), we construct the Mgb-<Fe> grid. In this regard, we use models at an age that has been selected randomly from the PDF of step one. Then, we measure [α/Fe] PDF by going through 100 MC realizations. We repeat this test for 50 randomly selected ages from step one's PDF. The final [α/Fe] PDF, which is passed to step three, is the median of constructed PDFs from each of these 50 selections. In this step, there are no constraints on [M/H].

- **Step 3:** In this step (bottom right panel of Fig.4.3.7), we repeat the same methodology of step two but revisiting the Hβ_0-[MgFe] grid. Here we randomly select 100 α values from step two's PDF and execute 200 MC iterations for each selected α. We repeat step
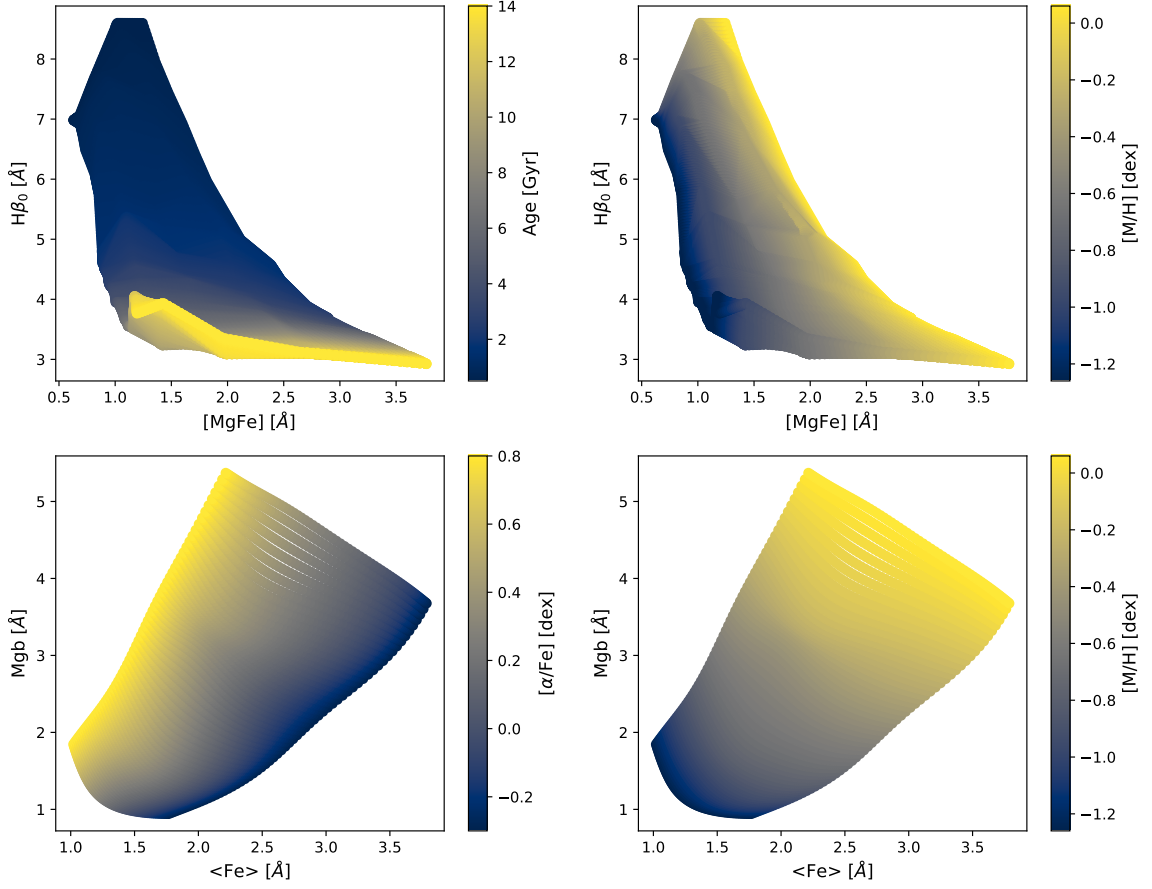
Figure 4.3.6: *Top row:* The interpolated Hβ_0-[MgFe] grids. Thanks to a reduced spacing between SSPs, a continuous distribution of models is presented in each panel. Models are color coded based on their age (left panel) and [M/H] (right panel) values. *Bottom row:* The interpolated Mgb-<Fe> grids. Similar to the top row, each point is color coded based on its [α/Fe] (left panel) and [M/H] (right panel) values. Please note that [α/Fe] values are also extrapolated and now cover a wider range than the lower left panel of Fig. 4.3.5.

one to account for the dependency of Hβ_0 on the α abundance. The final age (in Gyr) and [M/H] (in dex) are measured as the median of their corresponding PDFs, retrieved in this step.

- **Step 4:** Finally, we repeat the same methodology of step two by randomly selecting 100 ages from the age PDF of step three and execute 200 MC iterations for each selected age. The final [α/Fe] (in dex) is measured as the median of retrieved PDF in this step (bottom left panel of Fig.4.3.7).

In the last three columns of Table 4.3.3, we report the stellar population parameters of our sampled dEs, measured by using the averaged and integrated spectra. The upper and lower range of errors are 84th and 16th percentiles of the final PDFs (from steps three and four), respectively. By executing this loop for each binned spectra of each dE, we derived their age, metallicity and [α/Fe] maps presented in Fig. 4.3.8 and 4.3.9 and their corresponding error maps

Four-step X² minimization index fitting approach
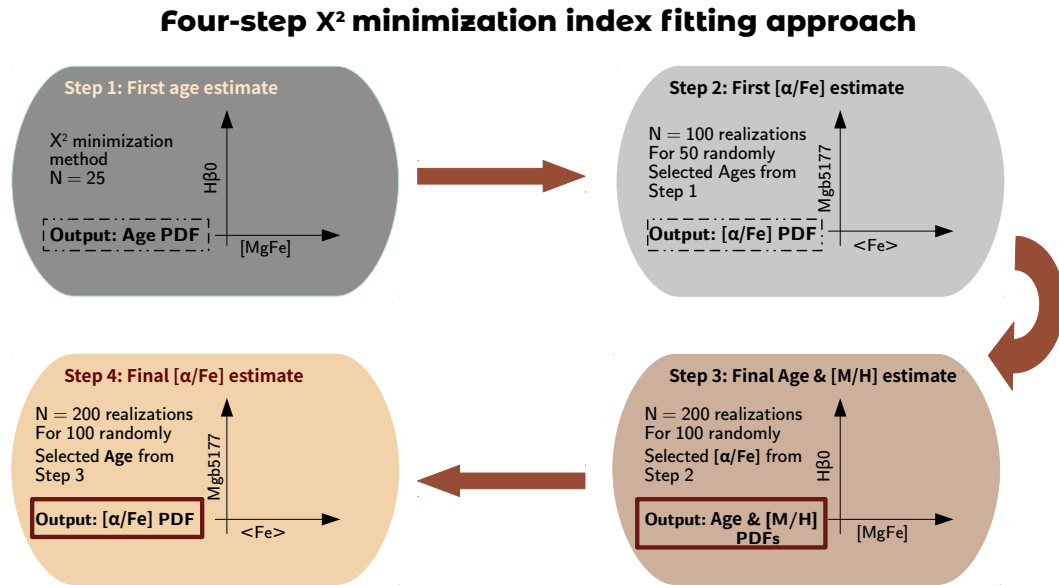
Figure 4.3.7: A schematic representation of our developed four-step fitting routine. *Top left:* Step one where the initial fitting takes place over the $H\beta_0$ -[MgFe] grid, constructed for solar-scaled models, to first measure the Age PDF. *Top right:* Second step where the fitting takes place over the Mgb-<Fe> grid, using the results of the first step, to measure the $[\alpha/Fe]$ PDF. *Bottom right:* Step three, where fitting takes place over the $H\beta_0$ -[MgFe] grid, constructed for SSP models within the $[\alpha/Fe]$ range of step two's PDF. The final Age and [M/H] PDFs are derived in this step. *Bottom left:* Step four, where fitting takes place over the Mgb-<Fe> grid, constructed for SSP models within the age range of step three's PDF. The final $[\alpha/Fe]$ PDF is derived in this step.

are presented in Section 8.2 of Chapter 8. It should be noted that extracted stellar population properties in this study are light-weighted values. The recent formation of even a few young and hot stars in galaxies can affect their composite light drastically. Thus, our measurements are biased toward recent formation of young stars in galaxies, if any. The contribution of hot and young stars to metal lines of the integrated spectra, on the other hand, is not significant (Trager et al. 2005; Serra and Trager 2007). Hence, metallicity's dependence on recent star formation activity is expected to be less severe.

4.4 Results

4.4.1 Integrated values

As summarized in Table 4.3.3, dEs in our sample fall within the age range of 1.85 to 10.50 Gyr, the metallicity range of -0.77 < [M/H] [dex]< -0.18 and 0.14 < $[\alpha/Fe]$ [dex]< 0.43. Among our sampled dEs, the youngest stellar populations, with age = 1.85 Gyr and [M/H] $= -0.18$ dex, were detected in VCC1833. On the other hand, the oldest stellar populations were observed in VCC1896 and VCC2019. VCC1836 is the most metal−poor dE in our sample with [M/H]
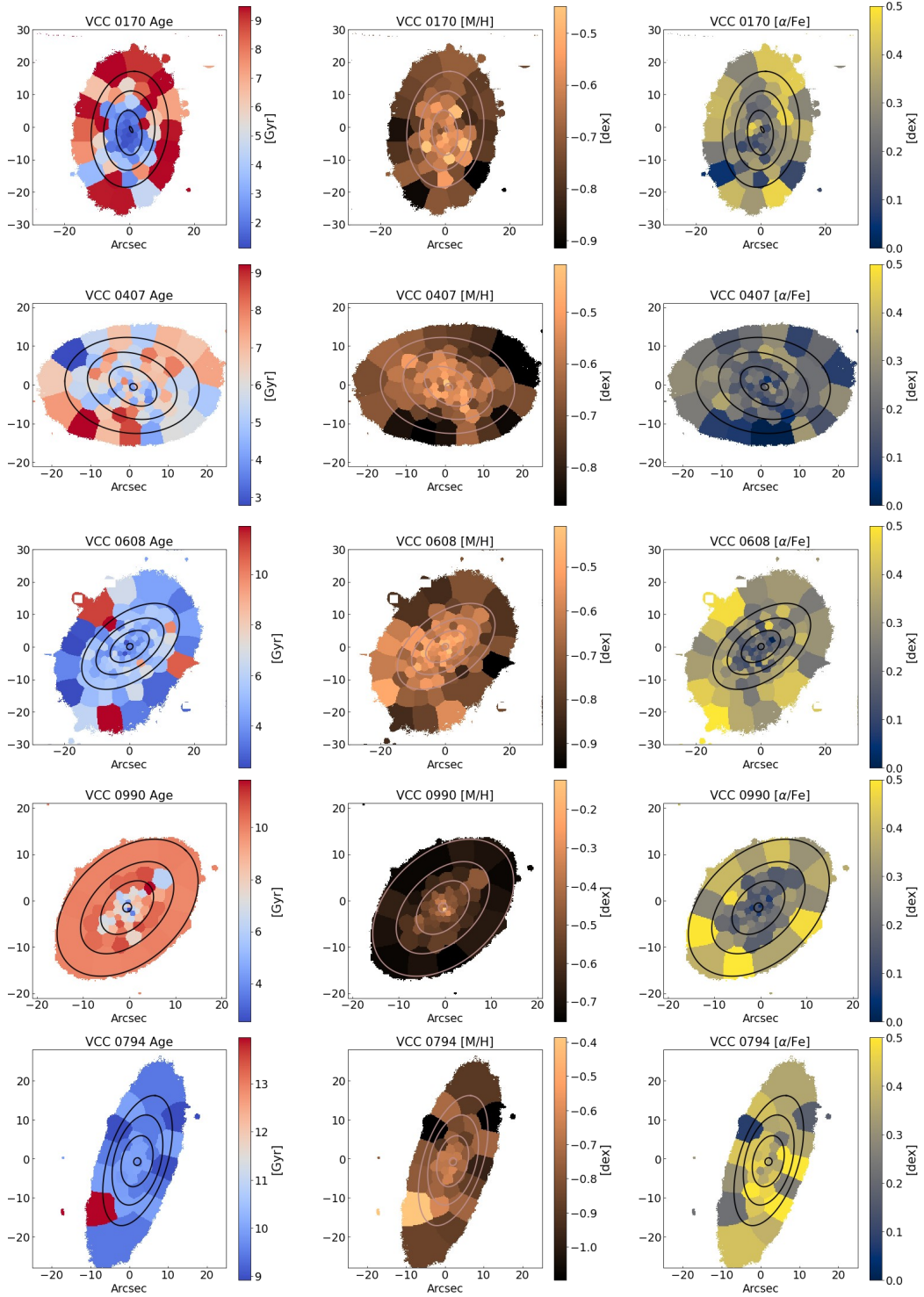
Figure 4.3.8: Stellar population maps of our sample of dEs. For each dE and from left to right, Age, [M/H] and [α/Fe] maps are presented. On all three maps, isophotes (measured from MUSE stack images in Section 3.3.1) are overplotted. From the inside out, the isophotes indicate regions with a surface brightness of 20.59, 21.00, 21.85, and 22.52 mag/arcsec^2 (ABmag).
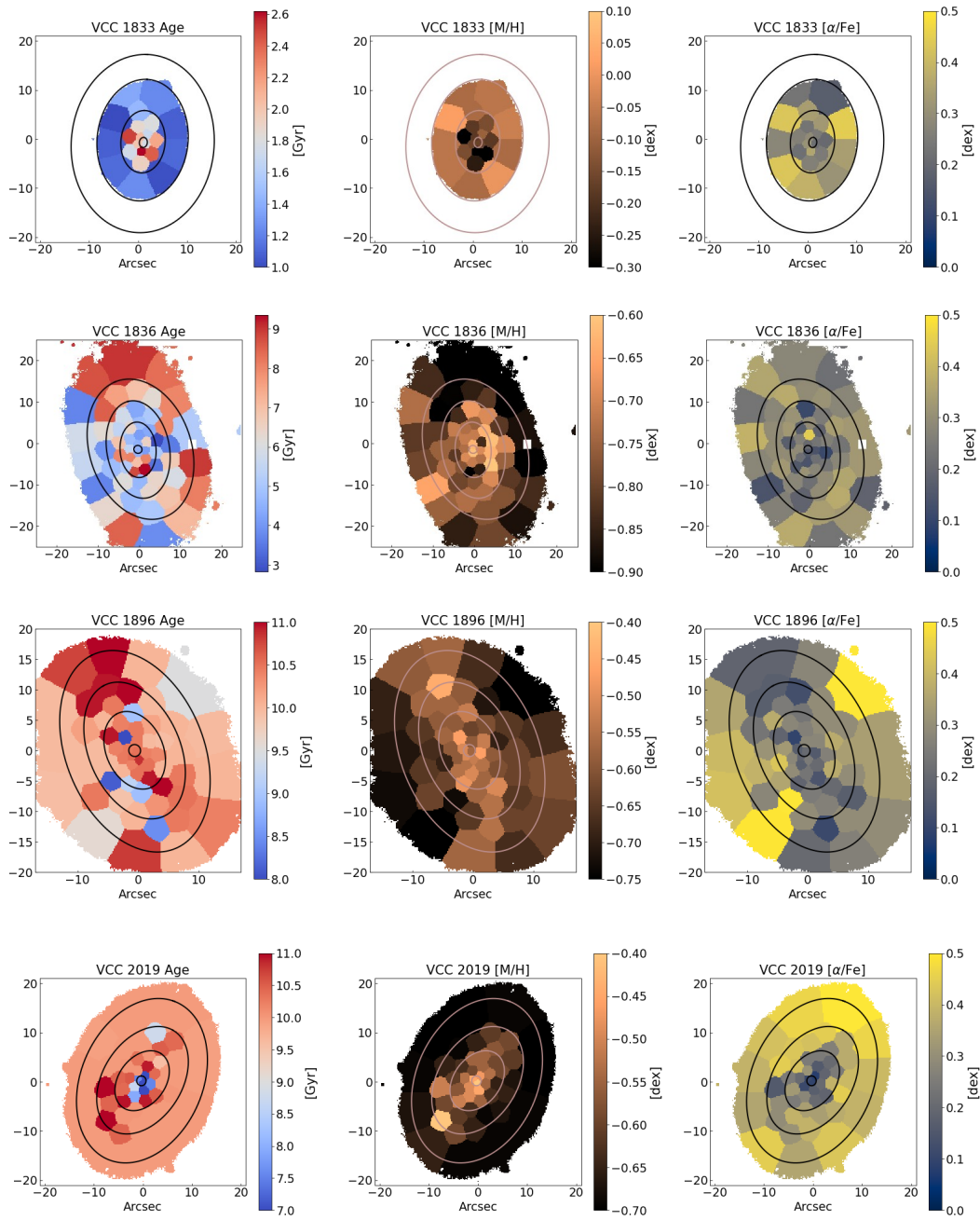
Figure 4.3.9: Continued.

$= -0.77$ dex. Additionally, VCC0794 is the most α-enhanced member of our sample with $[\alpha/\text{Fe}] = 0.43$ dex. Given their stellar mass range, we found our [M/H] measurements to be in good agreement with the general mass$-$metallicity scaling relation (e.g., Gallazzi et al. 2005; Panter et al. 2008; González Delgado et al. 2014; Sybilska et al. 2017). In terms of derived stellar population parameters, we found our sampled dEs to be comparable with other Virgo dEs (Michielsen et al. 2008; Paudel et al. 2011; Koleva et al. 2011; Toloba et al. 2014; Sybilska et al. 2017; Şen et al. 2018), dwarf galaxies in the Fornax cluster (Koleva et al. 2011), Coma cluster (Smith et al. 2009), and low-luminosity early-type galaxies in the Abell 496 cluster (Chilingarian et al. 2008).

VCC0170, VCC0794, and VCC0990 have been investigated as part of the SMACKED project by Toloba et al. (2014). We found our measurements for VCC0170 and VCC0794 to be in good agreement with the results of Toloba et al. (2014). However, we have detected older ages for VCC0990 than what is reported in that study. The difference can be due to the utilization of different sets of absorption features and the dependency of Hβ indices on models' α-enhancement, which is considered in our work thanks to large wavelength coverage of MUSE.
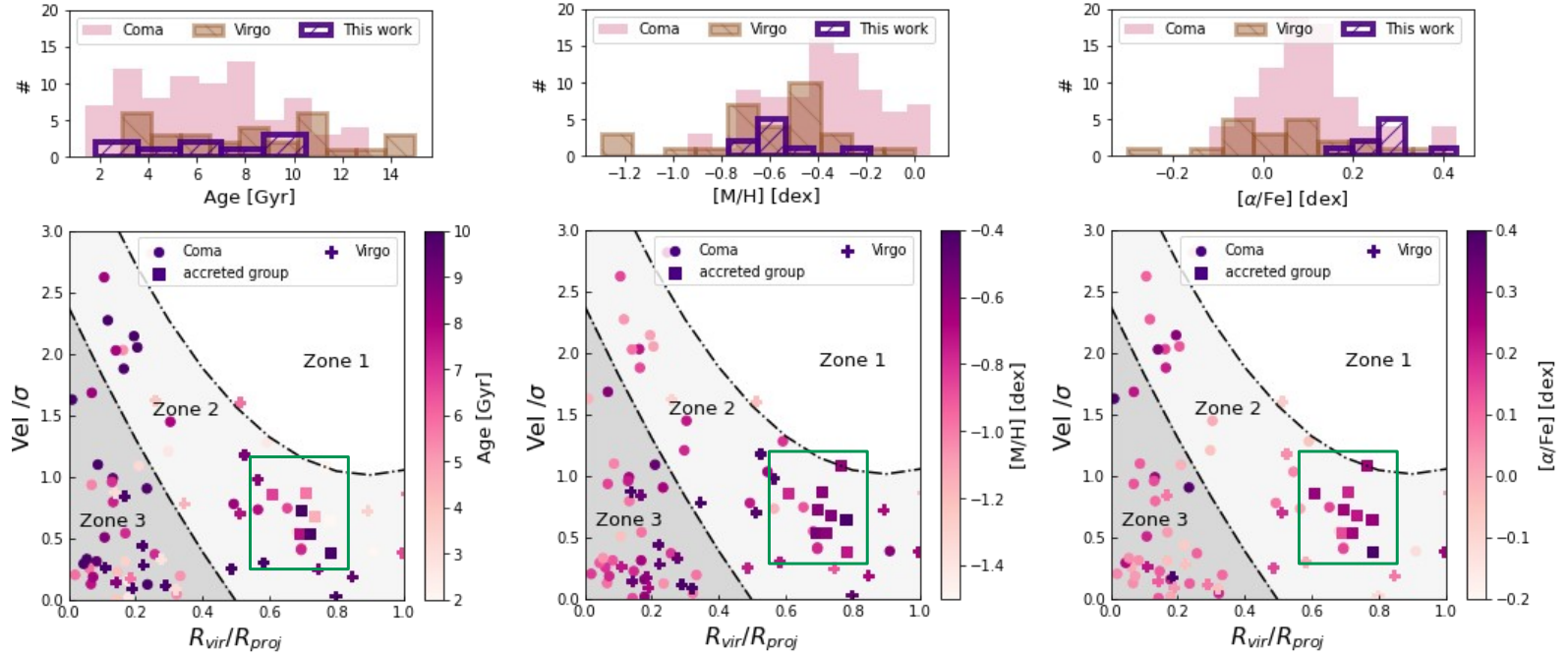
Figure 4.4.1: *On the top row*: From left to right, the age, [M/H], and [α/Fe] distribution of Coma dEs (in pink), Virgo dEs (in brown) and our sample dEs (in purple) are presented, respectively. These panels are plotted for dEs with -17≥M$_r$ >-18 mag. *On the bottom row*: From left to right, the projected phase-space distribution of the Virgo dEs (denoted with a plus symbol), Coma dEs (denoted with circle) and our sampled dEs (denoted with squares). Our sample dEs are further marked with a green solid-line rectangular. Different zones of the projected phase-space diagram indicate different average infall times to the host halo, obtained from Pasquali et al. (2019) and Smith et al. (2019). In details: Zone one: (T$_{inf}$ < 3 Gyr); Zone two: (3 Gyr<T$_{inf}$ < 5 Gyr); Zone three: (T$_{inf}$ >5 Gyr).

In Fig. 4.4.1 we compared the stellar population parameters of our sampled dEs with those of dEs in the Virgo and Coma clusters, at -17$\geq$ M$_r$ [mag]>-18. On the top row and from left to right, we present the age, [M/H] [1] and [α/Fe] distributions of Coma dEs (in pink), Virgo dEs (in light brown) and our sampled dEs (in purple). In terms of light-weighted age and [M/H], our sampled dEs are not different from other dwarf galaxies in the Virgo cluster. Yet, from the middle upper panel, we notice that at the fixed range of absolute r-band magnitude, Virgo dEs are more metal-poor than their counterparts in the Coma cluster. The distribution of [α/Fe] in the right panel indicates that our sample dEs are more α-enhanced than those in the Coma and Virgo clusters. Even in the case of dropping the fixed stellar mass threshold, the latter trend persists. We will elaborate more on this in Section 4.4.2.

In the bottom row of Fig. 4.4.1, we present the projected phase-space distribution of our sampled dEs along with the members of the Coma and Virgo cluster. In these lower three panels and from left to right, data points are color coded based on their age, [M/H] and [α/Fe]. Different symbols indicate different cluster members. In each panel, three different zones are marked, indicating different average infall times (i.e., how long ago a galaxy became a satellite of its present-day halo's environment), obtained from Pasquali et al. (2019); Smith et al. (2019). The members of the infalling group are denoted with colored squares and are further marked with a solid-line rectangle. The median age of dEs in zone three is 7.4 $\pm$ 0.5 Gyr and in zone two, after excluding our sampled dEs, is 7.7 $\pm$ 0.4 Gyr. This indicates that, going from zone 1 (recent infallers with T$_{inf}$ < 3 Gyr) to zone three (ancient infallers with T$_{inf}$ > 5 Gyr) light-weighted ages of dEs does not change. Despite their similar stellar mass range and average infall time, our sampled dEs are, on average, slightly younger (within 1 σ) than other dEs of zone two and three (with a median age of 6.8 $\pm$ 1.1 Gyr), albeit with a remarkable scatter in values. One possible explanation for the presence of such scatter can be the pre-processing these dEs experienced in their previous host halo. We will elaborate more on this in Section 4.5.1.

Similar to the age, the light-weighted metallicity of cluster dEs (at a fixed stellar mass range) tends to show no clear trend with their average infall time. Cluster dEs in zone three have a median [M/H] of -0.45 $\pm$ 0.03 dex, and this value does not change for dEs of zone two, with a median of -0.48 $\pm$ 0.03 dex. Our sampled dEs are more metal-poor than dEs of zone two and three, with a median [M/H] of -0.59 $\pm$ 0.05 dex. What is worth mentioning here is that in terms of light-weighted [M/H], our sampled dEs (excluding VCC1833) fall within a narrow range of metallicities (-0.77 < [M/H] [dex]< -0.57) and seemingly, do not obey the overall range of scattering as seen for other cluster dEs in zones two or three and with similar stellar mass.

4.4.2   On the [α/Fe] distribution of infalling dEs

As presented in the lower right panel of Fig. 4.4.1, the [α/Fe] of cluster dEs, on average, is less than 0.20 dex and without any evident correlation with their average infall time. Cluster dEs in both zones have a median [α/Fe] value of 0.1 $\pm$ 0.02 dex while our sampled dEs have a median value of 0.26 $\pm$ 0.02 dex, thus are more α-enhanced. Additionally, all of our sampled dEs fall within a narrow range of 0.2<[α/Fe] [dex]<0.43. These values are comparable with what is

---

[1]To convert [Fe/H] values reported in Smith et al. (2009) to [M/H] that we use in this study, we performed the conversion of $[M/H] \sim [Fe/H] + log(0.694 f_\alpha + 0.306)$, where $f_\alpha = 10^{[\alpha/Fe]}$ (Salaris and Cassisi 2005)

reported for giant early-type galaxies (e.g., Gallazzi et al. 2006; La Barbera et al. 2014; Gallazzi et al. 2021) and the Milky Way's thick disk (e.g., Bensby et al. 2003; Vincenzo et al. 2021).

One possible source of systematic biases between results of different studies could be the utilization of different Fe absorption indices. The latter may affect the derived $[\alpha/\text{Fe}]$ values. In the Virgo cluster, S17 has used the combination of Fe5015 and Mgb5177 Lick indices as a tracer of $[\alpha/\text{Fe}]$. For Coma dEs, this parameter was measured using Mgb5177 and Fe5270 Lick indices, which are more similar to the set of indices used in this study (Smith et al. 2009). Similar to S17, we have employed SSP models of Vazdekis et al. (2010) based on MILES stellar library while Coma dEs were investigated using Schiavon (2007) SSP models. Thus, observed trends in Fig. 4.4.1 may still suffer from systematic biases, and interpretations should be taken with caution.

As mentioned earlier, our sampled dEs show larger values of $[\alpha/\text{Fe}]$ compared to Virgo dEs of a similar stellar mass range. To test whether this distinct distribution is based on physical reasons or simply due to using different observational tracers (i.e., using Fe5015 in contrast to the set of Fe5270 and Fe5335 employed here), we repeated our measurements using a similar set of indices as S17. Furthermore, to eliminate any possible systematic biases, we followed similar measurement steps as in S17. The latter means measuring age, [M/H] and $[\alpha/\text{Fe}]$ solely by going through steps one and two in Section 4.3.4 and based on a different set of absorption features, namely $H\beta_0$, Mgb, and Fe5015. We applied this approach to our sampled dEs and S17's. A one-to-one comparison of measured [M/H] (top panel) and $[\alpha/\text{Fe}]$ (bottom panel) values are presented in Fig.4.4.2.
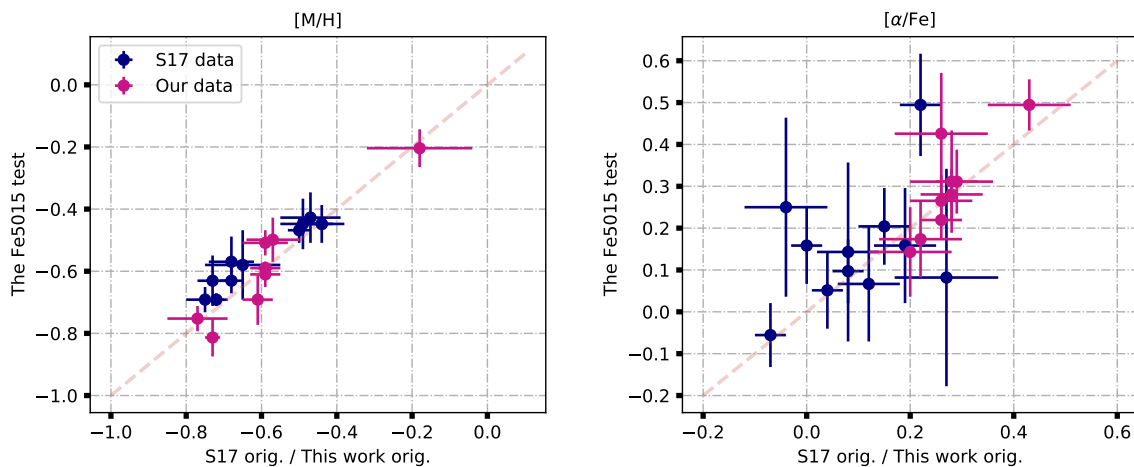
Figure 4.4.2: *Blue data points* denote dEs in the S17 sample. Both panels present one-to-one comparisons between original measurements of S17 (named as S17 orig.) for [M/H] (left panel) and $[\alpha/\text{Fe}]$ (right panel) on the x axes and results of the Fe5015 test performed here (y axes). *Pink data points* denote dEs of our sample. Both panels present one-to-one comparisons between results of [M/H] (left panel) and $[\alpha/\text{Fe}]$ (right panel) obtained from our original methodology (values reported in Table 4.3.3) on the x axes (named as this work orig.) and results obtained from the Fe5015 test (y axes). Error bars are computed in the same way as described in Section 4.3.4.

In Fig.4.4.2, we compare the original measurements of S17 (x-axis) with the results of the

Fe5015 test (y-axis, blue circles) that we performed on our sample dEs. For our sampled dEs (pink circles), we compared the values of [M/H] and [α/Fe] from our original method (x-axis) with the results of the Fe5015 test (y-axis). We find a similar distinct [α/Fe] distribution for our sampled dEs arising from the Fe5015 test. This comparison indicates that two sets of measurements are consistent with each other and the distinct [α/Fe] distribution of our sampled dEs, compared to the S17 sample, is not due to systematics. Based on the results of this test, we compared the [α/Fe] of our sampled dEs and those of the S17, using both the K-S test and the Anderson-Darling test. Both tests indicate that the difference between the [α/Fe] distributions of our sampled dEs and Virgo dEs is significant (with p-values = 0.03 and 0.009, respectively).

Unfortunately, measurements of the chemical abundance of Virgo dEs are very scarce. Hence, consideration of Coma cluster dEs in the projected phase-space diagram, not only compensates (partly) for the low number of data points in different zones, but also can remedy possible biases due to the dynamical stage of Virgo. Virgo is a dynamically young galaxy cluster featuring substructures to which the projected phase-space diagram is not sensible. Thus, adding the Coma cluster, which is more settled than Virgo, can be beneficial for generalizing observed trends in our study.

4.4.3   Age, Metallicity and [α/Fe] maps

Age, [M/H], and [α/Fe] maps of each sampled dE are presented in Fig.4.3.8 and 4.3.9. Except for VCC0170 and VCC2019, age maps are flat and show small fluctuations in values across the galactic body. Young stellar populations (i.e., less than 4 Gyr) are visible across VCC0407, VCC0608, VCC1833, VCC1836. Metallicity gradients are visible in the maps of all of sampled dEs. By going from the outskirts to the central regions of each dE (except for VCC0794 and VCC1833), the stellar population grows more metal-rich. Except for VCC0608, VCC0990, and VCC2019, we did not detect strong [α/Fe] gradients in our sampled dEs' maps. The stellar populations of VCC0407 appear to be globally solar-scaled α-enhanced. In contrast, VCC0794 exhibits highly α-enhanced stellar populations all over its body. In Section 4.4.4, we quantify these visible gradients and further compare them with available results in the literature.

Distinctive young and metal-rich stellar populations are visible in the center of VCC0170 and VCC2019. In Chapter 3 we have detected nebular gas emission lines in the central regions of VCC0170, which can explain the presence of young and metal-rich stellar populations in the core of this dE. The relatively young and metal-rich inner part of VCC2019 is due to the presence of a nuclear star cluster, as reported by Paudel et al. (2011) and Fahrion et al. (2021).

VCC1833 is the most compact, young, and metal-rich member of our sample that shows a peculiar behavior. Despite young light-weighted ages measured for this dE, we did not detect any nebular emission lines in its MUSE cube. Age and metallicity maps of this dE indicate the presence of older and metal-richer stellar populations in its core. However, the stellar population properties of VCC1833's core are not significantly different from what is observed at its outskirts (with ~ 1 Gyr difference in age and ~ 0.2 dex difference in [M/H]). The [α/Fe] map of this dE shows almost constant values for the entire galactic body. By considering [α/Fe] as a proxy of star formation timescale, one possible explanation would be the late formation of stars in dE's outskirts, on a similar time-scale as in the inner parts, from the enriched gas inflow.

Given the light-weighted values, VCC1896 is the oldest dE in our sample (with age = 10.50 Gyr). [M/H] and [α/Fe] maps of this particular dE exhibit a peculiar distribution of metal-rich and less α-enhanced stellar population along its photometric major axis. This feature is not visible in the dE's age map, which shows the presence of old stellar populations across the galactic body with small fluctuations in values. Deep photometric observations of VCC1896 (Lisker et al. 2006b, 2009; Michea et al. 2021) proved the presence of two faint spiral arms connected to the bright central bar of this dE. Here, given the characteristics of our data (MUSE field of view and total exposure time), we can only detect and analyze the stellar population of VCC1896's bar. We found the derived [M/H] and [α/Fe] distributions in this dE's bar to be consistent with the results of Neumann et al. (2020)'s investigations based on 24 nearby barred massive galaxies ($M_\star > 10^{10}$ $M_\odot$). Investigations of the stellar population of bars in this study show a characteristic V-shape signature perpendicular to the bar's major axis, with a more metal-rich and less α-enhanced population residing along the bar's major axis (Fig.14 of Neumann et al. 2020). Results of Auriga magneto hydrodynamical cosmological simulations also indicate a similar V-shape profile for stellar populations of bars of massive galaxies that are formed in isolated dark halos of Milky Way masses Grand et al. (2017). Our results for this dE indicate that a similar V-shape profile can also be expected in bars of low-mass galaxies (i.e., $M_\star < 10^{10}$ $M_\odot$). Based on our analysis, we cannot draw a robust conclusion on the origin of VCC1896's bar. This substructure could have been formed through a secular evolution of VCC1896, which explains the presence of more metal rich and less α-enhanced stellar population along the bar's major axis as footprints of the star formation that has taken place on more elongated orbits and after the formation of the bar. Yet, possible tidal interactions of VCC1896 could also have provoked instabilities causing the formation of such elongated orbits.

4.4.4   Radial gradients of stellar population properties

In this section, we quantify the spatial variation of stellar population properties (and indices) by assuming a linear relation between parameters and the log (R/Reff):

$$\mathrm{Param(R/R_{eff}) = Param_{Reff} + \nabla_{param} \times log(R/Reff)} \qquad (4.4)$$

where $\mathrm{Param_{Reff}}$ represents the fitted population property or Lick index at the galaxy effective radius and ∇_{param} is slope of the fitted line (hereafter referred as gradient). To account for biases due to the effect of seeing, we excluded bins within $1.5\mathrm{FWHM_{seeing}}$ prior to the fitting procedure. We noticed that in most cases, a linear trend best describes the variation of stellar population properties across the galaxy. We note that for VCC0990 and VCC2019, a linear trend might not be the best option, as their central stellar populations (affected by their nuclear star clusters) are noticeably different from what is observed in their outskirts. However, after masking the inner part, linear trends also fit well the variation of stellar populations in these two dEs. To measure the gradients, we employed the publicly available LINmix routine, which measures the slope and intercept of the fitted line through $\sim$ 1000 MCMC iterations by accounting for the measurements' errors. A complete explanation of this linear fitting procedure is presented in Kelly (2007). Gradients of stellar population parameters are presented in Table 4.4.1. Reported errors on slopes and intercepts are the standard deviation of 1000 MCMC runs. Gradients of

Table 4.4.1: Gradients of stellar population properties of the main sample

Object	log(Age)$_\text{Reff}$ [log yr]	∇_age [log yr]/[log(R/Re)]	[M/H]$_\text{Reff}$ [dex] [dex]	$\nabla_{[\text{M/H}]}$ [dex]/[log(R/Re)]	[α/Fe]$_\text{Reff}$ [dex] [dex]	$\nabla[\alpha/\text{Fe}]$ [dex]/[log(R/Re)]
VCC0170	10.16 ±0.08	0.99 ±0.12	-0.80 ± 0.04	-0.25 ±0.06	0.36 ±0.05	0.12 ±0.09
VCC0407	9.82 ± 0.3	0.12 ±0.07	-0.70 ±0.02	-0.23 ±0.04	0.23 ±0.0	0.06 ±0.04
VCC0608	9.81 ± 0.05	0.19 ±0.09	-0.71 ±0.02	-0.19 ±0.03	0.40 ±0.02	0.25 ±0.03
VCC0794	9.98 ± 0.02	0.00 ±0.02	-0.90 ±0.07	-0.18 ±0.09	0.33 ±0.09	-0.07 ±0.12
VCC0990	10.00 ± 0.01	0.12±0.04	-0.65 ± 0.1	-0.29 ± 0.04	0.32 ± 0.02	0.30 ±0.05
VCC1833	9.07 ± 0.04	-0.49 ±0.14	-0.05 ±0.04	0.34 ±0.15	0.31 ±0.03	0.08 ±0.11
VCC1836	9.96 ± 0.07	0.15 ±0.11	-0.89 ±0.04	-0.18 ±0.06	0.30 ±0.05	0.02 ±0.08
VCC1896	10.00 ± 0.01	-0.01 ±0.03	-0.65 ±0.02	-0.11±0.05	0.30 ±0.03	0.07 ±0.08
VCC2019	10.00 ± 0.01	-0.01±0.02	-0.72 ±0.02	-0.19±0.04	0.45 ±0.04	0.30 ±0.09

Columns are: Name of the target, log(age) at 1Re, slope of age gradient, [M/H] at 1Re, slope of [M/H] gradient, [α/Fe] at 1Re, and slope of [α/Fe] gradient.

indices are presented in Table 8.2.1 and 8.2.2 of Chapter 8.

In general, our sampled dEs show a rather wide range of gradients in age (-0.49 $< \nabla_\text{age} <$ 0.99) and [α/Fe] (-0.07 $< \nabla_{[\alpha/\text{Fe}]} <$ 0.30). On the other hand, the distribution of metallicity gradients is less spread (-0.25 $< \nabla_{[\text{M/H}]} <$ -0.11; excluding VCC1833 with $\nabla_{[\text{M/H}]} =$ 0.34 ±0.15).

On the top row of Fig. 4.4.3 and from left to right, dE's gradients of log(Age in yr), [M/H], and [α/Fe] are presented. The majority of our sampled dEs show mild positive age gradients and this parameter for VCC0170 is the largest (∇_age = 0.99 ± 0.12). On the contrary, VCC1833 is the only dE of our sample with noticeable negative age gradient (∇_age = -0.49 ± 0.14) and positive metallicity gradient ($\nabla_{[M/H]}$ =0.34 ± 0.15). Except for this peculiar galaxy, the rest of our sample members show negative metallicity gradients that indicate the presence of a relatively metal-rich stellar population in their center. These findings are consistent with previous studies of Virgo and Fornax dEs (e.g., Chilingarian et al. 2008; Koleva et al. 2009, 2011; Sybilska et al. 2017). All the members of our sample have positive $\nabla_{[\alpha/\text{Fe}]}$. This parameter is rather flat for VCC0794 ($\nabla_{[\alpha/\text{Fe}]}$ = -0.07 ± 0.12). VCC0608 and VCC2019 are two of our sample members that expose relatively steep and positive [α/Fe] gradients. This steep and positive $\nabla_{[\alpha/\text{Fe}]}$ in the latter dE can be due to its nuclear stellar cluster.

While population gradients presented on the top row of Fig. 4.4.3 are frequently addressed in the literature, it is important to note that their slopes and intercepts depend on the SSPs adopted and the method employed for their derivation. Thus, here we also provide model-independent results on the Lick indices of our sampled dEs to account for such biases while comparing with the literature. On the bottom row of Fig. 4.4.3 and from left to right, gradients on Hβ, Mgb, and Fe5015 are shown, respectively. Since Hβ is an adequate age tracer, similarities between $\nabla_{\text{H}\beta}$ (shown in the lower left panel) and ∇_Age are expected. Moreover, all dEs in our sample (except for VCC0170) show negative gradients in Mgb and Fe5015, which is consistent with their negative metallicity gradients discussed before.
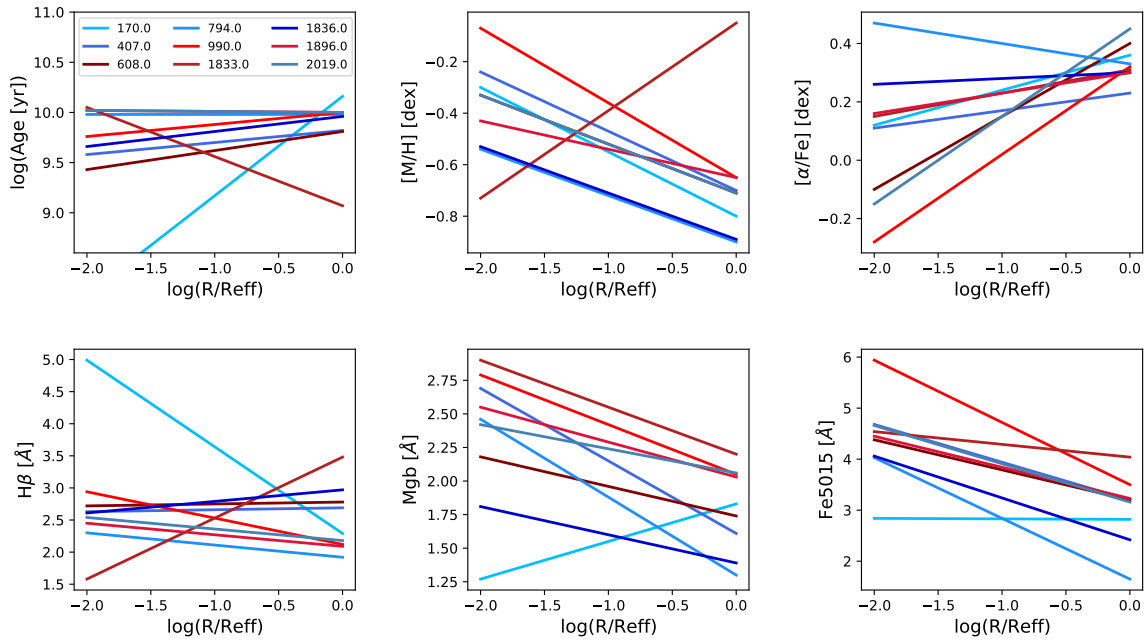
Figure 4.4.3: *Top row:* From left to right, gradients of age, [M/H], and [α/Fe] for each dE are plotted. *Bottom row:* For each dE and from left to right, gradients of H_β, Mgb, and Fe5015 are plotted. In all panels. dEs' profiles are marked with different colors.

4.4.5 Comparison with the literature: dEs

In Fig. 4.4.4 we investigate possible trends between stellar population gradients (left column) and Lick indices gradients (right column) of dEs as a function of their velocity dispersion (σ). Here the velocity dispersion traces the gravitational potential (directly) and the stellar mass (indirectly) of a given galaxy. We have chosen σ since this parameter is directly measured from observed data. Therefore, compared to the stellar mass, it is less affected by model assumptions and other biases. Moreover, different studies have mentioned that several galaxy properties (including those of stellar populations) correlate stronger with σ rather than stellar mass (e.g., Koleva et al. 2011; Barone et al. 2018; Ferreras et al. 2019). For this comparison, we selected 12 Virgo dEs (light purple) from the S17 sample and 13 Fornax dEs (light blue) from the K11 sample. The latter study did not provide any information on the indices gradients. As shown in the left columns of Fig. 4.4.4, dEs have slightly positive age gradients. This trend is accompanied by negative metallicity and positive [α/Fe] gradients.

For each sample of dEs, we performed a linear fit (using LINmix routine) to quantify possible correlations between stellar population gradients and velocity dispersion. Here we treated each sample of dEs separately, mainly to account for systematic biases that different methodologies and data sets could cause in measuring stellar population properties. While S17 has derived gradients from SAURON IFU data using a line indices fitting approach, K11 has obtained gradients from long-slit data using a full spectrum fitting technique. Our linear fits shown in the left column of Fig. 4.4.4 indicate that the stellar population gradients of dEs have
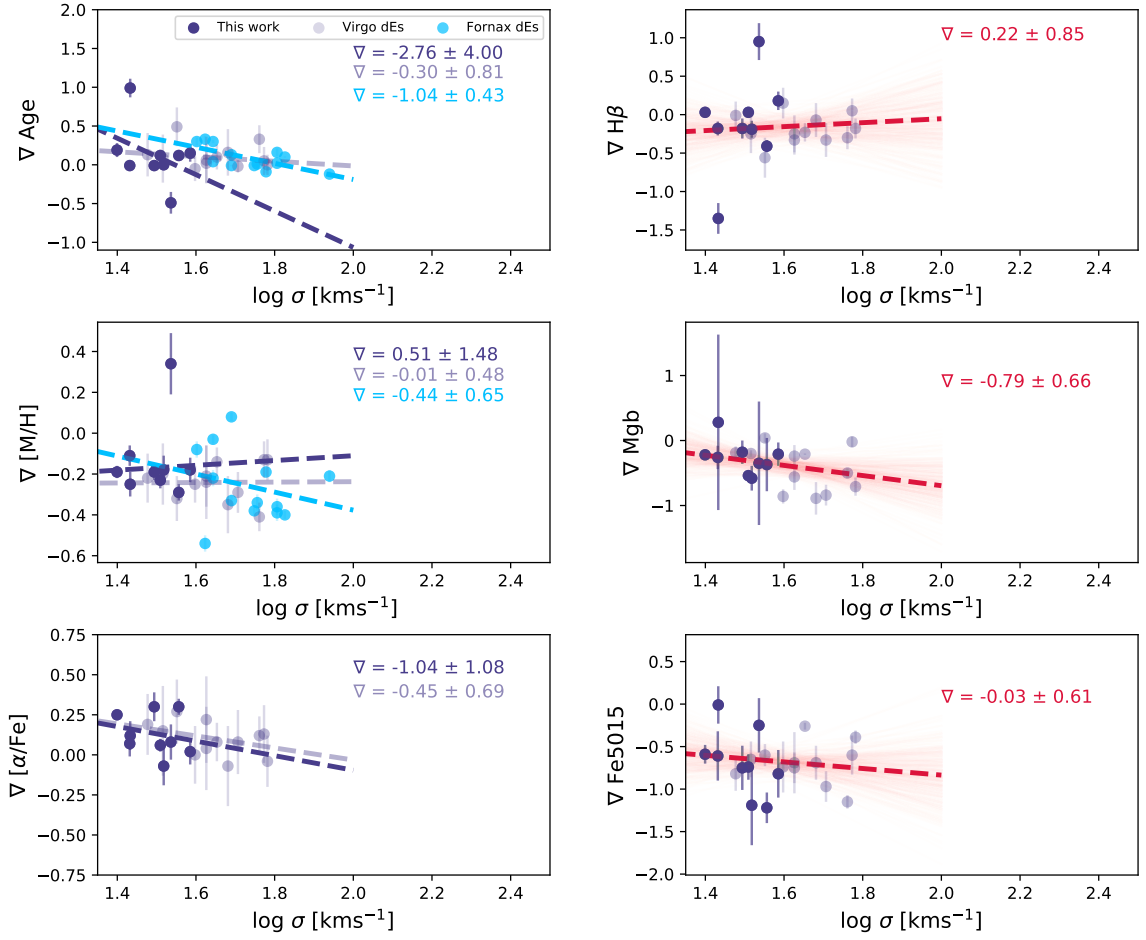
Figure 4.4.4: *Left columns:* From top to bottom, ∇_{age}, $\nabla_{\mathrm{[M/H]}}$ and $\nabla[\alpha/\mathrm{Fe}]$ of our sampled dEs (denoted with dark purple data points), S17 Virgo dEs (denoted with light purple data points) and Fornax dEs from K11 (denoted with light blue data points) as a function of $\log(\sigma)$. Fitted linear relations on each sample, performed by LINmix, are shown with similar colors and in dashed lines. Slopes and their corresponding errors are also reported on each panel. *Right columns:* From top to bottom, $\nabla \mathrm{H}\beta$, $\nabla \mathrm{Mgb}$, and $\nabla \mathrm{Fe}5015$ are presented for our sampled dEs and S17 Virgo dEs. Here the linear fit is performed on the combined data sets, and trends are shown as red dashed lines. Slopes and their corresponding errors are reported on each panel.

minor to no correlation with their velocity dispersion. Among different parameters, $\nabla_{[\alpha/\mathrm{Fe}]}$ shows a decreasing trend as a function of σ, which considering the fits errors is not significant. Furthermore, we did not detect any particular difference between dEs in the Virgo and Fornax clusters. Additionally, we did not detect any particular trend between stellar population gradients of Virgo dEs with respect to their average infall time.

In the right panels of Fig. 4.4.4, we performed a linear fit to quantify possible correlations between Lick indices gradients and the velocity dispersion of Virgo dEs. Given that Lick indices trace the stellar population properties of galaxies without being systematically affected by model

assumption and degeneracies, we can combine our measurements with those from S17 in the right column of Fig. 4.4.4. It should be noted that both measurements were performing in the LIS-5 Å system. All the investigated Virgo dEs have zero or slightly positive $\nabla_{H\beta}$ gradients. Negative ∇_{Mgb} and ∇_{Fe5015} gradients are also observed in all of Virgo dEs, with the former being steeper.

In the middle panel, we detect a possible correlation (albeit at 1 σ level) between ∇_{Mgb} and velocity dispersion for Virgo dEs, in a sense that ∇_{Mgb} becomes steeper with increasing σ. This is similar to the results of Ogando et al. (2006) who showed that ∇_{Mg2} steepens with increasing velocity dispersion in early-type galaxies with $\log(\sigma \, [\mathrm{km}s^{-1}]) > 2$. It should be noted that the trends we find are based on the analysis of a fairly small sample of dEs in both clusters; hence, they need to be evaluated through a systematic analysis over a statistically richer sample.

4.4.6 Comparison with the literature: massive ETGs

In this section and in Fig. 4.4.5, we compare cluster dEs (including our sample) with massive early-type galaxies (ETGs). To do so, we take advantage of different samples that are already analysed in the literature. This comparison is covering a wide range of velocity dispersion, hence, it may provide a general picture of how galaxies, up to 1Re, build up their stellar population with respect to their global properties. In this comparison (Fig. 4.4.5), we have utilized:

- **ETGs from the MANGA survey (denoted with stars)**: Parikh et al. (2021) covers 1900 galaxies in a wide stellar mass range $8.6 < \log(M_\star \, [M_\odot]) < 11.3$. Their stellar population properties were measured by modeling Lick absorption features (Hβ, Mgb, Fe5070, Fe5335) using the MILES stellar library. This analysis was performed on stacked spectra in different bins of stellar mass.

- **ETGs from the ATLAS3D project (denoted with small khaki circles)**: 260 massive ETGs that were observed with SAURON IFU. Their age, metallicity, and [α/Fe] maps were constructed by Krajnović et al. (2020), through modeling key absorption features (Hβ, Mgb, and Fe5015) using Schiavon (2007) SSPs.

- **Massive ETGs from the CALIFA survey (denoted with black triangles)**: 45 massive ETGs that were observed with PMAS/PPAK IFU. Their stellar population was retrieved by Martín-Navarro et al. (2018), through modeling Lick indices (Hβ_0, Fe4383, Fe5015, Fe5270, Mgb), using the MILES stellar library. In Fig.4.4.5, each data point represents the averaged stellar population property of galaxies in three different mass bins (read directly from Table 2 of their study).

Each data point of cluster dEs and ATLAS3D galaxies in Fig. 4.4.5, corresponmds to the median property of 10 galaxies within each velocity dispersion bin. The error bars are errors on the median. Data points from MANGA and massive ETGs of CALIFA are directly imported from their original study, thus representing properties over different numbers of galaxies per bin.

Cluster dEs, on average, show zero to slightly positive age gradients with ranges similar to more massive ETGs. At $\log(\sigma \, [\mathrm{km}s^{-1}]) \sim 1.8$, where the stellar mass of low-mass ETGs of the ATLAS3D sample and MANGA ETGs overlap with cluster dEs, we witness a noticeable discrepancy between gradients reported by different studies. Here, cluster dEs show flat
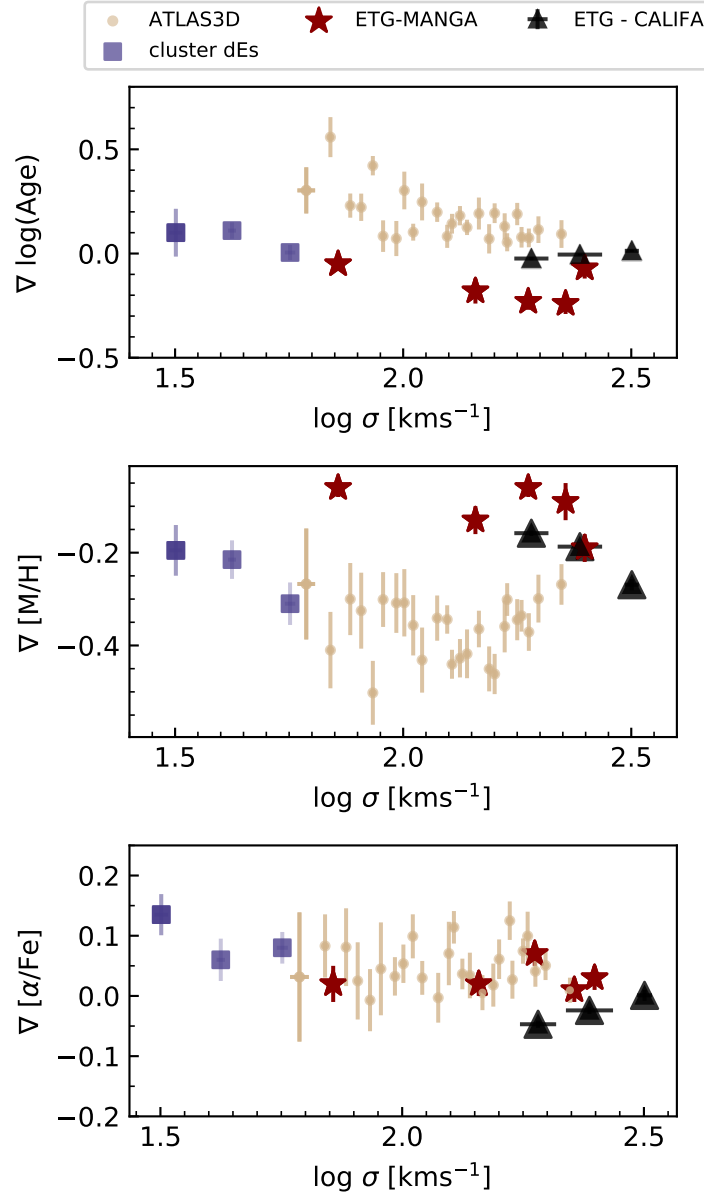
Figure 4.4.5: Comparison of stellar population gradients between cluster dEs (denoted in purple), AT-LAS3D ETGs (denoted in khaki), MANGA ETGs (denoted in red) and very massive CALIFA ETGs (denoted in black). From top to bottom, we compare the ∇_{age}, $\nabla_{\mathrm{[M/H]}}$, and $\nabla[\alpha/\mathrm{Fe}]$ of these galaxies, respectively. Each data point of ATLAS3D and cluster dEs represents the median value of 10 galaxies in a specific $\log(\sigma)$ bin. The error bars are errors on the median.

gradients similar to what Parikh et al. (2021) has reported for low-mass MANGA ETGS. Yet, this trend is noticeably different from the steep age gradients reported for low-mass ATLAS3D galaxies. Compared to very massive ETGs with $\log(\sigma\ [\mathrm{kms}^{-1}]) \geq 2.1$ from ATLAS3D and CAL-

IFA samples, cluster dEs have a similar range of age gradients. In the mid panel of Fig.4.4.5, the scatter in $\nabla_{[M/H]}$ among the samples is more substantial. Leaving this discrepancy aside and regardless of their size or environment, ETGs showcase negative metallicities, meaning that their center is metal richer than their outskirts at 1Re. Cluster dEs exhibit a qualitatively similar negative trend. By only considering cluster dEs and ATLAS3D ETGs, there might be a positive correlation between $\nabla_{[M/H]}$ and velocity dispersion, up to $\log(\sigma \ [kms^{-1}]) \sim 2.1$, in the sense that the metallicity gradient becomes more negative with increasing velocity dispersion. This trend seems to reverse itself for more massive ETGs. However, this correlation is mainly set by ATLAS3D data points. In fact, at any $\log(\sigma)$, and particularly at $\log(\sigma \ [kms^{-1}]) \sim 2.1$, MANGA ETGs and CALIFA ETGs deviate significantly from ATLAS3D. This prevents us from establishing any robust conclusion on possible trends between $\nabla_{[M/H]}$ and $\log(\sigma)$ for ETGs.

In the lower panel of Fig. 4.4.5, we plot $\nabla[\alpha/Fe]$ as a function of $\log(\sigma)$. Except for the very massive end of the distribution, ETGs show positive $\nabla[\alpha/Fe]$ that decreases with $\log(\sigma)$, albeit with significant scatter. On the low-mass end of the distribution, the steepest $\nabla[\alpha/Fe]$ are observed for cluster dEs with the lowest σ. In general, cluster dEs have steeper $\nabla[\alpha/Fe]$, compared to ETGs more massive than $\log(\sigma \ [kms^{-1}]) \geq 1.8$.

This comparison is covering a wide range of velocity dispersion, hence, it would be useful in providing a general picture of similarities/differences between stellar population gradients in dEs and more massive ETGs, up to 1Re. The main drawback of this comparison is the noticeable systematic uncertainties and biases (rooted in, e.g., different methodologies) that possibly produce a noticeable scatter among the results of different studies (for instance, between AT-LAS3D and MANGA ETGs). Thus, we will not comment further on the physical interpretation of observed trends between gradients and the velocity dispersion of galaxies in Fig. 4.4.5.

4.5 Discussion

4.5.1 Stellar populations of Virgo dEs: Age and [M/H]

The nine dEs investigated in this study were accreted onto Virgo as gravitationally bound members of a rather massive galaxy group ($\sim 10^{13}$ M$_\odot$) where, according to Donnari et al. (2021), pre-processing can be potent. Such a galaxy group can alter the stellar population properties of its satellites through different mechanisms. For instance, tidal interactions can affect the star formation activity, kinematics, morphology and gas content of satellites. On the other hand, starvation and ram pressure stripping can also play vital roles in gas removal and alteration of star formation activity of group satellites (e.g., Boselli and Gavazzi 2006). While ram pressure stripping is only dominant in high density parts of the host galaxy group (i.e., the inner regions), starvation is believed to be more efficient in quenching group satellites (Kawata and Mulchaey 2008). Along these lines, the efficiency of environmental effects in a given galaxy group depends on the halo size, satellite stellar masses, orbits, and the time spent in the halo's environment.

In Chapter 3, we have detected signatures of pre-processing in the kinematics of our sampled dEs. Despite their similar average infall time and stellar mass range, the large scatter of their

specific angular momentum profiles was interpreted as evidence of their kinematic evolution in the parent group halo rather than in Virgo. This reasoning was based on the fact that, the Virgo cluster can modify a satellite's kinematics only after several pericenter passages (i.e., several Gyr Boselli and Gavazzi 2006), while our sample dEs have been accreted onto Virgo less than 3 Gyr (Chapter 2). Through the work undertaken in this Chapter, we investigated further possible imprints of pre-processing in the stellar populations of our sampled dEs.

Except for VCC0170, our sampled dEs are gas deficient. Thus, they have already experienced some environmental modifications either in the Virgo cluster or in their parent halo. Rich galaxy clusters such as Virgo are believed to quench their infalling satellites following a "delayed-then-rapid" scenario (e.g., Wetzel et al. 2013; Rhee et al. 2020). Within this context, the star formation rate of infalling satellites remains almost intact during the early phases of accretion (2-4 Gyr). This duration is known as the "delayed phase". Once satellites go through their first pericenter passage, the quenching accelerates and becomes more efficient in reducing the star formation rate of satellite galaxies (Wetzel et al. 2013; Rhee et al. 2020). Wetzel et al. (2013) have shown that during the delayed phase, satellites with adequate gas reservoir experience noticeable mass growth, which can be traced as young stars in light-weighted age measurements. Inevitably, this may not be the case for those infalling satellites that are already quenched or left gas deficient due to pre-processing. The presence of relatively younger (light-weighted) dEs in the outskirts of the Virgo (Michielsen et al. 2008) and Coma clusters (Smith et al. 2009), along with the observed correlation between light-weighted ages and average infall time of satellites (Pasquali et al. 2019; Rhee et al. 2020; Gallazzi et al. 2021), endorse the scenario proposed by Wetzel et al. (2013).

Our sampled dEs generally fall within the age range of other dEs in the Virgo, Fornax, and Coma clusters. As shown in Fig. 4.4.1 and based on their integrated spectra, the majority of our sampled dEs (i.e., 55 percent) accommodate young light-weighted stellar populations (i.e., < 4 Gyr). From their light-weighted age maps (presented in Fig. 4.3.8 and 4.3.9), one can further notice the presence of such young stellar populations across most of dEs' spatial extent (up to ∼ 1Re). Given the accretion time of our sampled dEs, these young stellar populations could have formed through the regular star formation activity of the galaxy and (or) fostered by the accretion event via bow shocks (see Chapter 1). The presence of a rather limited gas reservoir in the central regions of VCC0170, which is forming stars at a low rate (Fig.4.3.8 as reported in Chapter 3) fits well in this picture. However, this young population is not observed in all of our sample members. Given their similar stellar mass range and accretion time, the absence of such young stellar populations in some of our dEs' age maps (including VCC0794, VCC1896, and VCC2019) indicates that their star formation activity and gas content might have been altered prior to their accretion to Virgo and possibly by their parent group halo. The scattering in light-weighted ages measured from the integrated spectra of our sample (Fig. 4.4.1) also supports this picture. This scenario can be further evaluated through investigation of our sampled dEs' star formation history. The latter is going to be the topic of Chapter 5.

As presented in Fig. 4.4.1, at a fixed stellar mass range, our sampled dEs generally fall within the metallicity range of other Virgo and Coma dEs. Precisely, our newly accreted dEs are even more metal-poor (with 2-3σ significance) than dEs with similar average infall time

(i.e., zone two of Fig.4.4.1). On the other hand, studies have shown that at a fixed stellar mass range, satellites in less massive host halos ($\log(M_\star \, [M_\odot]) \sim 12$ - 13) are on average more metal-poor than their counterparts in massive environments (e.g., Gallazzi et al. 2021). This is expected as the gas removal from the satellite's disk or halo, induced by environmental quenching mechanisms in massive halos, can result in the suppression of gas inflow which is metal-deficient, and reprocessing of Fe-enriched gas (Pasquali et al. 2019; Gallazzi et al. 2021). Our results in Fig. 4.4.1 position themselves in this context and indicate that, compared to equally massive cluster dEs with similar average infall time, our sample dEs were not efficient in enriching their ISM with metals. This can be either due to low star formation efficiency in the group's environment or inflows of metal-poor gas (e.g., Pasquali et al. 2012; Peng et al. 2015). This comparison can be regarded as an additional evidence for pre-processing of our sample in their parent group.

From the top panel of Fig. 4.4.1, one may notice the difference between the metallicity distributions of Virgo and Coma dEs. According to this figure Virgo dEs, on average, tend to be more metal-poor than their counterparts in the Coma cluster. This can be either due to the lower number of investigated Virgo dEs within this stellar mass regime or different characteristics of these two clusters (in particular, their dynamical stage and halo mass).

4.5.2 Pre-processing in light of chemical enrichment

Our sampled dEs are moderate α-enhanced with light-weighted values when compared with more massive ETGs (e.g., Gallazzi et al. 2006; La Barbera et al. 2014; Gallazzi et al. 2021) and the thick disk of the Milky Way (e.g., Bensby et al. 2003; Vincenzo et al. 2021). This result is at odds with previous studies, which have shown that dEs are dominated mainly by stellar populations with solar α abundance ratios (e.g., Sybilska et al. 2017).

The [α/Fe] abundance ratio is often regarded as a 'metal production clock' (Sparke and Gallagher 2007) that can track the galactic chemical enrichment. In the early stages of a galaxy's life, the ratio between light α elements, such as Mg and Ca, and Fe-peak elements in the ISM is expected to be high. This is mainly due to the fast (within 100 Myr) evolution of massive stars (with $\log(M \, [M_\star]) > 10$) that leads to Supernova type II and α-enrichment of the ISM. As the galaxy continues forming new stars, Fe-peak elements contaminate the ISM on longer time scales (> 1 Gyr). The latter takes place through Supernova Type I that marks the endpoint of binary stars' lives. Hence, the [α/Fe] ratio decreases. In this regard, star formation on short timescales can result in a low abundance of Fe-peak elements and, consequently, α-enhancement. Thus, rapid quenching of star formation or removal of metal enriched gas, which are quite probable in high density environments, can result in higher [α/Fe] ratios (e.g., Thomas et al. 1999).

In the right panels of Fig 4.4.1, we compared our sampled dEs with their equally-massive counterparts in the Coma and Virgo clusters. Equal mass allows us to neglect systematic effects on [α/Fe] due to galaxy secular evolution. Through this comparison, we noticed that our sampled dEs are noticeably α-enhanced (with median [α/Fe] $= 0.26$ dex) than other cluster dEs, and especially when compared to those having a similar average infall time (i.e., with 8σ significance for dEs in zone two).

In earlier phases of our sampled dEs' evolution, the ISM was enriched mainly by massive stars and on a rather short time scale. Thus, their [α/Fe] ratios were relatively high. While the Fe-enrichment of ISM took place only Gyrs later, their star formation rate might also have been altered by the environment of their host group. The latter reasoning is based on the results of Erfanianfar et al. (2014) which show that the decline of a galaxy's star formation activity correlates with its host halo mass in that it becomes more significant in more massive galaxy groups. Rasmussen et al. (2012) showed that at fixed stellar mass, the specific star formation rate of group galaxies is suppressed, on average, by 40 percent compared to the field members. Authors have shown that this suppression effect is stronger in massive galaxy groups ($\sim 10^{12}$ $M_{\odot}$) (see also Schaefer et al. 2019). Moreover, Barsanti et al. (2018) showed that in the core of a group with $10^{12} < M_{200}/M_{\odot} < 10^{14}$ the specific star formation rate of galaxies drop by a factor of ~ 1.2 with respect to the field. The declination of star formation activity can result in prolonged metal enrichment of our dEs' ISM, hence, causing them to maintain their relatively higher [α/Fe] ratio for a longer time. This is also observed for dEs in the core of Coma cluster (Smith et al. 2009).

Our proposed picture of pre-processing for our sample dEs gains further support by the fact that despite their similar accretion time and stellar mass range, they exhibit scatter in their [α/Fe] ratios and ages. For instance, VCC0794, the most [α/Fe]-enhanced dE in our sample with light-weighted median age of ~ 10 Gyr, shows no signs of recent star formation activity. This galaxy might have formed the bulk of its stars on a rather short timescale. On the other hand, some of our sampled dEs have been accreted onto Virgo while retaining gas (directly observed in VCC0170) and showing less enhanced [α/Fe] ratios comparable with other dEs in the literature. Additionally, the presence of young (with light-weighted age of < 4 Gyr) and less α-enhanced stellar populations in some of the other dEs, such as VCC0407 or VCC0608, endorse the fact that star formation has been continued for longer timescales in some of our dEs, but not all of them.

Galaxy clusters are gradually built up through time by accreting galaxy groups with different masses, galaxy pairs, and isolated field galaxies. Since this hierarchical formation is frequent, one reasonable concern would then be the small fraction of [α/Fe]-enhanced clusters dEs observed in zone two and three of projected phase-space diagrams in Fig.4.4.1. One vivid explanation behind this is the lack of adequate data points. What is presented in Fig 4.4.1 does not include the entire cluster dEs within the defined stellar mass range, but only those with available results on [α/Fe] to date. A second possible explanation comes from results of Barsanti et al. (2018) which showed that low-mass satellites of less massive galaxy groups ($< 10^{12.5}$ $M_{\odot}$) experience enhanced star formation rate (hence, lowering [α/Fe] ratios), rather than suppression. Thus, not all the pre-processed dEs necessarily exhibit enhanced levels of [α/Fe]. Based on this statement, it stands to reason that cluster dEs show different levels of ISM enrichment as a result of not only their evolutionary path within their current host halo but also the characteristics of their previous environment(s).

In Section 4.4.2, we could not conclude any trend between average infall time of dEs and their [α/Fe] values. In particular, similarities between dEs in zone three of the phase-space diagram (with average infall time more than 5 Gyr) to the more recent infallers in zone two might be

unexpected since dEs of zone three have, on average, experienced longer exposures to clusters' environments. In this regard, Pasquali et al. (2019), and Gallazzi et al. (2021) found that ancient infallers tend to be more α-enhanced (within 2σ) compared to recent infallers. This has been concluded based on a much larger sample of low-mass galaxies in different environments. Hence, to have a more robust conclusion on this trend and to evaluate whether results of Pasquali et al. (2019) and Gallazzi et al. (2021) could also be the case for the Virgo cluster or not, we need to increase the size of our Virgo dEs.

There is no doubt that our reasoning here can be benefited from populating different zones of the projected phase-space diagram through investigations of larger dE samples. Furthermore, model predictions on efficiency and duration of (particularly) dE's star formation in massive galaxy groups can provide additional valuable information on ISM enrichment in such environments.

4.5.3 Nature or Nurture, that is the question

In Section 4.4.6, we compared the gradients of dEs in different clusters together and with more massive ETGs, up to 1Re. By far similar comparisons have been done by a number of studies in the literature, but only a very few of them have included galaxies as massive as early-type dwarfs ($\log(M_\star \, [M_\odot]) < 9.5$) (e.g., Harbeck et al. 2001; Chilingarian et al. 2008; Koleva et al. 2009, 2011; Sybilska et al. 2017; Goddard et al. 2017).

Based on their characteristics and environment, galaxies experience different evolutionary histories. The latter also manifests itself in the spatial distribution of the galaxy's stellar population, as well as their kinematics and dynamics. In fact, the scatter observed in most of the stellar population gradient's scaling relations reflects galaxies different evolutionary tracks (e.g., Pipino et al. 2008). Nonetheless, the extent to which environment or stellar mass effects shape galaxies' observed scaling relations is not clear yet. Considering a wide range of stellar masses ($9 < M_\star \, [M_\odot] < 11.5$), Goddard et al. (2017) showed that stellar population gradients (light- and mass-weighted) in ETGs are mainly mass dependent. They concluded that, within such stellar mass range, the environment has negligible, if any, effect on altering the spatial distribution of galaxies' stellar populations. Similar conclusions were presented also by studies which investigated massive galaxies (e.g.,: Annibali et al. 2007; Koleva et al. 2011; Rosa et al. 2018; Ferreras et al. 2019). Additionally, Santucci et al. (2020) showed no particular difference between stellar population gradients of satellites and central galaxies, up to 2Re. They suggested that regardless of their environment, galaxies follow similar formation trends in their inner regions. La Barbera et al. (2011) showed that ETGs more massive than $10^{10.5}$ $M_\odot$ have steeper negative metallicity and positive age gradients in low-density environments (such as groups), compared to those in massive clusters. On the other hand, a marginal flattening of metallicity gradients for low-mass halo satellites, compared to those in rich clusters, is reported by Greene et al. (2015). The latter was based on investigating 100 massive ETGs up to 2Re. This trend becomes less evident when considering the 1-1.5Re region, as mentioned by Greene et al. (2015).

Consistent with previous investigations of dEs, we also detected slightly positive $\nabla_{\rm age}$ (if any), negative $\nabla_{\rm [M/H]}$ and positive $\nabla[\alpha/{\rm Fe}]$ for our sample of dEs with $M_\star < 10^{9.5}$ $M_\odot$ in Fig. 4.4.6. These observed trends in stellar population gradients of dEs indicate that, in general,

dEs host younger, metal-richer and less α-enhanced stellar populations in their inner parts, thus are consistent with the out-side quenching scenario (Pipino et al. 2008, 2010). These results suggest that star formation in dEs, on average, takes place on longer timescales and is more centrally concentrated. K11 reported an average ∇_{age} of $+0.10 \pm 0.14$ for Fornax dEs, with extreme cases reaching up to $+0.30$. We detected a similar range of ∇_{age} for our sampled dEs, but with two extreme cases (namely VCC0170 and VCC1833). Similarly, investigations of K11 show a median range of $\nabla_{\mathrm{[M/H]}} = -0.26 \pm 0.16$ for Fornax dEs which is similar to the range reported for Virgo dEs by S17 and in this study. These reported ranges are consistent with results of hydrodynamical simulations which predict an average $\nabla_{\mathrm{[M/H]}} = -0.3$ dex for low-mass early-type galaxies, as a result of dissipative collapse formation scenario (Kobayashi and Arimoto 1999; Pipino et al. 2010).

Some studies predict flat $\nabla_{\mathrm{[M/H]}}$ for dEs with higher degrees of rotation (Schroyen et al. 2011; Koleva et al. 2009). This is mainly due to the fact that rotation of the galactic body is expected to act against its gas sinking. In Chapter 3 we showed that the majority of our sampled dEs are fast-rotating structures with relatively large values of specific angular momentum (λ_{Re}). Yet, eight out of 9 dEs in this sample have distinct negative $\nabla_{\mathrm{[M/H]}}$. Thus, similar to K11, our results are not consistent with mentioned predictions. However, we agree with K11 that our conclusion in this regard might be (partly) affected by the projection effect.

What is the role of the environment in the alteration of stellar population gradients in cluster dEs? The shallow potential well of dEs makes them susceptible to environmental effects, such as ram pressure stripping, tidal interactions, and starvation. Each of these mechanisms leaves imprints on stellar orbits and star formation activity of a given satellite galaxy, differently and on unlike timescales (e.g., Boselli and Gavazzi 2006). Interestingly, K11 detected metallicity gradients even in the old stellar populations of their investigated dE sample. Authors interpreted these findings as minor to null environmental effects on galactic stellar population gradients. It was only later that S17 challenged this interpretation by pointing to considerable chances of possible, but not directly detectable, environmental-induced alteration. Virgo dEs constitute the majority of our cluster dEs sample and have been exposed to environmental effects, on average, more than 3 Gyr (according to their position on the projected phase-space diagram). The latter is long enough to reasonably expect Virgo altering the spatial distribution of stellar populations within these galaxies. Yet, we did not detect any correlation between gradients and the average infall time of Virgo dEs, up to 1Re. Furthermore, we did not detect any difference between Virgo and Fornax dEs, in terms of the gradients of their stellar population properties. These results are partly affected by observed data constraints in both clusters. One other possible explanation could also be that either environment has no effect on shaping the stellar population gradients in the inner regions of cluster dEs or, as suggested by S17, its effect is too complicated to be traced by current diagnostic tools.

What is the role of galaxy stellar mass in modifying stellar population gradients in cluster dEs? In Fig.4.4.4 we did not detect any strong correlation between $\log(\sigma)$ and stellar population gradients of cluster dEs. The latter is consistent with results of Kuntschner et al. (2010); Koleva et al. (2011); Sybilska et al. (2017). Nonetheless, this trend might change after adding more data points to the comparison. On the other hand, we have detected a correlation between

∇Mgb and $\log(\sigma)$ in that ∇Mgb becomes flatter with increasing velocity dispersion. This is consistent with results of Pipino et al. (2010) who report a similar trend for ∇Mg2. In Fig.4.4.6 we compared our sample of cluster dEs with more massive ETGs of ATLAS3D, MANGA, and CALIFA surveys. In general, cluster dEs have ∇_{age}, $\nabla_{[\mathrm{M/H}]}$, and $\nabla[\alpha/\mathrm{Fe}]$ values comparable with those of more massive ETGs, measured up to 1Re.

Low-mass ETGs of ATLAS3D (at $\log(\sigma\ [\mathrm{kms}^{-1}]) \sim 1.8$) show steeper positive ∇_{age} which is not seen among cluster dEs. This has been noticed through comparisons of S17, where authors mentioned the presence of ATLAS3D field members as a possible explanation for this discrepancy. However, we witness similar differences for low-mass MANGA ETGs that also include field members within this mass range. This offset between results of Parikh et al. (2021) for MANGA survey, and Krajnović et al. (2020) for ATLAS3D survey persist at all stellar mass ranges and becomes even more drastic for $\nabla_{[\mathrm{M/H}]}$. One might notice a weak dependency between $\nabla_{[\mathrm{M/H}]}$ and $\log(\sigma)$ traced by ATLAS3D ETGs and cluster dEs. This trend shows that the $\nabla_{[\mathrm{M/H}]}$ becomes steeper toward galaxies with $\log(\sigma\ [\mathrm{kms}^{-1}]) \sim 2.2$ and decreases by moving toward very massive ETGs. The latter is in agreement with results of Annibali et al. (2007) who showed that the $\nabla_{[\mathrm{M/H}]}$ values becomes flatter toward more massive ETGs with $\log(\sigma\ [\mathrm{kms}^{-1}])$ ~ 2.5. In addition, Carollo et al. (1993) have also shown a positive correlation between ∇Mg$_2$ (as a tracer of stellar metallicity) and stellar mass of ETGs up to 10^{11} M$_\odot$. We have further witnessed a similar trend for ∇Mgb of Virgo dEs in Fig. 4.4.4. However, the correlation between $\nabla_{[\mathrm{M/H}]}$ and $\log(\sigma)$ in Fig.4.4.5 is solely based on the ATLAS3D data points, which are not quite consistent, particularly in $\nabla_{[\mathrm{M/H}]}$ values, with results of Parikh et al. (2021) for MANGA ETGs. Thus, it prevents us from making any robust conclusion here.

In addition, we have noticed that toward the lower $\log(\sigma)$, the $\nabla[\alpha/\mathrm{Fe}]$ of cluster dEs becomes steeper compared to more massive galaxies. Interestingly, the bin with the smallest $\log(\sigma)$ has the most positive $\nabla[\alpha/\mathrm{Fe}]$ gradient. Albeit, the latter is a weak trend and certainly can be benefited from the increase of data points in the low-mass end of the distribution.

Similarities of stellar population gradients between cluster dEs and more massive ETGs can be best understood in the context of two-phase formation scenario (e.g., Bullock and Johnston 2005). In the first phase, galaxies experience "in-situ" formation through dissipative collapse (i.e., forming stars in their inner region). Hence, positive age and negative metallicity gradients, particularly within 1Re, are expected (Zibetti et al. 2020). The latter trends are observed in cluster dEs, relatively weaker for dSphs of the Local Group (e.g., Harbeck et al. 2001; Chilingarian et al. 2008; Lianou et al. 2010; Koleva et al. 2011; Sybilska et al. 2017) and are predicted for this range of stellar mass by several authors (e.g., Larson 1974; Pipino et al. 2008). In the second phase of formation, known as the "ex-situ" phase, galaxies gain more mass through mergers. In this picture, mergers can reduce the slope of pre-existing gradients (Hopkins et al. 2009; Taylor and Kobayashi 2017) or, under special conditions such as wet mergers, can steepen them (Hopkins et al. 2009). Since the latter phase of formation affects the distribution of stellar population properties at a higher effective radius (i.e., > 1 - 1.5Re), their possible effects on our comparison in Fig. 4.4.5 may be marginal. This comparison indicates that probably regardless of their present-day environment, low-mass galaxies ($< 10^{9.5}$ M$_\odot$) have built up their inner regions mainly through the in-situ formation scenario that is more similar to the inner parts of massive

ETGs. This is consistent with the galactic formation scenario that several studies have pictured (e.g., Clauwens et al. 2018).

What Fig.4.4.5 demonstrates inevitably suffers from systematic biases, due to which we will not further comment on possible structural differences between cluster dEs and massive ETGs. Characteristics of different observed data and/or methods and approaches by which results are obtained, are the main sources of such systematic biases. This may explain the difference between the measured $\nabla_{\mathrm{[M/H]}}$ value of ATLAS3D and MANGA ETGs. The fitting approach (full spectrum fitting or the standard fit on Lick absorption indices), chosen stellar library and set of employed absorption features, can affect results of different investigations and may also persist in the comparison we performed here. We believe these results would benefit from statistically rich data sets, particularly including low-mass galaxies from different environments, analyzed in the same way and with the same tools.

4.6 Conclusion

In this chapter, we investigated the properties of our sampled dEs' stellar populations and compared our measurements with results in the literature. In this study, we developed a four-step index fitting routine, based on a χ^2 minimization approach, that fitted observed Lick indices with SSPs' predictions for age, [M/H], and [α/Fe]. In this study, we have employed the following absorption indices: Hβ_0, Mgb5177, Fe5270, Fe5335. We constructed the age, [M/H] and [α/Fe] maps of our main sample members using their MUSE data set. We quantified the spatial variation of these properties by fitting linear relations between stellar population values and galactocentric distances, using the publicly available LINmix routine. We compared our results with dEs of Virgo, Coma and Fornax clusters, as well as more massive ETGs coming from surveys such as CALIFA, ATLAS3D and MANGA. The main results of our analysis can be summarized as follow:

- Our sampled dEs fall within the age range of 1.85 to 10.50 Gyr, the metallicity range of -0.77 < [M/H] [dex]< -0.18 and α abundance range of 0.20 < [α/Fe] [dex] < 0.43. We have measured the median age of 6.8 $\pm$ 1.1 Gyr, median [M/H] of -0.59 $\pm$ 0.05 dex, and median of [α/Fe] = 0.26 $\pm$ 0.02 dex for our sampled dEs.

- We found our sampled dEs to be younger (with the significance of 1σ), metal-poorer (with the significance of 2-3 σ) and more α-enhanced (with the significance of 8σ) than other dEs of Virgo and Coma cluster in the same stellar mass range and with similar average infall time. These results, and in particular the α-enhancement of our sampled dEs, can be evidence for satellites' pre-processing in the previous galaxy group, and prior to their infall to the Virgo.

- We measured an average $\nabla_{\mathrm{age}} = 0.12 \pm 0.12$ [log yr]/[log(R/Re)], $\nabla_{\mathrm{[M/H]}} = $ -0.14 $\pm$ 0.06 [dex]/[log(R/Re)], and $\nabla[\alpha/\mathrm{Fe}] = 0.12 \pm 0.04$ [dex]/[log(R/Re)] [2] for our sampled dEs. These results are consistent with previous studies and reinforce the out-side in quenching scenario for these low-mass systems.

---

[2] errors are computed as the standard error of the average.

- We did not detect any meaningful correlation between stellar population gradients of dEs and their $\log(\sigma)$ (as a prob of their stellar mass) or environment. We could only detect a correlation between ∇Mgb and $\log(\sigma)$ for cluster dEs, which is consistent with the results of those studies which reported a similar correlation for ∇Mg2.

- We found that cluster dEs show a similar range of ∇_{age}, $\nabla_{[\mathrm{M/H}]}$, and $\nabla[\alpha/\mathrm{Fe}]$ as more massive ETGs, up to 1Re. Nonetheless, compared to these massive systems, cluster dEs have steeper positive $\nabla[\alpha/\mathrm{Fe}]$. Due to systematic biases in the analysis of these galaxy samples, we could not conclude any possible general trends or structural differences between cluster dEs and massive ETGs.

Adam's sons are body limbs, to say;
For they're created of the same clay.
Should one organ be troubled by pain,
Others would suffer severe strain.
Thou, careless of people's suffering,
Deserve not the name, "human being".

— Saadi, a major Persian poet and prose writer.
Translation by: H. Vahid Dastjerdi

5

Imprints of the accretion event

This chapter is based on the preliminary results of an ongoing project. Final results will be submitted for publication in MNRAS as Bidaran et al.

In this chapter, we investigate possible imprints of the accretion of our sampled dEs, onto Virgo, on their star formation activity. To do so, we perform the full spectrum fitting technique, using the public STARLIGHT routine, over the averaged spectra of our sampled dEs. We expound our (preliminary) results concerning dEs' accretion time onto Virgo.

5.1 Introduction

Satellites are exposed to different environmental mechanisms, following their accretion onto high-density environments. Inside their host halo, ram pressure stripping (RPS) can effectively exhaust satellites' star formation activity by depleting their cold gas reservoir (Gunn and Gott 1972). This hydrodynamical effect generates stripped tails in some cluster satellites (referred to as jellyfish galaxies) and alters galaxies' star formation activity (e.g., Hester et al. 2010; Fumagalli et al. 2011; Kenney et al. 2014). Furthermore, the gravitational potential well of the host halo and multiple close encounters with other halo members can exert a combination of tidal forces on the accreted satellites that leave marks on their dynamics, morphology, and star formation activity. The effect of these combined tidal interactions is known as galaxy harassment (Moore et al. 1996, 1998). In addition to harassment and RPS, other environmental mechanisms, such as starvation, are also responsible for converting star-forming galaxies into quiescent ones. These environmental mechanisms efficiently leave imprints on different properties of infalling satellites, but on relatively different timescales (for more details on environmental mechanisms check Section 1.2 of Chapter 1 or review of Boselli and Gavazzi 2006).

Among different mechanisms introduced so far, RPS acts relatively fast and efficiently (e.g.,

Boselli and Gavazzi 2006; Boselli et al. 2009). RPS eliminates the low-density gas from satellites' outskirts, modifies their color on short time scales (Boselli et al. 2009), and creates truncated radial gas density profiles (e.g., Chung et al. 2009). However, as mentioned in Chapter 1, the strength of the RPS depends on the environment's density (i.e., the density of intra-cluster medium), the velocity of the infalling satellite, and its orbital configuration. While on longer timescales, RPS is conducive in ceasing the star formation activity of a given satellite, in shorter intervals, it can trigger local star formation enhancements, as a result of gas compression in the infalling satellite's leading part and core (but see: Mun et al. 2021). This effect is severe for those gas-rich satellites with (nearly) edge-on infalling orbits in massive galaxy clusters (Boselli and Gavazzi 2006). Additionally, the dark matter distribution of the infalling satellite (Mori and Burkert 2000), and its stellar mass (Abadi et al. 1999; Vollmer et al. 2001; Smith et al. 2015) are some of the other factors that determine RPS's efficiency in triggering or suppressing satellite's star formation activity.

An infalling satellite may experience bow shocks, turbulent motions, and thermal instabilities while moving within the intergalactic medium of its host halo. Such hydrodynamical interactions likely increase the rate of gas cloud collisions within the satellite's inner disk (Evrard 1991; Bekki and Couch 2003; Bekki 2014). This effect has been directly observed in the spiral galaxy NGC 4921 of the Coma cluster by Cramer et al. (2021). On the other hand, along the direction of the velocity vector and particularly in (nearly) edge-on accretion events, the outer low-density gas reservoir of the galaxy may be trapped in its inner disc, thus the gas density of central parts increases by a factor of 1.5 (Vollmer et al. 2001). These two effects can eventually trigger star formation episodes or enhance the preexisting one for a short time. In a massive galaxy cluster, such as Virgo, this effect is more substantial. Models predict the star formation rate of infalling satellites in a Virgo-like halo to increase by a factor of 2 (e.g., Fujita 1998; Fujita and Nagashima 1999) on timescales less than 1 Gyr. This effect has been observed in jellyfish galaxies (e.g., Hester et al. 2010; Safarzadeh and Loeb 2019). Results of Bekki and Couch (2003) suggest that star formation enhancement is expected to be triggered in the early stages of accretion and even in the outskirts of massive host halos.

In chapter 4 we detected a young population of stars (i.e., age < 4 Gyr) across some of our sampled dEs' bodies. We discussed that the average age of these young components correlates with the average infall time that we measured for our sample (Chapter 2). These young stellar populations might be the result of star formation activity intrinsic to our sampled dEs or it might have been triggered by RPS upon accretion onto Virgo. In particular, if the velocity vector of a satellite within a merging galaxy group aligns with the group's merging axis, the relative velocities add up together, and the RPS effect becomes more severe (McPartland et al. 2016; Ebeling and Kalita 2019). To this end, we believe that our sampled dEs, although limited by size and (likely) different levels of pre-processing, constitute an informative testbed for investigating the possible effects of RPS during early stages of low-mass galaxies' infall.

Two questions shape the main objectives of this chapter: How would a cluster's environment affect the star formation activity of accreted satellites in their early stages of infalling? And what are possible imprints of pre-processing on star formation history [1] of infalling satellites? We have

---

[1]The number of stars that are formed inside a galaxy as a function of time.

performed the full spectrum fitting technique that provides the most plausible fitting solution by combining a set of single stellar population (SSP) models but not relying solely on a single model as presented in Chapter 4. With this approach, we will account for the contribution of SSPs, with different ages and metallicities, to the observed spectrum simultaneously. Determining average age and [M/H] in this way also reassures us about the reliability of the average ages and metallicities derived through the spectral line indices in Chapter 4.

This chapter is organized as follows: In Section 5.2 we describe the full spectrum fitting technique we employed to measure stellar population properties of our sample dEs. In Section 5.3 we present our results and we discuss them in Section 5.4. Conclusions and outlook are presented in Section 5.5.

5.2 Method

One possible way of retrieving stellar population properties from observed spectra is to create a synthetic spectrum by linearly combining SSP models so that the constructed spectrum best matches the observations. This approach shapes the basis of the well-known full-spectrum fitting technique and several publicly available routines (such as pPXF (Cappellari and Emsellem 2004; Cappellari 2017), STARLIGHT (CidFernandes et al. 2005), and Ulyss (Koleva et al. 2009)) perform it. Through full-spectrum fitting, we consider no only absorption features (such as $H\beta$ or Fe absorption lines), but also the shape of the stellar continuum in the observed spectrum. Thus, this method is sensitive to the flux calibration of the data. In this chapter, we perform this technique using the well-known STARLIGHT code.

5.2.1 Full spectrum fitting by STARLIGHT

STARLIGHT is a publicly available full-spectrum fitting code that provides the most plausible spectral fit to the observed data by constructing a synthetic spectrum (M_λ) from a linear combination of a set of defined SSP models of different age and metallicity. The most plausible combination of parameters in the fitted spectrum can be quantified as suggested by CidFernandes et al. (2005):

$$M_\lambda(x, M_{\lambda 0}, A_V, v_\star, \sigma_\star) = M_{\lambda 0} \left(\sum_{j=1}^{N_\star} x_j b_{j,\lambda} r_\lambda \right) \bigotimes G(v_\star, \sigma_\star) \qquad (5.1)$$

where $M_{\lambda 0}$ is the scaling parameter and is set equal to the synthetic flux at the user-defined normalizing wavelength range. The latter is used by the code for normalizing the observed data. The summation is over $N_\star$ that is the number of base models. x_j denotes the population vector, $b_{j,\lambda}$ represents the jth SSP model and r_λ represents the reddening term. The A_V is the Galactic extinction in V-band, and similar to Chapter 4, we used Cardeli Galactic extinction law (Cardelli et al. 1989) for the full spectrum fitting analysis here. $G(v_\star, \sigma_\star)$ denotes a Gaussian model with broadening $\sigma_\star$ (the stellar velocity dispersion) that is centered at $v_\star$ (the rotational velocity of stars). The plausibility of the fitted spectrum with respect to the input observed data (O_λ) is

evaluated based on the least χ^2 test, as described by CidFernandes et al. (2005):

$$\chi^2(x, M_{\lambda 0}, A_V, v_\star, \sigma_\star) = \sum_{\lambda=1}^{N_\lambda} [(O_\lambda - M_\lambda)w_\lambda]^2 \qquad (5.2)$$

where w_λ is the inversed noise of the observed spectrum. Once the most feasible solution is found, the code creates a report containing the best-fitted spectrum and a population vector that defines the contribution of each SSP model to the final fitting solution. This report is used to compute light-/mass-weighted age and [M/H] along with the star formation history and mass assembly of the galaxy under study (see Section 5.3).

5.2.2 Setup and measurement
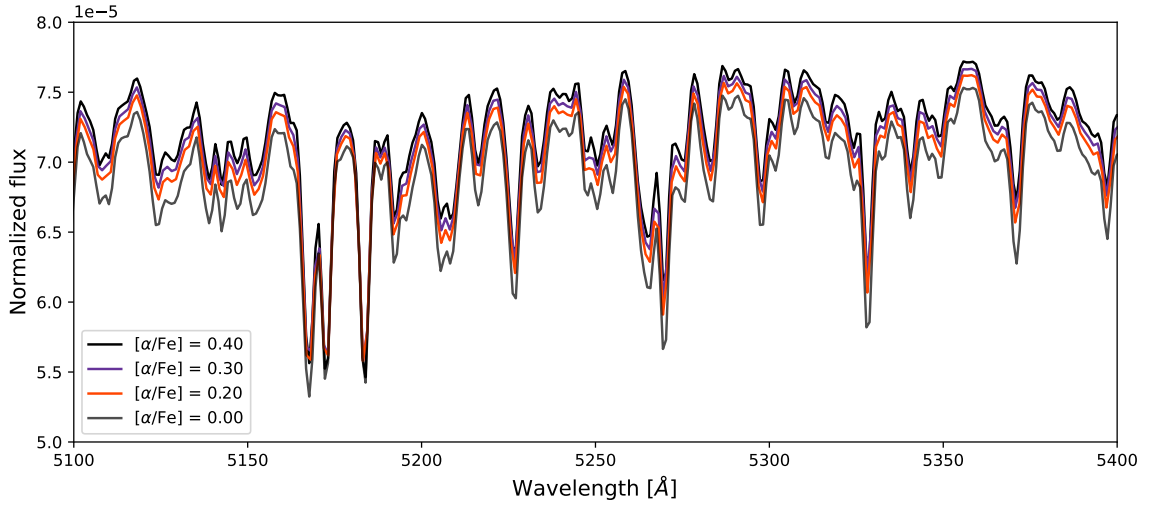
Figure 5.2.1:]
An example of the interpolation of interpolated SSP models of fixed age (4 Gyr) and metallicity ([M/H] = -0.66 dex). Different colors show SSPs with different values of [α/Fe].

We have employed the integrated averaged spectrum of each dE, as constructed in Section 4.3.2, to derive its light- and mass-weighted age and metallicity. This spectrum is corrected for nebular emission lines and Galactic extinction, as described in 4.3.1. In this work, we perform the spectral fitting in the spectral range of 475 to 554 (nm). This wavelength range contains the most crucial absorption features that are sensitive to age and [M/H] and is less affected by telluric lines that are most dominant at longer wavelengths (for more explanation on possible impacts of selected wavelength ranges on the full spectrum fitting results, please check: Gonçalves et al. 2020). To normalize the input flux, STARLIGHT uses the median of the observed spectrum in a specific user-defined wavelength range, called the "S/N window". In this study, we have defined our preferred S/N window in the wavelength range of 475 to 480 (nm).

In order to compare the results of this chapter with those of Chapter 4 (i.e., Lick indices fitting), here we have utilized SSP models with a similar configuration. In detail, we use Vazdekis et al. (2010) SSP models based on the MILES library with BASTI isochrones and bimodal IMF with a slope of 1.3. Our base SSP models have the age range of 1 to 14 Gyr with a stepping of 1 Gyr and the metallicity range of -1.26 to -0.25 dex. As explained in Chapter 4, absorption features that are present in our adopted fitting wavelength range are not only age and [M/H] dependent but also are sensitive to $[\alpha/\mathrm{Fe}]$. On the other hand, STARLIGHT only accepts a limited number of SSP models as its pre-defined base (up to 300). Thus, to take our dEs' α enrichment into account and compensate for the limited size of STARLIGHT's stellar models base, we decided to use SSPs with $[\alpha/\mathrm{Fe}]$ values equal to what we have measured for each dE in Table 4.3.3 of Chapter 4.

Unfortunately, by the time of writing this thesis, the MILES library only provides SSP models for three sets of $[\alpha/\mathrm{Fe}]$ values (i.e., 0, 0.2, and 0.4 dex). This problem will be solved once sMILES library becomes available (Knowles et al. 2021). This new semi-empirical MILES library will provide a wider range of $[\alpha/\mathrm{Fe}]$ values (-0.20 to 0.60 dex) for SSP models, at the spectral resolution of FWHM = 2.5 Å. In this study, we have compensated for the stellar library limited coverage of $[\alpha/\mathrm{Fe}]$ by interpolating the flux of available models and constructing SSPs at our desired $[\alpha/\mathrm{Fe}]$ range.

To do so, for models at each age and [M/H], we linearly interpolated the flux at each wavelength and based on their $[\alpha/\mathrm{Fe}]$ values. Hence, we constructed new SSP models with different levels of α-enrichment. Per α values, we name these new sets of models, per $[\alpha/\mathrm{Fe}]$ values, as a new "SSP family". In Fig. 5.2.1, an example of this flux interpolation is presented for SSP models with age 4 Gyr and [M/H] = -0.66 dex. In this plot, the α-enhanced model (with $[\alpha/\mathrm{Fe}]$ = 0.4 dex) is presented with a black line, and the model with solar-scaled α is presented as a gray line. Two interpolated spectra are presented with purple (with α= 0.3 dex) and orange (with α =0.2 dex) lines in the same figure. In the case of VCC0794, which is the most α-enhanced dE in our sample (with $[\alpha/\mathrm{Fe}]$ = 0.43 dex), desired SSP families were constructed by linearly extrapolating available SSP models.

To perform fits on each dE, we considered three α values (hence three SSP families). These values are the measured $[\alpha/\mathrm{Fe}]$ values and their corresponding upper and lower errors, as reported in Table 4.3.3 of Chapter 4.

To account for possible systematic errors, we ran STARLIGHT for 100 MC realizations. To do so, we performed a single fit over the observed spectrum. We created 100 perturbed spectra by adding to the original flux, per wavelength, a value randomly selected from the residuals of the STARLIGHT fit. The final stellar population properties that are reported in this chapter are the average of these 100 iterations, and errors are their corresponding standard deviations. In Fig.5.2.2, we show an example of the fit performed by STARLIGHT over the averaged integrated spectrum of VCC2019 (the dark blue spectrum). The best-fitted solution of STARLIGHT (shown in red) and the fit residuals (shown in light purple) are also plotted. Please note that residuals are shifted up by 0.3 for legibility.
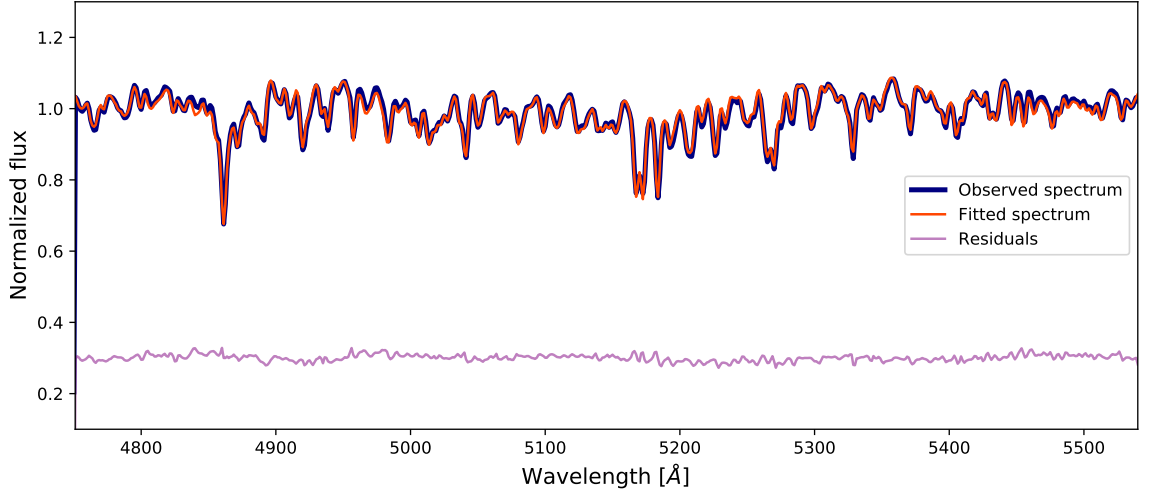
Figure 5.2.2: An example of the full spectral fitting over the averaged spectrum of VCC2019. The observed and normalized data is shown in the dark blue spectrum. STARLIGHT's best-fitting model spectrum is shown in red, and residuals of the fit are shown in light purple. For better legibility, residuals are shifted up by 0.3.

5.3 Results

5.3.1 Integrated Age and [M/H]

STARLIGHT quantifies each SSP's contribution to the total best fitting spectrum and reports it as assigned weight. Hence, per STARLIGHT run, we can derive light-weighted age and [M/H] following the definitions below:

$$< Age >_L= \sum_{t,Z,\alpha} \epsilon_{t,Z,\alpha} Age \tag{5.3}$$

$$< [M/H] >_L= \sum_{t,Z,\alpha} \epsilon_{t,Z,\alpha}[M/H] \tag{5.4}$$

where t, Z, and α denote age, metallicity, and α-enrichment of a given SSP model and $\epsilon_{t,Z,\alpha}$ is the light-weighted stellar population vector. Here the summation is over the entire SSPs of the base. To compute the mass-weighted age and metallicity, we use the same equation above, but by using $\mu_{t,Z,\alpha}$, which is the mass-weighted stellar population vector. This vector is computed by multiplying $\epsilon_{t,Z,\alpha}$ by the mass-to-light ratio of each SSP (measured by STARLIGHT per fit) after normalizing each SSP's stellar mass to 1 $M_\odot$. For each dE and for each of the 100 MC runs, we computed light-/mass-weighted age and metallicity using the equations above. In Table 5.3.1 and for each galaxy, we report the age and metallicity averaged over the results of these 100 MC runs. The upper and lower range of errors is 84th and 16th percentiles of their corresponding distributions.

Table 5.3.1: STARLIGHT results on integrated light-/mass-weighted stellar population properties

Object	$<$Age$>_L$ [Gyr]	$<$[M/H]$>_L$ [dex]	$<$Age$>_M$ [Gyr]	$<$[M/H]$>_M$ [dex]
VCC0170	$2.09^{+0.20}_{-0.24}$	$-0.54^{+0.04}_{-0.04}$	$2.78^{+0.21}_{-0.19}$	$-0.61^{+0.12}_{-0.10}$
VCC0407	$4.11^{+0.35}_{-0.42}$	$-0.50^{+0.03}_{-0.03}$	$4.70^{+0.31}_{-0.34}$	$-0.56^{+0.13}_{-0.11}$
VCC0608	$3.16^{+0.27}_{-0.66}$	$-0.44^{+0.04}_{-0.04}$	$4.58^{+0.20}_{-0.34}$	$-0.48^{+0.14}_{-0.11}$
VCC0794	$9.54^{+0.58}_{-0.52}$	$-0.69^{+0.05}_{-0.05}$	$9.91^{+0.83}_{-0.78}$	$-0.62^{+0.14}_{-0.10}$
VCC0990	$4.37^{+0.43}_{-0.50}$	$-0.38^{+0.04}_{-0.04}$	$5.30^{+0.40}_{-0.38}$	$-0.37^{+0.09}_{-0.11}$
VCC1833	$3.63^{+0.48}_{-0.82}$	$-0.26^{+0.04}_{-0.04}$	$5.96^{+0.28}_{-0.25}$	$-0.25^{+0.11}_{-0.08}$
VCC1836	$3.98^{+0.45}_{-0.38}$	$-0.66^{+0.05}_{-0.05}$	$4.56^{+0.33}_{-0.28}$	$-0.72^{+0.20}_{-0.16}$
VCC1896	$8.60^{+0.43}_{-0.57}$	$-0.49^{+0.04}_{-0.03}$	$9.06^{+0.76}_{-0.70}$	$-0.43^{+0.18}_{-0.10}$
VCC2019	$6.51^{+0.60}_{-0.65}$	$-0.46^{+0.05}_{-0.04}$	$6.81^{+0.49}_{-0.41}$	$-0.45^{+0.12}_{-0.08}$

Columns are: name of the target, light-weighted age, light-weighted metallicity, mass-weighted age, and mass-weighted metallicity.
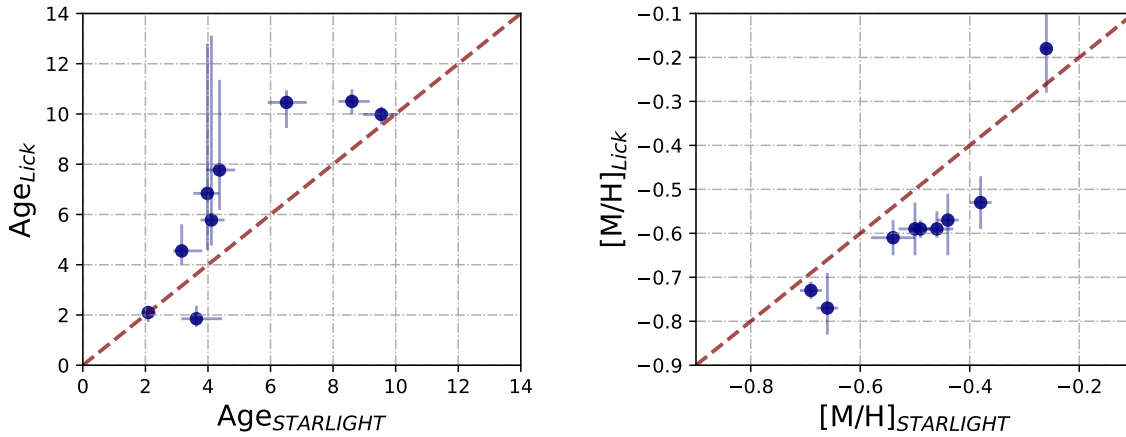
Figure 5.3.1: *Left panel*: Comparing light-weighted age values obtained from STARLIGHT full spectrum fitting (x-axis) with those measured through Lick indices fitting (y-axis). Data points represent dEs in our main sample. *Right panel*: Same comparison as the right panel but for light-weighted [M/H] values.

In Fig. 5.3.1 we compare results of STARLIGHT fits with those from Lick indices fitting (values reported in table 4.3.3 of Chapter 4). In the left panel of this figure, we compare light-weighted mean ages obtained from STARLIGHT (on the x-axis) and averaged age values obtained from fitting over Lick indices (on the y-axis). Same comparison, but for light-weighted mean [M/H], is presented in the right panel of Fig. 5.3.1. A KS-test applied to these two sets reveals consistency between the two fitting approaches (with p-value = 0.35 and 0.12 for results on age and metallicity, respectively).

5.3.1 shows that STARLIGHT generally underestimates age while overestimating metallicity

with respect to Lick indices. This can partly be due to systematic and fundamental differences between the two employed fitting methods in this comparison. STARLIGHT considers a mixture of SSP models to construct the best fitting model. Thus, for galaxies with multiple epochs of star formation, STARLIGHT is a more realistic approach than the single stellar population fitting that we have performed in Chapter 4. Precisely, the light-weighted age and [M/H] in Table 5.3.1 are measured by accounting for the possible contribution of both young and old SSPs in the observed spectrum, whereas in Chapter 4, we have based our analysis solely on single stellar populations and not simultaneously considering different SSP components.

In Section 5.2.1, we have already stated that STARLIGHT accepts only a limited number of SSP models (maximum number of 300) while for the Lick indices fitting, such limitation does not hold (we used $\sim$ 2,410,000 SSP models in the analysis of Chapter 4). Hence, STARLIGHT constructs the final fitted spectrum based on a limited model space that has uneven spacing in the [M/H] axis and a spacing of 1 Gyr in the age axis. This may affect STARLIGHT's judgment on computing the contribution of each SSP model, thus the final average age and [M/H]. In addition, it should also be noted that the uncertainties due to model degeneracies that we already mentioned in Section 4.3.3 are still relevant for the results of the full-spectrum fitting. Last but not least, results of Lick indices fitting noticeably suffer from the well-known issue of "age-metallicity degeneracy". According to Sánchez-Blázquez et al. (2011), this issue is less dominant for full-spectrum fitting, yet it should be taken into account while interpreting the present discrepancy between the results of these two approaches.

5.3.2   Star formation through galactic lifetime

On the top row of Fig.5.3.2, we present the stellar light fraction as a function of age for our sampled dEs. Each distribution has been constructed by summing $\epsilon_{t,Z,\alpha}$ values over metallicities and α values, at any given age. Hence each distribution shows the contribution of SSPs of different ages to the final fitted spectrum. These light distributions are systematically more sensitive to the contribution of young stars to the total observed light. Thus, they trace recently formed stars in a given galaxy. In the bottom panels of this figure, we present the stellar mass fraction as a function of age which was constructed by summing $\mu_{t,Z,\alpha}$ values over metallicities and α values at any given age. For each dE, the mass-weighted distribution follows a similar trend as the light-weighted one.

In Fig.5.3.2, we have divided galaxies into two sub-samples based on the presence or absence of a peak in their light fraction profiles at $\sim$ 2-3 Gyr. As shown in the top left panel of Fig. 5.3.2, a peak is present in the stellar light fraction distributions of six dEs, with similar but less pronounced peaks in their mass distributions (bottom left panels of Fig.5.3.2). The stellar light fraction of VCC0170, for which we have detected a central gas reservoir and ongoing star formation in Chapter 3, shows a steep rise from $\sim$ 10 percent at 4 Gyr ago to $\sim$ 40 percent at 1 Gyr.

We do not detect such a peak in the stellar light and mass fraction distributions of the other three dEs, as shown in the right panels of Fig. 5.3.2. In Chapter 4, we showed that VCC0794 is the most α-enhanced member of our sample. Based on the analysis in that Chapter, this galaxy hosts old ($\sim$ 10 Gyr) and metal-poor ($\sim$ -0.73 dex) stellar populations. In the top right
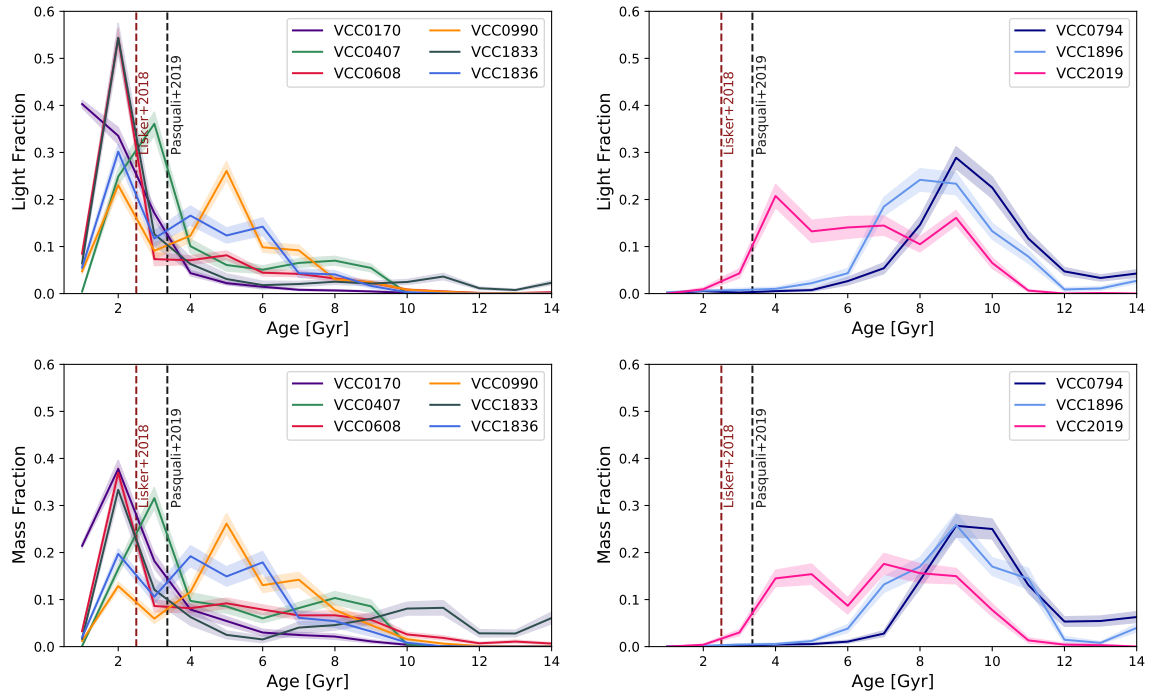
Figure 5.3.2: *Top row:* Stellar light fraction of our sampled dEs as a function of time. The distributions of those dEs that exhibit prominent peaks after their accretion time onto the Virgo cluster are presented in the left panel, and the distributions of those dEs without similar peaks are shown in the right panel. *Bottom row:* Same as the top row but for mass weighted profiles.

panel of Fig. 5.3.2, this particular dE shows a peak in its stellar light fraction profile at the age of 9 Gyr, which is consistent with our previous results and endorses the fact that this dE has been accreted to Virgo, gas deficient, pre-processed and with low star formation rate, if any. VCC1896, for which we could only map the central bar in Chapters 3 and 4, is another old dE that shows a peak in its stellar light and mass fraction distributions at about 8 Gyr ago. This is consistent with our results in the previous Chapter.

Two dEs of our sample, namely VCC0990 and VCC2019, show double-peak stellar light and mass fraction distributions in Fig. 5.3.2. In Chapter 4 we showed the presence of a very localized young stellar population in the core of these two dEs, consistent with the presence of a nuclear stellar cluster in their central region as reported by Paudel et al. (2011) and Fahrion et al. (2021). Fahrion et al. (2021) shows a similar double peak profile in the star formation history of these two dEs. According to their results, the peak at younger ages (i.e., at ~ 2 Gyr for VCC0990 and at ~ 4 Gyr for VCC2019) belongs to their nuclear stellar cluster. The second peak at older ages instead appears to be related to star formation in the galaxy's main body. In this regard, VCC0990 may not show a peak in its stellar light and mass fraction at the time of its accretion after excluding its central nuclear stellar cluster. Our findings are also consistent with the spatial distribution of light-weighted age and [M/H] of these two dEs, shown in Fig.4.3.8 and 4.3.9 of Chapter 4. Two vertical lines in panels of Fig. 5.3.2 indicate the average infall

time of our sampled dEs (according to two approaches in Chapter 2). Interestingly enough, the peaks of both light- and mass-weighted distributions coincide with the accretion time of our sample dEs and in some cases, the peaks are even more recent than the accretion event.
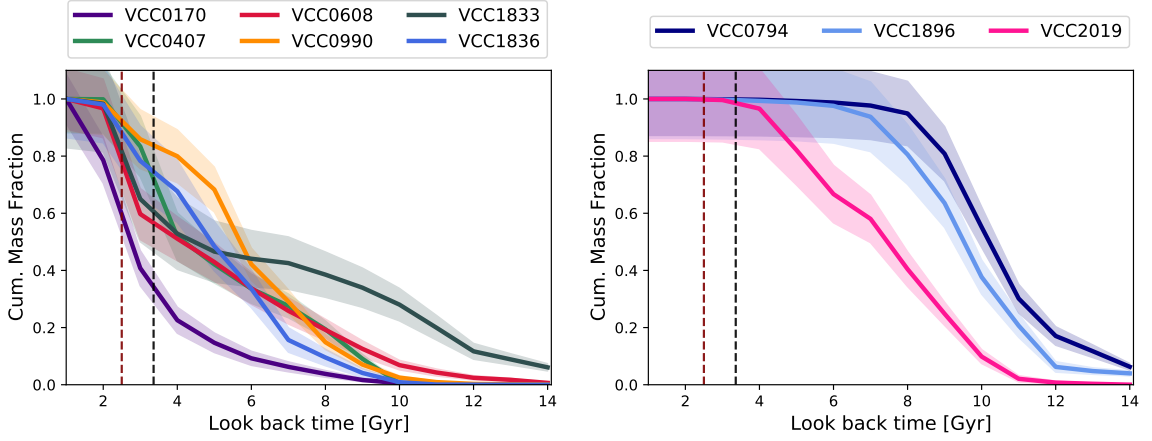
Figure 5.3.3: Cumulative mass distribution as a function of each dE's age. Here galaxies are divided into two sub-samples following Fig. 5.3.2.

From STARLIGHT results, we built the cumulative mass distributions as a function of the age of our sampled dEs and presented them in Fig. 5.3.3, where we also indicate the accretion times from Lisker et al. (2018) and Pasquali et al. (2019). On the left panel of this figure, the cumulative mass distributions of six dEs are presented, for which we could detect prominent peaks in their light and mass fraction distributions. These six dEs have experienced distinguishable mass growth during/after the accretion event according to their cumulative mass distributions. Specifically, these six dEs have experienced diverse ranges of mass growth, ranging from 5 to more than 70 percent, between 4 to 1 Gyr ago. VCC0170 has experienced the most drastic mass growth ($\sim$ 70 percent) since $\sim$ 4 Gyr ago. These findings are in agreement with the "delayed-then-rapid" quenching scenario of Wetzel et al. (2013) who predicted that, in their early stages of infalling and prior to their complete quenching, satellites might experience more than 50 percent of mass growth. On the right panel of Fig. 5.3.3, we present the cumulative mass fraction of three dEs that did not exhibit any peaks in their stellar light or mass fraction distributions at the period of their accretion. According to the results presented in this panel, the star formation activity of these three dEs ceased before their accretion onto Virgo.

5.4 Discussion

Dwarf galaxies have shallow potential well, thus are more vulnerable to environmental effects. Based on this fact, one can expect fast gas removal and star formation suppression in cluster dEs due to ram pressure stripping (RPS). Despite that, studies have shown that, compared to more massive galaxies, low-mass ones (with $M_\star < 10^{10.2}$ $M_\odot$) have longer quenching timescales in clusters and follow the "delayed-then-rapid" quenching scenario (e.g., Wetzel et al. 2013; Wheeler et al. 2014; Oman and Hudson 2016; Rhee et al. 2020). One explanation can be the

presence of a large gas reservoir in such low-mass galaxies, accompanied by low star formation efficiency (Wheeler et al. 2014). One other explanation behind this trend can be gas compression by the cause of ram pressure which leads to gas over-density in the central parts of some dEs. This gas may remain bound to the galaxy contrasting the RPS induced momentum transfer (e.g., Steyrleithner et al. 2020) and fuel the star formation activity of the galaxy.

In this Chapter, we investigated the star formation history of our sampled dEs. In this study, we were more focused on the possible effects of their accretion event and its imprints on their star formation activity. In Fig. 5.3.2, we showed that young stellar populations (with age < 4 Gyr) contribute significantly to the observed light of six out of nine dEs of our sample. Interestingly, the age of these young stellar populations is consistent with the average infall time of these dEs (more details in Chapter 2), and amount to 5 to 30 percent of the galaxy stellar mass in five dEs and form up to 70 percent of VCC0170's total stellar mass.

As suggested in Chapter 4, these results can be interpreted in the context of the "delayed-then-rapid" quenching scenario. Our dEs have been accreted onto Virgo, likely preserving part of their gas reservoir. According to the results of Rhee et al. (2020), the star formation rate of infalling satellites remains intact during the early stages of their accretion (i.e., 2-4 Gyr), commonly referred to as the "delayed-phase" (see also Wetzel et al. 2013). Thus, it stands to reason that the observed young stellar populations of these six dEs may have been formed during this delayed phase and during or after their accretion onto the Virgo.

Nonetheless, the star formation enhancement of these dEs at this recent epoch with respect to their star formation rate in the past may also indicate the temporary effect of ram pressure stripping inside the Virgo cluster and during the accretion event. This hypothesis gets further endorsement since results of McPartland et al. (2016) and Ebeling and Kalita (2019) show that satellites of an infalling galaxy group may experience extreme cases of ram pressure stripping. The ISM's gas can be compressed in the leading side of an infalling satellite or be captured by its central regions in cases of (nearly) edge-on infalls. This can increase the central gas density by a factor of 1.5 (Vollmer et al. 2001). Such central gas overdensity may lead to a temporary enhanced (by a factor of 2 Steyrleithner et al. 2020) and (mainly) centrally located star formation activity in infalling satellites, during the early stages of their accretion (Bekki 2014; Steinhauser et al. 2016; Vulcani et al. 2018). The presence of blue cores in some of cluster dEs' indicates a relatively recent star formation activity in the core of these galaxies (Lisker et al. 2006a; Urich et al. 2017; Hamraz et al. 2019). The presence of young and metal-rich stellar populations in the core of VCC0170 (Chapter 4) together with a centrally located gas reservoir (shown in Chapter 3) fits into the picture of extended but centrally localized star formation activity of this dE. In this regard, the models of Wetzel et al. (2013) show that the star formation rate of infalling satellites with a sufficient gas reservoir might increase by a factor of 2. This picture fits well with our observations for VCC0170, which experienced a 70 percent increase in its total stellar mass during the last $\sim$ 4 Gyr. Furthermore, light-weighted age and metallicity maps of some of our sampled dEs indicate the presence of metal-enhanced and relatively young stellar populations in the central parts of these galaxies. These shreds of evidence further support the positive but temporary role of ram pressure stripping in the star formation activity of infalling dEs.

Three dEs, namely VCC0794, VCC1896, and VCC2019, do not show any recent peak of stellar light fraction (right panels of Fig. 5.3.2). From the right panel of Fig. 5.3.3 we further notice that these three dEs have completed the formation of their current total stellar mass more than 4 Gyr ago, likely before their accretion onto Virgo and thus, in their parent host halo. According to its cumulative mass profile, VCC0794 has formed most of its total stellar mass $\sim$ 5 Gyr before its accretion onto the Virgo cluster and within a short time interval of $\sim$ 4 Gyr. This dE has the shortest duration of star formation among our sampled dEs. This result is in agreement with our findings in Chapter 4 where we detected significantly α-enhanced (i.e., 0.43 dex) and moderately metal-poor (0.73 dex) stellar populations for this dE.

We observe two peaks in both the light and mass fraction distributions of VCC0990 and VCC2019. This is due to the presence of a stellar nuclear cluster (NSC) in the center of these two dEs (Paudel et al. 2010; Fahrion et al. 2021). According to the spatial maps presented in Chapter 4 and results of Fahrion et al. (2021), the inner peak (i.e., at the younger ages) belongs to the NSC while the outer one is related to the galaxy's main body. To compute the cumulative mass fraction distribution, we did not account for the possible effects of central NSC. Thus, interpreting these results should be done with caution. This issue endorses the importance of performing a detailed star formation history investigation on different parts of the galactic body (i.e., inner and outer regions). This will be done in the future, and results will be reported in a companion paper.

Our results, constructed from 100 MC iterations, present only 100 possible fitting solutions for each observed dE. In order to have a realistic interpretation of these preliminary results, however, we need to also take inevitable sources of uncertainty into account. Our full spectrum fitting approach (performed with STARLIGHT) is based on a limited number of SSP models, and this puts constraints on our measurements, undeniably. This limited number of SSP models may feed the well-known "age-metallicity degeneracy". The latter means that to construct the most plausible combination of SSPs, the code cannot accurately decide between using old and metal-poor stellar populations or, in contrast, young and metal-rich SSP models. This effect becomes more prominent for SSPs with ages older than 1 Gyr (Shen and Yin 2020). Nevertheless, Sánchez-Blázquez et al. (2011) showed that the age-metallicity degeneracy is less prominent in the full spectrum fitting technique compared to the Lick indices approach. This degeneracy may affect the accurate age dating of stellar light fraction peaks in Fig. 5.3.2 (possibly shifting them by 1 to 2 Gyr), but given the uncertainties in the accretion time of the sampled group, we are confident that this issue leaves a marginal effect on our results and conclusions.

5.5   Conclusion and outlook

In this Chapter we investigated the star formation history of our sampled dEs by performing full spectrum fitting. To do so, we employed the STARLIGHT fitting routine over a limited wavelength range of each dE's averaged spectrum. These spectra were constructed from MUSE data of our sampled dEs in Chapter 4. We compared the light-weighted average ages and metallicities from STARLIGHT with those obtained by fitting Lick indices in Chapter 4. We provide average mass-weighted age and [M/H] values, derived with STARLIGHT, in Table 5.3.1.

Based on the STARLIGHT outputs, we constructed light and mass fraction distributions of our sampled dEs and computed the cumulative mass distribution for each dE. The main (preliminary) results of our analysis can be summarized as follow:

- Six out of nine dEs show noticeable peaks in their stellar light and mass fraction distributions between 1 to 4 Gyr. This corresponds to mass growth of 5 to 30 percent during this time interval. VCC 0170 experienced a prominent mass growth as it built more than ~ 60 percent of its total stellar mass within the marked time interval. Enhanced star formation rate due to ram pressure stripping or bow shocks during the pericenter passages or moving in Virgo's high-density regions are some of the possible explanations for this behavior. An alternative interpretation of these observed trends can be the delayed quenching phase that newly accreted satellites experience. Hence, our results may also endorse the predictions of a "delayed-then-rapid" quenching scenario in the low-mass end of cluster satellites' distribution.

- Our results indicate that the star formation in three dEs of our sample (namely VCC0794, VCC1896, and VCC2019) has been quenched before their accretion onto the Virgo cluster. Hence, these three dEs have experienced higher degrees of pre-processing prior to their accretion onto Virgo.

- Two dEs of our sample (namely VCC0990 and VCC2019) show double-peaked distributions in Fig. 5.3.2. The most recent peak is consistent with the presence of a nuclear stellar cluster within the core of these dEs. Our results for these two cases endorse previous findings of Paudel et al. (2010) and Fahrion et al. (2021), indicating that NSC may have prominent effects on the measurements of galaxy's stellar population properties, particularly in low-mass galaxies. Therefore, the interpretation of the results for such cases should be done with caution.

Outlook: Models predict that enhanced star formation activity of an infalling satellite with sufficient gas reservoir and ideal infalling orbital configurations should be prominent in its core and central regions. To test this and as the next step of our investigations, we will radially bin each dEs' MUSE data cube and perform a similar round of measurements (i.e., full-spectrum fitting using STARLIGHT code). This investigation will shed more light on the spatial distribution of star formation enhancements with respect to the accretion event. Moreover, with this set of detailed investigations, we can have better control over galactic substructures (such as NSC). Thus, we can account for their different effects on the star formation history and stellar population properties of their host galaxies.

"What you seek is seeking you."
                        —Mawlana Jalal-al-Din Rumi

6

Newly Discovered Galaxies

This chapter is a partially revised version of Appendix E of Bidaran et al. (2020). "On the accretion of a new group of galaxies onto Virgo: I. Internal kinematics of nine in-falling dEs", published in MNRAS 497, Issue 2, pp.1904-1924

This chapter presents the general properties of two new galaxies (BB1 and BB2) that have been serendipitously detected during the analysis of our original data set.

6.1 Detection of BB1: A new background galaxy in the center of VCC1836

In the projected vicinity of the VCC1836 center, we detected redshifted nebular emission lines. Apart from a bright nucleus, the SDSS images of VCC1836 also show a faint light concentration in the galaxy's central region. Thanks to the high spatial resolution of our data, this detected source is better resolved in the stacked images of the MUSE cube, as shown in the left panel of Fig. 6.1.1 (red box). We extracted the spectrum of this particular region (hereafter BB1) within an aperture with a radius of 5 pixels, corresponding to an area of 3 arcsec^2. We considered the possible light contamination of VCC 1836 by subtracting a spectrum extracted within an aperture of the same size around the detected source. The final spectrum is plotted in the right panel of Fig. 6.1.1. We measured the redshift of this background galaxy using the Doppler shift of each detected nebular emission line. The averaged measured redshift from the detected lines indicates that this galaxy is located at z = 0.5528 ± 0.0002 (Table 6.1.1). We modeled the continuum of this spectrum using pPXF to subtract the emission of the underlying stellar population and measure the flux of the nebular emission lines. Fluxes are reported in the second column of Table 6.1.2.
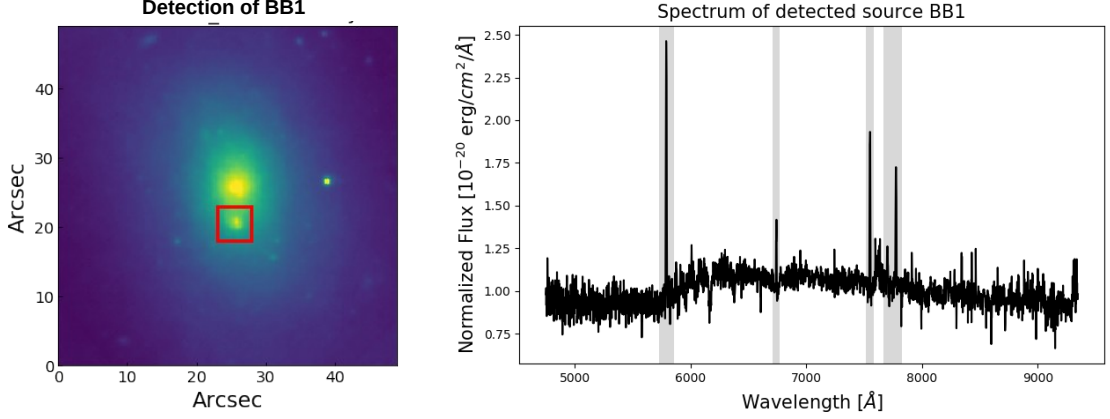
Figure 6.1.1: A source detected in the projected vicinity of VCC1836 central region. *Left panel*: The location of the detected source (BB1) is marked with a red box with a size of 8×8 arcsec^2 on the MUSE stacked image. *Right panel*: The observed spectrum of the detected source, corrected for the underlying emission of VCC1836. The following emission lines are marked from left to right: O[II]λ 3727, Hγ, Hβ, [OIII]λ 4958, [OIII]λ 5007.

Table 6.1.1: New galaxies in the MUSE cubes: BB1 and BB2

Name	RA (J2000)	Dec (J2000)	redshift	total $M_{V,AB}$
BB1	12 40 19.50	+14 43 0.0	0.5528 ± 0.0002	21.32
BB2	12 14 20.50	+14 26 2.0	0.349 ± 0.013	21.50

Columns are: Name of the target, RA, DEC, redshift and total AB magnitude in V band.

6.2 Detection of BB2: A new galaxy in the field of view of VCC0170

Another source with strong emission lines was detected in the MUSE cube of VCC0170 (hereafter BB2). In Fig. 6.2.1 we marked the location of this extended source with a red box. Following a similar strategy, we extracted the spectrum of this source, here within a radius of 7 pixels which corresponds to an area of 6 arcsec^2. The emission of the sky and VCC0170 was removed by subtracting a spectrum extracted within an aperture of the same size near the source. The resulting spectrum is plotted in the right panel of Fig. 6.2.1. We measured the redshift of this source using the nebular emission lines. This background galaxy is at a redshift of $z = 0.349 \pm 0.013$. We modeled its continuum and absorption features using pPXF and subtracted the model from the source spectrum to measure the line fluxes. They are reported in the third

Table 6.1.2: List of optical emission lines and their observed fluxes in BB1 and BB2

Emission Lines	Observed Flux in BB1 $\times 10^{-17}(erg\,s^{-1}cm^{-2})$	Observed Flux in BB2 $\times 10^{-17}(erg\,s^{-1}cm^{-2})$
H_α	–	15.8
H_γ	3.62	–
H_β	7.43	51.5
[OII]	14.7	17.6
[OIII]λ 4959	1.68	1.66
[OIII]λ 5007	5.64	4.86
[NII]λ 6548	0.35	2.33
[NII]λ 6583	1.04	7.08

Figure 6.2.1: Detected background source in the FOV of VCC0170. *Left panel*: The location of the detected source (BB2) is marked with a red box with a size of 8×8 arcsec^2 on the MUSE stacked image. **Right panel**: The observed spectrum of the detected source, corrected for the underlying emission of VCC0170. Marked emission lines from left to right: [OII]λ 3727, Hβ, [OIII]λ 4958, [OIII]λ 5007, Hα, [NII]λ 6548, [NII]λ 6583, [SII]λ 6717 and [SII]λ 6731.

column of Table 6.1.2.

To locate this galaxy on the "Baldwin, Phillips, and Terlevich" (BPT; Fig. 6.2.2) diagram (Baldwin et al. 1981), we corrected the emission line of Hα, [OIII]λ 5007, Hβ and [NII] for intrinsic reddening using the same Balmer decrements as described in Chapters 3 and 4. The emission lines were also corrected for Galactic foreground extinction, using $A_v = 0.089$ mag reported by Schlafly and Finkbeiner (2011) for VCC0170. For both corrections, we used the
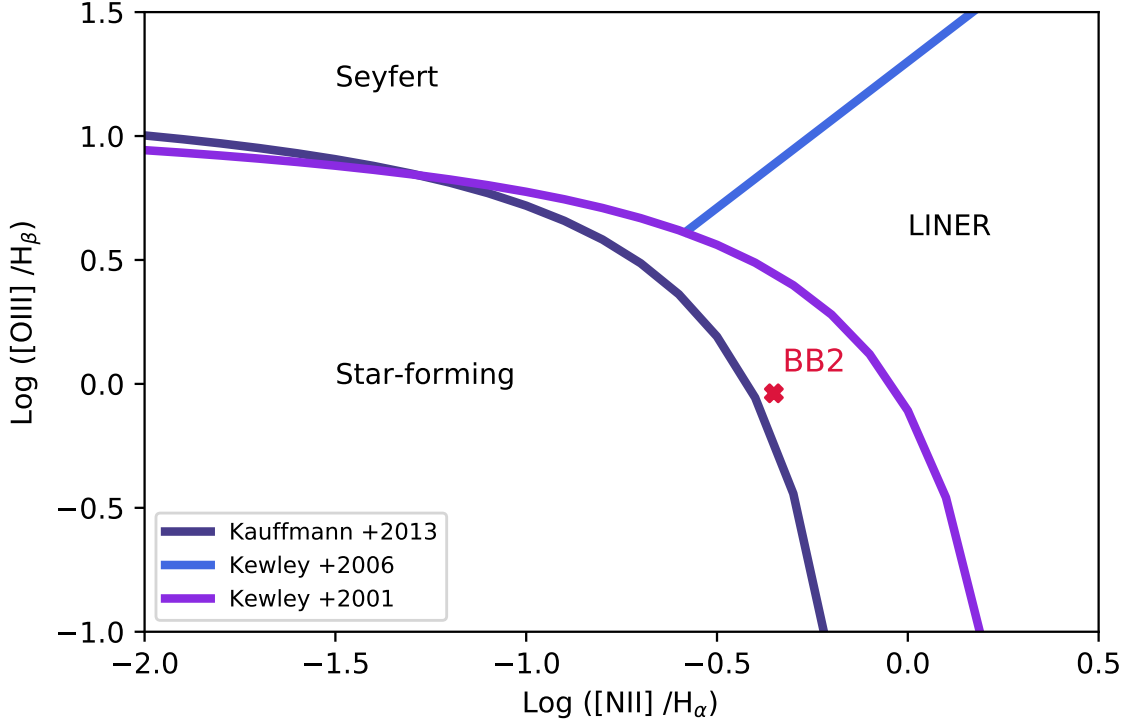
Figure 6.2.2: The BPT diagnostic diagram for BB2. The empirical division of Kauffmann et al. (2003) and the theoretical division of Kewley et al. (2001) between AGN (right side of the diagram) and star-forming (left side of diagram) galaxies are plotted with solid dark blue and purple lines, respectively. The Seyfert-LINER division of Kewley et al. (2006) is also marked with a light blue line.

extinction law of Cardelli et al. (1989). We also corrected the observed flux for redshift dimming following Calvi et al. (2014):

$$I = I_0 \, (1+z)^{-4}$$

Where I and I_0 are the observed and intrinsic surface brightness. We measured log [[OIII] λ 5007/Hβ] = -0.038 and log [[NII] λ 6583/Hα] = -0.351. The location of BB2 on the BPT diagram is presented in Fig. 6.2.2. According to this plot, the detected galaxy is located between the Kauffmann et al. (2003)'s empirical division and the Kewley et al. (2001)'s theoretical division, which separate AGNs and star-forming galaxies. Galaxies falling within this zone, including our detected galaxy, are regarded as composite (AGN/SF) galaxies. We used the measured redshift (z) to estimate its co-moving radial distance, which turns out to be $\approx$ 1376.8 Mpc[1]. Using this value and following the method of Calzetti et al. (2007), we measured the star formation rate of this background galaxy to be $\sim$ 0.66 M$_\odot$ yr^{-1}.

Further analysis of the gas emission lines present in the spectrum of this galaxy shows that the Hα, [SII], and [NII] lines are split (Fig. 6.2.3). This can likely be due to the rotation of

---

[1]considering H$_0$=70(km/s)/Mpc, Ω_M = 0.286, and Ω_{vac} = 0.714
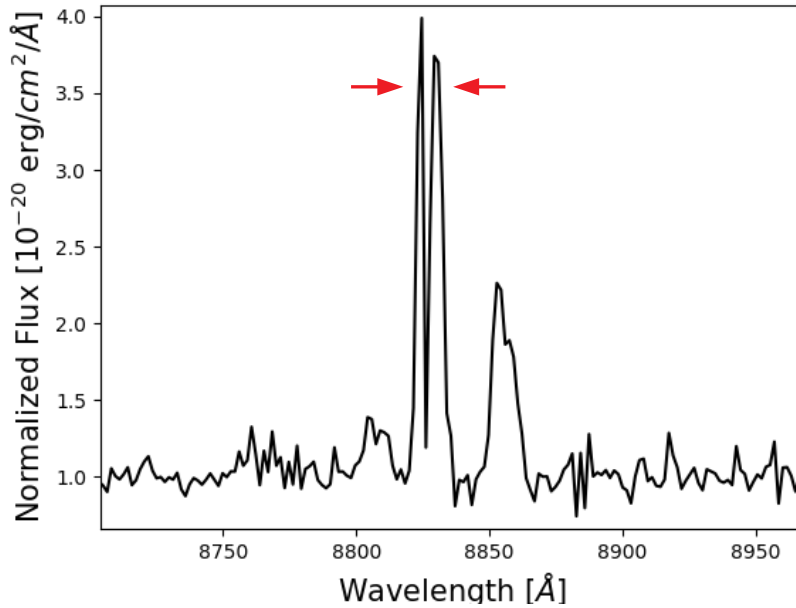
Figure 6.2.3: Split Hα and [NII] 6584 emission lines in the red part of the spectrum of BB2. This split corresponds to a rotation velocity of 90 ± 10 km s^{-1}.

BB2. We used the split in the lines and measured the rotation of this galaxy to be of the order of $\approx 90 \pm 10$ km s^{-1}.

6.3 Conclusion

In this chapter we introduced two galaxies (BB1 and BB2) that we discovered during the analysis of our MUSE data set. BB1 was detected initially as a flux over-density in the projected vicinity of VCC1836's core. Thanks to the high spatial and spectral resolution of MUSE, we could investigate the properties of this background galaxy in more detail and could derive its general properties (such as its redshift and a number of optical emission lines). BB2 has been detected as an extended light source in the projected vicinity of VCC0170, and thanks to MUSE power, we could derive the star formation rate of this background galaxy along with its other general properties. These two examples indicate the high sensitivity of MUSE in resolving low surface brightness substructures (even in low-mass galaxies) and its striking possibilities in-detailed analysis of galaxies at higher redshifts.

"I've reached the end of this great history, And all the land will talk of me: I shall not die, these seeds I've sown will save My name and reputation from the grave, And men of sense and wisdom will proclaim When I have gone, my praises and my fame."

—Ferdowsi, "Shahnameh: The Persian Book of Kings"

7

Thesis conclusion and future perspectives

Early-type dwarf galaxies (dEs) shape a large yet diverse galaxy population in galaxy groups and clusters. DEs are numerous, and thanks to their shallow potential, they can be informative testbeds for us to better understand the role of the environment in galaxy evolution. Nonetheless, the diverse properties of dEs are ambiguous in the sense that they can be explained by different galaxy formation channels. One well-reputed scenario suggests dEs as remnants of late-type star-forming galaxies that have been transformed by environmental effects inside galaxy clusters or groups [1]. Several studies have focused on this scenario and could pinpoint those galaxy properties that are altered due to different environmental mechanisms. Yet, details of such environmental-induced transformations are not clear to us. For instance, to what extent has the environment of massive clusters or groups changed the properties of present-day dEs' progenitors? Answering this question is not trivial, as, with our commonly used diagnostic approaches and observation facilities, we can not accurately distinguish different origins (i.e., different formation channels mentioned in Chapter 1) of observed dEs. For instance, discriminating between dEs that has been born inside galaxy clusters and those that have been accreted to the cluster during later stages, particularly in the core of clusters, is not straightforward. Furthermore, pre-processing of infalling satellites is a crucial factor that is often underestimated or even completely neglected in ongoing studies, mainly due to its complex detection and challenges that it introduces in the interpretation of the results. In an attempt to find missing critical pieces of this incomplete puzzle, we summarized the main objectives of this thesis as follow (repeated from Chapter 1):

- How would cluster environment affect its infalling satellites during their early stages of accretion?
- How relevant is pre-processing in the present-day properties of cluster early-type galaxies?

---

[1]The other well-known scenario suggests dEs as primordial structures formed in the early Universe.

- For a typical dwarf galaxy observed today, which one matters the most: their birth site (nature) or their environment in later stages (nurture)?

In this thesis, we tried to address these questions by investigating a sample of nine Virgo dEs that, according to Lisker et al. (2018), have been accreted onto this dynamically young galaxy cluster, likely as gravitationally bound members of a massive galaxy group, about 2-3 Gyr ago (for more detail check Chapter 2). In this thesis, we took advantage of high-resolution MUSE data sets, combined with state-of-the-art techniques (such as full-spectrum fitting) and time-sensitive diagnostic tools (such as projected phase-space diagram) to investigate possible imprints of pre-processing on the present-day properties of these dEs. Furthermore, we focused on the prominent environmental effects of the Virgo cluster on these dEs, which have taken place mainly at the early stages of their infall. In the following, we summarize the key results of each chapter presented in this thesis and outline the directions of our future work.

7.1   Summary

Kinematics of our sample dEs have been investigated in Chapter 3. To do so, we performed full-spectrum fitting (through the pPXF routine) over spatially binned MUSE data of our dEs. We drew kinematic maps of each dE (i.e., their stellar rotational velocities and velocity dispersions) and further quantified the stellar rotation of these systems through the specific angular momentum (λ_R). In spite of their similar stellar mass range and average infall time onto the Virgo cluster, we detected a spread in measured λ_R profiles that we interpreted as footprints of pre-processing of these low-mass systems in their parent group. Dynamical transformation of low-mass galaxies likely occurs after their longer exposures to high-density environments (i.e., several pericenter passages). Hence, recently accreted cluster dEs do not fulfill this criterion. In Chapter 3, we concluded that dEs with low λ_R profiles, comparable to those cluster dEs with somewhat larger infall times, have been accreted onto Virgo with higher degrees of pre-processing. In contrast, those dEs with higher λ_R profiles, comparable to the field star-forming low-mass galaxies, have been accreted onto Virgo possibly as low-mass late-type members of their parent group, having experienced less significant pre-processing. The observed spread in the λ_R profiles of our sample dEs may also be due to their different intrinsic kinematics. Based on our observations in Chapter 3, we could not discard the latter hypothesis.

Stellar populations of our sample dEs have been investigated in Chapter 4. In this chapter, we performed a four-step Lick index fitting procedure (based on a least χ^2 approach) over diagnostic absorption features (namely Hβ_0, Mgb, Fe5270, and Fe5335) that are present in the wavelength range delivered by our dEs' MUSE data. Based on the results of this fitting procedure, we constructed age, [M/H], and [α/Fe] maps of our sample dEs. The majority of our sample exhibit metallicity gradients with negative slopes, in the sense that a relatively more metal-rich stellar population is confined in the central parts of these dEs. Gradients are also detected in the age and [α/Fe] maps of some of our sample members. On average, our dEs are younger, metal-poorer, and significantly α-enhanced systems compared to equally massive dEs of Virgo, Fornax, and Coma clusters. However, we did not detect any distinct difference in terms of stellar population gradients between our sampled members and other cluster dEs. In Chapter

4, we showed that compared to more massive ETGs, dEs have steeper positive [α/Fe] gradients, flat age gradients, and less steep negative [M/H] gradients. While part of our sampled members exhibits young stellar populations (i.e., age <4 Gyr with a median error of 1.5 Gyr), others contain older stellar populations that, given their infall time onto Virgo, have been formed likely prior to their infall. Despite their recent accretion, all of our sampled dEs exhibit noticeably high values of [α/Fe] values that are only observed in the core of the Coma cluster and for those dEs with larger infall times (hence longer exposure times) to high-density environments. These results, we believe, further endorse the pre-processed nature of our sample.

Star formation history of our sample dEs has been investigated in Chapter 5. In this chapter, we employed the full-spectrum fitting technique (using the STARLIGHT routine) over the averaged MUSE spectrum of each sample dE. In this approach, we simultaneously account for the possible contribution of several single stellar population (SSP) models with different ages and metallicities to the total observed flux. Therefore, we managed to construct light- and mass-fraction distributions as a function of each dE's age. According to these (preliminary) results, six dEs of our sample show a noticeable peak in their light fraction distributions at about 1 to 4 Gyr ago, corresponding to 5 to 70 percent mass growth in these systems during this time interval. These epochs are consistent with or even more recent than our sampled dEs' accretion time onto the Virgo cluster. For the other three dEs, the peak is shifted to older ages. In this chapter, we argued that the recent enhanced star formation activity in some of our sample dEs is likely induced by ram pressure stripping and bow shocks or thermal instabilities, inside the Virgo cluster and at the early stages of their infall. Given their similar range of stellar mass and infall time to Virgo, the absence of such a peak for three members of our sample endorses their pre-processed nature.

Last but not least, in Chapter 6 of this thesis, we introduced two new background galaxies that were detected during the analysis of our MUSE cubes. Their detection emphasizes the high spatial and spectral resolution of the MUSE instrument and its high sensitivity for the analysis of galaxies' low surface brightness substructures.

7.2   Future perspectives

In this section, we outline the future perspectives and our research directions related to this work.

Dynamical modeling of dwarf galaxies: As mentioned in Chapter 1, stars that are formed at different stages of a given galaxy's evolution exhibit different orbital properties within the system. For instance, stars on non-circular orbits (known as hot orbits) are believed to be formed at later stages of galaxy formation, mainly from its unsettled gas. On the other hand, stars on circular orbits (known as cold orbits) are believed to be born in quiescent environments. Hence, the dynamical configuration of any given galaxy can provide valuable information on possible long-term environmentally induced perturbations (e.g., tidal interactions). This information can also shed light on the dark matter distribution and the shape of the system's potential well. The MUSE data of our sample provides a unique opportunity for such investigations on galaxies as low-mass as dEs. On the left panel of Fig.7.2.1 we show the VCC2019 MUSE image that

The (preliminary) detected PNe system in VCC2019
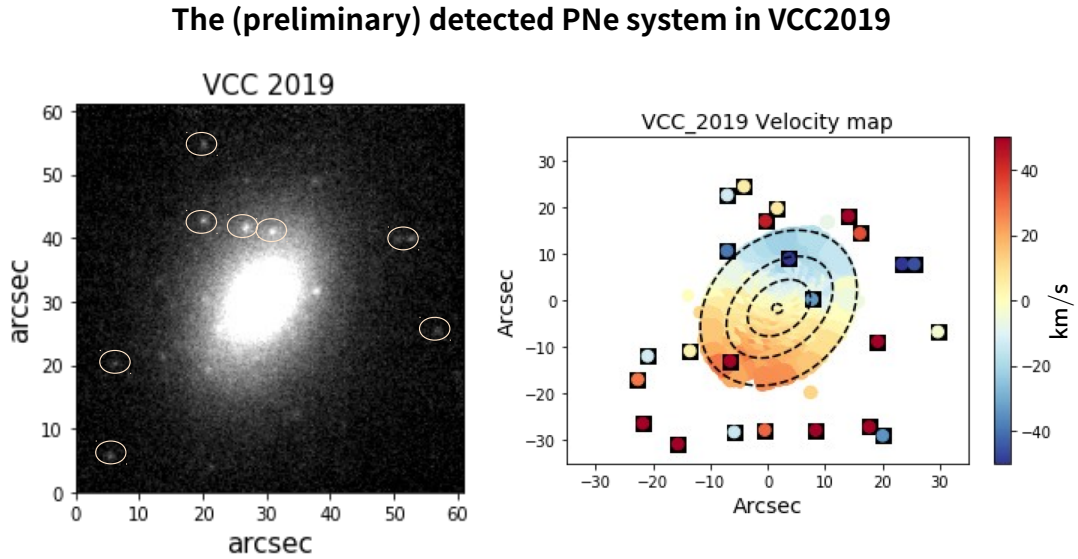
Figure 7.2.1: On the left panel, we present the MUSE image of VCC2019 that is constructed by stacking the observed data around the characteristic [OIII]λ 5007 emission line. Marked point sources are some of the detected PNe in VCC2019. On the right panel, we show the stellar rotation velocity map of VCC2019, which is a repetition of Fig. 3.3.2 in Chapter 3. Color-coded squares on this map denote the velocity of these preliminary detected PNe in VCC2019.

is stacked around the characteristic [OIII]λ 5007 emission line. Point sources that are marked in this panel are this dE's confirmed gravitationally bound planetary nebulae (PNe). On the right panel of this figure, we present a stellar rotation map of this particular dE. In the same panel, we color-coded (preliminary) detected PNe based on their measured velocities. The latter is derived by accounting for the Doppler shift of the [OIII]λ 5007 emission line for each confirmed PNe point source. To perform dynamical modeling on this dE, we will utilize the velocity and radial distributions of PNe, as well as globular clusters, in combination with the kinematic structure of the system (as derived in Chapter 3). We will employ the Schwarzschild orbital-superposition method (Schwarzschild 1979) to investigate the dark matter distribution and the dynamical structure of the galaxy. A similar approach will be employed for the rest of our sample members.

stellar populations of dEs' substructures: Galaxies are complicated structures that feature different substructures with different properties. As we discussed in Chapter 1, different stellar populations, kinematics, color, or surface brightness profiles are expected for different substructures of a given galaxy. Recently, decomposition of bulges and discs of the S0 galaxies in the CALIFA survey showed that discs of low-mass S0s are relatively less metal-rich than their bulges (Pak et al. 2021). These results also suggest a more complicated star formation history in discs of S0 galaxies. Thanks to the high-quality of our MUSE data, we can isolate substructures through spatial decomposition of the MUSE images and derive their kinematic

Possible spiral arms in VCC2019
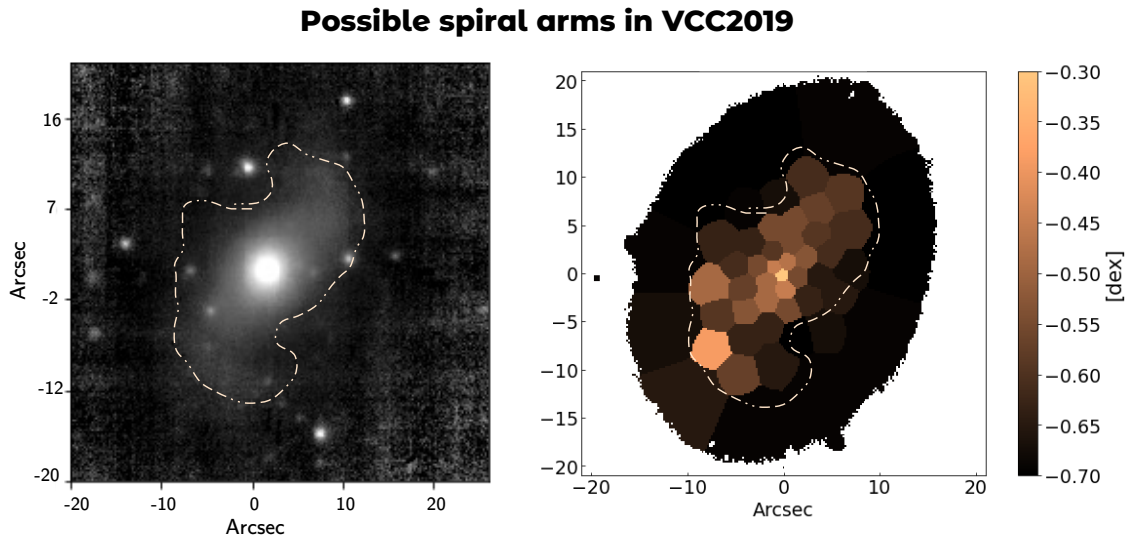
Figure 7.2.2: The metallicity map of faint disk and possible spiral arms in VCC2019. On the left panel, we show the unsharp mask of the staked MUSE image of VCC2019. On the right panel, we show the metallicity map of this particular dE. On both panels, the dashed line marks the spatial region of the galaxy where [M/H] > -0.6 dex. The unsharp mask was kindly provided by Josefina Michea.

and stellar population properties via analysis already described in Chapters 3, 4 and 5. A very preliminary yet promising example of this analytical approach is shown in Fig. 7.2.2. On the left panel of Fig. 7.2.2 we present the unsharp mask of the stacked MUSE image of VCC2019. The unsharp mask is provided by Josefina Michea (private communication). To perform the unsharp masking, a Gaussian kernel has been used that mimics the ellipticity and position angle of VCC2019, reported in Table 3.3.1 of Chapter 3. The size of the Gaussian kernel is $7 \times$ FWHM$_{PSF}$ (which is 1.6 arcsec). On the right panel of this figure, we show the metallicity map of VCC2019, which is a repetition of Fig. 4.3.9 in Chapter 4. The dashed line marks those spatial regions of the galaxy where [M/H] is more than $\sim$ -0.6 dex. These regions of a rather high metallicity are consistent with the spatial position of VCC2019's faint disk and possible spiral arms.

Stellar population gradients of low-mass galaxies in different environments: The number of studies focused on the stellar population gradients of low-mass galaxies (including dEs) is limited. Those studies which have investigated this mass range also suffer from observation constraints and limited spatial coverage of the galaxy body. Nevertheless, to gain a better perception of the role of different environments and the conditions of their birth site in shaping stellar populations of low-mass galaxies, we need to investigate statistically rich samples of dEs in different environments. In Chapter 4 we mentioned limitations for comparing our stellar population gradients results with those available in the literature, including possible systematic biases due to different approaches taken for retrieving stellar population properties. To compensate

for this effect, we can take advantage of publicly available IFU data for low-mass galaxies (including dEs) in different environments, such as Virgo and Fornax clusters, and fields to perform a robust and systematic analysis. Furthermore, surveys such as the CALIFA and the ATLAS3D can provide adequate data points for more massive galaxies in this comparison. Additionally, we can derive element abundances (such as C, N, O, Fe, and Mg) from MUSE data and other available IFU data sets and construct their maps to investigate the abundances spatial variation in galaxies (e.g., on this topic Greene et al. 2013, 2019; La Barbera et al. 2021). We can employ this information for deriving the initial mass function slope of dEs and investigate their radial gradients (e.g., on this topic La Barbera et al. 2021). In this manner, we can better evaluate the dependence of the stellar properties gradients on galaxy velocity dispersion and stellar mass as a way to better understand how galaxies form.

<div align="right">

8

</div>

<div align="right">

Appendix

</div>

This chapter contains appendixes to Chapters 3 and 4. Additionally, we provide stellar mass estimates based on three different approaches for our sample of dEs.

8.1 Appendix to Chapter 3

In Fig. 8.1.1, 8.1.2, and 8.1.3 we provide error maps of stellar rotation velocity and velocity dispersion for each dE. Errors are measured through Monte Carlo simulations, as described in Section 3.2 of Chapter 3.

8.2 Appendix to Chapter 4

In Fig. 8.2.1 and 8.2.2 we provide error maps of three measured indices (namely Hβ, Mgb, and Fe5015) are presented for each dE. Errors are measured through Monte Carlo simulations, as described in Section 4.3.2 of Chapter 4.

The error maps of stellar age, [M/H] and [α/Fe] values are presented in Fig. 8.2.3 and 8.2.4. Errors are measured through Monte Carlo simulations, as described in Section 4.3.3 of Chapter 4.

In Table 8.2.1 and 8.2.2 we report indices gradients (i.e., slopes and intercepts) for each dE. Similar to what is described in Section 4.4.4 of Chapter 4, we have measured slopes and intercepts of indices gradients by employing the public LINMIX routine and by accounting for the measured errors of each indices. Errors of intercepts and slopes reported in this table are the standard deviation of 1000 MC iterations performed by LINMIX as part of its fitting procedure.

Table 8.2.1: Gradients of measured indices

Object	Hβ_{Re} [Å]	∇Hβ [Å]/[log(R/Re)]	H$\beta_{0,\mathrm{Re}}$ [Å]	∇Hβ_0 [Å]/[log(R/Re)]	Mgb$_{\mathrm{Re}}$ [Å]	∇Mgb [Å]/[log(R/Re)]
VCC0170	2.29 ± 0.12	-1.35 ± 0.20	2.88 ± 0.15	-2.03 ± 0.25	1.83 ± 0.06	0.28 ± 0.09
VCC0407	2.69 ± 0.03	0.03 ± 0.06	3.59 ± 0.03	-0.06 ± 0.07	1.61 ± 0.03	-0.54 ± 0.08
VCC0608	2.78 ± 0.03	0.03 ± 0.06	3.77 ± 0.04	0.04 ± 0.08	1.74 ± 0.04	-0.21 ± 0.07
VCC0794	1.92 ± 0.08	-0.19 ± 0.11	2.56 ± 0.09	-0.30 ± 0.12	1.31 ± 0.16	-0.56 ± 0.21
VCC0990	2.12 ± 0.12	-0.41 ± 0.08	2.97 ± 0.17	-0.82±0.12	2.05 ± 0.20	-0.37 ± 0.08
VCC1833	3.47 ± 0.07	0.95 ± 0.24	4.94 ± 0.09	1.58 ± 0.31	2.20 ± 0.05	-0.34 ± 0.16
VCC1836	2.96 ± 0.08	0.17 ± 0.12	3.55 ± 0.09	-0.23 ± 0.11	1.40 ± 0.05	-0.21 ± 0.07
VCC1896	2.09 ± 0.04	-0.18 ± 0.09	2.86 ± 0.05	-0.49 ± 0.12	2.03 ± 0.04	-0.27 ± 0.11
VCC2019	2.17 ± 0.06	-0.21 ± 0.13	2.28 ± 0.1	-1.20 ± 0.19	2.06 ± 0.06	-0.18 ± 0.13

olumns are: Name of the target, Hβ at 1Re, the slope of Hβ gradient, Hβ_0 at 1Re, the slope of Hβ_0 gradient, Mgb at 1Re, the slope of Mgb gradient.

Table 8.2.2: Gradients of measured indices

Object	Fe5015$_{\mathrm{Re}}$ [Å]	∇Fe5015 [Å]/[log(R/Re)]	Fe5270$_{\mathrm{Re}}$ [Å]	∇Fe5270 [Å]/[log(R/Re)]	Fe5335$_{\mathrm{Re}}$ [Å]	∇Fe5335 [Å]/[log(R/Re)]
VCC0170	2.82 ± 0.14	0.00 ± 0.22	1.82 ± 0.07	0.12 ± 0.11	1.72 ± 0.09	0.27 ± 0.13
VCC0407	3.19 ± 0.07	-0.74 ± 0.15	1.87 ± 0.03	-0.28 ± 0.07	1.65 ± 0.04	-0.34 ± 0.09
VCC0608	3.20 ± 0.06	-0.59 ± 0.11	1.68 ± 0.03	-0.41 ± 0.06	1.40 ± 0.05	-0.53 ± 0.08
VCC0794	1.65 ± 0.35	-1.19 ± 0.47	1.42 ± 0.14	-0.33 ± 0.18	1.23 ± 0.17	-0.30 ± 0.20
VCC0990	3.50 ± 0.20	-1.22 ±0.17	1.92 ± 0.12	-0.65 ± 0.09	1.77 ± 0.09	-0.42 ± 0.09
VCC1833	4.03 ± 0.10	-0.25 ± 0.32	2.08 ± 0.05	-0.32 ± 0.17	1.74 ± 0.06	-0.39 ± 0.21
VCC1836	2.42 ± 0.20	-0.82 ± 0.28	1.51 ± 0.08	-0.28 ± 0.11	1.29 ± 0.09	-0.31 ± 0.13
VCC1896	3.23 ± 0.10	-0.61 ± 0.29	1.83 ± 0.05	-0.37 ± 0.14	2.01 ± 0.06	0.24 ± 0.17
VCC2019	3.16 ± 0.13	-0.76 ± 0.25	1.70 ± 0.05	-0.62 ± 0.10	1.55 ±0.11	-0.46 ± 0.22

olumns are: Name of the target, Fe5015 at 1Re, the slope of Fe5015 gradient, Fe5270 at 1Re, slope of Fe5270 gradient, Fe5335 at 1Re, and slope of Fe5335 gradient.

Table 8.3.1: Stellar mass estimates for our sample dEs

Object	$\log(\mathrm{M}_{color}$ [M$_\odot$])	$\log(\mathrm{M}_{vir}$ [M$_\odot$])	$\log(\mathrm{M}_{pop}$ [M$_\odot$])
VCC 0170	9.14	7.43	8.64
VCC 0407	9.06	7.35	8.85
VCC 0608	9.14	7.27	8.87
VCC 0794	9.02	7.67	9.00
VCC 0990	9.10	7.19	8.97
VCC 1833	9.09	7.07	8.60
VCC 1836	9.06	7.86	8.60
VCC 1896	8.94	7.10	8.91
VCC 2019	9.16	7.32	9.16

olumns are: Name of the target, stellar mass estimates based on the g-r color, virial masses, and stellar mass estimates based on the stellar population properties of each dE.

8.3   Stellar mass estimates for our sample of dEs

In Table 8.3.1 we present three stellar mass estimates for our sampled dEs. These are simplified estimates based on the color (M$_{color}$), velocity dispersion (M$_{vir}$), and stellar populations (M$_{pop}$) retrieved from the integrated light of dEs.

In the second column of Table 8.3.1, we estimate the stellar mass of our sample dEs based on the color-to-(M/L) conversion (M and L denote mass and light of the system, respectively) introduced by Bell et al. (2003). For this purpose we have used the absolute magnitude and (g-r) colours (reported in Table 2.1.1 of Chapter 2) using a distance modulus of m-M = 31.09 mag.

In the third column, we estimated the dynamical mass of each dE (M$_{vir}$), following Cappellari et al. (2006):

$$M_{vir} = c \times \sigma_e^2 \times R_e/G \qquad (8.1)$$

Where σ_e is the velocity dispersion of dEs within their effective radius (in Table 3.3.1) and R_e is the effective radius of dEs taken from Table 2.1.1. C is a scaling factor and is set to 5.0 for low-mass early-type galaxies, based on the results of Ryś et al. (2014).

In the fourth column of Table 8.3.1, we estimate the stellar mass of our sample dEs based on the stellar population properties (M$_{pop}$) measured for their averaged spectra in Table 4.3.3 of Chapter 4. To do so, we have taken the (M/L)$_R$ estimate of MILES library into account and used the M$_r$ values reported in Table 2.1.1.
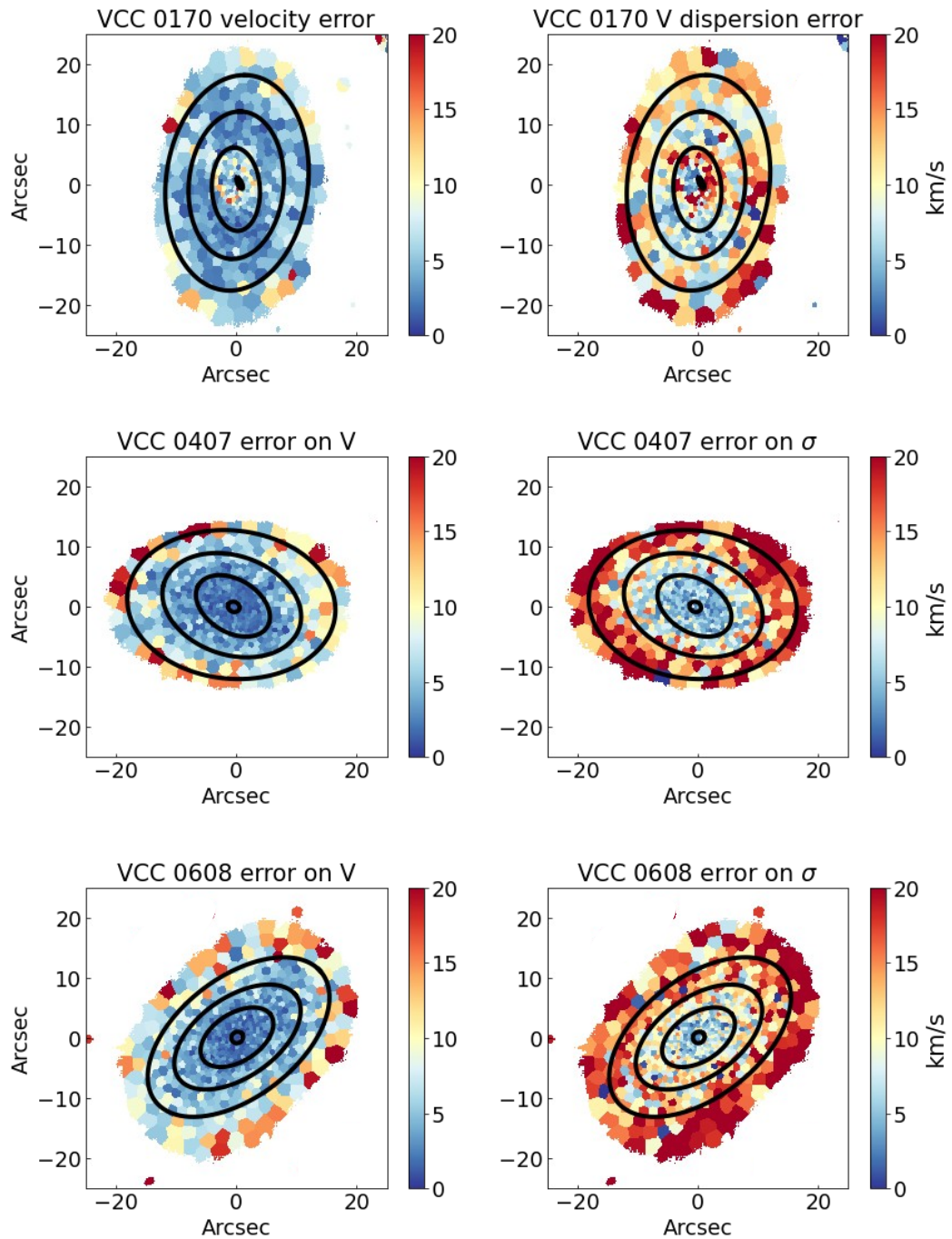
Figure 8.1.1: Error maps of velocity and velocity dispersion for our sample of dEs. For a better comparison, the isophotes from Fig. 3.3.1 of Chapter 3 are repeated in all the panels here.
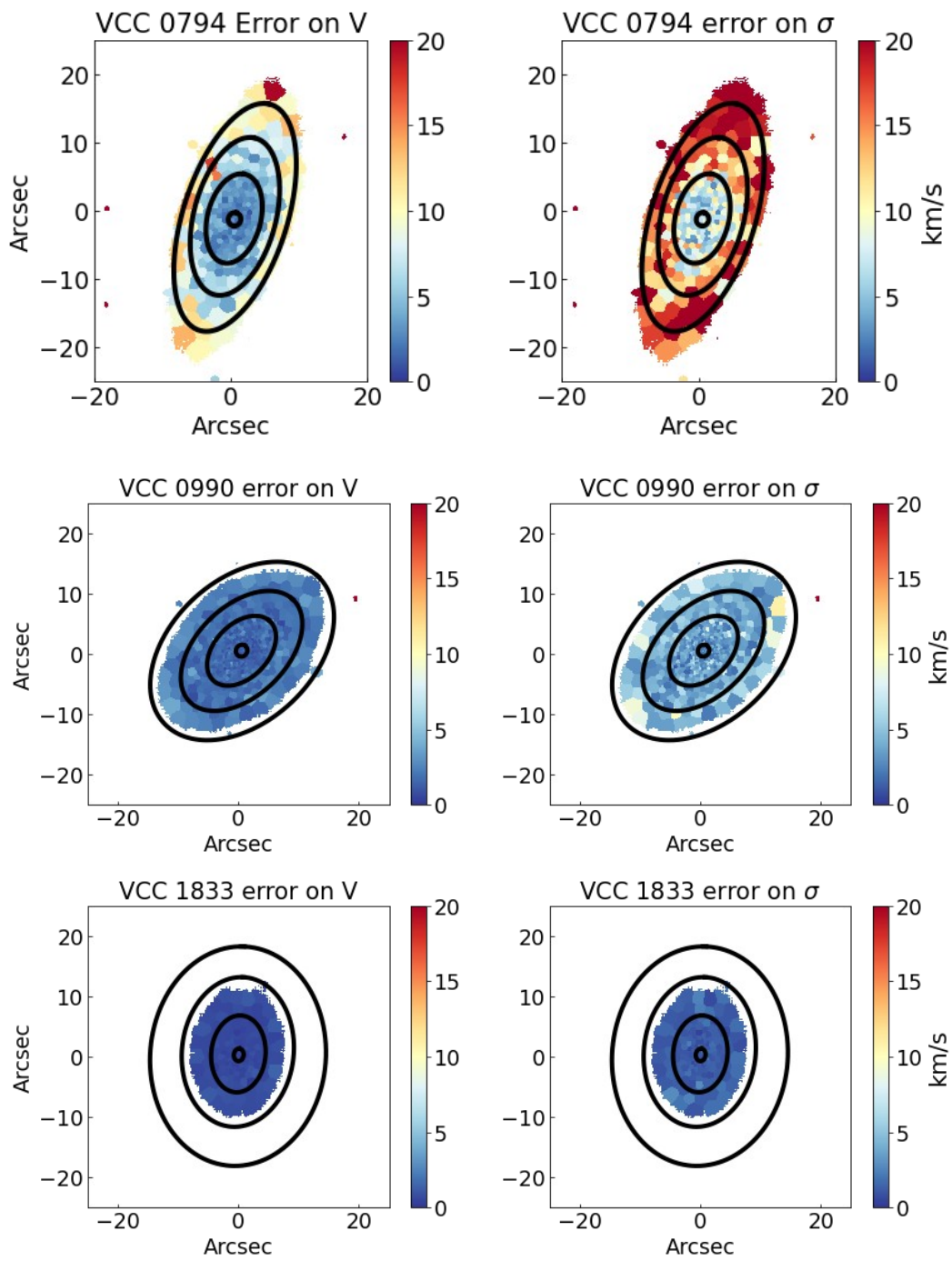
Figure 8.1.2: Continued.
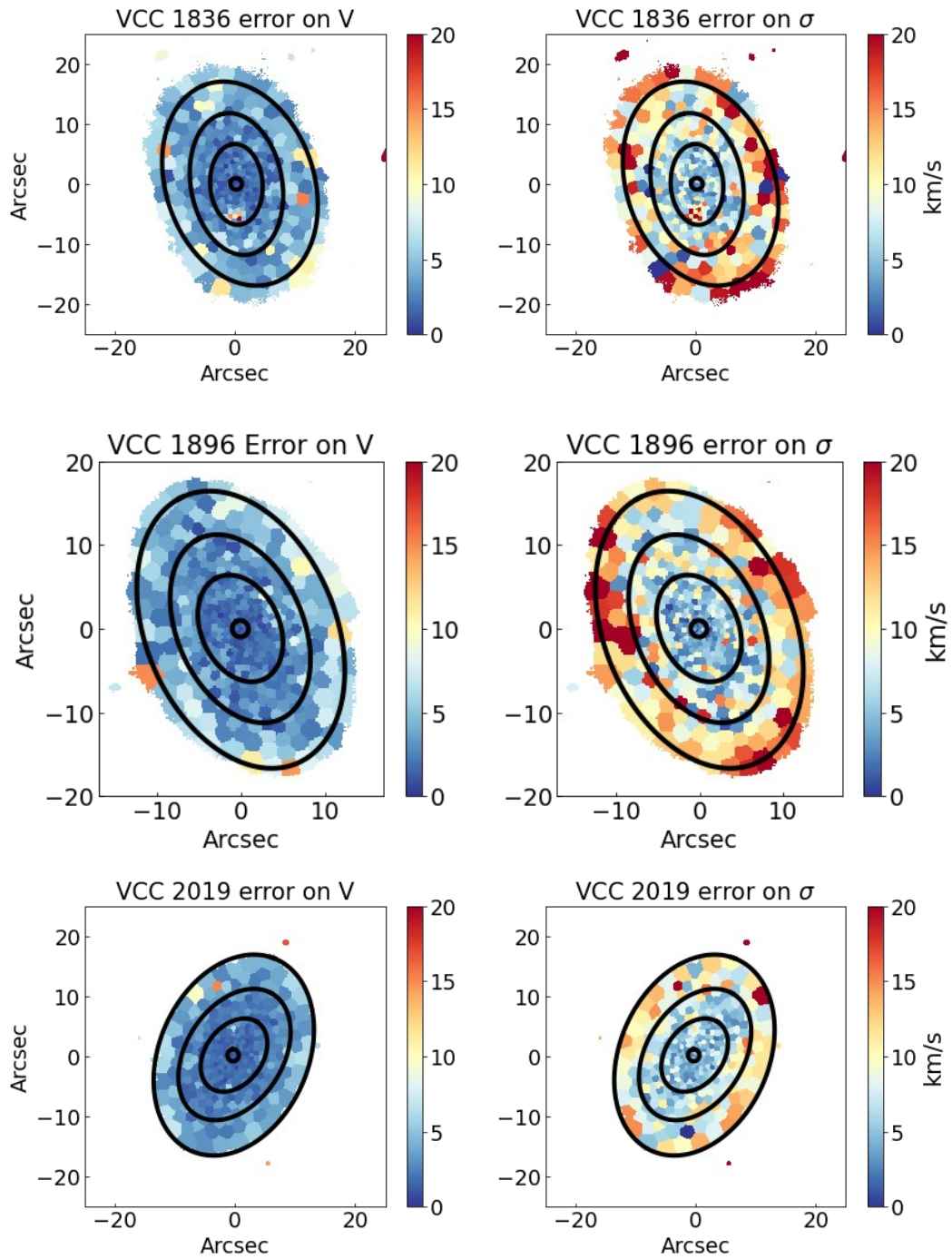
Figure 8.1.3: Continued.
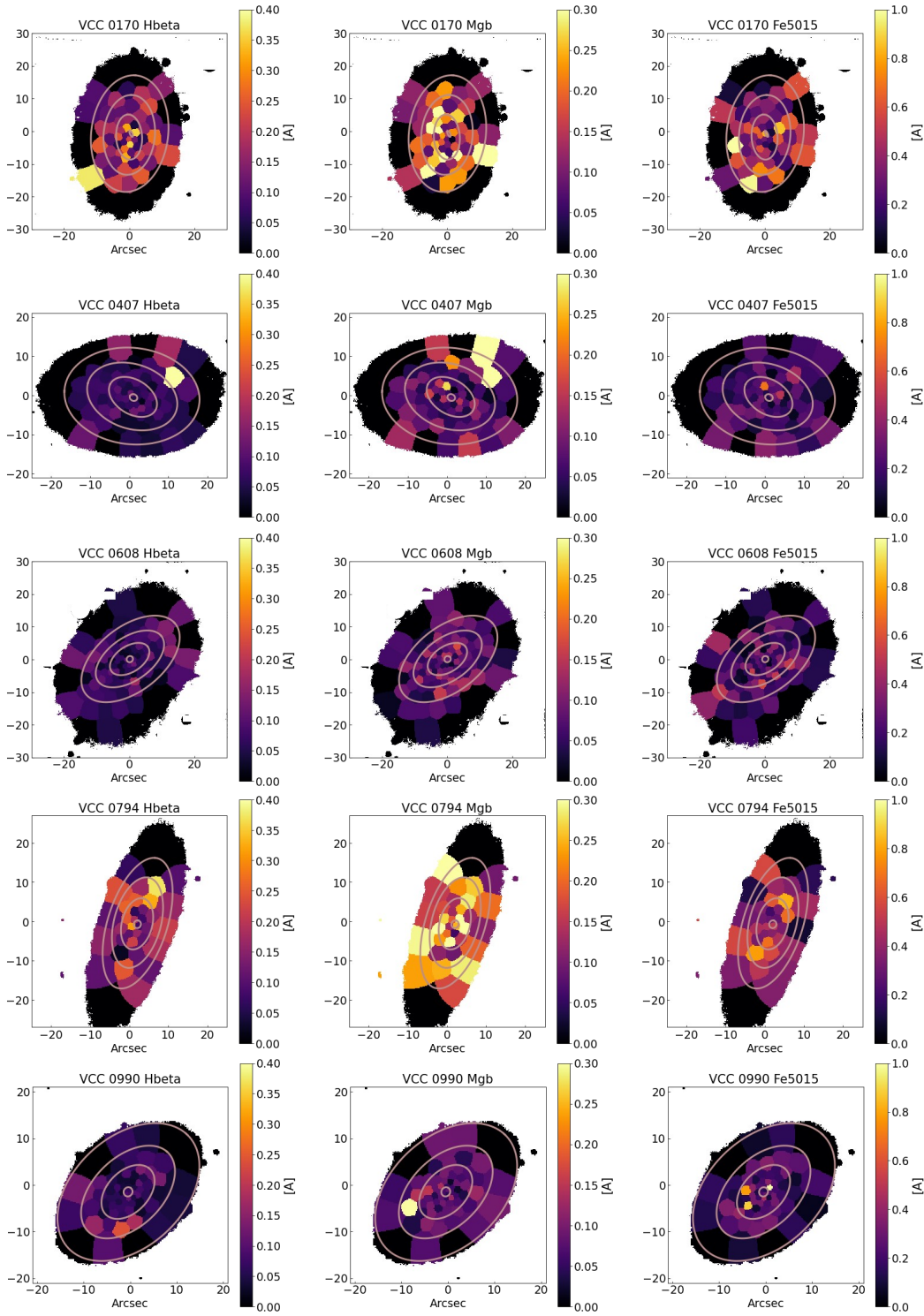
Figure 8.2.1: Error maps of Hβ, Mgb, and Fe5015 indices for our sample of dEs. For a better comparison, the isophotes from Fig. 3.3.1 of Chapter 3 are repeated in all the panels here.
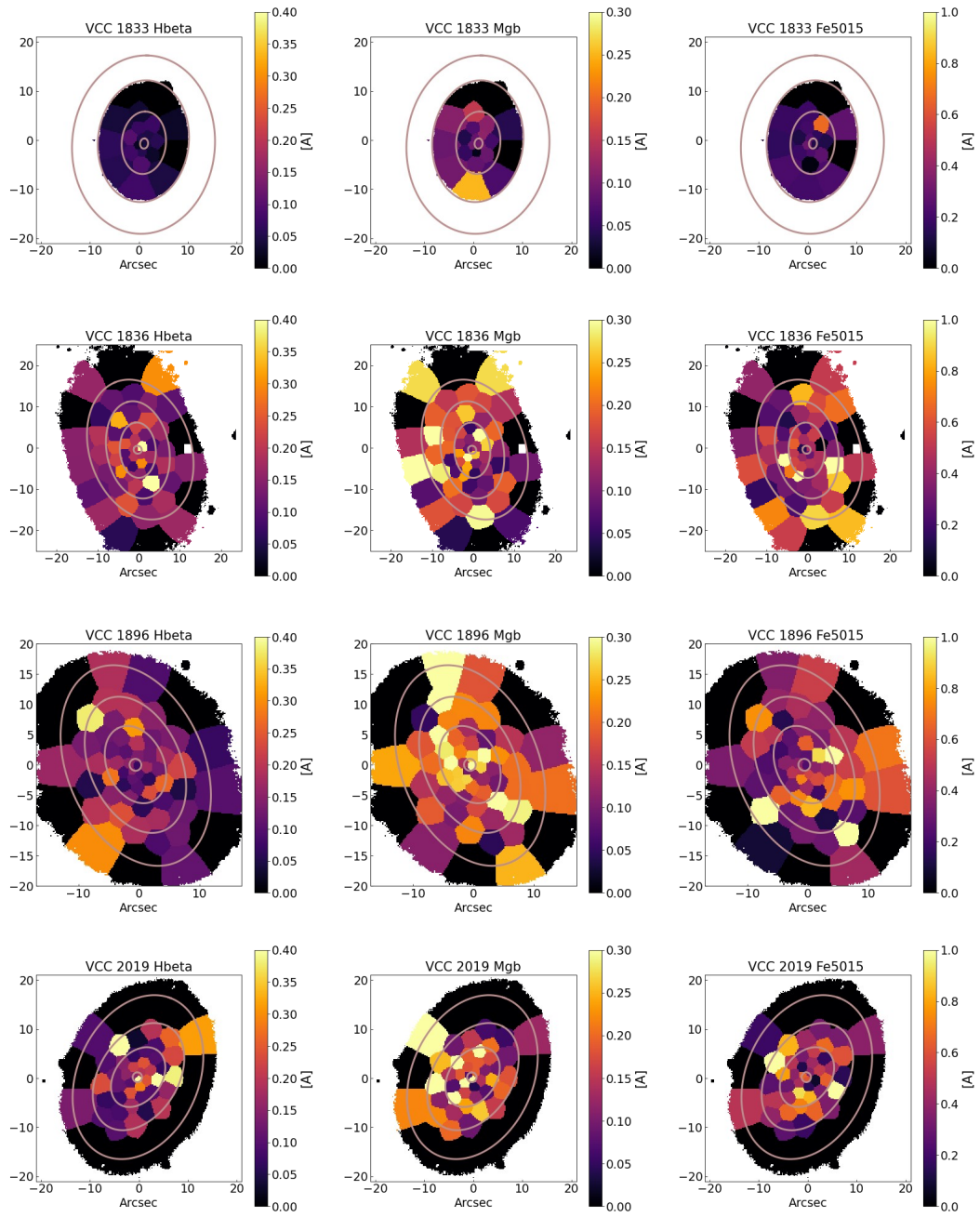
Figure 8.2.2: Continued.
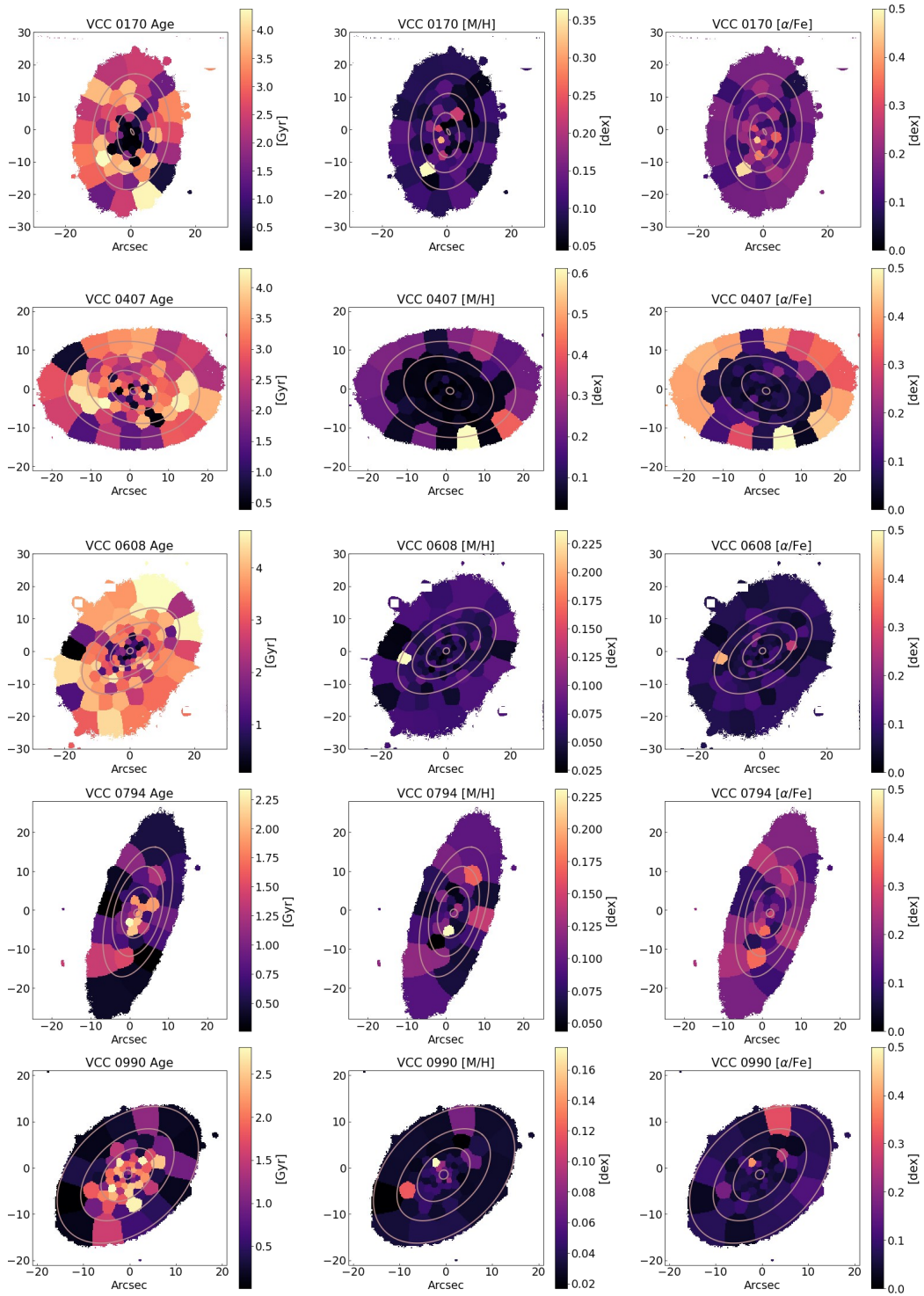
Figure 8.2.3: Error maps of age, [M/H] and [α/Fe] for our sample of dEs. For a better comparison, the isophotes from Fig. 3.3.1 of Chapter 3 are repeated in all the panels here.
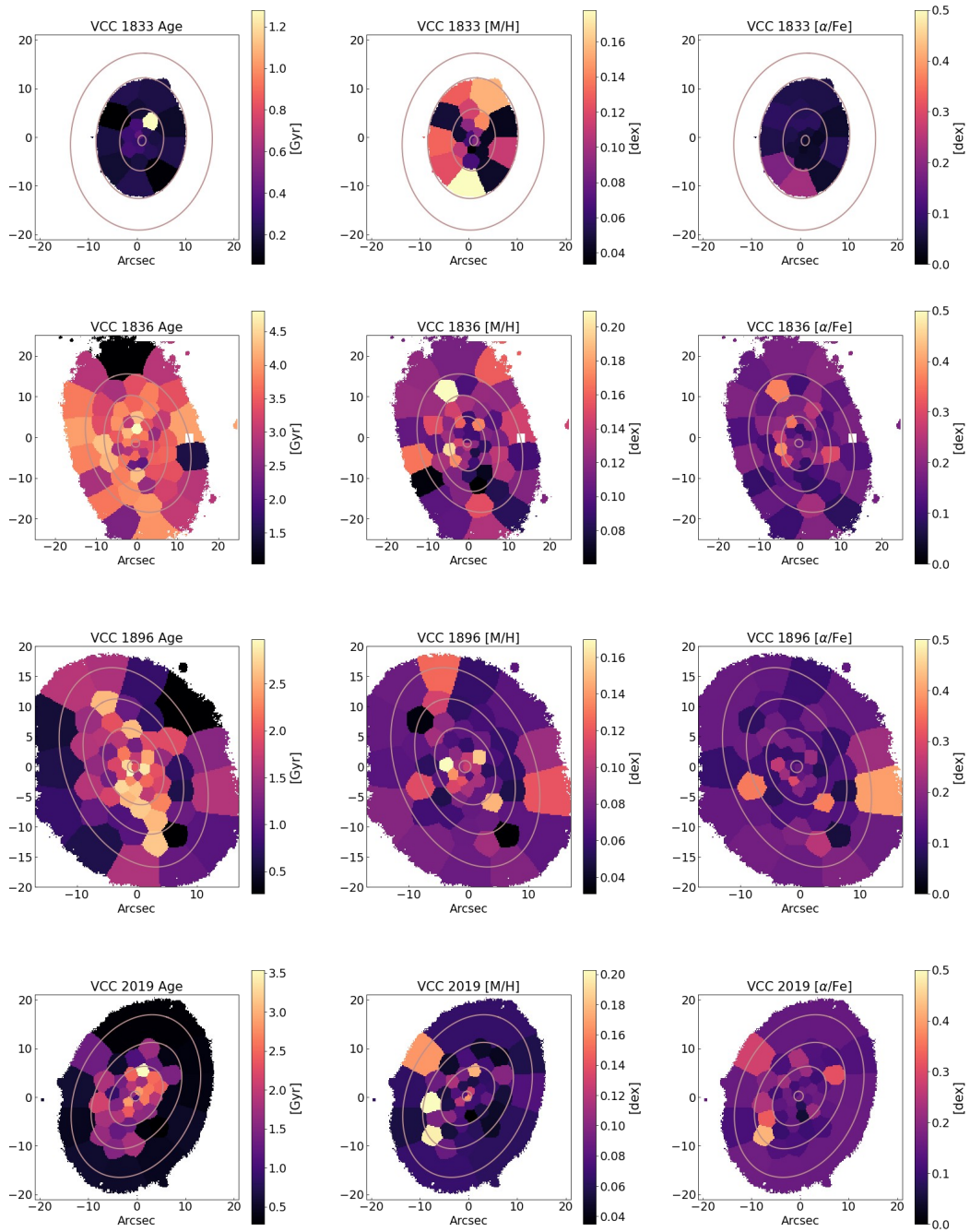
Figure 8.2.4: Continued.

Acknowledgments

Four years ago, I started my PhD in a new continent, a new country, a new education system, and a new topic. This journey was filled with challenges, scary moments, achievements, excitements, regrets, happiness, friendships, satisfaction, and growth. However, I was not alone through this adventure, and I was privileged to have amazing people in my life, such as my supervisors, colleagues, mentors, friends, family, and even strangers, who have held my hand and helped me to make my dream come true. I would like to dedicate the last notes of my thesis to these people.

I would like to thank my amazing supervisors for the constant support, time, and effort they dedicated to enriching this thesis and enhancing my professional skills so that I can become a better researcher. I would like to thank Prof. Eva K. Grebel, my supervisor, for her support through my PhD and insightful comments on my research and this thesis. Eva, thank you for your patience with me and for not letting me get lost in the world of complicated bureaucratic procedures and regulations! I would like to sincerely thank Dr. Anna Pasquali, my second supervisor, for her patience with me, her scientific comments and suggestions on my work and this thesis, for all those scientific and non-scientific enjoyable conversations, as well as the time and effort she dedicated to me through my PhD. Anna, without you, I could not function successfully through my PhD. I would like to thank Dr. Thorsten Lisker, my ex-supervisor, for believing in me in the first place by offering me this PhD position and providing me the opportunity to work on the most fantastic dataset ever! Thorsten, thanks for all those comments, discussions, support and for planting questions as seeds in my mind so that they can shape my next steps in the world of tiny dwarf galaxies!

I would like to thank all the members of the SUNDIAL team for providing me the opportunity of working, collaborating, learning, and improving in a scientific and friendly community which is a rare blessing these days. In particular, I would like to thank Prof. Reynier Peletier, the coordinator of the SUNDIAL ITN network, for his constant support any day and in any circumstances, his guidance, his resourceful help, and insightful comments. A special thanks to my supervisors and mentors in the SUNDIAL ITN network, particularly Prof. Sven De Rijcke, Prof. Peter Tino, and Dr. Kerstin Bunte, who were always ready to help me and keep me hopeful through the PhD.

I am grateful to Prof. Jochen Heidt for accepting to be the second referee of this thesis. I also would like to thank Prof. F. Roepke and Prof. B. M. Schaefer for accepting to be part of

References

Abadi, M. G., Moore, B., and Bower, R. G. (1999). Ram pressure stripping of spiral galaxies in clusters. *MNRAS*, 308, 947.

Abadi, M. G., Navarro, J. F., Steinmetz, M., and Eke, V. R. (2003). Simulations of Galaxy Formation in a Λ Cold Dark Matter Universe. II. The Fine Structure of Simulated Galactic Disks. *ApJ*, 597, 21.

Abell, G. O. (1958). The Distribution of Rich Clusters of Galaxies. *ApJS*, 3, 211.

Abell, G. O., Corwin, Harold G., J., and Olowin, R. P. (1989). A Catalog of Rich Clusters of Galaxies. *ApJS*, 70, 1.

Adami, C., Biviano, A., Durret, F., and Mazure, A. (2005). The build-up of the Coma cluster by infalling substructures. *A&A*, 443, 17.

Adami, C., Le Brun, V., Biviano, A., Durret, F., Lamareille, F., Pelló, R., Ilbert, O., Mazure, A., Trilling, R., and Ulmer, M. P. (2009). Very deep spectroscopy of the Coma cluster line of sight: exploring new territories. *A&A*, 507, 1225.

Aguado, D. S., Ahumada, R., Almeida, A., Anderson, S. F., Andrews, B. H., Anguiano, B., Aquino Ortíz, E., Aragón-Salamanca, A., Argudo-Fernández, M., Aubert, M., Avila-Reese, V., Badenes, C., Barboza Rembold, S. r., Barger, K., Barrera-Ballesteros, J., Bates, D., Bautista, J., Beaton, R. L., Beers, T. C., Belfiore, F., Bernardi, M., Bershady, M., Beutler, F., Bird, J., Bizyaev, D., Blanc, G. A., Blanton, M. R., Blomqvist, M., Bolton, A. S., Boquien, M., Borissova, J., Bovy, J., Brand t, W. N., Brinkmann, J., Brownstein, J. R., Bundy, K., Burgasser, A., Byler, N., Cano Diaz, M., Cappellari, M., Carrera, R., Cervantes Sodi, B., Chen, Y., Cherinka, B., Choi, P. D., Chung, H., Coffey, D., Comerford, J. M., Comparat, J., Covey, K., da Silva Ilha, G., da Costa, L., Dai, Y. S., Damke, G., Darling, J., Davies, R., Dawson, K., de Sainte Agathe, V., Deconto Machado, A., Del Moro, A., De Lee, N., Diamond-Stanic, A. M., Domínguez Sánchez, H., Donor, J., Drory, N., du Mas des Bourboux, H., Duckworth, C., Dwelly, T., Ebelke, G., Emsellem, E., Escoffier, S., Fernández-Trincado, J. G., Feuillet, D., Fischer, J.-L., Fleming, S. W., Fraser-McKelvie, A., Freischlad, G., Frinchaboy, P. M., Fu, H., Galbany, L., Garcia-Dias, R., García-Hernández, D. A., Garma Oehmichen, L. A., Geimba Maia, M. A., Gil-Marín, H., Grabowski, K., Gu, M., Guo, H., Ha, J., Harrington, E., Hasselquist, S., Hayes, C. R., Hearty, F., Hernandez Toledo, H., Hicks, H., Hogg, D. W., Holley-Bockelmann, K., Holtzman, J. A., Hsieh, B.-C., Hunt, J. A. S., Hwang, H. S., Ibarra-Medel, H. J., Jimenez Angel, C. E., Johnson, J., Jones, A., Jönsson, H., Kinemuchi, K., Kollmeier, J., Krawczyk, C., Kreckel, K., Kruk, S., Lacerna, I., Lan, T.-W., Lane, R. R., Law, D. R., Lee, Y.-B., Li, C., Lian, J., Lin, L., Lin, Y.-T., Lintott, C., Long, D., Longa-Peña, P., Mackereth, J. T., de la Macorra, A., Majewski, S. R., Malanushenko, O., Manchado, A., Maraston, C., Mariappan, V., Marinelli, M., Marques-Chaves, R., Masseron, T., Masters, K. L., McDermid, R. M., Medina Peña, N., Meneses-Goytia, S., Merloni, A., Merrifield, M., Meszaros, S., Minniti, D., Minsley, R., Muna, D., Myers, A. D., Nair, P., Correa do Nascimento, J., Newman, J. A., Nitschelm, C., Olmstead, M. D., Oravetz, A., Oravetz, D., Ortega Minakata, R. A., Pace, Z., Padilla, N., Palicio, P. A., Pan, K., Pan, H.-A., Parikh, T., Parker, James, I., Peirani, S., Penny, S., Percival, W. J., Perez-Fournon, I., Peterken, T., Pinsonneault, M. H., Prakash, A., Raddick, M. J., Raichoor, A., Riffel, R. A., Riffel, R., Rix, H.-W., Robin, A. C., Roman-Lopes, A., Rose, B., Ross, A. J., Rossi, G., Rowlands, K., Rubin, K. H. R., Sánchez, S. F., Sánchez-Gallego, J. R., Sayres, C., Schaefer, A., Schiavon, R. P., Schimoia, J. S., Schlafly, E., Schlegel, D., Schneider, D. P., Schultheis, M., Seo, H.-J., Shamsi, S. J., Shao, Z., Shen, S., Shetty, S., Simonian, G., Smethurst, R. J., Sobeck, J., Souter, B. J., Spindler, A., Stark, D. V., Stassun, K. G., Steinmetz, M., Storchi-Bergmann, T., Stringfellow, G. S., Suárez, G., Sun, J., Taghizadeh-Popp, M., Talbot, M. S., Tayar, J., Thakar, A. R., Thomas, D., Tissera, P., Tojeiro, R., Troup, N. W., Unda-Sanzana, E., Valenzuela, O., Vargas-Magaña, M., Vázquez-Mata, J. A., Wake, D., Weaver, B. A., Weijmans, A.-M., Westfall, K. B., Wild, V., Wilson, J., Woods, E., Yan, R., Yang,

M., Zamora, O., Zasowski, G., Zhang, K., Zheng, Z., Zheng, Z., Zhu, G., Zinn, J. C., and Zou, H. (2019). The Fifteenth Data Release of the Sloan Digital Sky Surveys: First Release of MaNGA-derived Quantities, Data Visualization Tools, and Stellar Library. *ApJS*, 240, 23.

Aguerri, J. A. L. (2016). Early-type dwarf galaxies with multicomponent stellar structure: Are they remnants of disc galaxies strongly transformed by their environment? *A&A*, 587, A111.

Alam, S., Albareti, F. D., Allende Prieto, C., Anders, F., Anderson, S. F., Anderton, T., Andrews, B. H., Armengaud, E., Aubourg, É., Bailey, S., Basu, S., Bautista, J. E., Beaton, R. L., Beers, T. C., Bender, C. F., Berlind, A. A., Beutler, F., Bhardwaj, V., Bird, J. C., Bizyaev, D., Blake, C. H., Blanton, M. R., Blomqvist, M., Bochanski, J. J., Bolton, A. S., Bovy, J., Shelden Bradley, A., Brandt, W. N., Brauer, D. E., Brinkmann, J., Brown, P. J., Brownstein, J. R., Burden, A., Burtin, E., Busca, N. G., Cai, Z., Capozzi, D., Carnero Rosell, A., Carr, M. A., Carrera, R., Chambers, K. C., Chaplin, W. J., Chen, Y.-C., Chiappini, C., Chojnowski, S. D., Chuang, C.-H., Clerc, N., Comparat, J., Covey, K., Croft, R. A. C., Cuesta, A. J., Cunha, K., da Costa, L. N., Da Rio, N., Davenport, J. R. A., Dawson, K. S., De Lee, N., Delubac, T., Deshpande, R., Dhital, S., Dutra-Ferreira, L., Dwelly, T., Ealet, A., Ebelke, G. L., Edmondson, E. M., Eisenstein, D. J., Ellsworth, T., Elsworth, Y., Epstein, C. R., Eracleous, M., Escoffier, S., Esposito, M., Evans, M. L., Fan, X., Fernández-Alvar, E., Feuillet, D., Filiz Ak, N., Finley, H., Finoguenov, A., Flaherty, K., Fleming, S. W., Font-Ribera, A., Foster, J., Frinchaboy, P. M., Galbraith-Frew, J. G., García, R. A., García-Hernández, D. A., García Pérez, A. E., Gaulme, P., Ge, J., Génova-Santos, R., Georgakakis, A., Ghezzi, L., Gillespie, B. A., Girardi, L., Goddard, D., Gontcho, S. G. A., González Hernández, J. I., Grebel, E. K., Green, P. J., Grieb, J. N., Grieves, N., Gunn, J. E., Guo, H., Harding, P., Hasselquist, S., Hawley, S. L., Hayden, M., Hearty, F. R., Hekker, S., Ho, S., Hogg, D. W., Holley-Bockelmann, K., Holtzman, J. A., Honscheid, K., Huber, D., Huehnerhoff, J., Ivans, I. I., Jiang, L., Johnson, J. A., Kinemuchi, K., Kirkby, D., Kitaura, F., Klaene, M. A., Knapp, G. R., Kneib, J.-P., Koenig, X. P., Lam, C. R., Lan, T.-W., Lang, D., Laurent, P., Le Goff, J.-M., Leauthaud, A., Lee, K.-G., Lee, Y. S., Licquia, T. C., Liu, J., Long, D. C., López-Corredoira, M., Lorenzo-Oliveira, D., Lucatello, S., Lundgren, B., Lupton, R. H., Mack, Claude E., I., Mahadevan, S., Maia, M. A. G., Majewski, S. R., Malanushenko, E., Malanushenko, V., Manchado, A., Manera, M., Mao, Q., Maraston, C., Marchwinski, R. C., Margala, D., Martell, S. L., Martig, M., Masters, K. L., Mathur, S., McBride, C. K., McGehee, P. M., McGreer, I. D., McMahon, R. G., Ménard, B., Menzel, M.-L., Merloni, A., Mészáros, S., Miller, A. A., Miralda-Escudé, J., Miyatake, H., Montero-Dorta, A. D., More, S., Morganson, E., Morice-Atkinson, X., Morrison, H. L., Mosser, B., Muna, D., Myers, A. D., Nand ra, K., Newman, J. A., Neyrinck, M., Nguyen, D. C., Nichol, R. C., Nidever, D. L., Noterdaeme, P., Nuza, S. E., O'Connell, J. E., O'Connell, R. W., O'Connell, R., Ogando, R. L. C., Olmstead, M. D., Oravetz, A. E., Oravetz, D. J., Osumi, K., Owen, R., Padgett, D. L., Padmanabhan, N., Paegert, M., Palanque-Delabrouille, N., Pan, K., Parejko, J. K., Pâris, I., Park, C., Pattarakijwanich, P., Pellejero-Ibanez, M., Pepper, J., Percival, W. J., Pérez-Fournon, I., rez-Ra'fols, I., Petitjean, P., Pieri, M. M., Pinsonneault, M. H., Porto de Mello, G. F., Prada, F., Prakash, A., Price-Whelan, A. M., Protopapas, P., Raddick, M. J., Rahman, M., Reid, B. A., Rich, J., Rix, H.-W., Robin, A. C., Rockosi, C. M., Rodrigues, T. S., Rodríguez-Torres, S., Roe, N. A., Ross, A. J., Ross, N. P., Rossi, G., Ruan, J. J., Rubiño-Martín, J. A., Rykoff, E. S., Salazar-Albornoz, S., Salvato, M., Samushia, L., Sánchez, A. G., Santiago, B., Sayres, C., Schiavon, R. P., Schlegel, D. J., Schmidt, S. J., Schneider, D. P., Schultheis, M., Schwope, A. D., Scóccola, C. G., Scott, C., Sellgren, K., Seo, H.-J., Serenelli, A., Shane, N., Shen, Y., Shetrone, M., Shu, Y., Silva Aguirre, V., Sivarani, T., Skrutskie, M. F., Slosar, A., Smith, V. V., Sobreira, F., Souto, D., Stassun, K. G., Steinmetz, M., Stello, D., Strauss, M. A., Streblyanska, A., Suzuki, N., Swanson, M. E. C., Tan, J. C., Tayar, J., Terrien, R. C., Thakar, A. R., Thomas, D., Thomas, N., Thompson, B. A., Tinker, J. L., Tojeiro, R., Troup, N. W., Vargas-Magaña, M., Vazquez, J. A., Verde, L., Viel, M., Vogt, N. P., Wake, D. A., Wang, J., Weaver, B. A., Weinberg, D. H., Weiner, B. J., White, M., Wilson, J. C., Wisniewski, J. P., Wood-Vasey, W. M., Ye'che, C., York, D. G., Zakamska, N. L., Zamora, O., Zasowski, G., Zehavi, I., Zhao, G.-B., Zheng, Z., Zhou, X., Zhou, Z., Zou, H., and Zhu, G. (2015). The Eleventh and Twelfth Data Releases of the Sloan Digital Sky Survey: Final Data from SDSS-III. *ApJS*, 219, 12.

Allen, S. W., Evrard, A. E., and Mantz, A. B. (2011). Cosmological Parameters from Observations of Galaxy Clusters. *ARA&A*, 49, 409.

Annibali, F., Bressan, A., Rampazzo, R., Zeilinger, W. W., and Danese, L. (2007). Nearby early-type galaxies with ionized gas. III. Analysis of line-strength indices with new stellar population models. *A&A*, 463, 455.

Arimoto, N. and Yoshii, Y. (1987). Chemical and photometric properties of a galactic wind model for elliptical

galaxies. *A&A*, 173, 23.

Babcock, H. W. (1939). The rotation of the Andromeda Nebula. *Lick Observatory Bulletin*, 498, 41.

Bacon, R., Accardo, M., Adjali, L., Anwand, H., Bauer, S., Biswas, I., Blaizot, J., Boudon, D., Brau-Nogue, S., Brinchmann, J., Caillier, P., Capoani, L., Carollo, C. M., Contini, T., Couderc, P., Daguisé, E., Deiries, S., Delabre, B., Dreizler, S., Dubois, J., Dupieux, M., Dupuy, C., Emsellem, E., Fechner, T., Fleischmann, A., François, M., Gallou, G., Gharsa, T., Glindemann, A., Gojak, D., Guiderdoni, B., Hansali, G., Hahn, T., Jarno, A., Kelz, A., Koehler, C., Kosmalski, J., Laurent, F., Le Floch, M., Lilly, S. J., Lizon, J.-L., Loupias, M., Manescau, A., Monstein, C., Nicklas, H., Olaya, J.-C., Pares, L., Pasquini, L., Pécontal-Rousset, A., Pelló, R., Petit, C., Popow, E., Reiss, R., Remillieux, A., Renault, E., Roth, M., Rupprecht, G., Serre, D., Schaye, J., Soucail, G., Steinmetz, M., Streicher, O., Stuik, R., Valentin, H., Vernet, J., Weilbacher, P., Wisotzki, L., and Yerle, N. (2010). The MUSE second-generation VLT instrument. In *Ground-based and Airborne Instrumentation for Astronomy III*, volume 7735 of *Proc. SPIE*, page 773508.

Bacon, R., Conseil, S., Mary, D., Brinchmann, J., Shepherd, M., Akhlaghi, M., Weilbacher, P. M., Piqueras, L., Wisotzki, L., Lagattuta, D., Epinat, B., Guerou, A., Inami, H., Cantalupo, S., Courbot, J. B., Contini, T., Richard, J., Maseda, M., Bouwens, R., Bouché, N., Kollatschny, W., Schaye, J., Marino, R. A., Pello, R., Herenz, C., Guiderdoni, B., and Carollo, M. (2017). The MUSE Hubble Ultra Deep Field Survey. I. Survey description, data reduction, and source detection. *A&A*, 608, A1.

Bacon, R., Vernet, J., Borisova, E., Bouché, N., Brinchmann, J., Carollo, M., Carton, D., Caruana, J., Cerda, S., Contini, T., Franx, M., Girard, M., Guerou, A., Haddad, N., Hau, G., Herenz, C., Herrera, J. C., Husemann, B., Husser, T. O., Jarno, A., Kamann, S., Krajnovic, D., Lilly, S., Mainieri, V., Martinsson, T., Palsa, R., Patricio, V., Pécontal, A., Pello, R., Piqueras, L., Richard, J., Sandin, C., Schroetter, I., Selman, F., Shirazi, M., Smette, A., Soto, K., Streicher, O., Urrutia, T., Weilbacher, P., Wisotzki, L., and Zins, G. (2014). MUSE Commissioning. *The Messenger*, 157, 13.

Baldwin, J. A., Phillips, M. M., and Terlevich, R. (1981). Classification parameters for the emission-line spectra of extragalactic objects. *PASP*, 93, 5.

Barazza, F. D., Binggeli, B., and Jerjen, H. (2002). More evidence for hidden spiral and bar features in bright early-type dwarf galaxies. *A&A*, 391, 823.

Barone, T. M., D'Eugenio, F., Colless, M., Scott, N., van de Sande, J., Bland-Hawthorn, J., Brough, S., Bryant, J. J., Cortese, L., Croom, S. M., Foster, C., Goodwin, M., Konstantopoulos, I. S., Lawrence, J. S., Lorente, N. P. F., Medling, A. M., Owers, M. S., and Richards, S. N. (2018). The SAMI Galaxy Survey: Gravitational Potential and Surface Density Drive Stellar Populations. I. Early-type Galaxies. *ApJ*, 856, 64.

Barsanti, S., Owers, M. S., Brough, S., Davies, L. J. M., Driver, S. P., Gunawardhana, M. L. P., Holwerda, B. W., Liske, J., Loveday, J., Pimbblet, K. A., Robotham, A. S. G., and Taylor, E. N. (2018). Galaxy and Mass Assembly (GAMA): Impact of the Group Environment on Galaxy Star Formation. *ApJ*, 857, 71.

Battaglia, G., Tolstoy, E., Helmi, A., Irwin, M., Parisi, P., Hill, V., and Jablonka, P. (2011). Study of the Sextans dwarf spheroidal galaxy from the DART Ca II triplet survey. *MNRAS*, 411, 1013.

Bekki, K. (2014). Galactic star formation enhanced and quenched by ram pressure in groups and clusters. *MNRAS*, 438, 444.

Bekki, K. and Couch, W. J. (2003). Starbursts from the Strong Compression of Galactic Molecular Clouds due to the High Pressure of the Intracluster Medium. *ApJL*, 596, L13.

Bekki, K., Couch, W. J., and Shioya, Y. (2002). Passive Spiral Formation from Halo Gas Starvation: Gradual Transformation into S0s. *ApJ*, 577, 651.

Bekki, K. and Shioya, Y. (1999). Stellar Populations in Gas-rich Galaxy Mergers. II. Feedback Effects of Type IA and Type II Supernovae. *ApJ*, 513, 108.

Bell, E. F., McIntosh, D. H., Katz, N., and Weinberg, M. D. (2003). The Optical and Near-Infrared Properties of Galaxies. I. Luminosity and Stellar Mass Functions. *ApJS*, 149, 289.

Bender, R., Burstein, D., and Faber, S. M. (1992). Dynamically hot galaxies. I - Structural properties. *ApJ*, 399, 462.

Bensby, T., Feltzing, S., and Lundström, I. (2003). Elemental abundance trends in the Galactic thin and thick disks as traced by nearby F and G dwarf stars. *A&A*, 410, 527.

Bialas, D., Lisker, T., Olczak, C., Spurzem, R., and Kotulla, R. (2015). On the occurrence of galaxy harassment. *A&A*, 576, A103.

Binggeli, B. and Cameron, L. M. (1991). Dwarf galaxies in the Virgo cluster. I. The systematic photometric properties of early-type dwarfs. *A&A*, 252, 27.

Binggeli, B., Sandage, A., and Tammann, G. A. (1985). Studies of the Virgo cluster. II. A catalog of 2096 galaxies in the Virgo cluster area. *AJ*, 90, 1681.

Binggeli, B., Sandage, A., and Tammann, G. A. (1988). The luminosity function of galaxies. *ARA&A*, 26, 509.

Binggeli, B., Sandage, A., and Tarenghi, M. (1984). Studies of the Virgo Cluster. I. Photometry of 109 galaxies near the cluster center to serve as standards. *AJ*, 89, 64.

Binggeli, B., Tammann, G. A., and Sandage, A. (1987). Studies of the Virgo cluster. VI - Morphological and kinematical structure of the Virgo cluster. *AJ*, 94, 251.

Binney, J. and Tremaine, S. (2008). *Galactic Dynamics: Second Edition*.

Böhringer, H., Briel, U. G., Schwarz, R. A., Voges, W., Hartner, G., and Trümper, J. (1994a). The structure of the Virgo cluster of galaxies from Rosat X-ray images. *Nature*, 368, 828.

Böhringer, H., Briel, U. G., Schwarz, R. A., Voges, W., Hartner, G., and Trümper, J. (1994b). The structure of the Virgo cluster of galaxies from Rosat X-ray images. *Nature*, 368, 828.

Bolatto, A. D., Wolfire, M., and Leroy, A. K. (2013). The CO-to-H_2 Conversion Factor. *ARA&A*, 51, 207.

Boselli, A., Boissier, S., Cortese, L., and Gavazzi, G. (2008). The Origin of Dwarf Ellipticals in the Virgo Cluster. *ApJ*, 674, 742.

Boselli, A., Boissier, S., Cortese, L., and Gavazzi, G. (2009). The effect of ram-pressure stripping and starvation on the star formation properties of cluster galaxies. *Astronomische Nachrichten*, 330, 904.

Boselli, A., Boissier, S., Heinis, S., Cortese, L., Ilbert, O., Hughes, T., Cucciati, O., Davies, J., Ferrarese, L., Giovanelli, R., Haynes, M. P., Baes, M., Balkowski, C., Brosch, N., Chapman, S. C., Charmandaris, V., Clemens, M. S., Dariush, A., De Looze, I., di Serego Alighieri, S., Duc, P. A., Durrell, P. R., Emsellem, E., Erben, T., Fritz, J., Garcia-Appadoo, D. A., Gavazzi, G., Grossi, M., Jordán, A., Hess, K. M., Huertas-Company, M., Hunt, L. K., Kent, B. R., Lambas, D. G., Lançon, A., MacArthur, L. A., Madden, S. C., Magrini, L., Mei, S., Momjian, E., Olowin, R. P., Papastergis, E., Smith, M. W. L., Solanes, J. M., Spector, O., Spekkens, K., Taylor, J. E., Valotto, C., van Driel, W., Verstappen, J., Vlahakis, C., Vollmer, B., and Xilouris, E. M. (2011). The GALEX Ultraviolet Virgo Cluster Survey (GUViCS). I. The UV luminosity function of the central 12 sq. deg. *A&A*, 528, A107.

Boselli, A., Fossati, M., Ferrarese, L., Boissier, S., Consolandi, G., Longobardi, A., Amram, P., Balogh, M., Barmby, P., Boquien, M., Boulanger, F., Braine, J., Buat, V., Burgarella, D., Combes, F., Contini, T., Cortese, L., Côté, P., Côté, S., Cuilland re, J. C., Drissen, L., Epinat, B., Fumagalli, M., Gallagher, S., Gavazzi, G., Gomez-Lopez, J., Gwyn, S., Harris, W., Hensler, G., Koribalski, B., Marcelin, M., McConnachie, A., Miville-Deschenes, M. A., Navarro, J., Patton, D., Peng, E. W., Plana, H., Prantzos, N., Robert, C., Roediger, J., Roehlly, Y., Russeil, D., Salome, P., Sanchez-Janssen, R., Serra, P., Spekkens, K., Sun, M., Taylor, J., Tonnesen, S., Vollmer, B., Willis, J., Wozniak, H., Burdullis, T., Devost, D., Mahoney, B., Manset, N., Petric, A., Prunet, S., and Withington, K. (2018). A Virgo Environmental Survey Tracing Ionised Gas Emission (VESTIGE). I. Introduction to the survey. *A&A*, 614, A56.

Boselli, A. and Gavazzi, G. (2006). Environmental Effects on Late-Type Galaxies in Nearby Clusters. *PASP*, 118, 517.

Boselli, A. and Gavazzi, G. (2014). On the origin of the faint-end of the red sequence in high-density environments. *A&A Rv*, 22, 74.

Boselli, A., Voyer, E., Boissier, S., Cucciati, O., Consolandi, G., Cortese, L., Fumagalli, M., Gavazzi, G., Heinis, S., Roehlly, Y., and Toloba, E. (2014). The GALEX Ultraviolet Virgo Cluster Survey (GUViCS). IV. The role of the cluster environment on galaxy evolution. *A&A*, 570, A69.

Bothun, G. D. and Caldwell, C. N. (1984). Infrared photometry and optical spectroscopy of dwarf galaxies in theVirgo cluster. *ApJ*, 280, 528.

Bothun, G. D., Mould, J. R., Wirth, A., and Caldwell, N. (1985). An investigation of dwarf galaxies in the Virgo cluster. *AJ*, 90, 697.

Boulanger, F., Cox, P., and Jones, A. P. (2000). Course 7: Dust in the Interstellar Medium. In Casoli, F., Lequeux, J., and David, F., editors, *Infrared Space Astronomy, Today and Tomorrow*, volume 70, page 251.

Bournaud, F., Elmegreen, B. G., and Martig, M. (2009). The Thick Disks of Spiral Galaxies as Relics from Gas-rich, Turbulent, Clumpy Disks at High Redshift. *ApJL*, 707, L1.

Brook, C. B., Gibson, B. K., Martel, H., and Kawata, D. (2005). The Emergence of the Thick Disk in a CDM Universe. II. Colors and Abundance Patterns. *ApJ*, 630, 298.

Brook, C. B., Governato, F., Roškar, R., Stinson, G., Brooks, A. M., Wadsley, J., Quinn, T., Gibson, B. K., Snaith, O., Pilkington, K., House, E., and Pontzen, A. (2011). Hierarchical formation of bulgeless galaxies: why outflows have low angular momentum. *MNRAS*, 415, 1051.

Brook, C. B., Kawata, D., Gibson, B. K., and Freeman, K. C. (2004). The Emergence of the Thick Disk in a Cold Dark Matter Universe. *ApJ*, 612, 894.

Brown, T., Catinella, B., Cortese, L., Lagos, C. d. P., Davé, R., Kilborn, V., Haynes, M. P., Giovanelli, R., and Rafieferantsoa, M. (2017). Cold gas stripping in satellite galaxies: from pairs to clusters. *MNRAS*, 466, 1275.

Bullock, J. S. and Johnston, K. V. (2005). Tracing Galaxy Formation with Stellar Halos. I. Methods. *ApJ*, 635, 931.

Buyle, P., De Rijcke, S., Michielsen, D., Baes, M., and Dejonghe, H. (2005). The HI content of Fornax dwarf elliptical galaxies: FCC032 and FCC336. *MNRAS*, 360, 853.

Byrd, G. and Valtonen, M. (1990). Tidal Generation of Active Spirals and S0 Galaxies by Rich Clusters. *ApJ*, 350, 89.

Caldwell, N. and Bothun, G. D. (1987). Dwarf Elliptical Galaxies in the Fornax Cluster. II. Their Structure and Stellar Populations. *AJ*, 94, 1126.

Caldwell, N., Rose, J. A., and Concannon, K. D. (2003). Star Formation Histories of Early-Type Galaxies. I. Higher Order Balmer Lines as Age Indicators. *AJ*, 125, 2891.

Calvi, V., Stiavelli, M., Bradley, L., Pizzella, A., and Kim, S. (2014). The Effect of Surface Brightness Dimming in the Selection of High-z Galaxies. *ApJ*, 796, 102.

Calzetti, D., Kennicutt, R. C., Engelbracht, C. W., Leitherer, C., Draine, B. T., Kewley, L., Moustakas, J., Sosey, M., Dale, D. A., Gordon, K. D., Helou, G. X., Hollenbach, D. J., Armus, L., Bendo, G., Bot, C., Buckalew, B., Jarrett, T., Li, A., Meyer, M., Murphy, E. J., Prescott, M., Regan, M. W., Rieke, G. H., Roussel, H., Sheth, K., Smith, J. D. T., Thornley, M. D., and Walter, F. (2007). The Calibration of Mid-Infrared Star Formation Rate Indicators. *ApJ*, 666, 870.

Cappellari, M. (2002). Efficient multi-Gaussian expansion of galaxies. *MNRAS*, 333, 400.

Cappellari, M. (2016). Structure and Kinematics of Early-Type Galaxies from Integral Field Spectroscopy. *ARA&A*, 54, 597.

Cappellari, M. (2017). Improving the full spectrum fitting method: accurate convolution with Gauss-Hermite functions. *MNRAS*, 466, 798.

Cappellari, M., Bacon, R., Bureau, M., Damen, M. C., Davies, R. L., de Zeeuw, P. T., Emsellem, E., Falcón-Barroso, J., Krajnović, D., Kuntschner, H., McDermid, R. M., Peletier, R. F., Sarzi, M., van den Bosch, R. C. E., and van de Ven, G. (2006). The SAURON project - IV. The mass-to-light ratio, the virial mass estimator and the Fundamental Plane of elliptical and lenticular galaxies. *MNRAS*, 366, 1126.

Cappellari, M. and Copin, Y. (2003). Adaptive spatial binning of integral-field spectroscopic data using Voronoi tessellations. *MNRAS*, 342, 345.

Cappellari, M. and Emsellem, E. (2004). Parametric Recovery of Line-of-Sight Velocity Distributions from Absorption-Line Spectra of Galaxies via Penalized Likelihood. *PASP*, 116, 138.

Cappellari, M., Emsellem, E., Krajnović, D., McDermid, R. M., Serra, P., Alatalo, K., Blitz, L., Bois, M., Bournaud, F., Bureau, M., Davies, R. L., Davis, T. A., de Zeeuw, P. T., Khochfar, S., Kuntschner, H., Lablanche, P.-Y., Morganti, R., Naab, T., Oosterloo, T., Sarzi, M., Scott, N., Weijmans, A.-M., and Young, L. M. (2011). The ATLAS^{3D} project - VII. A new look at the morphology of nearby galaxies: the kinematic morphology-density relation. *MNRAS*, 416, 1680.

Cardelli, J. A., Clayton, G. C., and Mathis, J. S. (1989). The relationship between infrared, optical, and ultraviolet extinction. *ApJ*, 345, 245.

Carollo, C. M., Danziger, I. J., and Buson, L. (1993). Metallicity gradients in early-type galaxies. *MNRAS*, 265, 553.

Cavanagh, M. K. and Bekki, K. (2020). Bars formed in galaxy merging and their classification with deep learning. *A&A*, 641, A77.

Cenarro, A. J., Cardiel, N., Gorgas, J., Peletier, R. F., Vazdekis, A., and Prada, F. (2001). Empirical calibration of the near-infrared Ca ii triplet - I. The stellar library and index definition. *MNRAS*, 326, 959.

Cenarro, A. J., Peletier, R. F., Sánchez-Blázquez, P., Selam, S. O., Toloba, E., Cardiel, N., Falcón-Barroso, J., Gorgas, J., Jiménez-Vicente, J., and Vazdekis, A. (2007). Medium-resolution Isaac Newton Telescope library of empirical spectra - II. The stellar atmospheric parameters. *MNRAS*, 374, 664.

Cervantes, J. L. and Vazdekis, A. (2009). An optimized Hβ index for disentangling stellar population ages. *MNRAS*, 392, 691.

Chiba, M. and Beers, T. C. (2000). Kinematics of Metal-poor Stars in the Galaxy. III. Formation of the Stellar Halo and Thick Disk as Revealed from a Large Sample of Nonkinematically Selected Stars. *AJ*, 119, 2843.

Chilingarian, I. V., Cayatte, V., Durret, F., Adami, C., Balkowski, C., Chemin, L., Laganá, T. F., and Prugniel, P. (2008). Kinematics and stellar populations of low-luminosity early-type galaxies in the Abell 496 cluster. *A&A*, 486, 85.

Choi, H. and Yi, S. K. (2017). On the Evolution of Galaxy Spin in a Cosmological Hydrodynamic Simulation of Galaxy Clusters. *ApJ*, 837, 68.

Chung, A., van Gorkom, J. H., Kenney, J. D. P., Crowl, H., and Vollmer, B. (2009). VLA Imaging of Virgo Spirals in Atomic Gas (VIVA). I. The Atlas and the H I Properties. *AJ*, 138, 1741.

CidFernandes, R., Mateus, A., Sodré, L., Stasińska, G., and Gomes, J. M. (2005). Semi-empirical analysis of Sloan Digital Sky Survey galaxies - I. Spectral synthesis method. *MNRAS*, 358, 363.

Clauwens, B., Schaye, J., Franx, M., and Bower, R. G. (2018). The three phases of galaxy formation. *MNRAS*, 478, 3994.

Cole, S., Lacey, C. G., Baugh, C. M., and Frenk, C. S. (2000). Hierarchical galaxy formation. *MNRAS*, 319, 168.

Conselice, C. J., Gallagher, John S., I., and Wyse, R. F. G. (2001). Galaxy Populations and Evolution in Clusters. I. Dynamics and the Origin of Low-Mass Galaxies in the Virgo Cluster. *ApJ*, 559, 791.

Côté, P., Blakeslee, J. P., Ferrarese, L., Jordán, A., Mei, S., Merritt, D., Milosavljević, M., Peng, E. W., Tonry, J. L., and West, M. J. (2004). The ACS Virgo Cluster Survey. I. Introduction to the Survey. *ApJS*, 153, 223.

Cowie, L. L. and Songaila, A. (1977). Thermal evaporation of gas within galaxies by a hot intergalactic medium. *Nature*, 266, 501.

Cramer, W. J., Kenney, J. D. P., Tonnesen, S., Smith, R., Wong, T., Jáchym, P., Cortés, J. R., Cortés, P. C., and Wu, Y.-T. (2021). Molecular gas filaments and fallback in the ram pressure stripped Coma spiral NGC 4921. *arXiv e-prints*, page arXiv:2107.11731.

Şen, Ş., Peletier, R. F., Boselli, A., den Brok, M., Falcón-Barroso, J., Hensler, G., Janz, J., Laurikainen, E., Lisker, T., Mentz, J. J., Paudel, S., Salo, H., Sybilska, A., Toloba, E., van de Ven, G., Vazdekis, A., and Yesilyaprak, C. (2018). Abundance ratios in dwarf elliptical galaxies. *MNRAS*, 475, 3453.

Dalcanton, J. J., Spergel, D. N., and Summers, F. J. (1997). The Formation of Disk Galaxies. *ApJ*, 482, 659.

Davies, J. and Morgan, I. (1994). Why are Dwarf Galaxies so Difficult to Find? In *European Southern Observatory Conference and Workshop Proceedings*, volume 49 of *European Southern Observatory Conference and Workshop Proceedings*, page 19.

Davies, J. I., Baes, M., Bendo, G. J., Bianchi, S., Bomans, D. J., Boselli, A., Clemens, M., Corbelli, E., Cortese, L., Dariush, A., De Looze, I., di Serego Alighieri, S., Fadda, D., Fritz, J., Garcia-Appadoo, D. A., Gavazzi, G., Giovanardi, C., Grossi, M., Hughes, T. M., Hunt, L. K., Jones, A. P., Madden, S., Pierini, D., Pohlen, M., Sabatini, S., Smith, M. W. L., Verstappen, J., Vlahakis, C., Xilouris, E. M., and Zibetti, S. (2010). The Herschel Virgo Cluster Survey. I. Luminosity function. *A&A*, 518, L48.

De Rijcke, S., Dejonghe, H., Zeilinger, W. W., and Hau, G. K. T. (2003). Embedded disks in Fornax dwarf elliptical galaxies. *A&A*, 400, 119.

de Rijcke, S., Michielsen, D., Dejonghe, H., Zeilinger, W. W., and Hau, G. K. T. (2005). Formation and evolution of dwarf elliptical galaxies. I. Structural and kinematical properties. *A&A*, 438, 491.

de Vaucouleurs, G. (1977). Qualitative and Quantitative Classifications of Galaxies. In Tinsley, B. M. and Larson, Richard B. Gehret, D. C., editors, *Evolution of Galaxies and Stellar Populations*, page 43.

D'Eugenio, F., Houghton, R. C. W., Davies, R. L., and Dalla Bontà, E. (2015). On the distribution of galaxy ellipticity in clusters. *MNRAS*, 451, 827.

Diplas, A. and Savage, B. D. (1991). Neutral Hydrogen in the Outer Galaxy. *ApJ*, 377, 126.

Donnari, M., Pillepich, A., Joshi, G. D., Nelson, D., Genel, S., Marinacci, F., Rodriguez-Gomez, V., Pakmor, R., Torrey, P., Vogelsberger, M., and Hernquist, L. (2021). Quenched fractions in the IllustrisTNG simulations:

the roles of AGN feedback, environment, and pre-processing. *MNRAS*, 500, 4004.

Draine, B. T. (2003). Interstellar Dust Grains. *ARA&A*, 41, 241.

Dressler, A. (1980). Galaxy morphology in rich clusters: implications for the formation and evolution of galaxies. *ApJ*, 236, 351.

Duc, P. A. and Brinks, E. (2001). H I Recycling: Formation of Tidal Dwarf Galaxies. In Hibbard, J. E., Rupen, M., and van Gorkom, J. H., editors, *Gas and Galaxy Evolution*, volume 240 of *Astronomical Society of the Pacific Conference Series*, page 181.

Ebeling, H. and Kalita, B. S. (2019). Jellyfish: Ram Pressure Stripping As a Diagnostic Tool in Studies of Cluster Collisions. *ApJ*, 882, 127.

Eigenthaler, P., Puzia, T. H., Taylor, M. A., Ordenes-Briceño, Y., Muñoz, R. P., Ribbeck, K. X., Alamo-Martínez, K. A., Zhang, H., Ángel, S., Capaccioli, M., Côté, P., Ferrarese, L., Galaz, G., Grebel, E. K., Hempel, M., Hilker, M., Lançon, A., Mieske, S., Miller, B., Paolillo, M., Powalka, M., Richtler, T., Roediger, J., Rong, Y., Sánchez-Janssen, R., and Spengler, C. (2018). The Next Generation Fornax Survey (NGFS). II. The Central Dwarf Galaxy Population. *ApJ*, 855, 142.

Emsellem, E., Cappellari, M., Krajnović, D., Alatalo, K., Blitz, L., Bois, M., Bournaud, F., Bureau, M., Davies, R. L., Davis, T. A., de Zeeuw, P. T., Khochfar, S., Kuntschner, H., Lablanche, P.-Y., McDermid, R. M., Morganti, R., Naab, T., Oosterloo, T., Sarzi, M., Scott, N., Serra, P., van de Ven, G., Weijmans, A.-M., and Young, L. M. (2011). The ATLAS^{3D} project - III. A census of the stellar angular momentum within the effective radius of early-type galaxies: unveiling the distribution of fast and slow rotators. *MNRAS*, 414, 888.

Emsellem, E., Cappellari, M., Krajnović, D., van de Ven, G., Bacon, R., Bureau, M., Davies, R. L., de Zeeuw, P. T., Falcón-Barroso, J., Kuntschner, H., McDermid, R., Peletier, R. F., and Sarzi, M. (2007). The SAURON project - IX. A kinematic classification for early-type galaxies. *MNRAS*, 379, 401.

Emsellem, E., Cappellari, M., Peletier, R. F., McDermid, R. M., Bacon, R., Bureau, M., Copin, Y., Davies, R. L., Krajnović, D., Kuntschner, H., Miller, B. W., and de Zeeuw, P. T. (2004). The SAURON project - III. Integral-field absorption-line kinematics of 48 elliptical and lenticular galaxies. *MNRAS*, 352, 721.

Emsellem, E., Monnet, G., and Bacon, R. (1994). The multi-gaussian expansion method: a tool for building realistic photometric and kinematical models of stellar systems I. The formalism. *A&A*, 285, 723.

Emsellem, E., van der Burg, R. F. J., Fensch, J., Jeřábková, T., Zanella, A., Agnello, A., Hilker, M., Müller, O., Rejkuba, M., Duc, P.-A., Durrell, P., Habas, R., Lelli, F., Lim, S., Marleau, F. R., Peng, E., and Sánchez-Janssen, R. (2019). The ultra-diffuse galaxy NGC 1052-DF2 with MUSE. I. Kinematics of the stellar body. *A&A*, 625, A76.

Erfanianfar, G., Popesso, P., Finoguenov, A., Wuyts, S., Wilman, D., Biviano, A., Ziparo, F., Salvato, M., Nandra, K., Lutz, D., Elbaz, D., Dickinson, M., Tanaka, M., Mirkazemi, M., Balogh, M. L., Altieri, M. B., Aussel, H., Bauer, F., Berta, S., Bielby, R. M., Brandt, N., Cappelluti, N., Cimatti, A., Cooper, M., Fadda, D., Ilbert, O., Le Floch, E., Magnelli, B., Mulchaey, J. S., Nordon, R., Newman, J. A., Poglitsch, A., and Pozzi, F. (2014). The evolution of star formation activity in galaxy groups. *MNRAS*, 445, 2725.

Eskridge, P. B., Frogel, J. A., Pogge, R. W., Quillen, A. C., Davies, R. L., DePoy, D. L., Houdashelt, M. L., Kuchinski, L. E., Ramírez, S. V., Sellgren, K., Terndrup, D. M., and Tiede, G. P. (2000). The Frequency of Barred Spiral Galaxies in the Near-Infrared. *AJ*, 119, 536.

Evrard, A. E. (1991). Clues to galaxy activity from rich cluster simulations. *MNRAS*, 248, 8P.

Fadda, D., Yan, L., Lagache, G., Sajina, A., Lutz, D., Wuyts, S., Frayer, D. T., Marcillac, D., Le Floc'h, E., Caputi, K., Spoon, H. W. W., Veilleux, S., Blain, A., and Helou, G. (2010). Ultra-deep Mid-infrared Spectroscopy of Luminous Infrared Galaxies at z ~1 and z ~2. *ApJ*, 719, 425.

Fahrion, K., Lyubenova, M., van de Ven, G., Hilker, M., Leaman, R., Falcón-Barroso, J., Bittner, A., Coccato, L., Corsini, E. M., Gadotti, D. A., Iodice, E., McDermid, R. M., Martín-Navarro, I., Pinna, F., Poci, A., Sarzi, M., de Zeeuw, P. T., and Zhu, L. (2021). Diversity of nuclear star cluster formation mechanisms revealed by their star formation histories. *arXiv e-prints*, page arXiv:2104.06412.

Falcón-Barroso, J., Bacon, R., Bureau, M., Cappellari, M., Davies, R. L., de Zeeuw, P. T., Emsellem, E., Fathi, K., Krajnović, D., Kuntschner, H., McDermid, R. M., Peletier, R. F., and Sarzi, M. (2006). The SAURON project - VII. Integral-field absorption and emission-line kinematics of 24 spiral galaxy bulges. *MNRAS*, 369, 529.

Falcón-Barroso, J., Lyubenova, M., van de Ven, G., Mendez-Abreu, J., Aguerri, J. A. L., García-Lorenzo, B., Bekeraité, S., Sánchez, S. F., Husemann, B., García-Benito, R., Mast, D., Walcher, C. J., Zibetti, S., Barrera-

Ballesteros, J. K., Galbany, L., Sánchez-Blázquez, P., Singh, R., van den Bosch, R. C. E., Wild, V., Zhu, L., Bland-Hawthorn, J., Cid Fernandes, R., de Lorenzo-Cáceres, A., Gallazzi, A., González Delgado, R. M., Marino, R. A., Márquez, I., Pérez, E., Pérez, I., Roth, M. M., Rosales-Ortega, F. F., Ruiz-Lara, T., Wisotzki, L., Ziegler, B., and Califa Collaboration (2017). Stellar kinematics across the Hubble sequence in the CALIFA survey: general properties and aperture corrections. *A&A*, 597, A48.

Falcón-Barroso, J., Sánchez-Blázquez, P., Vazdekis, A., Ricciardelli, E., Cardiel, N., Cenarro, A. J., Gorgas, J., and Peletier, R. F. (2011). An updated MILES stellar library and stellar population models. *A&A*, 532, A95.

Falcón-Barroso, J., van de Ven, G., Lyubenova, M., Mendez-Abreu, J., Aguerri, J. A. L., García-Lorenzo, B., Bekeraité, S., Sánchez, S. F., Husemann, B., García-Benito, R., González Delgado, R. M., Mast, D., Walcher, C. J., Zibetti, S., Zhu, L., Barrera-Ballesteros, J. K., Galbany, L., Sánchez-Blázquez, P., Singh, R., van den Bosch, R. C. E., Wild, V., Bland-Hawthorn, J., Cid Fernandes, R., de Lorenzo-Cáceres, A., Gallazzi, A., Marino, R. A., Márquez, I., Peletier, R. F., Pérez, E., Pérez, I., Roth, M. M., Rosales-Ortega, F. F., Ruiz-Lara, T., Wisotzki, L., and Ziegler, B. (2019). The CALIFA view on stellar angular momentum across the Hubble sequence. *A&A*, 632, A59.

Fall, S. M. and Efstathiou, G. (1980). Formation and rotation of disc galaxies with haloes. *MNRAS*, 193, 189.

Fan, X., Carilli, C. L., and Keating, B. (2006). Observational Constraints on Cosmic Reionization. *ARA&A*, 44, 415.

Ferguson, H. C. and Binggeli, B. (1994). Dwarf elliptical galaxies. *A&A Rv*, 6, 67.

Ferguson, H. C. and Sandage, A. (1989). The Spatial Distributions and Intrinsic Shapes of Dwarf Elliptical Galaxies in the Virgo and Fornax Clusters. *ApJL*, 346, L53.

Ferrarese, L., Côté, P., Cuillandre, J.-C., Gwyn, S. D. J., Peng, E. W., MacArthur, L. A., Duc, P.-A., Boselli, A., Mei, S., Erben, T., McConnachie, A. W., Durrell, P. R., Mihos, J. C., Jordán, A., Lançon, A., Puzia, T. H., Emsellem, E., Balogh, M. L., Blakeslee, J. P., van Waerbeke, L., Gavazzi, R., Vollmer, B., Kavelaars, J. J., Woods, D., Ball, N. M., Boissier, S., Courteau, S., Ferriere, E., Gavazzi, G., Hildebrandt, H., Hudelot, P., Huertas-Company, M., Liu, C., McLaughlin, D., Mellier, Y., Milkeraitis, M., Schade, D., Balkowski, C., Bournaud, F., Carlberg, R. G., Chapman, S. C., Hoekstra, H., Peng, C., Sawicki, M., Simard, L., Taylor, J. E., Tully, R. B., van Driel, W., Wilson, C. D., Burdullis, T., Mahoney, B., and Manset, N. (2012). The Next Generation Virgo Cluster Survey (NGVS). I. Introduction to the Survey. *ApJS*, 200, 4.

Ferreras, I., Scott, N., La Barbera, F., Croom, S., van de Sande, J., Hopkins, A., Colless, M., Barone, T. M., d'Eugenio, F., Bland-Hawthorn, J., Brough, S., Bryant, J. J., Konstantopoulos, I. S., Lagos, C., Lawrence, J. S., López-Sánchez, A., Medling, A. M., Owers, M. S., and Richards, S. N. (2019). The SAMI galaxy survey: stellar population radial gradients in early-type galaxies. *MNRAS*, 489, 608.

Fisher, D. B. and Drory, N. (2008). The Structure of Classical Bulges and Pseudobulges: the Link Between Pseudobulges and SÉRSIC Index. *AJ*, 136, 773.

Förster Schreiber, N. M. and Wuyts, S. (2020). Star-Forming Galaxies at Cosmic Noon. *ARA&A*, 58, 661.

Franx, M., Illingworth, G., and de Zeeuw, T. (1991). The Ordered Nature of Elliptical Galaxies: Implications for Their Intrinsic Angular Momenta and Shapes. *ApJ*, 383, 112.

Freeman, K. C. (1970). On the Disks of Spiral and S0 Galaxies. *ApJ*, 160, 811.

Fujita, Y. (1998). Quantitative Estimates of Environmental Effects on the Star Formation Rate of Disk Galaxies in Clusters of Galaxies. *ApJ*, 509, 587.

Fujita, Y. (2004). Pre-Processing of Galaxies before Entering a Cluster. *PASJ*, 56, 29.

Fujita, Y. and Nagashima, M. (1999). Effects of Ram Pressure from the Intracluster Medium on the Star Formation Rate of Disk Galaxies in Clusters of Galaxies. *ApJ*, 516, 619.

Fumagalli, M., Gavazzi, G., Scaramella, R., and Franzetti, P. (2011). Constraining the ages of the fireballs in the wake of the dIrr galaxy VCC 1217/IC 3418. *A&A*, 528, A46.

Gajda, G., Łokas, E. L., and Athanassoula, E. (2016). The Orbital Structure of a Tidally Induced Bar. *ApJ*, 830, 108.

Gallazzi, A., Bell, E. F., Zibetti, S., Brinchmann, J., and Kelson, D. D. (2014). Charting the Evolution of the Ages and Metallicities of Massive Galaxies since z = 0.7. *ApJ*, 788, 72.

Gallazzi, A., Charlot, S., Brinchmann, J., and White, S. D. M. (2006). Ages and metallicities of early-type galaxies in the Sloan Digital Sky Survey: new insight into the physical origin of the colour-magnitude and the Mg_2-σ_V relations. *MNRAS*, 370, 1106.

Gallazzi, A., Charlot, S., Brinchmann, J., White, S. D. M., and Tremonti, C. A. (2005). The ages and metallicities of galaxies in the local universe. *MNRAS*, 362, 41.

Gallazzi, A. R., Pasquali, A., Zibetti, S., and Barbera, F. L. (2021). Galaxy evolution across environments as probed by the ages, stellar metallicities, and [α /Fe] of central and satellite galaxies. *MNRAS*, 502, 4457.

Ganda, K., Falcón-Barroso, J., Peletier, R. F., Cappellari, M., Emsellem, E., McDermid, R. M., de Zeeuw, P. T., and Carollo, C. M. (2006). Late-type galaxies observed with SAURON: two-dimensional stellar and emission-line kinematics of 18 spirals. *MNRAS*, 367, 46.

Gastaldello, F., Limousin, M., Foex, G., Munoz, R. P., Verdugo, T., Motta, V., More, A., Cabanac, R., Buote, D. A., Eckert, D., Ettori, S., Fritz, A., Ghizzardi, S., Humphrey, P. J., Meneghetti, M., and Rossetti, M. (2014). Dark matter-baryons separation at the lowest mass scale: the Bullet Group{star}. *MNRAS*, 442, L76.

Gavazzi, G., Boselli, A., Scodeggio, M., Pierini, D., and Belsole, E. (1999). The 3D structure of the Virgo cluster from H-band Fundamental Plane and Tully-Fisher distance determinations. *MNRAS*, 304, 595.

Gavazzi, G., Boselli, A., van Driel, W., and O'Neil, K. (2005). Completing H I observations of galaxies in the Virgo cluster. *A&A*, 429, 439.

Geha, M., Blanton, M. R., Yan, R., and Tinker, J. L. (2012). A Stellar Mass Threshold for Quenching of Field Galaxies. *ApJ*, 757, 85.

Geha, M., Guhathakurta, P., Rich, R. M., and Cooper, M. C. (2006). Local Group Dwarf Elliptical Galaxies. I. Mapping the Dynamics of NGC 205 Beyond the Tidal Radius. *AJ*, 131, 332.

Geha, M., Guhathakurta, P., and van der Marel, R. P. (2003). Internal Dynamics, Structure, and Formation of Dwarf Elliptical Galaxies. II. Rotating versus Nonrotating Dwarfs. *AJ*, 126, 1794.

Geha, M., van der Marel, R. P., Guhathakurta, P., Gilbert, K. M., Kalirai, J., and Kirby, E. N. (2010). Local Group Dwarf Elliptical Galaxies. II. Stellar Kinematics to Large Radii in NGC 147 and NGC 185. *ApJ*, 711, 361.

Giovanelli, R. and Haynes, M. P. (1985). Gas deficiency in cluster galaxies : a comparison of nine clusters. *ApJ*, 292, 404.

Giovanelli, R., Haynes, M. P., Kent, B. R., Perillat, P., Saintonge, A., Brosch, N., Catinella, B., Hoffman, G. L., Stierwalt, S., Spekkens, K., Lerner, M. S., Masters, K. L., Momjian, E., Rosenberg, J. L., Springob, C. M., Boselli, A., Charmandaris, V., Darling, J. K., Davies, J., Garcia Lambas, D., Gavazzi, G., Giovanardi, C., Hardy, E., Hunt, L. K., Iovino, A., Karachentsev, I. D., Karachentseva, V. E., Koopmann, R. A., Marinoni, C., Minchin, R., Muller, E., Putman, M., Pantoja, C., Salzer, J. J., Scodeggio, M., Skillman, E., Solanes, J. M., Valotto, C., van Driel, W., and van Zee, L. (2005). The Arecibo Legacy Fast ALFA Survey. I. Science Goals, Survey Design, and Strategy. *AJ*, 130, 2598.

Goddard, D., Thomas, D., Maraston, C., Westfall, K., Etherington, J., Riffel, R., Mallmann, N. D., Zheng, Z., Argudo-Fernández, M., Bershady, M., Bundy, K., Drory, N., Law, D., Yan, R., Wake, D., Weijmans, A., Bizyaev, D., Brownstein, J., Lane, R. R., Maiolino, R., Masters, K., Merrifield, M., Nitschelm, C., Pan, K., Roman-Lopes, A., and Storchi-Bergmann, T. (2017). SDSS-IV MaNGA: stellar population gradients as a function of galaxy environment. *MNRAS*, 465, 688.

Gómez, A., Di Matteo, P., Stefanovitch, N., Haywood, M., Combes, F., Katz, D., and Babusiaux, C. (2016). A new look at the kinematics of the bulge from an N-body model. *A&A*, 589, A122.

Gonçalves, G., Coelho, P., Schiavon, R., and Usher, C. (2020). How well can we determine ages and chemical abundances from spectral fitting of integrated light spectra? *MNRAS*, 499, 2327.

González Delgado, R. M., Cid Fernandes, R., García-Benito, R., Pérez, E., de Amorim, A. L., Cortijo-Ferrero, C., Lacerda, E. A. D., López Fernández, R., Sánchez, S. F., Vale Asari, N., Alves, J., Bland-Hawthorn, J., Galbany, L., Gallazzi, A., Husemann, B., Bekeraite, S., Jungwiert, B., López-Sánchez, A. R., de Lorenzo-Cáceres, A., Marino, R. A., Mast, D., Mollá, M., del Olmo, A., Sánchez-Blázquez, P., van de Ven, G., Vílchez, J. M., Walcher, C. J., Wisotzki, L., Ziegler, B., and CALIFA Collaboration (2014). Insights on the Stellar Mass-Metallicity Relation from the CALIFA Survey. *ApJL*, 791, L16.

Graham, A. W. and Guzmán, R. (2003). HST Photometry of Dwarf Elliptical Galaxies in Coma, and an Explanation for the Alleged Structural Dichotomy between Dwarf and Bright Elliptical Galaxies. *AJ*, 125, 2936.

Graham, A. W., Spitler, L. R., Forbes, D. A., Lisker, T., Moore, B., and Janz, J. (2012). LEDA 074886: A Remarkable Rectangular-looking Galaxy. *ApJ*, 750, 121.

Grand, R. J. J., Gómez, F. A., Marinacci, F., Pakmor, R., Springel, V., Campbell, D. J. R., Frenk, C. S., Jenkins,

A., and White, S. D. M. (2017). The Auriga Project: the properties and formation mechanisms of disc galaxies across cosmic time. *MNRAS*, 467, 179.

Grebel, E. K. (1999). Evolutionary Histories of Dwarf Galaxies in the Local Group. In Whitelock, P. and Cannon, R., editors, *The Stellar Content of Local Group Galaxies*, volume 192, page 17.

Grebel, E. K. (2001). Dwarf Galaxies in the Local Group and in the Local Volume (Invited Talk). In de Boer, K. S., Dettmar, R.-J., and Klein, U., editors, *Dwarf galaxies and their environment*, volume 40, page 45.

Greene, J., Leauthaud, A., Emsellem, E., Ge, J., Aragon-Salamanca, A., Greco, J., Lin, Y. T., Mao, S., Masters, K., Merrifield, M., More, S., Okabe, N., Schneider, D., Thomas, D., Wake, D., Pan, K., Bizyaev, D., Oravetz, D., Simmons, A., Yan, R., and van den Bosch, F. (2018). SDSS-IV MaNGA: Uncovering the Angular Momentum Content of Central and Satellite Early-type Galaxies. *ApJ*, 852, 36.

Greene, J. E., Janish, R., Ma, C.-P., McConnell, N. J., Blakeslee, J. P., Thomas, J., and Murphy, J. D. (2015). The MASSIVE Survey. II. Stellar Population Trends Out to Large Radius in Massive Early-type Galaxies. *ApJ*, 807, 11.

Greene, J. E., Murphy, J. D., Graves, G. J., Gunn, J. E., Raskutti, S., Comerford, J. M., and Gebhardt, K. (2013). The Stellar Halos of Massive Elliptical Galaxies. II. Detailed Abundance Ratios at Large Radius. *ApJ*, 776, 64.

Greene, J. E., Veale, M., Ma, C.-P., Thomas, J., Quenneville, M. E., Blakeslee, J. P., Walsh, J. L., Goulding, A., and Ito, J. (2019). The MASSIVE Survey. XII. Connecting Stellar Populations of Early-type Galaxies to Kinematics and Environment. *ApJ*, 874, 66.

Greggio, L. and Renzini, A. (1983). The binary model for type I supernovae - Theoretical rates. *A&A*, 118, 217.

Gu, Q., Zhao, Y., Shi, L., Peng, Z., and Luo, X. (2006). IC 225: A Dwarf Elliptical Galaxy with a Peculiar Blue Core. *AJ*, 131, 806.

Guérou, A., Emsellem, E., McDermid, R. M., Côté, P., Ferrarese, L., Blakeslee, J. P., Durrell, P. R., MacArthur, L. A., Peng, E. W., Cuilland re, J.-C., and Gwyn, S. (2015). The Next Generation Virgo Cluster Survey. XII. Stellar Populations and Kinematics of Compact, Low-mass Early-type Galaxies from Gemini GMOS-IFU Spectroscopy. *ApJ*, 804, 70.

Gunn, J. E. and Gott, III, J. R. (1972). On the Infall of Matter Into Clusters of Galaxies and Some Effects on Their Evolution. *ApJ*, 176, 1.

Haines, C. P., Pereira, M. J., Smith, G. P., Egami, E., Babul, A., Finoguenov, A., Ziparo, F., McGee, S. L., Rawle, T. D., Okabe, N., and Moran, S. M. (2015). LoCuSS: The Slow Quenching of Star Formation in Cluster Galaxies and the Need for Pre-processing. *ApJ*, 806, 101.

Hamraz, E., Peletier, R. F., Khosroshahi, H. G., Valentijn, E. A., den Brok, M., and Venhola, A. (2019). Young stellar populations in early-type dwarf galaxies. Occurrence, radial extent, and scaling relations. *A&A*, 625, A94.

Harbeck, D., Grebel, E. K., Holtzman, J., Guhathakurta, P., Brandner, W., Geisler, D., Sarajedini, A., Dolphin, A., Hurley-Keller, D., and Mateo, M. (2001). Population Gradients in Local Group Dwarf Spheroidal Galaxies. *AJ*, 122, 3092.

Harrington, R. G. and Wilson, A. G. (1950). Two New Stellar Systems in Leo. *PASP*, 62, 118.

Hester, J. A., Seibert, M., Neill, J. D., Wyder, T. K., Gil de Paz, A., Madore, B. F., Martin, D. C., Schiminovich, D., and Rich, R. M. (2010). IC 3418: Star Formation in a Turbulent Wake. *ApJL*, 716, L14.

Ho, N., Geha, M., Tollerud, E. J., Zinn, R., Guhathakurta, P., and Vargas, L. C. (2015). Metallicity Evolution of the Six Most Luminous M31 Dwarf Satellites. *ApJ*, 798, 77.

Hodge, P. W. (1959). Dwarf Members of a Southern Cluster of Galaxies. *PASP*, 71, 28.

Hodge, P. W. (1960). Dwarf Members of a Southern Cluster of Galaxies. II. *PASP*, 72, 188.

Hodge, P. W., Pyper, D. M., and Webb, C. J. (1965). Dwarf galaxies in the Fornax cluster. *AJ*, 70, 559.

Holmberg, E. (1950). A photometric study of nearby galaxies. *Meddelanden fran Lunds Astronomiska Observatorium Serie II*, 128, 5.

Holmberg, E. (1969). A study of physical groups of galaxies. *Arkiv for Astronomi*, 5, 305.

Hopkins, P. F., Bundy, K., Croton, D., Hernquist, L., Keres, D., Khochfar, S., Stewart, K., Wetzel, A., and Younger, J. D. (2010). Mergers and Bulge Formation in ΛCDM: Which Mergers Matter? *ApJ*, 715, 202.

Hopkins, P. F., Cox, T. J., Dutta, S. N., Hernquist, L., Kormendy, J., and Lauer, T. R. (2009). Dissipation and Extra Light in Galactic Nuclei. II. "Cusp" Ellipticals. *ApJS*, 181, 135.

Hubble, E. P. (1926). Extragalactic nebulae. *ApJ*, 64, 321.

Hubble, E. P. (1936). *Realm of the Nebulae*.

Hunter, D. A., Hunsberger, S. D., and Roye, E. W. (2000). Identifying Old Tidal Dwarf Irregulars. *ApJ*, 542, 137.

Hwang, J.-S., Park, C., Banerjee, A., and Hwang, H. S. (2018). Evolution of Late-type Galaxies in a Cluster Environment: Effects of High-speed Multiple Encounters with Early-type Galaxies. *ApJ*, 856, 160.

Impey, C., Bothun, G., and Malin, D. (1988). Virgo Dwarfs: New Light on Faint Galaxies. *ApJ*, 330, 634.

Jáchym, P., Kenney, J. D. P., Ržuička, A., Sun, M., Combes, F., and Palouš, J. (2013). Search for cold and hot gas in the ram pressure stripped Virgo dwarf galaxy IC 3418. *A&A*, 556, A99.

Jaffé, Y. L., Smith, R., Candlish, G. N., Poggianti, B. M., Sheen, Y.-K., and Verheijen, M. A. W. (2015). BUDHIES II: a phase-space view of H I gas stripping and star formation quenching in cluster galaxies. *MNRAS*, 448, 1715.

Janz, J., Laurikainen, E., Lisker, T., Salo, H., Peletier, R. F., Niemi, S.-M., den Brok, M., Toloba, E., Falcón-Barroso, J., Boselli, A., and Hensler, G. (2012). Dissecting Early-type Dwarf Galaxies into Their Multiple Components. *ApJL*, 745, L24.

Janz, J. and Lisker, T. (2008). The Sizes of Early-Type Galaxies. *ApJL*, 689, L25.

Janz, J. and Lisker, T. (2009). On the Color-Magnitude Relation of Early-Type Galaxies. *ApJL*, 696, L102.

Janz, J., Penny, S. J., Graham, A. W., Forbes, D. A., and Davies, R. L. (2017). Implications for the origin of early-type dwarf galaxies - the discovery of rotation in isolated, low-mass early-type galaxies. *MNRAS*, 468, 2850.

Jedrzejewski, R. I. (1987). CCD surface photometry of elliptical galaxies. I - Observations, reduction and results. *MNRAS*, 226, 747.

Jenkins, E. B. (2013). The Fractional Ionization of the Warm Neutral Interstellar Medium. *ApJ*, 764, 25.

Jerjen, H., Kalnajs, A., and Binggeli, B. (2000). IC3328: A "dwarf elliptical galaxy" with spiral structure. *A&A*, 358, 845.

Jesseit, R., Cappellari, M., Naab, T., Emsellem, E., and Burkert, A. (2009). Specific angular momentum of disc merger remnants and the λ_R-parameter. *MNRAS*, 397, 1202.

Johnston, E. J., Eigenthaler, P., Puzia, T. H., Ordenes-Briceño, Y., Taylor, M. A., Alamo-Martínez, K., Côté, P., Galaz, G., Grebel, E. K., Hilker, M., Lançon, A., Mieske, S., Sánchez-Janssen, R., and Rong, Y. (2019). The Next Generation Fornax Survey (NGFS). V. Discovery of a Dwarf-Dwarf Galaxy Pair at z = 0.30 and Its Characterization Using Deep VLT/MUSE Observations. *ApJ*, 873, 59.

Jones, B. J. T. and Wyse, R. F. G. (1983). The formation of disc galaxies. *A&A*, 120, 165.

Kapferer, W., Sluka, C., Schindler, S., Ferrari, C., and Ziegler, B. (2009). The effect of ram pressure on the star formation, mass distribution and morphology of galaxies. *A&A*, 499, 87.

Kauffmann, G., Heckman, T. M., Tremonti, C., Brinchmann, J., Charlot, S., White, S. D. M., Ridgway, S. E., Brinkmann, J., Fukugita, M., Hall, P. B., Ivezić, Ž., Richards, G. T., and Schneider, D. P. (2003). The host galaxies of active galactic nuclei. *MNRAS*, 346, 1055.

Kawata, D. and Mulchaey, J. S. (2008). Strangulation in Galaxy Groups. *ApJL*, 672, L103.

Kelly, B. C. (2007). Some Aspects of Measurement Error in Linear Regression of Astronomical Data. *ApJ*, 665, 1489.

Kenney, J. D. P., Geha, M., Jáchym, P., Crowl, H. H., Dague, W., Chung, A., van Gorkom, J., and Vollmer, B. (2014). Transformation of a Virgo Cluster Dwarf Irregular Galaxy by Ram Pressure Stripping: IC3418 and Its Fireballs. *ApJ*, 780, 119.

Kewley, L. J., Dopita, M. A., Sutherland, R. S., Heisler, C. A., and Trevena, J. (2001). Theoretical Modeling of Starburst Galaxies. *ApJ*, 556, 121.

Kewley, L. J., Groves, B., Kauffmann, G., and Heckman, T. (2006). The host galaxies and classification of active galactic nuclei. *MNRAS*, 372, 961.

Kim, S., Rey, S.-C., Bureau, M., Yoon, H., Chung, A., Jerjen, H., Lisker, T., Jeong, H., Sung, E.-C., Lee, Y., Lee, W., and Chung, J. (2016). Large-scale Filamentary Structures around the Virgo Cluster Revisited. *ApJ*, 833, 207.

Kleiner, D., Serra, P., Maccagni, F. M., Venhola, A., Morokuma-Matsui, K., Peletier, R., Iodice, E., Raj, M. A., de Blok, W. J. G., Comrie, A., Józsa, G. I. G., Kamphuis, P., Loni, A., Loubser, S. I., Molnár, D. C., Passmoor, S. S., Ramatsoku, M., Sivitilli, A., Smirnov, O., Thorat, K., and Vitello, F. (2021). A MeerKAT view of

pre-processing in the Fornax A group. *arXiv e-prints*, page arXiv:2101.10347.

Knowles, A. T., Sansom, A. E., Allende Prieto, C., and Vazdekis, A. (2021). sMILES: a library of semi-empirical MILES stellar spectra with variable [α/Fe] abundances. *MNRAS*, 504, 2286.

Kobayashi, C. and Arimoto, N. (1999). Gradients of Absorption-Line Strengths in Elliptical Galaxies. *ApJ*, 527, 573.

Kodama, T. and Smail, I. (2001). Testing the hypothesis of the morphological transformation from field spiral to cluster S0. *MNRAS*, 326, 637.

Koleva, M., de Rijcke, S., Prugniel, P., Zeilinger, W. W., and Michielsen, D. (2009). Formation and evolution of dwarf elliptical galaxies - II. Spatially resolved star formation histories. *MNRAS*, 396, 2133.

Koleva, M., Prugniel, P., De Rijcke, S., and Zeilinger, W. W. (2011). Age and metallicity gradients in early-type galaxies: a dwarf-to-giant sequence. *MNRAS*, 417, 1643.

Kormendy, J. (1982). Observations of Galaxy Structure and Dynamics. *Saas-Fee Advanced Course*, 12, 115.

Kormendy, J. (1985). Families of ellipsoidal stellar systems and the formation of dwarf elliptical galaxies. *ApJ*, 295, 73.

Kormendy, J. and Bender, R. (1996). A Proposed Revision of the Hubble Sequence for Elliptical Galaxies. *ApJL*, 464, L119.

Kormendy, J. and Bender, R. (2012). A Revised Parallel-sequence Morphological Classification of Galaxies: Structure and Formation of S0 and Spheroidal Galaxies. *ApJS*, 198, 2.

Kormendy, J., Fisher, D. B., Cornell, M. E., and Bender, R. (2009). Structure and Formation of Elliptical and Spheroidal Galaxies. *ApJS*, 182, 216.

Kormendy, J. and Kennicutt, Robert C., J. (2004). Secular Evolution and the Formation of Pseudobulges in Disk Galaxies. *ARA&A*, 42, 603.

Krajnović, D., Cappellari, M., de Zeeuw, P. T., and Copin, Y. (2006). Kinemetry: a generalization of photometry to the higher moments of the line-of-sight velocity distribution. *MNRAS*, 366, 787.

Krajnović, D., Emsellem, E., Cappellari, M., Alatalo, K., Blitz, L., Bois, M., Bournaud, F., Bureau, M., Davies, R. L., Davis, T. A., de Zeeuw, P. T., Khochfar, S., Kuntschner, H., Lablanche, P.-Y., McDermid, R. M., Morganti, R., Naab, T., Oosterloo, T., Sarzi, M., Scott, N., Serra, P., Weijmans, A.-M., and Young, L. M. (2011). The ATLAS^{3D} project - II. Morphologies, kinematic features and alignment between photometric and kinematic axes of early-type galaxies. *MNRAS*, 414, 2923.

Krajnović, D., Ural, U., Kuntschner, H., Goudfrooij, P., Wolfe, M., Cappellari, M., Davies, R., de Zeeuw, T. P., Duc, P.-A., Emsellem, E., Karick, A., McDermid, R. M., Mei, S., and Naab, T. (2020). Formation channels of slowly rotating early-type galaxies. *A&A*, 635, A129.

Krajnović, D., Weilbacher, P. M., Urrutia, T., Emsellem, E., Carollo, C. M., Shirazi, M., Bacon, R., Contini, T., Epinat, B., Kamann, S., Martinsson, T., and Steinmetz, M. (2015). Unveiling the counter-rotating nature of the kinematically distinct core in NGC 5813 with MUSE. *MNRAS*, 452, 2.

Kronberger, T., Kapferer, W., Ferrari, C., Unterguggenberger, S., and Schindler, S. (2008). On the influence of ram-pressure stripping on the star formation of simulated spiral galaxies. *A&A*, 481, 337.

Kuntschner, H., Emsellem, E., Bacon, R., Bureau, M., Cappellari, M., Davies, R. L., de Zeeuw, P. T., Falcón-Barroso, J., Krajnović, D., McDermid, R. M., Peletier, R. F., and Sarzi, M. (2006). The SAURON project - VI. Line strength maps of 48 elliptical and lenticular galaxies. *MNRAS*, 369, 497.

Kuntschner, H., Emsellem, E., Bacon, R., Cappellari, M., Davies, R. L., de Zeeuw, P. T., Falcón-Barroso, J., Krajnović, D., McDermid, R. M., Peletier, R. F., Sarzi, M., Shapiro, K. L., van den Bosch, R. C. E., and van de Ven, G. (2010). The SAURON project - XVII. Stellar population analysis of the absorption line strength maps of 48 early-type galaxies. *MNRAS*, 408, 97.

Kwak, S., Kim, W.-T., Rey, S.-C., and Quinn, T. R. (2019). Origin of Nonaxisymmetric Features of Virgo Cluster Early-type Dwarf Galaxies. II. Tidal Effects on Disk Features and Stability. *ApJ*, 887, 139.

La Barbera, F., Ferreras, I., de Carvalho, R. R., Lopes, P. A. A., Pasquali, A., de la Rosa, I. G., and De Lucia, G. (2011). On the Radial Stellar Content of Early-type Galaxies as a Function of Mass and Environment. *ApJL*, 740, L41.

La Barbera, F., Pasquali, A., Ferreras, I., Gallazzi, A., de Carvalho, R. R., and de la Rosa, I. G. (2014). SPIDER - X. Environmental effects in central and satellite early-type galaxies through the stellar fossil record. *MNRAS*, 445, 1977.

La Barbera, F., Vazdekis, A., Ferreras, I., and Pasquali, A. (2021). Mild radial variations of the stellar IMF in the bulge of M31. *MNRAS*, 505, 415.

Larson, R. B. (1974). Dynamical models for the formation and evolution of spherical galaxies. *MNRAS*, 166, 585.

Larson, R. B., Tinsley, B. M., and Caldwell, C. N. (1980). The evolution of disk galaxies and the origin of S0 galaxies. *ApJ*, 237, 692.

Lee, Y., Kim, S., Rey, S.-C., and Chung, J. (2021). Properties of Galaxies in Cosmic Filaments around the Virgo Cluster. *ApJ*, 906, 68.

Lewis, I., Balogh, M., De Propris, R., Couch, W., Bower, R., Offer, A., Bland-Hawthorn, J., Baldry, I. K., Baugh, C., Bridges, T., Cannon, R., Cole, S., Colless, M., Collins, C., Cross, N., Dalton, G., Driver, S. P., Efstathiou, G., Ellis, R. S., Frenk, C. S., Glazebrook, K., Hawkins, E., Jackson, C., Lahav, O., Lumsden, S., Maddox, S., Madgwick, D., Norberg, P., Peacock, J. A., Percival, W., Peterson, B. A., Sutherland, W., and Taylor, K. (2002). The 2dF Galaxy Redshift Survey: the environmental dependence of galaxy star formation rates near clusters. *MNRAS*, 334, 673.

Li, H., Mao, S., Cappellari, M., Graham, M. T., Emsellem, E., and Long, R. J. (2018). SDSS-IV MaNGA: The Intrinsic Shape of Slow Rotator Early-type Galaxies. *ApJL*, 863, L19.

Lianou, S., Grebel, E. K., and Koch, A. (2010). Dwarf spheroidals in the M 81 group - Metallicity distribution functions and population gradients. *A&A*, 521, A43.

Lisker, T., Brunngräber, R., and Grebel, E. K. (2009). Early-type dwarf galaxies with spiral structure. *Astronomische Nachrichten*, 330, 966.

Lisker, T., Glatt, K., Westera, P., and Grebel, E. K. (2006a). Virgo Cluster Early-Type Dwarf Galaxies with the Sloan Digital Sky Survey. II. Early-Type Dwarfs with Central Star Formation. *AJ*, 132, 2432.

Lisker, T., Grebel, E. K., and Binggeli, B. (2006b). Virgo Cluster Early-Type Dwarf Galaxies with the Sloan Digital Sky Survey. I. On the Possible Disk Nature of Bright Early-Type Dwarfs. *AJ*, 132, 497.

Lisker, T., Grebel, E. K., Binggeli, B., and Glatt, K. (2007). Virgo Cluster Early-Type Dwarf Galaxies with the Sloan Digital Sky Survey. III. Subpopulations: Distributions, Shapes, Origins. *ApJ*, 660, 1186.

Lisker, T., Vijayaraghavan, R., Janz, J., Gallagher, III, J. S., Engler, C., and Urich, L. (2018). The Active Assembly of the Virgo Cluster: Indications for Recent Group Infall From Early-type Dwarf Galaxies. *ApJ*, 865, 40.

Lisker, T., Weinmann, S. M., Janz, J., and Meyer, H. T. (2013). Dwarf galaxy populations in present-day galaxy clusters - II. The history of early-type and late-type dwarfs. *MNRAS*, 432, 1162.

Łokas, E. L., Ebrová, I., del Pino, A., Sybilska, A., Athanassoula, E., Semczuk, M., Gajda, G., and Fouquet, S. (2016). Tidally Induced Bars of Galaxies in Clusters. *ApJ*, 826, 227.

Mahajan, S., Raychaudhury, S., and Pimbblet, K. A. (2012). Plunging fireworks: why do infalling galaxies light up on the outskirts of clusters? *MNRAS*, 427, 1252.

Majewski, S. R. (1993). Galactic structure surveys and the evolution of the Milky Way. *ARA&A*, 31, 575.

Marcolini, A., Brighenti, F., and D'Ercole, A. (2003). Three-dimensional simulations of the interstellar medium in dwarf galaxies - I. Ram pressure stripping. *MNRAS*, 345, 1329.

Marsakov, V. A., Koval', V. V., Borkova, T. V., and Shapovalov, M. V. (2011). The age-metallicity relation in the thin disk of the galaxy. *Astronomy Reports*, 55, 667.

Martín-Navarro, I., Vazdekis, A., Falcón-Barroso, J., La Barbera, F., Yıldırım, A., and van de Ven, G. (2018). Timing the formation and assembly of early-type galaxies via spatially resolved stellar populations analysis. *MNRAS*, 475, 3700.

Mastropietro, C., Moore, B., Mayer, L., Debattista, V. P., Piffaretti, R., and Stadel, J. (2005). Detailed kinematics and morphological features in tidally heated disks. In Jerjen, H. and Binggeli, B., editors, *IAU Colloq. 198: Near-fields cosmology with dwarf elliptical galaxies*, pages 244–248.

Mateo, M. L. (1998). Dwarf Galaxies of the Local Group. *ARA&A*, 36, 435.

McConnachie, A. W. (2012). The Observed Properties of Dwarf Galaxies in and around the Local Group. *AJ*, 144, 4.

McConnachie, A. W., Irwin, M. J., Ferguson, A. M. N., Ibata, R. A., Lewis, G. F., and Tanvir, N. (2005). Distances and metallicities for 17 Local Group galaxies. *MNRAS*, 356, 979.

McPartland, C., Ebeling, H., Roediger, E., and Blumenthal, K. (2016). Jellyfish: the origin and distribution of

extreme ram-pressure stripping events in massive galaxy clusters. *MNRAS*, 455, 2994.

Mebold, U., Winnberg, A., Kalberla, P. M. W., and Goss, W. M. (1982). An Effelsberg - Green Bank galactic H I absorption line survey. II - Results and interpretation. *A&A*, 115, 223.

Mentz, J. J., La Barbera, F., Peletier, R. F., Falcón-Barroso, J., Lisker, T., van de Ven, G., Loubser, S. I., Hilker, M., Sánchez-Janssen, R., Napolitano, N., Cantiello, M., Capaccioli, M., Norris, M., Paolillo, M., Smith, R., Beasley, M. A., Lyubenova, M., Munoz, R., and Puzia, T. (2016). Abundance ratios and IMF slopes in the dwarf elliptical galaxy NGC 1396 with MUSE. *MNRAS*, 463, 2819.

Merritt, D. (1984). Relaxation and tidal stripping in rich clusters of galaxies. II. Evolution of the luminosity distribution. *ApJ*, 276, 26.

Mezcua, M. (2017). Observational evidence for intermediate-mass black holes. *International Journal of Modern Physics D*, 26, 1730021.

Michea, J., Pasquali, A., Smith, R., Kraljic, K., Grebel, E. K., Calderón-Castillo, P., and Lisker, T. (2021). Brought to Light I: Quantification of Disk Substructure in Dwarf Early-Type Galaxies. *arXiv e-prints*, page arXiv:2103.16579.

Michielsen, D., Boselli, A., Conselice, C. J., Toloba, E., Whiley, I. M., Aragón-Salamanca, A., Balcells, M., Cardiel, N., Cenarro, A. J., Gorgas, J., Peletier, R. F., and Vazdekis, A. (2008). The relation between stellar populations, structure and environment for dwarf elliptical galaxies from the MAGPOP-ITP. *MNRAS*, 385, 1374.

Mihos, J. C. (2004). Interactions and Mergers of Cluster Galaxies. In Mulchaey, J. S., Dressler, A., and Oemler, A., editors, *Clusters of Galaxies: Probes of Cosmological Structure and Galaxy Evolution*, page 277.

Miller, R. H. (1986). Flyby : numerical experiments on a galaxy orbiting within a galaxy cluster. *A&A*, 167, 41.

Minchev, I. and Famaey, B. (2010). A New Mechanism for Radial Migration in Galactic Disks: Spiral-Bar Resonance Overlap. *ApJ*, 722, 112.

Mo, H. J., Mao, S., and White, S. D. M. (1998). The formation of galactic discs. *MNRAS*, 295, 319.

Moore, B., Katz, N., Lake, G., Dressler, A., and Oemler, A. (1996). Galaxy harassment and the evolution of clusters of galaxies. *Nature*, 379, 613.

Moore, B., Lake, G., and Katz, N. (1998). Morphological Transformation from Galaxy Harassment. *ApJ*, 495, 139.

Morales-Vargas, A., Torres-Papaqui, J. P., Rosales-Ortega, F. F., Sánchez, S. F., Chow-Martínez, M., Ortega-Minakata, R. A., Trejo-Alonso, J. J., Robleto-Orús, A. C., Romero-Cruz, F. J., Neri-Larios, D. M., and Califa Survey Collaboration (2020). Star formation in CALIFA survey perturbed galaxies - I. Effects of tidal interactions. *MNRAS*, 499, 4370.

Mori, M. and Burkert, A. (2000). Gas Stripping of Dwarf Galaxies in Clusters of Galaxies. *ApJ*, 538, 559.

Morokuma-Matsui, K., Kodama, T., Morokuma, T., Nakanishi, K., Koyama, Y., Yamashita, T., Koyama, S., and Okamoto, T. (2021). A phase-space view of cold-gas properties of Virgo-cluster galaxies: multiple quenching processes at work? *arXiv e-prints*, page arXiv:2103.05867.

Moster, B. P., Somerville, R. S., Maulbetsch, C., van den Bosch, F. C., Macciò, A. V., Naab, T., and Oser, L. (2010). Constraints on the Relationship between Stellar Mass and Halo Mass at Low and High Redshift. *ApJ*, 710, 903.

Mun, J. Y., Hwang, H. S., Lee, M. G., Chung, A., Yoon, H., and Lee, J. C. (2021). Star Formation Activity of Galaxies Undergoing Ram Pressure Stripping in the Virgo Cluster. *Journal of Korean Astronomical Society*, 54, 17.

Murray, N. (2011). Star Formation Efficiencies and Lifetimes of Giant Molecular Clouds in the Milky Way. *ApJ*, 729, 133.

Naab, T., Oser, L., Emsellem, E., Cappellari, M., Krajnović, D., McDermid, R. M., Alatalo, K., Bayet, E., Blitz, L., Bois, M., Bournaud, F., Bureau, M., Crocker, A., Davies, R. L., Davis, T. A., de Zeeuw, P. T., Duc, P.-A., Hirschmann, M., Johansson, P. H., Khochfar, S., Kuntschner, H., Morganti, R., Oosterloo, T., Sarzi, M., Scott, N., Serra, P., van de Ven, G., Weijmans, A., and Young, L. M. (2014). The ATLAS^{3D} project - XXV. Two-dimensional kinematic analysis of simulated galaxies and the cosmological origin of fast and slow rotators. *MNRAS*, 444, 3357.

Naab, T. and Trujillo, I. (2006). Surface density profiles of collisionless disc merger remnants. *MNRAS*, 369, 625.

Neumann, J., Fragkoudi, F., Pérez, I., Gadotti, D. A., Falcón-Barroso, J., Sánchez-Blázquez, P., Bittner, A., Husemann, B., Gómez, F. A., Grand, R. J. J., Donohoe-Keyes, C. E., Kim, T., de Lorenzo-Cáceres, A., Martig, M., Méndez-Abreu, J., Pakmor, R., Seidel, M. K., and van de Ven, G. (2020). Stellar populations across galaxy bars in the MUSE TIMER project. *A&A*, 637, A56.

Niemiec, A., Jullo, E., Giocoli, C., Limousin, M., and Jauzac, M. (2019). Dark matter stripping in galaxy clusters: a look at the stellar-to-halo mass relation in the Illustris simulation. *MNRAS*, 487, 653.

Norris, J. E., Yong, D., Venn, K. A., Dotter, A., Casagrande, L., and Gilmore, G. (2017). The Populations of Carina. I. Decoding the Color-Magnitude Diagram. *ApJS*, 230, 27.

Nulsen, P. E. J. (1982). Transport processes and the stripping of cluster galaxies. *MNRAS*, 198, 1007.

Ogando, R. L. C., Maia, M. A. G., Chiappini, C., Pellegrini, P. S. S., Schiavon, R. P., and da Costa, L. N. (2006). Metallicity Gradient and The Hybrid Formation Scenario for Early-Type Galaxies. In *Revista Mexicana de Astronomia y Astrofisica Conference Series*, volume 26 of *Revista Mexicana de Astronomia y Astrofisica Conference Series*, pages 119–120.

Okamoto, S., Arimoto, N., Yamada, Y., Onodera, M., Tolstoy, E., Irwin, M., Helmi, A., Battaglia, G., Jablonka, P., Hill, V., Venn, K., Shetrone, M., Letarte, B., Primas, F., Francois, P., Sadakane, K., Kaufer, A., Szeifert, T., and Abel, T. (2008). The Star Formation History and Stellar Population Structures in the Sextans Dwarf Spheroidal Galaxy. In Kodama, T., Yamada, T., and Aoki, K., editors, *Panoramic Views of Galaxy Formation and Evolution*, volume 399 of *Astronomical Society of the Pacific Conference Series*, page 469.

Oman, K. A., Bahé, Y. M., Healy, J., Hess, K. M., Hudson, M. J., and Verheijen, M. A. W. (2021). A homogeneous measurement of the delay between the onsets of gas stripping and star formation quenching in satellite galaxies of groups and clusters. *MNRAS*, 501, 5073.

Oman, K. A. and Hudson, M. J. (2016). Satellite quenching time-scales in clusters from projected phase space measurements matched to simulated orbits. *MNRAS*, 463, 3083.

Oman, K. A., Hudson, M. J., and Behroozi, P. S. (2013). Disentangling satellite galaxy populations using orbit tracking in simulations. *MNRAS*, 431, 2307.

Oosterloo, T. and van Gorkom, J. (2005). A large H I cloud near the centre of the Virgo cluster. *A&A*, 437, L19.

Pak, M., Oh, S., Lee, J. H., Scott, N., Smith, R., van de Sande, J., Croom, S. M., D'Eugenio, F., Bekki, K., Brough, S., Foster, C., Barone, T. M., Kraljic, K., Jeong, H., Bland-Hawthorn, J., Bryant, J. J., Goodwin, M., Lawrence, J., Owers, M. S., and Richards, S. N. (2021). The SAMI Galaxy Survey: Stellar Populations of Passive Spiral Galaxies in Different Environments. *ApJ*, 906, 43.

Panter, B., Jimenez, R., Heavens, A. F., and Charlot, S. (2008). The cosmic evolution of metallicity from the SDSS fossil record. *MNRAS*, 391, 1117.

Parikh, T., Thomas, D., Maraston, C., Westfall, K. B., Andrews, B. H., Boardman, N. F., Drory, N., and Oyarzun, G. (2021). SDSS-IV MaNGA: radial gradients in stellar population properties of early-type and late-type galaxies. *MNRAS*, 502, 5508.

Pasquali, A., Gallazzi, A., Fontanot, F., van den Bosch, F. C., De Lucia, G., Mo, H. J., and Yang, X. (2010). Ages and metallicities of central and satellite galaxies: implications for galaxy formation and evolution. *MNRAS*, 407, 937.

Pasquali, A., Gallazzi, A., and van den Bosch, F. C. (2012). The gas-phase metallicity of central and satellite galaxies in the Sloan Digital Sky Survey. *MNRAS*, 425, 273.

Pasquali, A., Smith, R., Gallazzi, A., De Lucia, G., Zibetti, S., Hirschmann, M., and Yi, S. K. (2019). Physical properties of SDSS satellite galaxies in projected phase space. *MNRAS*, 484, 1702.

Paudel, S., Lisker, T., and Kuntschner, H. (2011). Nuclei of early-type dwarf galaxies: insights from stellar populations. *MNRAS*, 413, 1764.

Paudel, S., Lisker, T., Kuntschner, H., Grebel, E. K., and Glatt, K. (2010). Stellar populations of Virgo cluster early-type dwarf galaxies with and without discs: a dichotomy in age? *MNRAS*, 405, 800.

Pedraz, S., Gorgas, J., Cardiel, N., Sánchez-Blázquez, P., and Guzmán, R. (2002). Evidence of fast rotation in dwarf elliptical galaxies. *MNRAS*, 332, L59.

Peletier, R. F. (2013). *Stellar Populations*, page 353.

Peng, Y., Maiolino, R., and Cochrane, R. (2015). Strangulation as the primary mechanism for shutting down star formation in galaxies. *Nature*, 521, 192.

Penny, S. J., Forbes, D. A., Pimbblet, K. A., and Floyd, D. J. E. (2014). Dwarf galaxies in the Perseus Cluster:

further evidence for a disc origin for dwarf ellipticals. *MNRAS*, 443, 3381.

Penny, S. J., Janz, J., Forbes, D. A., Benson, A. J., and Mould, J. (2015). The scaling relations of early-type dwarf galaxies across a range of environments. *MNRAS*, 453, 3635.

Penoyre, Z., Moster, B. P., Sijacki, D., and Genel, S. (2017). The origin and evolution of fast and slow rotators in the Illustris simulation. *MNRAS*, 468, 3883.

Pietrinferni, A., Cassisi, S., Salaris, M., and Castelli, F. (2004a). A Large Stellar Evolution Database for Population Synthesis Studies. I. Scaled Solar Models and Isochrones. *ApJ*, 612, 168.

Pietrinferni, A., Cassisi, S., Salaris, M., and Castelli, F. (2004b). A Large Stellar Evolution Database for Population Synthesis Studies. I. Scaled Solar Models and Isochrones. *ApJ*, 612, 168.

Pipino, A., D'Ercole, A., Chiappini, C., and Matteucci, F. (2010). Abundance gradient slopes versus mass in spheroids: predictions by monolithic models. *MNRAS*, 407, 1347.

Pipino, A., D'Ercole, A., and Matteucci, F. (2008). Formation of [α/Fe] radial gradients in the stars of elliptical galaxies. *A&A*, 484, 679.

Poggianti, B. M., Bridges, T. J., Mobasher, B., Carter, D., Doi, M., Iye, M., Kashikawa, N., Komiyama, Y., Okamura, S., Sekiguchi, M., Shimasaku, K., Yagi, M., and Yasuda, N. (2001). A Photometric and Spectroscopic Study of Dwarf and Giant Galaxies in the Coma Cluster. III. Spectral Ages and Metallicities. *ApJ*, 562, 689.

Quinn, P. J., Hernquist, L., and Fullagar, D. P. (1993). Heating of Galactic Disks by Mergers. *ApJ*, 403, 74.

Rasmussen, J., Mulchaey, J. S., Bai, L., Ponman, T. J., Raychaudhury, S., and Dariush, A. (2012). The Suppression of Star Formation and the Effect of the Galaxy Environment in Low-redshift Galaxy Groups. *ApJ*, 757, 122.

Rasmussen, J., Ponman, T. J., Verdes-Montenegro, L., Yun, M. S., and Borthakur, S. (2008). Galaxy evolution in Hickson compact groups: the role of ram-pressure stripping and strangulation. *MNRAS*, 388, 1245.

Reaves, G. (1983). A catalog of dwarf galaxies in Virgo. *ApJS*, 53, 375.

Rhee, J., Smith, R., Choi, H., Contini, E., Jung, S. L., Han, S., and Yi, S. K. (2020). YZiCS: Unveiling the Quenching History of Cluster Galaxies Using Phase-space Analysis. *ApJS*, 247, 45.

Rhee, J., Smith, R., Choi, H., Yi, S. K., Jaffé, Y., Candlish, G., and Sánchez-Jánssen, R. (2017). Phase-space Analysis in the Group and Cluster Environment: Time Since Infall and Tidal Mass Loss. *ApJ*, 843, 128.

Roberts, I. D. and Parker, L. C. (2020). Ram pressure stripping candidates in the coma cluster: evidence for enhanced star formation. *MNRAS*, 495, 554.

Roediger, E., Brüggen, M., Owers, M. S., Ebeling, H., and Sun, M. (2014). Star formation in shocked cluster spirals and their tails. *Monthly Notices of the Royal Astronomical Society: Letters*, 443, L114.

Rosa, D. A., Milone, A. C., Krabbe, A. C., and Rodrigues, I. (2018). Eight luminous early-type galaxies in nearby pairs and sparse groups. I. Stellar populations spatially analysed. *Ap&SS*, 363, 131.

Rubin, V. C., Ford, W. K., J., and Thonnard, N. (1978). Extended rotation curves of high-luminosity spiral galaxies. IV. Systematic dynamical properties, Sa -¿ Sc. *ApJL*, 225, L107.

Ryś, A., Falcón-Barroso, J., and van de Ven, G. (2013). Virgo cluster and field dwarf ellipticals in 3D - I. On the variety of stellar kinematic and line-strength properties. *MNRAS*, 428, 2980.

Ryś, A., van de Ven, G., and Falcón-Barroso, J. (2014). Virgo Cluster and field dwarf ellipticals in 3D - II. Internal dynamics points to tidal harassment? *MNRAS*, 439, 284.

Safarzadeh, M. and Loeb, A. (2019). Explaining the enhanced star formation rate of Jellyfish galaxies in galaxy clusters. *MNRAS*, 486, L26.

Salaris, M. and Cassisi, S. (2005). *Evolution of Stars and Stellar Populations*.

Sánchez, S. F., Kennicutt, R. C., Gil de Paz, A., van de Ven, G., Vílchez, J. M., Wisotzki, L., Walcher, C. J., Mast, D., Aguerri, J. A. L., Albiol-Pérez, S., Alonso-Herrero, A., Alves, J., Bakos, J., Bartáková, T., Bland-Hawthorn, J., Boselli, A., Bomans, D. J., Castillo-Morales, A., Cortijo-Ferrero, C., de Lorenzo-Cáceres, A., Del Olmo, A., Dettmar, R. J., Díaz, A., Ellis, S., Falcón-Barroso, J., Flores, H., Gallazzi, A., García-Lorenzo, B., González Delgado, R., Gruel, N., Haines, T., Hao, C., Husemann, B., Iglésias-Páramo, J., Jahnke, K., Johnson, B., Jungwiert, B., Kalinova, V., Kehrig, C., Kupko, D., López-Sánchez, Á. R., Lyubenova, M., Marino, R. A., Mármol-Queraltó, E., Márquez, I., Masegosa, J., Meidt, S., Mendez-Abreu, J., Monreal-Ibero, A., Montijo, C., Mourão, A. M., Palacios-Navarro, G., Papaderos, P., Pasquali, A., Peletier, R., Pérez, E., Pérez, I., Quirrenbach, A., Relaño, M., Rosales-Ortega, F. F., Roth, M. M., Ruiz-Lara, T., Sánchez-Blázquez,

P., Sengupta, C., Singh, R., Stanishev, V., Trager, S. C., Vazdekis, A., Viironen, K., Wild, V., Zibetti, S., and Ziegler, B. (2012a). CALIFA, the Calar Alto Legacy Integral Field Area survey. I. Survey presentation. *A&A*, 538, A8.

Sánchez, S. F., Kennicutt, R. C., Gil de Paz, A., van de Ven, G., Vílchez, J. M., Wisotzki, L., Walcher, C. J., Mast, D., Aguerri, J. A. L., Albiol-Pérez, S., Alonso-Herrero, A., Alves, J., Bakos, J., Bartáková, T., Bland-Hawthorn, J., Boselli, A., Bomans, D. J., Castillo-Morales, A., Cortijo-Ferrero, C., de Lorenzo-Cáceres, A., Del Olmo, A., Dettmar, R. J., Díaz, A., Ellis, S., Falcón-Barroso, J., Flores, H., Gallazzi, A., García-Lorenzo, B., González Delgado, R., Gruel, N., Haines, T., Hao, C., Husemann, B., Iglésias-Páramo, J., Jahnke, K., Johnson, B., Jungwiert, B., Kalinova, V., Kehrig, C., Kupko, D., López-Sánchez, Á. R., Lyubenova, M., Marino, R. A., Mármol-Queraltó, E., Márquez, I., Masegosa, J., Meidt, S., Mendez-Abreu, J., Monreal-Ibero, A., Montijo, C., Mourão, A. M., Palacios-Navarro, G., Papaderos, P., Pasquali, A., Peletier, R., Pérez, E., Pérez, I., Quirrenbach, A., Relaño, M., Rosales-Ortega, F. F., Roth, M. M., Ruiz-Lara, T., Sánchez-Blázquez, P., Sengupta, C., Singh, R., Stanishev, V., Trager, S. C., Vazdekis, A., Viironen, K., Wild, V., Zibetti, S., and Ziegler, B. (2012b). CALIFA, the Calar Alto Legacy Integral Field Area survey. I. Survey presentation. *A&A*, 538, A8.

Sánchez-Blázquez, P., Ocvirk, P., Gibson, B. K., Pérez, I., and Peletier, R. F. (2011). Star formation history of barred disc galaxies. *MNRAS*, 415, 709.

Sánchez-Blázquez, P., Peletier, R. F., Jiménez-Vicente, J., Cardiel, N., Cenarro, A. J., Falcón-Barroso, J., Gorgas, J., Selam, S., and Vazdekis, A. (2006). Medium-resolution Isaac Newton Telescope library of empirical spectra. *MNRAS*, 371, 703.

Sandage, A. and Binggeli, B. (1984). Studies of the Virgo cluster. III. A classification system and an illustrated Atlas of Virgo cluster dwarf galaxies. *AJ*, 89, 919.

Sandage, A., Binggeli, B., and Tammann, G. A. (1985). Studies of the Virgo cluster. V. Luminosity functions of Virgo cluster galaxies. *AJ*, 90, 1759.

Santucci, G., Brough, S., Scott, N., Montes, M., Owers, M. S., van Sande, J., Bland-Hawthorn, J., Bryant, J. J., Croom, S. M., Ferreras, I., Lawrence, J. S., López-Sánchez, Á. R., and Richards, S. N. (2020). The SAMI Galaxy Survey: Stellar Population Gradients of Central Galaxies. *ApJ*, 896, 75.

Sarzi, M., Falcón-Barroso, J., Davies, R. L., Bacon, R., Bureau, M., Cappellari, M., de Zeeuw, P. T., Emsellem, E., Fathi, K., Krajnović, D., Kuntschner, H., McDermid, R. M., and Peletier, R. F. (2006). The SAURON project - V. Integral-field emission-line kinematics of 48 elliptical and lenticular galaxies. *MNRAS*, 366, 1151.

Schaefer, A. L., Croom, S. M., Scott, N., Brough, S., Allen, J. T., Bekki, K., Bland-Hawthorn, J., Bloom, J. V., Bryant, J. J., Cortese, L., Davies, L. J. M., Federrath, C., Fogarty, L. M. R., Green, A. W., Groves, B., Hopkins, A. M., Konstantopoulos, I. S., López-Sánchez, A. R., Lawrence, J. S., McElroy, R. E., Medling, A. M., Owers, M. S., Pracy, M. B., Richards, S. N., Robotham, A. S. G., van de Sande, J., Tonini, C., and Yi, S. K. (2019). The SAMI Galaxy Survey: observing the environmental quenching of star formation in GAMA groups. *MNRAS*, 483, 2851.

Schiavon, R. P. (2007). Population Synthesis in the Blue. IV. Accurate Model Predictions for Lick Indices and UBV Colors in Single Stellar Populations. *ApJS*, 171, 146.

Schindler, S., Binggeli, B., and Böhringer, H. (1999). Morphology of the Virgo cluster: Gas versus galaxies. *A&A*, 343, 420.

Schlafly, E. F. and Finkbeiner, D. P. (2011). Measuring Reddening with Sloan Digital Sky Survey Stellar Spectra and Recalibrating SFD. *ApJ*, 737, 103.

Schönrich, R. and Binney, J. (2009). Chemical evolution with radial mixing. *MNRAS*, 396, 203.

Schroyen, J., de Rijcke, S., Valcke, S., Cloet-Osselaer, A., and Dejonghe, H. (2011). Simulations of the formation and evolution of isolated dwarf galaxies - II. Angular momentum as a second parameter. *MNRAS*, 416, 601.

Schwarzschild, M. (1979). A numerical model for a triaxial stellar system in dynamical equilibrium. *ApJ*, 232, 236.

Scott, N., Eftekhari, F. S., Peletier, R. F., Bryant, J. J., Bland-Hawthorn, J., Capaccioli, M., Croom, S. M., Drinkwater, M., Falcón-Barroso, J., Hilker, M., Iodice, E., Lorente, N. F. P., Mieske, S., Spavone, M., van de Ven, G., and Venhola, A. (2020). The SAMI-Fornax Dwarfs Survey I: sample, observations, and the specific stellar angular momentum of dwarf elliptical galaxies. *MNRAS*, 497, 1571.

Serna, A. and Gerbal, D. (1996). Dynamical search for substructures in galaxy clusters. A hierarchical clustering method. *A&A*, 309, 65.

Serra, P. and Trager, S. C. (2007). On the interpretation of the age and chemical composition of composite stellar populations determined with line-strength indices. *MNRAS*, 374, 769.

Shapley, H. (1938). Two Stellar Systems of a New Kind. *Nature*, 142, 715.

Shen, S. and Yin, J. (2020). Stellar population synthesis of galaxies with chemical evolution model. In Boquien, M., Lusso, E., Gruppioni, C., and Tissera, P., editors, *Panchromatic Modelling with Next Generation Facilities*, volume 341, pages 147–151.

Shi, J., Wang, H., and Mo, H. J. (2015). Flow Patterns around Dark Matter Halos: The Link between Halo Dynamical Properties and Large-scale Tidal Field. *ApJ*, 807, 37.

Simien, F. and Prugniel, P. (2002). Kinematical data on early-type galaxies. VI. *A&A*, 384, 371.

Skrutskie, M. F., Cutri, R. M., Stiening, R., Weinberg, M. D., Schneider, S., Carpenter, J. M., Beichman, C., Capps, R., Chester, T., Elias, J., Huchra, J., Liebert, J., Lonsdale, C., Monet, D. G., Price, S., Seitzer, P., Jarrett, T., Kirkpatrick, J. D., Gizis, J. E., Howard, E., Evans, T., Fowler, J., Fullmer, L., Hurt, R., Light, R., Kopan, E. L., Marsh, K. A., McCallon, H. L., Tam, R., Van Dyk, S., and Wheelock, S. (2006). The Two Micron All Sky Survey (2MASS). *AJ*, 131, 1163.

Smith, R., Michea, J., Pasquali, A., Calderón-Castillo, P., Kraljic, K., Paudel, S., Lisker, T., Shin, J., Ko, J., Peletier, R. F., and Grebel, E. K. (2021). Brought to Light. II. Revealing the Origins of Cloaked Spiral Features in Cluster Passive Dwarf Galaxies. *ApJ*, 912, 149.

Smith, R., Pacifici, C., Pasquali, A., and Calderón-Castillo, P. (2019). Investigating the Stellar Mass Growth Histories of Satellite Galaxies as a Function of Infall Time Using Phase-space. *ApJ*, 876, 145.

Smith, R., Sánchez-Janssen, R., Beasley, M. A., Candlish, G. N., Gibson, B. K., Puzia, T. H., Janz, J., Knebe, A., Aguerri, J. A. L., Lisker, T., Hensler, G., Fellhauer, M., Ferrarese, L., and Yi, S. K. (2015). The sensitivity of harassment to orbit: mass loss from early-type dwarfs in galaxy clusters. *MNRAS*, 454, 2502.

Smith, R. J., Lucey, J. R., Hudson, M. J., Allanson, S. P., Bridges, T. J., Hornschemeier, A. E., Marzke, R. O., and Miller, N. A. (2009). A spectroscopic survey of dwarf galaxies in the Coma cluster: stellar populations, environment and downsizing. *MNRAS*, 392, 1265.

Somerville, R. S. and Primack, J. R. (1999). Semi-analytic modelling of galaxy formation: the local Universe. *MNRAS*, 310, 1087.

Sommer-Larsen, J., Beers, T. C., Flynn, C., Wilhelm, R., and Christensen, P. R. (1997). A Dynamical and Kinematic Model of the Galactic Stellar Halo and Possible Implications for Galaxy Formation Scenarios. *ApJ*, 481, 775.

Sorce, J. G., Dubois, Y., Blaizot, J., McGee, S. L., Yepes, G., and Knebe, A. (2021). I - A hydrodynamical CLONE of the Virgo cluster of galaxies to confirm observationally driven formation scenarios. *MNRAS*, 504, 2998.

Soto, K. T., Lilly, S. J., Bacon, R., Richard, J., and Conseil, S. (2016). ZAP - enhanced PCA sky subtraction for integral field spectroscopy. *MNRAS*, 458, 3210.

Sparke, L. S. and Gallagher, John S., I. (2000). *Galaxies in the universe : an introduction*.

Sparke, L. S. and Gallagher, John S., I. (2007). *Galaxies in the Universe*.

Statler, T. S. (1988). Orbital Decay in Aspherical Galaxies. I. Oblate Systems. *ApJ*, 331, 71.

Steinhauser, D., Schindler, S., and Springel, V. (2016). Simulations of ram-pressure stripping in galaxy-cluster interactions. *A&A*, 591, A51.

Steinmetz, M. and Navarro, J. F. (2002). The hierarchical origin of galaxy morphologies. *NewA*, 7, 155.

Stetson, P. B., Hesser, J. E., and Smecker-Hane, T. A. (1998). Homogeneous Photometry for Star Clusters and Resolved Galaxies. I. A Survey of Bright Stars in the Fornax Dwarf Spheroidal Galaxy. *PASP*, 110, 533.

Steyrleithner, P., Hensler, G., and Boselli, A. (2020). The effect of ram-pressure stripping on dwarf galaxies. *MNRAS*, 494, 1114.

Stoughton, C., Lupton, R. H., Bernardi, M., Blanton, M. R., Burles, S., Castander, F. J., Connolly, A. J., Eisenstein, D. J., Frieman, J. A., Hennessy, G. S., Hindsley, R. B., Ivezić, Ž., Kent, S., Kunszt, P. Z., Lee, B. C., Meiksin, A., Munn, J. A., Newberg, H. J., Nichol, R. C., Nicinski, T., Pier, J. R., Richards, G. T., Richmond, M. W., Schlegel, D. J., Smith, J. A., Strauss, M. A., SubbaRao, M., Szalay, A. S., Thakar, A. R., Tucker, D. L., Vanden Berk, D. E., Yanny, B., Adelman, J. K., Anderson, John E., J., Anderson, S. F., Annis, J., Bahcall, N. A., Bakken, J. A., Bartelmann, M., Bastian, S., Bauer, A., Berman, E., Böhringer, H., Boroski, W. N., Bracker, S., Briegel, C., Briggs, J. W., Brinkmann, J., Brunner, R., Carey, L., Carr, M. A., Chen, B.,

Christian, D., Colestock, P. L., Crocker, J. H., Csabai, I., Czarapata, P. C., Dalcanton, J., Davidsen, A. F., Davis, J. E., Dehnen, W., Dodelson, S., Doi, M., Dombeck, T., Donahue, M., Ellman, N., Elms, B. R., Evans, M. L., Eyer, L., Fan, X., Federwitz, G. R., Friedman, S., Fukugita, M., Gal, R., Gillespie, B., Glazebrook, K., Gray, J., Grebel, E. K., Greenawalt, B., Greene, G., Gunn, J. E., de Haas, E., Haiman, Z., Haldeman, M., Hall, P. B., Hamabe, M., Hansen, B., Harris, F. H., Harris, H., Harvanek, M., Hawley, S. L., Hayes, J. J. E., Heckman, T. M., Helmi, A., Henden, A., Hogan, C. J., Hogg, D. W., Holmgren, D. J., Holtzman, J., Huang, C.-H., Hull, C., Ichikawa, S.-I., Ichikawa, T., Johnston, D. E., Kauffmann, G., Kim, R. S. J., Kimball, T., Kinney, E., Klaene, M., Kleinman, S. J., Klypin, A., Knapp, G. R., Korienek, J., Krolik, J., Kron, R. G., Krzesiński, J., Lamb, D. Q., Leger, R. F., Limmongkol, S., Lindenmeyer, C., Long, D. C., Loomis, C., Loveday, J., MacKinnon, B., Mannery, E. J., Mantsch, P. M., Margon, B., McGehee, P., McKay, T. A., McLean, B., Menou, K., Merelli, A., Mo, H. J., Monet, D. G., Nakamura, O., Narayanan, V. K., Nash, T., Neilsen, Eric H., J., Newman, P. R., Nitta, A., Odenkirchen, M., Okada, N., Okamura, S., Ostriker, J. P., Owen, R., Pauls, A. G., Peoples, J., Peterson, R. S., Petravick, D., Pope, A., Pordes, R., Postman, M., Prosapio, A., Quinn, T. R., Rechenmacher, R., Rivetta, C. H., Rix, H.-W., Rockosi, C. M., Rosner, R., Ruthmansdorfer, K., Sandford, D., Schneider, D. P., Scranton, R., Sekiguchi, M., Sergey, G., Sheth, R., Shimasaku, K., Smee, S., Snedden, S. A., Stebbins, A., Stubbs, C., Szapudi, I., Szkody, P., Szokoly, G. P., Tabachnik, S., Tsvetanov, Z., Uomoto, A., Vogeley, M. S., Voges, W., Waddell, P., Walterbos, R., Wang, S.-i., Watanabe, M., Weinberg, D. H., White, R. L., White, S. D. M., Wilhite, B., Wolfe, D., Yasuda, N., York, D. G., Zehavi, I., and Zheng, W. (2002). Sloan Digital Sky Survey: Early Data Release. *AJ*, 123, 485.

Sybilska, A., Lisker, T., Kuntschner, H., Vazdekis, A., van de Ven, G., Peletier, R., Falcón-Barroso, J., Vijayaraghavan, R., and Janz, J. (2017). The hELENa project - I. Stellar populations of early-type galaxies linked with local environment and galaxy mass. *MNRAS*, 470, 815.

Tal, T., van Dokkum, P. G., Nelan, J., and Bezanson, R. (2009). The Frequency of Tidal Features Associated with Nearby Luminous Elliptical Galaxies From a Statistically Complete Sample. *AJ*, 138, 1417.

Taylor, P. and Kobayashi, C. (2017). The metallicity and elemental abundance gradients of simulated galaxies and their environmental dependence. *MNRAS*, 471, 3856.

Teyssier, R. (2002). Cosmological hydrodynamics with adaptive mesh refinement. A new high resolution code called RAMSES. *A&A*, 385, 337.

Thomas, D., Greggio, L., and Bender, R. (1999). Constraints on galaxy formation from alpha-enhancement in luminous elliptical galaxies. *MNRAS*, 302, 537.

Thomas, D., Maraston, C., and Bender, R. (2003). Stellar population models of Lick indices with variable element abundance ratios. *MNRAS*, 339, 897.

Tinker, J. L. and Wetzel, A. R. (2010). WHAT DOES CLUSTERING TELL US ABOUT THE BUILDUP OF THE RED SEQUENCE? *The Astrophysical Journal*, 719, 88.

Tinsley, B. M. (1979). Stellar lifetimes and abundance ratios in chemical evolution. *ApJ*, 229, 1046.

Toloba, E., Boselli, A., Cenarro, A. J., Peletier, R. F., Gorgas, J., Gil de Paz, A., and Muñoz-Mateos, J. C. (2011). Formation and evolution of dwarf early-type galaxies in the Virgo cluster. I. Internal kinematics. *A&A*, 526, A114.

Toloba, E., Boselli, A., Gorgas, J., Peletier, R. F., Cenarro, A. J., Gadotti, D. A., Gil de Paz, A., Pedraz, S., and Yildiz, U. (2009). Kinematic Properties as Probes of the Evolution of Dwarf Galaxies in the Virgo Cluster. *ApJL*, 707, L17.

Toloba, E., Boselli, A., Peletier, R. F., Falcón-Barroso, J., van de Ven, G., and Gorgas, J. (2012). Formation and evolution of dwarf early-type galaxies in the Virgo cluster. II. Kinematic scaling relations. *A&A*, 548, A78.

Toloba, E., Guhathakurta, P., Boselli, A., Peletier, R. F., Emsellem, E., Lisker, T., van de Ven, G., Simon, J. D., Falcón-Barroso, J., Adams, J. J., Benson, A. J., Boissier, S., den Brok, M., Gorgas, J., Hensler, G., Janz, J., Laurikainen, E., Paudel, S., Ryś, A., and Salo, H. (2015). Stellar Kinematics and Structural Properties of Virgo Cluster Dwarf Early-type Galaxies from the SMAKCED Project. III. Angular Momentum and Constraints on Formation Scenarios. *ApJ*, 799, 172.

Toloba, E., Guhathakurta, P., van de Ven, G., Boissier, S., Boselli, A., den Brok, M., Falcón-Barroso, J., Hensler, G., Janz, J., Laurikainen, E., Lisker, T., Paudel, S., Peletier, R. F., Ryś, A., and Salo, H. (2014). Stellar Kinematics and Structural Properties of Virgo Cluster Dwarf Early-type Galaxies from the SMAKCED Project. I. Kinematically Decoupled Cores and Implications for Infallen Groups in Clusters. *ApJ*, 783, 120.

Trager, S. C., Worthey, G., Faber, S. M., Burstein, D., and González, J. J. (1998). Old Stellar Populations. VI.

Absorption-Line Spectra of Galaxy Nuclei and Globular Clusters. *ApJS*, 116, 1.

Trager, S. C., Worthey, G., Faber, S. M., and Dressler, A. (2005). Hot stars in old stellar populations: a continuing need for intermediate ages. *MNRAS*, 362, 2.

Urich, L., Lisker, T., Janz, J., van de Ven, G., Leaman, R., Boselli, A., Paudel, S., Sybilska, A., Peletier, R. F., den Brok, M., Hensler, G., Toloba, E., Falcón-Barroso, J., and Niemi, S.-M. (2017). Young, metal-enriched cores in early-type dwarf galaxies in the Virgo cluster based on colour gradients. *A&A*, 606, A135.

Valluri, M. (1994). A Model for the Declining Rotation Curves of Cluster Spiral Galaxies. *ApJ*, 430, 101.

van den Bergh, S. (1976). A new classification system for galaxies. *ApJ*, 206, 883.

van den Bosch, F. C. (2002). The impact of cooling and feedback on disc galaxies. *MNRAS*, 332, 456.

van den Bosch, F. C., Aquino, D., Yang, X., Mo, H. J., Pasquali, A., McIntosh, D. H., Weinmann, S. M., and Kang, X. (2008). The importance of satellite quenching for the build-up of the red sequence of present-day galaxies. *MNRAS*, 387, 79.

van den Bosch, F. C., Burkert, A., and Swaters, R. A. (2001). The angular momentum content of dwarf galaxies: new challenges for the theory of galaxy formation. *MNRAS*, 326, 1205.

van Zee, L., Skillman, E. D., and Haynes, M. P. (2004). Rotationally Supported Virgo Cluster Dwarf Elliptical Galaxies: Stripped Dwarf Irregular Galaxies? *AJ*, 128, 121.

Vaughan, S. P., Davies, R. L., Zieleniewski, S., and Houghton, R. C. W. (2018). The stellar population and initial mass function of NGC 1399 with MUSE. *MNRAS*, 479, 2443.

Vazdekis, A., Casuso, E., Peletier, R. F., and Beckman, J. E. (1996). A New Chemo-evolutionary Population Synthesis Model for Early-Type Galaxies. I. Theoretical Basis. *ApJS*, 106, 307.

Vazdekis, A., Koleva, M., Ricciardelli, E., Röck, B., and Falcón-Barroso, J. (2016). UV-extended E-MILES stellar population models: young components in massive early-type galaxies. *MNRAS*, 463, 3409.

Vazdekis, A., Sánchez-Blázquez, P., Falcón-Barroso, J., Cenarro, A. J., Beasley, M. A., Cardiel, N., Gorgas, J., and Peletier, R. F. (2010). Evolutionary stellar population synthesis with MILES - I. The base models and a new line index system. *MNRAS*, 404, 1639.

Venhola, A., Peletier, R., Laurikainen, E., Salo, H., Iodice, E., Mieske, S., Hilker, M., Wittmann, C., Paolillo, M., Cantiello, M., Janz, J., Spavone, M., D'Abrusco, R., van de Ven, G., Napolitano, N., Verdoes Kleijn, G., Capaccioli, M., Grado, A., Valentijn, E., Falcón-Barroso, J., and Limatola, L. (2019). The Fornax Deep Survey (FDS) with VST. VI. Optical properties of the dwarf galaxies in the Fornax cluster. *A&A*, 625, A143.

Vijayaraghavan, R., Gallagher, J. S., and Ricker, P. M. (2015). The dynamical origin of early-type dwarfs in galaxy clusters: a theoretical investigation. *MNRAS*, 447, 3623.

Villalobos, Á., De Lucia, G., Borgani, S., and Murante, G. (2012). Simulating the evolution of disc galaxies in a group environment - I. The influence of the global tidal field. *MNRAS*, 424, 2401.

Villalobos, Á. and Helmi, A. (2008). Simulations of minor mergers - I. General properties of thick discs. *MNRAS*, 391, 1806.

Vincenzo, F., Weinberg, D. H., Miglio, A., Lane, R. R., and Roman-Lopes, A. (2021). The distribution of [α/Fe] in the Milky Way disc. *arXiv e-prints*, page arXiv:2101.04488.

Vollmer, B., Cayatte, V., Balkowski, C., and Duschl, W. J. (2001). Ram Pressure Stripping and Galaxy Orbits: The Case of the Virgo Cluster. *ApJ*, 561, 708.

Vulcani, B., Poggianti, B. M., Gullieuszik, M., Moretti, A., Tonnesen, S., Jaffé, Y. L., Fritz, J., Fasano, G., and Bettoni, D. (2018). Enhanced Star Formation in Both Disks and Ram-pressure-stripped Tails of GASP Jellyfish Galaxies. *ApJL*, 866, L25.

Walcher, C. J., Wisotzki, L., Bekeraité, S., Husemann, B., Iglesias-Páramo, J., Backsmann, N., Barrera Ballesteros, J., Catalán-Torrecilla, C., Cortijo, C., del Olmo, A., Garcia Lorenzo, B., Falcón-Barroso, J., Jilkova, L., Kalinova, V., Mast, D., Marino, R. A., Méndez-Abreu, J., Pasquali, A., Sánchez, S. F., Trager, S., Zibetti, S., Aguerri, J. A. L., Alves, J., Bland-Hawthorn, J., Boselli, A., Castillo Morales, A., Cid Fernandes, R., Flores, H., Galbany, L., Gallazzi, A., García-Benito, R., Gil de Paz, A., González-Delgado, R. M., Jahnke, K., Jungwiert, B., Kehrig, C., Lyubenova, M., Márquez Perez, I., Masegosa, J., Monreal Ibero, A., Pérez, E., Quirrenbach, A., Rosales-Ortega, F. F., Roth, M. M., Sanchez-Blazquez, P., Spekkens, K., Tundo, E., van de Ven, G., Verheijen, M. A. W., Vilchez, J. V., and Ziegler, B. (2014). CALIFA: a diameter-selected sample for an integral field spectroscopy galaxy survey. *A&A*, 569, A1.

Walo-Martín, D., Falcón-Barroso, J., Dalla Vecchia, C., Pérez, I., and Negri, A. (2020). Kinematic analysis of

EAGLE simulations: Evolution of λ_{Re} and its connection with mergers and gas accretion. *arXiv e-prints*, page arXiv:2004.08598.

Weijmans, A.-M., de Zeeuw, P. T., Emsellem, E., Krajnović, D., Lablanche, P.-Y., Alatalo, K., Blitz, L., Bois, M., Bournaud, F., Bureau, M., Cappellari, M., Crocker, A. F., Davies, R. L., Davis, T. A., Duc, P.-A., Khochfar, S., Kuntschner, H., McDermid, R. M., Morganti, R., Naab, T., Oosterloo, T., Sarzi, M., Scott, N., Serra, P., Verdoes Kleijn, G., and Young, L. M. (2014). The ATLAS ^{3D} project - XXIV. The intrinsic shape distribution of early-type galaxies. *MNRAS*, 444, 3340.

Weilbacher, P. M., Palsa, R., Streicher, O., Bacon, R., Urrutia, T., Wisotzki, L., Conseil, S., Husemann, B., Jarno, A., Kelz, A., Pécontal-Rousset, A., Richard, J., Roth, M. M., Selman, F., and Vernet, J. (2020). The data processing pipeline for the MUSE instrument. *A&A*, 641, A28.

Weilbacher, P. M., Streicher, O., and Palsa, R. (2016). MUSE-DRP: MUSE Data Reduction Pipeline.

Weilbacher, P. M., Streicher, O., Urrutia, T., Jarno, A., Pécontal-Rousset, A., Bacon, R., and Böhm, P. (2012). Design and capabilities of the MUSE data reduction software and pipeline. In *Proc. SPIE*, volume 8451 of *Society of Photo-Optical Instrumentation Engineers (SPIE) Conference Series*, page 84510B.

Wetzel, A. R. (2011). On the orbits of infalling satellite haloes. *MNRAS*, 412, 49.

Wetzel, A. R., Tinker, J. L., Conroy, C., and van den Bosch, F. C. (2013). Galaxy evolution in groups and clusters: satellite star formation histories and quenching time-scales in a hierarchical Universe. *MNRAS*, 432, 336.

Wheeler, C., Pace, A. B., Bullock, J. S., Boylan-Kolchin, M., Oñorbe, J., Elbert, O. D., Fitts, A., Hopkins, P. F., and Kereš, D. (2017). The no-spin zone: rotation versus dispersion support in observed and simulated dwarf galaxies. *MNRAS*, 465, 2420.

Wheeler, C., Phillips, J. I., Cooper, M. C., Boylan-Kolchin, M., and Bullock, J. S. (2014). The surprising inefficiency of dwarf satellite quenching. *MNRAS*, 442, 1396.

Whitmore, B. C., Gilmore, D. M., and Jones, C. (1993). What Determines the Morphological Fractions in Clusters of Galaxies? *ApJ*, 407, 489.

Wilson, A. G. (1955). Sculptor-Type Systems in the Local Group of Galaxies. *PASP*, 67, 27.

Yozin, C. and Bekki, K. (2016). The global warming of group satellite galaxies. *MNRAS*, 460, 3968.

Zibetti, S., Gallazzi, A. R., Hirschmann, M., Consolandi, G., Falcón-Barroso, J., van de Ven, G., and Lyubenova, M. (2020). Insights into formation scenarios of massive early-type galaxies from spatially resolved stellar population analysis in CALIFA. *MNRAS*, 491, 3562.

Zoldan, A., De Lucia, G., Xie, L., Fontanot, F., and Hirschmann, M. (2019). The evolution of sizes and specific angular momenta in hierarchical models of galaxy formation and evolution. *MNRAS*, 487, 5649.

Zwicky, F. (1933). Die Rotverschiebung von extragalaktischen Nebeln. *Helvetica Physica Acta*, 6, 110.